UNIVERSITÉ DU
LUXEMBOURG

PhD-FSTC-2017-38
The Faculty of Sciences, Technology and Communication

DISSERTATION

Defence held on 14/07/2017 in Luxembourg

to obtain the degree of

DOCTEUR DE L'UNIVERSITÉ DU LUXEMBOURG

EN SCIENCES DE L'INGÉNIEUR

by

Sebastian SCHOMMER

Born on 10th February 1982 in Lebach (Germany)

DAMAGE DETECTION IN PRESTRESSED CONCRETE BRIDGES BASED ON STATIC LOAD TESTING, SAGGING AND MODAL PARAMETERS, USING MEASUREMENTS AND MODEL UPDATING

Dissertation defence committee
Dr.-Ing. Stefan Maas, dissertation supervisor
Professeur, Université du Luxembourg

Dr.-Ing. Markus Schäfer, Chairman
Professeur, Université du Luxembourg

Dr.-Ing. Arno Zürbes, Vice-Chairman
Professor, Technische Hochschule Bingen

Dr. Alfred Strauss
Associate Professor, Universität für Bodenkultur Wien

Dr.-Ing. Michael Link
Professor, Universität Kassel

PREAMBLE

After my work as a scientific assistant at the Trier University of Applied Sciences, site Birkenfeld, in the field of automation technology and robotics, I was given the opportunity to undertake a research project at the University of Luxembourg (UL) as a PhD candidate. The subject was the detection of damages on civil engineering structures, especially bridges, based on experimentally determined dynamic properties as well as results from static tests.

The research group at the UL that I joined has been working on the topic since several years. Therefore, I continued the work of my three predecessors as PhD candidate who all dealt with different aspects of the topic. They appear as my first references: Waltering (2009) [1], Bungard (2011) [2] and Mahowald (2013) [3].

Here the basic idea for the damage detection is: changes in a structure due to damage must be reflected in the stiffness distribution. In a process called system identification, it may be experimentally determined as structural matrix based on dynamic measurements or static loading tests. Some useful dynamic features can be cited as eigenfrequencies, mode shapes, damping and modal masses. From static tests, deflection lines or influence lines appear also appropriate.

Therefore, the above-cited parameters can be used to calculate a wide range of so-called damage indicators. Generally, data for a reference state must be available which enables the determination of changes for another examined state. Depending on the nature of the specific damage indicator, it is either only possible to determine whether a damage is present or not or even better to locate it and to assess the severity of the damage. The highest level is an estimate of the remaining life time of the structure. These levels of damage assessment were already defined by Rytter (1993) [4].

At first view, this topic, which arose from civil engineering, seemed not to fit into my previous activity, which had dealt extensively with control engineering and robotics. On a closer look however, there are considerable parallels to methods customary in control engineering.

For instance, in a so-called experimental modal analysis, structures are excited to vibrations, whereby the forces are also measured. The resulting vibration of the structure is captured for instance by accelerometers or optically with laser vibrometers. Based on the recorded data, it

is possible to calculate the dynamic properties and the so-called transfer function or transfer function matrix of the system, which is typical for Multiple Degree Of Freedom systems (MDOF). With the latter, the vibration response of a system can be predicted to an arbitrary excitation. The methodology thus differs in no way from the already mentioned system identification customary in control engineering on the basis of measured input and output signals, actually it is part of it.

For a mechanical engineer, it is indeed interesting that the subject matter thus relates various fields of interest, system theory and modal analysis, which are generally used in mechanical engineering, to structural engineering, in which usually static analyses are common. This gave me the opportunity to contribute my knowledge and experience so far, to deepen it and to gain insight into civil engineering methods.

While the theoretical fundamentals of this topic, such as the modal analysis, have been already well developed, the research work in this area in the UL concentrates on carrying out experiments on real structures and thus under realistic ambient conditions such as variable temperatures. These environmental conditions show obviously considerable influence on the system properties and must be separated from the influence of damage in order to successfully carry out a damage assessment.

Therefore, during my four-years work, some very costly, time consuming and laborious experiments were performed, which would not have been possible without the help and experience of many people.

First I would like to thank Prof. Dr.-Ing. Stefan Maas for giving me, as a graduate of a university of applied sciences, the opportunity to work on a dissertation and for supervising the thesis. The same applies to the other two members of the dissertation supervisory committee (CET) Ass. Prof. Dr.-Ing. Danièle Waldmann and Prof. Dr.-Ing. Arno Zürbes. Furthermore, I thank Prof. Dr.-Ing. Markus Schäfer, Assoc. Prof. Dr. Alfred Strauss and Prof. Dr.-Ing. Michael Link for taking the time to participate in the jury for the defence of my doctoral thesis.

My colleague Dr. Viet Ha Nguyen helped me a lot in performing measurements and evaluating the results as well as in writing publications. Furthermore, the help of Prof. Dr. i.r. Guido De Roeck with corrections of publications was highly appreciated. In addition, I want to thank my predecessor Dr. Jean Mahowald above all for his explanations at the beginning of my research project.

A great thank-you goes to the technical support staff at the University of Luxembourg, namely Gilbert Klein, Ed Weyer, Marc Seil, Vicente Reis Adonis, Claude Colle, Ken Adam, Cédric Bruyère, Ralph Reiter, and Raphael Hinger. Without their hard work, knowledge and experience it would not have been possible to realise the experiments, which were necessary for the completion of the present thesis. This does not only include their support for the large test series at the Grevenmacher bridge and in the port of Mertert, but also their help at smaller issues, like for instance material tests, measurements of prestress in tendons, measurements at a traffic road bridge in Mersch before its demolition or also license management for software used in the thesis. Furthermore, the help of Felix Norman Teferle with optical measurements at a test setup, is not to forget. I also would like to thank the members of the SIU support unit Kirchberg, especially Marco de Cillia and Ulrich Siegel for their support when it comes to computer issues like software installation or hardware upgrades. Additionally, the help of the secretaries of the RUES unit, Simone Drees and Annabella Simon, in administrative issues shall not be forgotten here.

Furthermore, I would like to thank the students, who dealt with individual problems within their final theses and thus provided important impetus for this doctoral thesis. These were namely Jan Even, who helped with the design of experiments in his *travail de candidature* as well as Patrick Pereira Dias, Maximilien Garroi and Cedric Martin, who developed different varieties of Finite Element (FE) models of bridges for their bachelor theses.

I would also like to thank *l'Administration des Ponts et Chaussées Grand-Duché de Luxembourg (P&C)* for their help on many occasions. At first these are Didier Gilles and Fernandes Gilberto of *Division des Ouvrages d'Art* for giving occasions to perform in situ tests at real structures, for providing much information about the considered bridges and the way how bridge inspections are currently carried out in Luxembourg as well as for taking time for discussions about the topic. Furthermore, Philippe Goedert of *Service Régional Mersch* and René Goergen of *Division des Travaux Neufs* helped us a lot to organise measurements at an old bridge in Mersch (Luxembourg) before its demolition in 2016 and the transport of a concrete beam of this bridge to the new UL campus in Belval, which will be used for future experiments. Finally, Michel Maas of *Division des Géomètres et de la Photogrammétrie* provided useful information about the usage of photogrammetry by P&C for carrying out measurements by aerial survey. It is an idea to test the usability of such measurements for the damage assessment of bridges at future projects.

Preamble

ABSTRACT

English

Bridges are an essential part of nowadays infrastructure to cross natural and artificial obstacles like rivers, valleys or other roads and railways. Many concrete bridges were built in the last 70 years. The traffic density has increased immensely over the last decades and the bridges are suffering from corrosion and wear. Nevertheless, the safety of the infrastructure has to be guaranteed and therefore it is very important to find efficient methods for structural health monitoring.

For this purpose, visual inspections are the most widely adopted in reality today. Considering the size of most bridge structures, it is understandable that these tests are generally very time-consuming and many personnel are needed, so they are cost-intensive. However, it is not always guaranteed that all damage can be found as only the surface is accessible. For instance, internal damage, such as corrosion of passive reinforcements or prestressed tendons, is difficult to detect. In addition, small cracks can remain undetected when covered by paints or dirt.

Therefore, it is important to complement the standard methods with advanced alternatives. The aim is therefore not necessarily to replace visual inspections, but rather to find efficient methods for amendment.

An idea being vigorously discussed in the scientific community is based on vibration measurements of a structure to assess its dynamic behaviour. The occurrence of damage will change the system properties, as it changes above all the stiffness distribution. So the system identification process in principle allows detection of changes of eigenfrequencies and hence stiffness.

The main problem in practice on real bridges is that the robustness of a method is often insufficient, as the measured parameters are often also influenced by temperature changes. It will be shown that the impact of temperature change, e.g. between night and day, on the system properties is much higher than the influence of small damage. Furthermore, changes in soil and bearing conditions between different seasons can play a role. These environmental effects have to be taken into account while performing measurements for damage assessment. For this purpose, strategies are proposed to compensate environmental effects.

Abstract

Therefore, this thesis focuses on measurements under real environmental conditions, outside a laboratory. Different methods for damage assessment or stiffness tracking based on measured static and on dynamic properties of structures are deployed. Finally, the measured and analysed physical properties of the bridges in this thesis are: eigenfrequencies, mode shapes, sagging under own weight and the deflection line under a static test-loading. These quantities are tracked and artificial damage is introduced stepwise to a test-beam of a real bridge. Damage assessment and localisation is tried directly with the measured quantities but also by model-updating of a finite element model. This solid model is divided in a special way in different slices. It is possible to change the stiffness distribution along the axis of the simulated beam by varying the Young's moduli of these slices. Furthermore, to reduce the number of free parameters for the subsequent up-dating process, an exponential damage function is introduced that describes the stiffness distribution. At first, the model was designed to fit a healthy reference state. Now measurement data from the artificially damaged test-beam are introduced and the model is updated by changing the Young's moduli of the slices to minimise a special objective function containing the measured and simulated physical quantities. The comparison of initial and updated model allows a quantification and localisation of damage. Finally, the slice width is reduced around the identified damage region to improve the process.

Keywords: structural health monitoring, damage detection, damage indicators, dynamic properties, model updating

Deutsch

Brücken sind ein wesentlicher Bestandteil der heutigen Infrastruktur, um natürliche und künstliche Hindernisse zu überqueren, wie Flüsse, Täler oder andere Straßen und Eisenbahnen. Viele Betonbrücken wurden in den letzten 70 Jahren gebaut. Die Verkehrsdichte hat sich immens gesteigert über die letzten Jahrzehnte und Brücken leiden unter Korrosion und Abnutzung. Nichtsdestotrotz muss die Sicherheit der Infrastruktur garantiert werden und daher ist es sehr wichtig, effiziente Methoden zur Überwachung struktureller Schäden zu finden.

Zu diesem Zweck sind visuelle Inspektionen heute am weitesten verbreitet. In Anbetracht der Größe der meisten Brückenstrukturen ist es verständlich, dass diese Prüfungen im Allgemeinen sehr zeit- und personalaufwändig sind und daher kostenintensiv. Es ist jedoch nicht immer gewährleistet, dass alle Schäden gefunden werden können, da nur die Oberfläche zugänglich ist. Zum Beispiel sind innere Beschädigungen, wie Korrosion an passiven Verstärkungen oder vorgespannten Kabeln, schwer zu entdecken. Auch kleine Risse können unentdeckt bleiben, wenn sie von Anstrichen oder Schmutz bedeckt sind.

Daher ist es wichtig, die Standardmethoden durch fortgeschrittene Alternativen zu ergänzen. Ziel ist es dabei nicht notwendigerweise, visuelle Inspektionen zu ersetzen, sondern vielmehr effiziente zusätzliche Methoden zu finden.

Eine Idee, die von Wissenschaftlern ausgiebig diskutiert wird, beruht auf Schwingungsmessungen einer Struktur, um ihr dynamisches Verhalten zu beurteilen. Das Auftreten von Schäden ändert die Systemeigenschaften, da es vor allem die Steifigkeitsverteilung ändert. So erlaubt der Systemidentifizierungsprozess grundsätzlich die Erkennung von Änderungen der Eigenfrequenzen und damit der Steifigkeit.

Das Hauptproblem in der Praxis auf realen Brücken ist, dass die Robustheit eines Verfahrens oft unzureichend ist, da die gemessenen Eigenschaften oft auch durch Temperaturänderungen beeinflusst werden. Es wird gezeigt, dass der Einfluss der Temperaturänderung, z.B. zwischen Nacht und Tag, auf die Systemeigenschaften viel höher ist, als der Einfluss von kleinen Schäden. Darüber hinaus können Veränderungen der Boden- und Lagerbedingungen zwischen verschiedenen Jahreszeiten eine Rolle spielen. Diese Umweltauswirkungen sind bei der Durchführung von Messungen zur Schadensbeurteilung zu berücksichtigen. Zu diesem Zweck werden Strategien vorgeschlagen, um Umweltauswirkungen zu kompensieren.

Abstract

Daher konzentriert sich diese Arbeit auf Messungen unter realen Umgebungsbedingungen, außerhalb eines Labors.

Es werden verschiedene Methoden zur Schadensbeurteilung oder Steifigkeitsverfolgung basierend auf gemessenen statischen und dynamischen Eigenschaften von Strukturen eingesetzt. Schlussendlich sind die gemessenen und analysierten physikalischen Eigenschaften der Brücken in dieser Arbeit: Eigenfrequenzen, Schwingungsformen, Absacken unter Eigengewicht und die Biegelinie unter statischer Testbelastung. Diese Größen werden verfolgt und künstliche Schädigungen werden schrittweise an einem Testträger von einer echten Brücke verursacht. Schadensbeurteilung und Lokalisierung erfolgt direkt auf Grundlage der gemessenen Größen, und zusätzlich durch Updating eines Finite-Elemente-Modells. Dieses Solid Modell ist in einer speziellen Weise in verschiedene Scheiben unterteilt. Es ist möglich, die Steifigkeitsverteilung entlang der Achse des simulierten Trägers durch Variieren der Elastizitätsmoduln dieser Scheiben zu ändern. Des Weiteren wird zur Verringerung der Anzahl der freien Parameter für den nachfolgenden Updating-Prozess eine exponentielle Schadensfunktion eingeführt, welche die Steifigkeits-verteilung beschreibt. Zuerst wurde das Modell so entworfen, dass es zum ungeschädigten Referenzzustand passt. Nun werden Messdaten aus dem künstlich beschädigten Testträger eingeführt und das Modell wird durch Ändern der Elastizitätsmodule der Scheiben aktualisiert, mit dem Ziel eine spezielle Zielfunktion zu minimieren, die die gemessenen und simulierten physikalischen Größen enthält. Der Vergleich des ursprünglichen und des aktualisierten Modells ermöglicht eine Quantifizierung und Lokalisierung von Schäden. Schließlich wird die Scheibenbreite um den identifizierten Schadensbereich reduziert, um den Prozess zu verbessern.

Stichwörter: Überwachung struktureller Schäden, Schadensdetektion, Schadensindikatoren, Schwingungseigenschaften, Model Updating

Français

Actuellement des ponts occupent une grande partie de l'infrastructure pour franchir des obstacles naturels ainsi que artificiels comme rivières, vallées ou d'autres routes et chemins de fer. De nombreux ponts en béton ont été construits au cours des 70 dernières années. La densité de trafic a augmenté énormément au cours des dernières décennies alors que les ponts souffrent de corrosion et d'usure. Néanmoins, la sécurité de l'infrastructure doit être garantie et il est donc très important de trouver des méthodes efficaces pour la détection d'endommagement des structures.

Dans ce but, les inspections visuelles sont aujourd'hui les plus largement adoptées. Compte tenu de la taille de la plupart des structures de ponts, il est compréhensible que ces tests demandent du temps ainsi que d'importants moyens humains, ce qui implique des coûts élevés. Cependant, il n'est pas toujours garanti que tout endommagement puisse être trouvé car seule la surface est accessible. Par exemple, des dommages internes, tels que la corrosion des renforts passifs ou des tendons précontraints, sont difficiles à détecter. En outre, de petites fissures peuvent rester inaperçues lorsqu'elles sont recouvertes de peintures ou de saleté.

Par conséquent, il est important de complémenter des méthodes standardisées par des alternatives avancées. L'objectif n'est donc pas nécessairement de remplacer les inspections visuelles, mais plutôt de les améliorer avec des méthodes efficaces.

Une idée qui fait l'objet d'une discussion approfondie dans la communauté scientifique repose sur des mesures de vibration d'une structure pour évaluer ses caractéristiques dynamiques. La présence d'un endommagement modifierait des propriétés du système, parce qu'il change la distribution de la rigidité. Ainsi, le processus d'identification du système en principe permet de détecter des changements de fréquences propre et donc de rigidité.

En pratique, un grand problème sur des ponts réels est l'efficacité d'une méthode, parce que des mesures sont largement influencées par des changements de température. Il est montré que l'impact de ce changement, par exemple entre nuit et jour, sur les propriétés du système est beaucoup plus élevé que l'influence de petits endommagements. En outre, des changements dans le sol et les conditions d'appuis entre de différentes saisons peuvent jouer un rôle. Ces effets environnementaux doivent être pris en compte lors de la réalisation de mesures. A ce sujet, des stratégies sont proposées pour compenser les effets environnementaux.

Abstract

C'est ainsi que cette thèse se concentre sur des mesures dans des conditions environnementales réelles, en dehors d'un laboratoire.

De différentes méthodes d'évaluation d'endommagements ou de monitoring de la rigidité basées sur certaines propriétés statiques et dynamiques sont développées. En effet, les propriétés physiques mesurées et analysées des ponts dans cette thèse comprennent: fréquences propres, formes modales, fléchissement sous le poids propre et flexion sous un test de chargement statique. Une campagne de mesure a été réalisé sur une partie d'un pont réel où quelques endommagements artificiels ont été introduits étape par étape. L'évaluation et la localisation d'endommagement sont testées directement avec les quantités mesurées, mais aussi par model updating d'un modèle en éléments finis. Ce modèle de solide est construit d'un maillage spécial. Il permet de modifier la répartition de la rigidité le long de l'axe longitudinal de la structure en variant les modules de Young des tranches définies. En outre, pour réduire le nombre de paramètres libres du processus de model updating, une fonction d'endommagement en exponentielle est introduite pour décrire la distribution de la rigidité. Au début, le modèle a été construit pour un état de référence sans endommagement. Ensuite, les données de mesure d'un état endommagé sont introduites et le modèle est mis à jour en modifiant les modules de Young des tranches. Il s'agit de minimiser une fonction d'objectif spéciale qui contient les quantités physiques mesurées et simulées. La comparaison entre le modèle initial et actualisé permettrait une quantification et une localisation d'endommagement. En plus, l'épaisseur d'une tranche est raffinée autour de la région d'endommagement identifiée pour améliorer le processus.

Mots-clés: détection d'endommagement, indicateurs d'endommagement, propriétés dynamiques, model updating

CONTENTS

Contents

NOMENCLATURE

Symbols

The symbols are listed according to their first appearance.

$F(t)$	$[N]$	Input Force over time
$x(t)$	$[m]$	Displacement over time
$[\mathbf{G}(\mathbf{s})]$		Transfer function matrix
s		Laplace variable
ω	$\left[\dfrac{rad}{s}\right]$	Angular frequency
ξ	$[-]$	Damping ratio related to the critical damping
$[\mathbf{M}]$	$[kg]$	Mass matrix
$[\mathbf{C}]$	$\left[\dfrac{Ns}{m}\right]$	Damping matrix
$[\mathbf{K}]$	$\left[\dfrac{N}{m}\right]$	Stiffness matrix
$\{x(t)\}$	$[m]$	Output vector (displacements over time)
$\{f(t)\}$	$[N]$	Input vector (force over time)
$\{x\}^{n\times 1}$		Vector of dimension $n\times 1$
$[\mathbf{X}]^{n\times m}$		Matrix of dimension $n\times m$
$\{y(t)\}$		State vector
$[\mathbf{A}], [\mathbf{B}]$		Matrices derived from the structural matrices of a MDOF system (state space formulation)
$\{\mathbf{0}\}, [\mathbf{0}]$		Zero vector, matrix
$det([\mathbf{M}])$		Determinant of a matrix $[\mathbf{M}]$
$[\mathbf{\Psi}]$		Eigenvector matrix
$\{\psi\}_r$	$[m]$	Mode shape vector for mode r

Nomenclature

$$\lambda_r = \omega_r \left(-\xi_r \pm i\sqrt{1 - \xi_r^2} \right)$$
$$= \delta_r \pm i\omega_{dr}$$
$\left[\dfrac{rad}{s} \right]$ — Eigenvalue for mode r with low damping

ω_r — $[rad]$ — Angular eigenfrequency for mode r

ω_{dr} — $[rad]$ — Angular eigenfrequency of a damped system for mode r

$\delta_r = -\omega_r \xi_r$ — $[rad]$ — Damping coefficient for mode r

$x(s)$ — Laplace transform of $x(t)$

$[\mathbf{R}]_r$ — $\left[\dfrac{s}{kg} \right]$ — Residua matrix of mode r

$*$ — Complex conjugated

$\{\ldots\}^H, [\ldots]^H$ — So-called hermitian conjugated, conjugated transposed of a vector or matrix

a_r — $\left[\dfrac{kgm^2}{s} \right]$ — Scaling factor Modal A for mode r

b_r — $\left[\dfrac{kgm^2}{s^2} \right]$ — Scaling factor Modal B for mode r

$_r\psi_i$ — $[m]$ — Component i of mode shape r

Ω — $[rad]$ — Angular frequency of an input signal

$[\mathbf{F}] = [\mathbf{K}]^{-1}$ — $\left[\dfrac{m}{N} \right]$ — Flexibility matrix

m_r — $[kgm^2]$ — Modal mass for mode r

k_r — $\left[\dfrac{kgm^2}{s^2} \right]$ — Generalised stiffness for mode r

c_r — $\left[\dfrac{kgm^2}{s} \right]$ — Generalised damping for mode r

$\{\varphi\}_r$ — $\left[\dfrac{1}{\sqrt{kg}} \right]$ — Mode shape vector normalised to unit modal mass (UMM)

$[\mathbf{\Phi}]$	$\left[\dfrac{1}{\sqrt{kg}}\right]$	Matrix containing the UMM mode shapes
$[\mathbf{\Omega}]$	$\left[\dfrac{rad^2}{s^2}\right]$	diagonal matrix containing squared angular eigenfrequencies
$\bar{Q}_r$	$[-]$	Modal participation factor for mode r
$\{p\}$		Vector with model updating parameters
$[\mathbf{W}]$		Diagonal weighting matrix
$\{x_{meas}\}$		Experimentally obtained, i.e. measured values
$\{x_{sim}\}$		Values predicted by a simulation
$\|\{x\}\|_1$		L1 norm of vector $\{x\}$
$\|\{x\}\|_2$		L2 (Euclidian) norm of vector $\{x\}$
$\|[\mathbf{A}]\|_F$		Frobenius norm of matrix $[\mathbf{A}]$

Abbreviations

The abbreviations are listed in alphabetical order.

APDL	Ansys Parametric Design Language
ASH	Angle-between-String-and-Horizon
CMP	Correlated Mode shape Pair
COMAC	Coordinate Modal Assurance Criterion
DAQ	Data Acquisition
DLV	Damage Locating Vectors
DOF	Degree Of Freedom
DS	Damage Scenario
DP	Driving Point
EMA	Experimental Modal Analysis
FE(A)	Finite Element (Analysis)

FFT	Fast Fourier Transformation
FRF	Frequency Response Function
ICA	Imperialist Competitive Algorithm
MAC	Modal Assurance Criterion
MDOF	Multiple Degree Of Freedom
MSF	Modal Scale Factor
NCO	Normalised Cross Orthogonality
N-DOF	System with N degrees of freedom
NI	Novelty Index
NLPQL	Non Linear Programming by Quadratic Lagrangian
NMD	Normalised Modal Difference
NULS	Normalised Uniform Load Surface
P&C	L'administration des Ponts et Chaussées Grand-Duché de Luxembourg
PCA	Principal Component Analysis
PFM	Proportional Flexibility Matrix
SCBFI	Strain Change Based on Flexibility Index
SHM	Structural Health Monitoring
SSI	Stochastic Subspace Identification (SSI)
SVD	Singular Value Decomposition
UL	Université du Luxembourg
ULS	Uniform Load Surface
UMM	Unit Modal Mass

1   INTRODUCTION AND MOTIVATION OF THE THESIS

Civil engineering structures such as tunnels and bridges are essential components of the infrastructure, which help to overcome obstacles to avoid detours and often to relieve areas of heavy traffic. If such a structure must be blocked, this leads immediately to considerable costs. Traffic flows have to be diverted, usually done via less suitable routes, for example through localities or country roads. Freight transport and commuters also need a lot more time to travel, due to delays and traffic congestion. Even worse than this economic damage is if human lives are endangered by damage to buildings.

Numerous reinforced concrete bridges were built after the Second World War, but these were not designed for today's steadily increasing traffic and therefore reach limits of their resilience. In addition, weather influences as wind, frost and temperature fluctuations show a negative effect on the service life and the monitoring of buildings.

For these reasons, it is of particular importance to carry out regular inspections of buildings with the aim of finding and documenting damage. The information obtained is of use for decision-making about how the structure can be preserved while guaranteeing its security. Any new damage should be detected to prevent further widening of damage.

For regular investigations, most countries have developed their directives and standards. In Germany, DIN 1076 "Ingenieurbauwerke im Zuge von Straßen und Wegen. Überwachung und Prüfung" ("Civil engineering structures in the course of roads and paths. Monitoring and testing") is used. As a standard, it is not legally binding, but is considered as a "universally recognised rule of technology" and was introduced by the German federal states as binding for the roads, which they administer. The documentation „Bauwerksprüfung nach DIN 1076. Bedeutung, Organisation, Kosten" ("Test of civil engineering structures according to DIN 1076. Importance, organisation, costs") [5], which was issued by the Federal Ministry of Transport, Building and Urban Development in 2013, describes the monitoring of civil engineering structures in Germany on the basis of DIN 1076 in detail. It gives an impression of the considerable effort required for this.

One of the first statements of the document is that a large number of civil engineering structures, which are present today in the so-called Old Federal States, were built between

1965 and 1985. According to the current state of the art, they have constructive weaknesses and must therefore be monitored in particular.

The number of bridges to be inspected is considerable. According to the document, as of 31/12/2012 the government of the Federal Republic of Germany administered 39231 bridge structures with a bridge area of $30\ million\ m^2$ and this area quadrupled since 1970. An interesting fact is that 88% of the total area of all bridges of the federal roadways is accounted for by reinforced concrete and prestressed concrete bridges and only 6% by steel and steel composite bridges. In Germany, apart from roads administered by the Federal Republic, regional provincial roads exist that are administered and maintained by the federal states. These last add up again 26780 bridge structures with a total area of $5.5\ million\ m^2$.

This document also gives information about the load on the bridges in Germany and about their condition. According to that, an important fact is that the rate of heavy-load traffic has increased disproportionately and the permissible total weight for trucks in combined traffic has nearly doubled since 1956 from $24\ t$ to $44\ t$, which has an enormous influence on fatigue of the bridges. In the discussion about the admission of even heavier trucks with excess length, so-called "road trains", the question must be taken into account, whether these will exacerbate the problem. Moreover, the proportion of road freight traffic is very high in the overall freight transport performance. In 2004 it amounted to $367 \cdot 10^9\ tkm$, compared to $92 \cdot 10^9\ tkm$ for rail transport and to $63 \cdot 10^9\ tkm$ for inland waterway transport with. By 2025, it is expected that the difference will even increase.

By reason of this considerable load on the existing bridges, it is therefore understandable that inspections have to be carried out regularly. According to DIN 1076, a main test (termed H) needs to be carried out every six years, and a simpler secondary test (termed E) three years after this. Furthermore, examinations from special occasions (S) and tests according to special technical regulations (V) may be supplemented. In addition, there are annual inspections without special aids. Various test methods are listed in [5], for instance measuring cracks and comparing them to former states, tapping for finding cavities or measuring deformations to determine reduced load bearing capacity. Such well-tried tests are increasingly supplemented or supported by newer methods. These are, for example, laser or radar measurements, which are performed using special measuring vehicles or even drones. Despite such tools, the effort is considerable and in inspections of the surface, damage covered by dirt or paintwork still may be missed. Moreover, visual tests show some

disadvantages for internal damage, for example corrosion in steel reinforcements or tendons inside the concrete, due to ingress of moisture through cracks, cannot be detected.

It is therefore important to explore further possibilities for the examination of structures that can supplement or improve existing methods. Considering the enormous number of structures to be tested, robust methods are needed that result in quick operation with little effort in terms of personnel and costs. The basic approach is to compare measured structural properties to a previous state to determine changes in the structure that may be caused by some damage. Such properties can be the deformation of a bridge due to a certain load as obtained from conventional static loading tests. Additionally, the influence of damage on the sagging of bridges is examined in the present thesis. This sagging is a constant downward movement of bridges over time due to their own weight and settlement effects. Damages, which reduce the stiffness of a bridge, will intensify the sagging. The idea is that the sagging provides better information than static load tests, because the own weight of a bridge is by far higher as its maximum service load that could be used for non-destructive static tests. Nowadays, the sagging is seldom measured, since absolute measurements with respect to fixed reference points are necessary for this purpose. They are difficult to realise, because it is difficult to define reference points, which are fix over several years. In future, improvements in GPS measurements or photogrammetry may lead to easy methods to measure the sagging.

Another idea that is examined in this thesis is to measure the modal parameters (for example the eigenfrequencies) of bridges and to use them for the detection or even localisation of damage. Methods exist to estimate these parameters based on measured vibrations of the structure. The main distinguishing feature of the methods is if only the output data, i.e. the vibrations, are used for the parameter estimation or if the force, which causes the vibrations, is also measured. For automatic monitoring systems mostly output-only methods are preferred, because for that no artificial excitation is necessary, but unmeasurable excitations like for instance by wind or traffic can be used. In contrast, a measured artificial excitation is used in the so-called experimental modal analysis (EMA). Because the excitation is known, clearer results are often obtained. The necessary measurements for modal parameter estimation can be carried out with little effort compared to most conventional testing methods.

Although the idea has already been pursued by many scientists, it remains a challenge for in-situ measurements on real buildings to separate the impact of environmental factors, such as temperature fluctuations, from the influence of damage. A method that delivers perfect results

in theory or under laboratory conditions may lose its robustness under real environmental conditions. Therefore, this thesis focuses on the experimental determination of dynamic as well as static properties under real conditions outside a laboratory environment.

2 OUTLINE OF THE THESIS

3 Literature review

At the beginning an overview is given of publications, which are representative for the state of the art. It is divided into different sections that describe topics, which are also important for the present thesis.

4 Theoretical background

Chapter 4 describes the physical and mathematical background, which was used in this thesis and hence is necessary to understand it. This theory is part of the state of the art as well, so this chapter can be seen as an extension of the literature review. The used nomenclature is listed above.

5 In-situ tests at a prestressed bridge beam

Here, the experimental tests are explained, which were performed and whose results were evaluated in the following chapters. Especially, Chapter 5.1 is very important. Here a test setup in the port of Mertert (Luxembourg) is described, where a prestressed concrete beam was examined that was part of a real bridge. Artificial damage was introduced at this beam and measurements were carried out in several pre-defined damage scenarios. The intention was to test different ways to detect damage based on measured static and dynamic properties. The test setup was exposed to real environmental conditions, such as temperature fluctuations and solar radiation, so that during the evaluation of the test results, the same challenges arose as for tests at a bridge still in operation.

6 Temperature compensation

One way to deal with the environmental influences on the measured properties of a bridge, is to compensate them. Here a method is proposed to perform such a compensation for the temperature influence on static deflections. It is described by using the test setup in the port of Mertert as an example. Furthermore, the obtained temperature-compensated data is used in the following chapters.

7 Evaluation of damage indicators

In this chapter, several methods to calculate damage indicators from measured data, which are know from literature and described in the theoretical background, are tested with the data, which was obtained during the tests in the port of Mertert.

8 Model updating

The methods to detect damage based on measured static and dynamic properties, which are described in Chapter 7, are not based on a mathematical model of the structure. This can be seen as an advantage, because such a model must be created in the first place, which can mean a lot of effort. Nevertheless, a model based approach is tested here for damage assessment. For this purpose, a finite element model of the test setup in the port of Mertert was created in the software ANSYS. This model was parametrised, thus it was possible to adjust these parameters with the aim of reconciling the simulated results with measurements on the real beam at various points in time during the different damage scenarios. The idea for the detection of damage is here, to evaluate the updated parameter values and to compare the updated models with a model, which matches the healthy state.
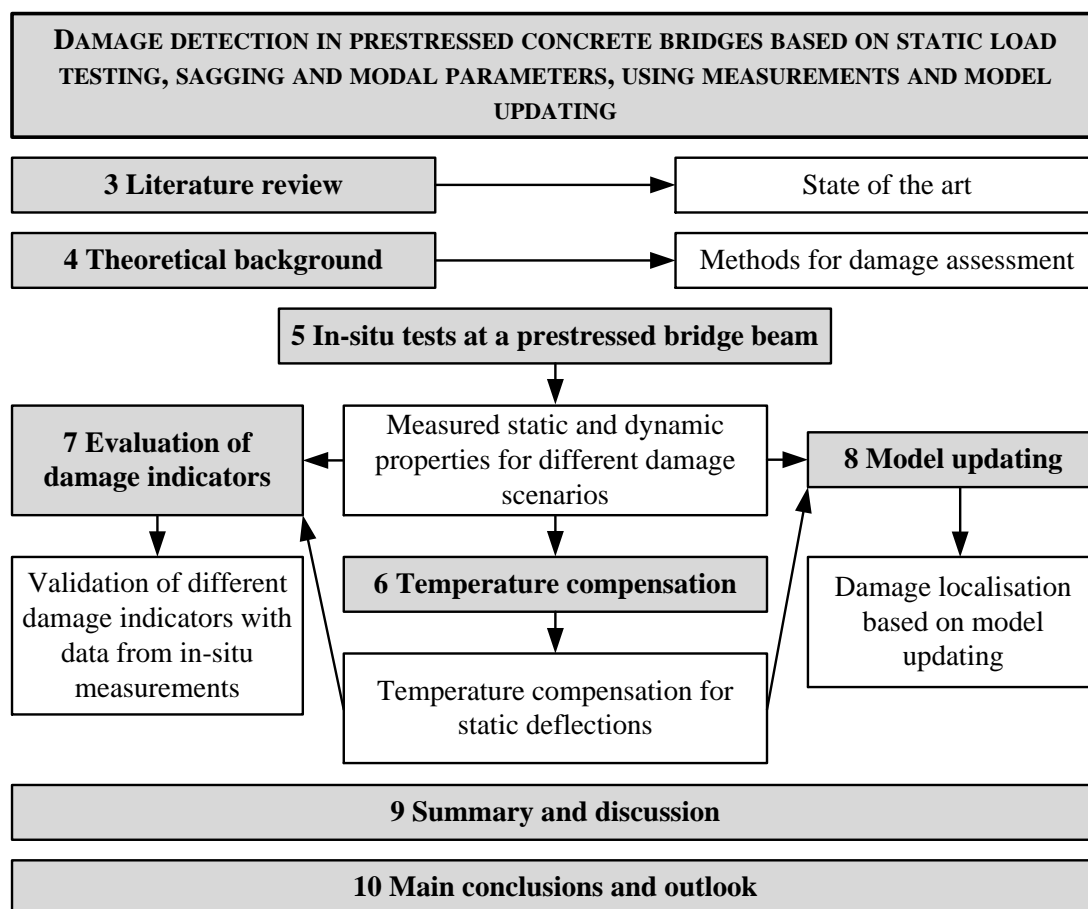

Figure 2.1: Outline of the thesis

3 LITERATURE REVIEW

3.1 Damage detection based on static and modal properties

A crack in a beam reduces evidently the supporting cross-section, i.e. the area as well as the area moment of inertia are reduced, which causes a local loss of rigidity. Therefore, it is often stated that the search for damages means searching for stiffness reductions. It is obvious that decreasing stiffness is reflected in deflection due to a certain static load. Additionally, the changes in the stiffness matrix are reflected in the dynamic response of a structure and thus in its modal parameters. The simplest effect is that the eigenfrequencies decrease with decreasing stiffness. Therefore, the idea to realise structural health monitoring (SHM) is to monitor the modal parameters, either by an automatic system or by repeated measurements in certain time intervals. This idea is vigorously discussed in the scientific community since several years.

Before the International Modal Analysis Conference (IMAC) in 2001, data resulting from vibration measurements at the Z24 highway bridge in Switzerland was made available to the research community. Three different types of excitation were used for the measurements: ambient sources, drop weight and shakers. Authors of conference papers for IMAC 2001 choose their preferred type of excitation and performed a modal analysis of the data with the methods, which they are used to. In a comparative study Peeters and Ventura (2003) [6] summarise and compare the results.

Parloo et al. 2003 [7] used mode shape sensitivities to changes in mass or stiffness of structures to obtain damage information through location and amount of changes in the mass and stiffness matrices. Mode shapes were experimentally obtained, so there was no prior FE-model necessary. The method was validated by data taken from a test setup under laboratory conditions as well as from experiments on the I-40 highway bridge in Albuquerque, New Mexico.

Nguyen and Golinval (2010) [8] used measurement data of the same bridge to validate an approach for damage localisation and quantification in beam-like structures. This approach is based on the dynamic response of the structure and does not require a modal analysis. The sensitivity of the dynamic response to predefined parameters is evaluated by calculating the partial derivatives of the response. In this study, the frequency response functions (FRFs)

measured at different locations, are taken as an example. A singular value decomposition (SVD) is performed on the partial derivatives and it is shown that the sensitivity of the dynamic response depends on the sensitivity of each SVD term. Furthermore, it is stated that the sensitivities of the left singular vectors are appropriate for damage localisation in beam-like structures. Therefore, the difference of the sensitivity of the first left singular vector compared to the healthy state is plotted vs. the considered degrees of freedom (DOF). The method is applied for three examples, at first for a numerical model of a cantilever beam then for a mass–spring system in laboratory and finally for the I-40 bridge. It is shown that the location of damage can be derived from the plotted curves even if damage is present at several positions, although the effectiveness of the method depends on the level of damage. Furthermore, it is stated that the method should be appropriate for online monitoring.

The conference paper for EVACES'15 by Maas et al. (2015) [9] is a summary of the experiences and results obtained by the research group at the University of Luxembourg in the field of structural health monitoring of real bridges. It provides an overview of different influences on modal-analysis that have been investigated in the work so far. These are environmental influences like temperature variations as well as nonlinear behaviour and aging of bridge structures and the repeatability of the measurements.

Nguyen et al. (2016) [10] contributed to COST ACTION TU1406 QUALITY SPECIFICATIONS FOR ROADWAY BRIDGES, STANDARDIZATION AT A EUROPEAN LEVEL. The paper was written for a meeting in Belgrad and dealt with the idea of using dynamic as well as static measurements for damage detection in a procedure that joints the advantages of both measurement modes in order to improve the success rate. While both measurement modes are treated separately here, the conclusion is proposed to combine them in a model updating procedure. A second contribution to a further meeting in Delft was Nguyen et al. (2016) [11], where the use of temperature compensated deflection lines for damage detection is described.

Before a standardisation can be defined, information about the state of the art must be collected. Therefore, in the course of the above mentioned COST ACTION TU1406, a performance indicator database was created based on a screening process of 36 countries. This process and the database itself are described in Strauss et al. [12].

3.2 Health monitoring based on modal flexibility matrix

In Chapter 4.1 and 4.2, the mathematical background will be explained to determine the inverse of the stiffness matrix, the so-called flexibility matrix, based on measured modal parameters. The so obtained matrix is often referred to as modal flexibility. In order to find cracks based on detection of stiffness reduction, the stiffness matrix would be more appropriate. However, in most practical cases, an experimentally obtained flexibility matrix is singular and so cannot be inverted to obtain the stiffness matrix. This comes from the fact that mostly the number of accurately identified modes (i.e. associated sets of modal properties including eigenfrequencies, eigenvectors or mode shapes, damping and modal mass) is smaller than the number of considered degrees of freedom and will be also explained in more detail in Chapter 4.2. Many examples of how a dynamically measured flexibility matrix can be obtained and afterwards used for damage localisation, can be found in literature.

An early example is the article of Pandey and Biswas (1994) [13] and a similar publication of the same authors in 1995 [14], where the authors already stated that a damage in a structure alters its dynamic parameters and therefore also the structural matrices change. These are the mass, damping, stiffness and flexibility matrices, from which especially the latter one was examined for damage localisation. They used FE-models of a cantilever beam, a simple supported beam as well as a free-free beam for a theoretical validation. Furthermore, data collected from a test setup under laboratory conditions were evaluated. Once flexibility matrices were determined based on modal parameters, the matrices in different damage states were compared to the ones in the intact state. The damage localisation was performed by evaluating the maximum of a column of the difference matrix for each degree of freedom. For instance, it was found that the maximum of the change occurred in the position of damage for the simple supported beam, whereas changes were visible for the cantilever beam only from the location of damage and rose up to the free end of the beam.

Yan and Golinval (2005) [15] applied a covariance-driven subspace identification technique to identify modal parameters, which are then used to calculate a flexibility matrix. Furthermore, a stiffness matrix is obtained from the flexibility matrix, which is in most practical cases singular, by a pseudo inversion. Damage may be localised from the comparison of these matrices between a damaged and a reference state. The relevance and the

limitations of the technique are illustrated by the numerical models of a cantilever beam and a three span bridge as well as experiments in laboratory conditions with an aircraft mock-up.

Duan et al. (2005) [16] performed output-only measurements and obtained arbitrary scaled mode shapes. But as it will be explained in Chapter 4.1, this is necessary to calculate the correct flexibility matrix. Instead of this, they estimated a "proportional flexibility matrix" (PFM), which is qualitatively the same but differs by an undetermined scalar factor from the real flexibility matrix. The PFM was integrated in the Damage Locating Vectors (DLV) method developed by Bernal (2002) [17]. In a subsequent publication [18], Duan et al. (2007) detect damage at a simulated planar truss structure, where only 23 out of simulated 53 DOFs were used to calculate the PFM.

Shih et al. (2009) [19] suggest a multi-criteria approach for damage assessment of beam and plate structures. Besides the flexibility matrix, changes in eigenfrequencies and a modal strain energy based damage index are evaluated. Furthermore, a method for damage identification was introduced by Nobahari and Seyedpoor (2013) [20], which as well based on flexibility and strain energy calculations. In 2014 Montazer and Seyedpoor [21] proposed a damage indicator called "Strain Change Based on Flexibility Index" (SCBFI). As the name implies, this index is based on strain changes in structural elements. Based on the flexibility matrix derived from modal analysis data, nodal displacements necessary to obtain the strain are separately calculated. In both publications, the proposed damage indicator was only tested by numerical results, whereby the mode shapes were perturbed with a random error to simulate measurement noise.

Reynders and De Roeck (2010) [22] propose a local flexibility method, which is capable of detecting local stiffness variations based on measured modal parameters. If the mass of the structure is equally distributed, this would be even possible if a mass-normalisation of the mode shapes is not possible, e.g. if they were determined by output-only measurements.

For damage detection in beam structures Yan et al. (2010) [23] propose a so-called angle-between-string-and-horizon (ASH) flexibility matrix, whose components are associated with elements instead of DOFs. According to their article damage indicators based on the ASH matrix are capable of identifying damaged elements without being affected by boundary conditions. For damage indicators based on the "conventional" flexibility matrix this is not the case. It is shown by numerical examples and experimental tests, that by using the ASH

matrix it is possible to identify multiple damage locations and to determine relative damage severity.

For large-scale structures Weng et al. (2013) [24] propose a substructuring method for damage assessment. In such structures local damage has usually only small impact on the global modal data. Therefore, the flexibility matrices of the substructures were decomposed into local eigenparameters, which would be more sensitive to local damage as the global parameters.

Chen et al. (2014) [25] present a mathematical approach to derive the free-free flexibility matrix from a singular stiffness matrix of the free-free system and vice versa.

Feng et al. (2014) [26] used the modal flexibility matrix for a Bayesian model updating for structural health monitoring. Their approach is demonstrated by a numerical example, where a model reduction technique is used to reduce the computing effort.

Sung et al. (2013) [27] propose the normalised uniform load surface (NULS) curvature derived from the modal flexibility for damage detection in beam-like structures. The method was tested numerically with a cantilever as well as a single supported beam. The results were compared to the uniform load surface (ULS) curvature method and the mode shape curvature method. In a later publication, Sung et al. (2014) [28] deals with damage detection based on the modal flexibility for cantilever beam-type structures such as high-rise buildings without requiring an FE-model.

Masoumi et al. (2015) [29] created FE models of a 2D-frame structure and of a Howe-truss. Then they calculated a generalised flexibility matrix as proposed by Li et al. (2010) [30] for these models. Cracks were modelled by stiffness reductions using an equation defined by Perera et al. (2009) [31]. They applied the "Imperialist Competitive Algorithm" (ICA) as described by Atashpaz-Gargari et al. (2007) [32] to identify these simulated damages.

For the purpose of model updating, Stutz et al. (2015) [33] calculated the difference between an experimentally measured flexibility matrix and the corresponding one predicted by an FE model. The Frobenius norm of the difference matrix was defined as objective value, which had to be minimised. As updating parameters dimensionless nodal cohesion factors were introduced. Through a simply supported Euler-Bernoulli beam, the influence of damage location and of noise in measurements was investigated. Furthermore, different stochastic optimisation methods were compared.

3.3   Model updating techniques

In model updating, parameters of a mathematical model, often an FE model, are adjusted until the deviation between the predictions of the model and real measurements is minimised. This approach is often used for the purpose of damage detection and localisation. A prerequisite is the validation of the model based on a set of reference measurements. At a later stage, this reference model can be updated according to new measurements, which may allow finding any change. If the parameters are appropriately chosen so that they correctly describe the location and impact of damage, it can be assumed that the optimal parameter values reflect the damage pattern in the real structure.

For a successful damage assessment, it is essential that the reference model reflects as accurately as possible the real structure. Nevertheless, there are always unavoidable modelling errors due to idealisation and assumptions. Additionally, the measurements of the physical properties of the real structure are never perfectly accurate, since there are systematic as well as stochastic measurement uncertainties. For instance, eigenfrequencies depend on the temperature of the structure, since change in temperature causes changes in the Young's moduli of materials. Therefore, measurements taken at different points in time under different environmental conditions will lead to changed responses that do not relate to damage. In order to take into account of the unavoidable modelling errors, Link (1998) [34] proposes, to separate the uncertain parameters, which are to be determined, into two groups. The first one includes local physical parameters, which relate to areas of the structure where model uncertainties can be expected. The second group comprises global generalised parameters that cover the effects of non-parametric model errors occurring in the remaining areas. Furthermore, he proposes to smooth measured mode shapes in order to minimise measurement errors.

An extensive review on numerical procedures and application aspects for model updating is presented in Link (1999) [35]. All necessary steps are mathematically described for a complete model updating procedure, including the choice of updating parameters and the definition of residuals, which compare physical measurements and analytical results. A weighted least squares technique is proposed in this reference, where the weighted sum of the residual vector including the differences between measured and simulated physical quantities, is the kernel of the objective function. This function assigns a single value to a set of

parameters, which measures the difference between simulation and measurement. It has to be minimised in order to find the optimal parameter set.

Teughels et al. (2002) [36] propose a model updating procedure for damage localisation for a beam, including so-called damage functions, which allows reducing the number of parameters to adjust. It should not be confused with the above mentioned objective function. The idea for damage detection was to search for local reductions of the bending stiffness of the beam. The objective is to find local reductions of the beam's bending stiffness. A general sensitivity based model updating procedure is firstly described, in which uncertain modal properties need to be adjusted. These properties can be the Young's modulus of every element in the FE-mesh. For a more complex structure or a fine FE-mesh this approach may lead to a vast number of parameters, yielding an underdetermined optimisation problem. In order to reduce the number of parameters Teughels et al. propose to define damage elements consisting of several neighbouring elements and then a damage function can be defined that describes a smooth progress of the bending stiffness over the length of a damage element. This damage function can be described by only a few parameters. In [36], the damage function is a sum of Legendre polynomials where the parameters are weighting factors used for the contributions of the individual polynomials. These factors are adjusted according to a least squares objective function containing residuals of modal properties frequencies and mode shapes through the Trust Region Newton algorithm. Then correction factors for Young's modulus of each element were calculated according to the damage functions. Damage can be localised by searching out high reductions of the bending stiffness. The approach was validated by laboratory tests.

In a subsequent publication Teughels and De Roeck (2004) [37] applied the method proposed in [36] to identify damage in the highway bridge Z24 in Switzerland. In addition, Unger, Teughels and De Roeck (2006) [38] performed damage detection by model updating for a prestressed concrete beam. In laboratory static load tests with increasing force magnitude were carried out and the modal properties were determined after each load step. These dynamic properties were used in the model updating procedure to detect the damage caused by the static loading. Since the cracks close again due to the pretension after removal of the load, it was difficult to detect damage of low severity. While the authors state, that for the tested beam the damage could be localised for a load level of 80% of the failure load, they expected for real structure that this should be possible on lower levels of the live load due to higher ratio of dead load to live load.

In two related papers, Titurus et al. (2003) [39,40] describes a model updating procedure for damage detection using so-called generic elements especially designed for model updating. The first paper presents the creation of the model of the reference state called the baseline model and its validation using model updating. This model is used for damage detection in the second paper.

The flexibility matrix was also calculated from modal parameters in Jaishi and Ren (2006) [41] to define the objective function for a sensitivity based model updating approach. The obtained flexibility matrix can be seen as a summary of all determined modal parameters, as they are all included in the calculation of the matrix. Therefore their objective function compared the dynamic parameters of the real structure with those of the FE-model, by calculating the difference between the measured and analytical flexibility matrices. The objective value is calculated as the Frobenius norm of the difference matrix. The effect of noise on the updating algorithm was also studied. The method was validated by tests on a reinforced concrete beam in laboratory and later on a real concrete-filled steel tubular arch bridge in Jaishi et al. (2007) [42].

Perera et al. (2007) [43] intended to improve the damage localisation capability by using modal flexibility in model updating. In addition to the first objective function dependent on the flexibility, a second one was introduced, which makes the localisation possible. An optimal damage distribution was determined in a Pareto optimisation that simultaneously minimises the two objective functions. Experimental and analytical flexibility matrices were compared based on the Modal Assurance Criterion (MAC) correlating the diagonals of the flexibility matrices. The approach is illustrated initially by simulated scenarios, then by experimental tests within an aluminium beam of 6m length. In a subsequent work, Perera et al. (2009) [31] compare multi-objective genetic algorithms for Pareto optimisations.

Mordini et al. (2007) [44] used a Scilab code named VCUPDATE for optimisation in conjunction with FE code for OpenSees or ANSYS to realise the FE-Analysis to establish a model updating procedure. The Scilab code can use two types of convergence criteria or objective functions. For the first option the relative differences between experimentally measured and simulated eigenfrequencies are summed up and then divided by the number of considered frequencies. In the second option the mode shapes are additionally compared. For this purpose, besides MAC, Normalised Modal Difference (NMD) is also suggested, which would be more sensitive when mode shapes are highly correlated. Therefore, for the second convergence criterion, they added the MAC values to the first criterion. Furthermore, the

measurement accuracy was taken into account through a weighting matrix while a sensitivity-based approach was used for the optimisation algorithm. It stops when the convergence criterion falls below a threshold value. The resulting damage distribution can be reported in terms of ratio between the element's Young's moduli before and after the updating process. The procedure was validated by a prestressed reinforced beam that was artificially damaged in laboratory and by real cables of the Lanaye bridge in Belgium.

Furthermore, Schlune et al. (2009) [45] aimed to improve FE model updating techniques for damage assessment which, according to them, often provide inaccurate results due to inaccurate modelling assumptions and too few measurements. For this purpose, they suggest to first carry out manual model refinements. Further, multi-response objective functions were introduced that allow combining different types of measurements such as static and dynamic features. The proposed method was tested on the Svinesund bridge (Sweden).

However, model updating usually requires a very high number of simulation runs, leading to very expensive computational cost even on advanced computers, especially in large models with abundant degrees of freedom. The number of updating parameters to be determined also strongly influences the computational effort. In order to reduce this effort, Weng et al. (2012) [46] decomposed their FE-models of large structures, for instance the $600\,m$ tall Guangzhou New TV Tower, in substructures. The measured modal data of the whole structure is disassembled into the substructure level and then the model updating is only performed for the substructures. This approach is called the inverse substructuring model updating method, in opposite to the forward method, where the numerically calculated dynamic properties of the whole structure are assembled from those of substructures while the model updating process is still performed on global level.

As mentioned before, damage assessment by model updating techniques can be complicated by systematic or stochastic measurement uncertainties as well as modelling errors. Link et al. (2014) [47] suggest two methods to consider these uncertainties in a model updating procedure. They monitored for several years the dynamic properties, i.e. eigenfrequencies and mode shapes, of the Gaertnerplatz Bridge over the Fulda River in Kassel, Germany. In the first method, measured eigenfrequencies were not used directly for the model updating but a regression line is evaluated to reflect the systematic dependence of eigenfrequencies on temperature. From this line, points at different temperatures are taken for the further process. Subsequently, the FE-model of the bridge was updated based on these points, analytically determined frequencies are supplemented by the measured random frequency distribution. In

this method, the updated model parameters reflect only the systematic changes in eigenfrequencies due to temperature. In the second method, in order to determine the parameter's uncertainty due to variations of the measured data, the authors updated the model with a large number of measured data sets. The results are validated by comparing the data clouds obtained by simulations with the updated model parameters to the measured ones.

3.4   Compensation of environmental effects

It is obvious for real structures, e.g. bridges, that the influence of environmental conditions, e.g. fluctuations of the ambient temperature, on physical properties is considerable. For instance, the Young's modulus of asphalt highly depends on temperature. Gutermann (2003) [48] provided the following table with Young's moduli of asphalt according to different temperatures.

Table 3.1: Young's modulus of asphalt as a function of temperature [48]

Temperature [°C]	-10	0	10	20	30	40
Young's modulus [N/mm^2]	25000	18000	10500	4500	1300	400

Therefore, eigenfrequencies of a bridge vary with temperature due to the stiffness change of traffic lanes, especially with a thick asphalt layer. This effect is observed in a small bridge in Useldange (Luxembourg), which is described in the thesis of J. Mahowald (2013) [3] and in Nguyen et al. (2017) [49]. The eigenfrequencies of this bridge show a huge variation with temperature, i.e. of 0.7 $\%/K$ for the first eigenfrequency. This high value is explained by the very thick asphalt layer of 25 cm as well as by the special hyperstatic bearing conditions of the bridge. Other environmental influences can be additionally cited as irregular temperature distribution due to solar irradiation as well as different soil conditions in winter and summer. Although the high temperature dependency of the Useldange bridge is an exception, variations of eigenfrequencies due to these influences may reach the order of magnitude caused by a possible damage, like small cracks. Therefore, it is crucial to compensate the environmental influences prior to any comparison of measured physical quantities for a successful damage assessment. The influences can be minimised by measuring always at the same time every year, with similar soil conditions and at cloudy days, when there is only diffuse solar irradiation. However, variations of the ambient temperature are the most difficult ones to avoid, because the necessary measurements often take longer time periods or have to be repeated a view times for statistical evaluations. Above all, static tests can take several hours, while the ambient temperature changes in the course of the day. Therefore, an

objective of the present thesis is to deal with the influence of temperature changes on the measurements.

In literature, different approaches were proposed to compensate environmental influences.

Peeters and De Roeck (2001) [50] examined data that was collected in a one year monitoring of the Z24-Bridge in Switzerland in the course of the European project SIMCES. After this period, the bridge was artificially damaged. For the vibration monitoring an automatic modal analysis was realised to estimate modal parameters based on output-only data of vibrations caused by unmeasurable excitations like wind and traffic. The stochastic subspace identification (SSI) algorithm, which was developed in 1991 by Van Overschee and De Moor [51], was used for this estimation. In [50] the authors deal with the fact, that for a proper damage detection the influence of damage on the modal parameters must be distinguished from natural fluctuations due to environmental factors like for instance temperature. From data, which was gathered in the healthy state of the bridge, so-called black-box models were derived for the eigenfrequencies as function of temperature. Data from measurements at a later point in time were compared to the models. The idea of the authors is that as long as the eigenfrequencies stay within certain confidence intervals, the fluctuations must mainly be caused by the temperature. Only when these intervals are exceeded, there must be another cause for the fluctuations, such as damage.

A multi-variate statistical method is proposed by Yan et al. (2005) [52,53], where it is not necessary to measure environmental quantities like temperature, air humidity or soil stiffness. These variables are considered as embedded in the variations of the determined properties of the structure, for instance eigenfrequencies. It is assumed that the fluctuations of these vibrational quantities mainly are caused by environmental changes and/or damage. The basic idea is to separate the influence of damage by statistical means and to quantify it by a so-called Novelty Index (NI) e.g. based on the Mahalanobis norm. An outlier limit is defined by the mean value and the standard deviation of NI in the reference state. The method was illustrated for linear and non-linear cases. Nguyen et al. (2014) [54] tested the approach at two real bridges in Luxembourg. For the purpose of testing damage detection methods, these bridges were artificially damaged in a predefined manner shortly before their demolition. Dynamic measurements were carried out with different measured excitations, such as hammer impacts and swept sine excitation. Among other evaluations, the eigenfrequencies were determined by wavelet transformation of the response data. These sometimes show an increase after the introduction of damage, which is not theoretically expected and was

explained by environmental influences. It is stated that the evaluation according to the method described above showed significant improvements compared to earlier evaluations [55–59].

In two associated publications, Zong et al. (2015) [60] and Lin et al. (2015) [61], a temperature updating model, which was based on modal analysis of 276 in-situ measurements, taken from one year's monitoring of Xiabaishi bridge (China), was used to exclude frequency variation due to temperature. The temperature compensated frequencies were used in a model updating approach for damage assessment using a response surface method.

4 THEORETICAL BACKGROUND

4.1 System identification based on modal parameters

In this chapter the mathematical formulation of a Multiple Degree of Freedom (MDOF) system is explained to lead over to the method of system identification based on measured modal parameters. It is a brief summary of the known theory of modal analysis to explain the physical quantities that are used in this thesis.

a) schematic view   **b) block diagram**
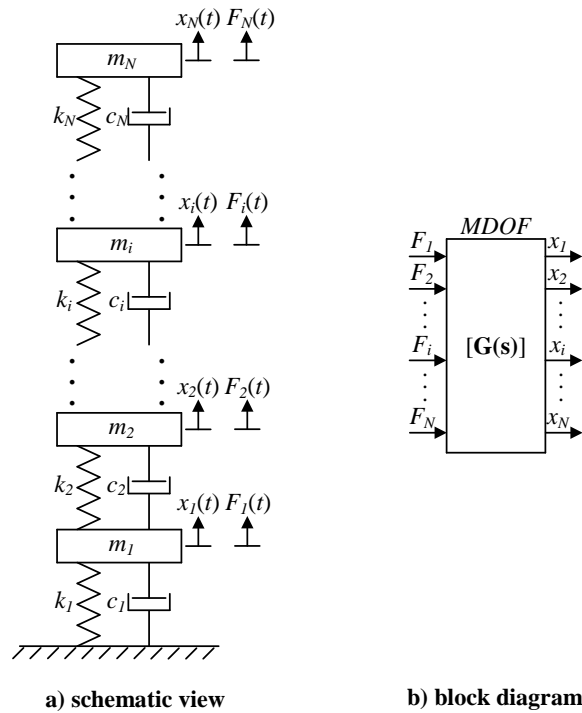
Figure 4.1: Lumped mass model of a MDOF system

In Figure 4.1 an example for a multiple degree of freedom system is shown, which consists of several lumped mass oscillators.

For such a mechanical multiple degree of freedom system the relation between outputs and inputs is described by the following differential equation.

$$[\mathbf{M}] \cdot \{\ddot{x}(t)\} + [\mathbf{C}] \cdot \{\dot{x}(t)\} + [\mathbf{K}] \cdot \{x(t)\} = \{f(t)\} \qquad (4\text{-}1)$$

For a system with N degrees of freedom $[\mathbf{M}]$, $[\mathbf{C}]$ and $[\mathbf{K}]$ are $N \times N$ matrices, which are called the mass-, damping- and stiffness-matrix, respectively. $\{x(t)\}^{N \times 1}$ and $\{f(t)\}^{N \times 1}$ are the input and the output vector. So the MDOF system is described by N coupled differential equations of the 2nd order. In Figure 4.1b the corresponding block diagram is also shown

together with the transfer function matrix $[\mathbf{G}(s)]$, which describes the system in the Laplace domain and so is equivalent to equation (4-1). The aim of system identification is to find this transfer function.

In order to find the homogenous solution for equation (4-1), the right side is set to $\{0\}$.

$$[\mathbf{M}] \cdot \{\ddot{x}(t)\} + [\mathbf{C}] \cdot \{\dot{x}(t)\} + [\mathbf{K}] \cdot \{x(t)\} = \{0\} \tag{4-2}$$

A differential equation of this kind has solutions of the form of an exponential function.

$$\{x(t)\} = \{X\}e^{\lambda t + i\varphi} = \{X\}e^{i\varphi}e^{\lambda t} = \{\bar{X}\}e^{\lambda t} \tag{4-3}$$

In this function $\{\bar{X}\}$ is a vector of complex amplitudes that includes the phase shift φ. Substituting it into equation (4-2) yields:

$$([\mathbf{M}]\lambda^2 + [\mathbf{C}]\lambda + [\mathbf{K}])\{\bar{X}\}e^{\lambda t} = \{0\} \tag{4-4}$$

It is possible to transform the N differential equations of the 2nd order into $2N$ of the first order to facilitate the solution of equation (4-6). For this purpose, a so-called state space model can be defined.

All possible states of the system are defined by the amount of energy in each of the energy storages of the system. Every single lumped mass oscillator in a MDOF systems stores kinetic and potential energy, so a N-DOF system has $2N$ energy storages. The amount of energy in every storage is given by the displacement x and the velocity $\dot{x}$ of every oscillator. So the state variable can be defined as

$$\{y(t)\} = \begin{Bmatrix} \{\dot{x}(t)\} \\ \{x(t)\} \end{Bmatrix} \tag{4-5}$$

Where $\{x(t)\}$ is a vector, which contains all displacements for every DOF as function of time. Now a system of differential equations of the 1st order can be defined:

$$[\mathbf{A}] \cdot \{\dot{y}(t)\} + [\mathbf{B}] \cdot \{y(t)\} = \{0\} \tag{4-6}$$

This transformation of a set of N differential equations of the second order to a set of $2N$ differential equations of the first order is not unique. In literature different definitions for the matrices $[\mathbf{A}]$ and $[\mathbf{B}]$ can be found, which than are called 'similar'. Here the one proposed in [63] shall be used.

$$[\mathbf{A}] = \begin{bmatrix} [\mathbf{0}] & [\mathbf{M}] \\ [\mathbf{M}] & [\mathbf{C}] \end{bmatrix}, [\mathbf{B}] = \begin{bmatrix} -[\mathbf{M}] & [\mathbf{0}] \\ [\mathbf{0}] & [\mathbf{K}] \end{bmatrix} \tag{4-7}$$

Apart from in Heylen et al. [63] further details can also be found in Maia et al. [64], where a similar but not the same definition of the matrices $[\mathbf{A}]$ and $[\mathbf{B}]$ is proposed.

Inserting the matrices defined in (4-7) and the state variable into equation (4-6) yields the system of $2N$ differential equations:

$$[\mathbf{M}]\{\dot{x}(t)\} - [\mathbf{M}]\{\dot{x}(t)\} = \{0\}$$

$$[\mathbf{M}]\{\ddot{x}(t)\} + [\mathbf{C}]\{\dot{x}(t)\} + [\mathbf{K}]\{x(t)\} = \{0\} \tag{4-8}$$

Now the solutions of (4-6) are of the form:

$$\{y(t)\} = \begin{Bmatrix} \lambda\{\bar{X}\}e^{\lambda t} \\ \{\bar{X}\}e^{\lambda t} \end{Bmatrix} = \begin{Bmatrix} \lambda\{\bar{X}\} \\ \{\bar{X}\} \end{Bmatrix} e^{\lambda t} \tag{4-9}$$

Again this equation is substituted into (4-6):

$$([\mathbf{A}] \cdot \lambda + [\mathbf{B}]) \begin{Bmatrix} \lambda\{\bar{X}\}e^{\lambda t} \\ \{\bar{X}\}e^{\lambda t} \end{Bmatrix} = \begin{Bmatrix} 0 \\ 0 \end{Bmatrix} \tag{4-10}$$

Since $e^{\lambda t}$ is non-zero for all points in time, this equation can be divided by this term. This yields the following general eigenvalue problem, whose solutions are the eigenvalues and the corresponding eigenvectors of the system.

$$([\mathbf{A}] \cdot \lambda + [\mathbf{B}]) \begin{Bmatrix} \lambda\{\bar{X}\} \\ \{\bar{X}\} \end{Bmatrix} = \begin{Bmatrix} 0 \\ 0 \end{Bmatrix} \tag{4-11}$$

The trivial but not very interesting solution is that $\begin{Bmatrix} \lambda\{\bar{X}\} \\ \{\bar{X}\} \end{Bmatrix}$ equals $\begin{Bmatrix} 0 \\ 0 \end{Bmatrix}$. This would mean that the system stores no energy, which is only the case for the initial conditions $x(0) = 0$ and $\dot{x}(0) = 0$, so consequently no movement can occur. For the case that the determinant of the matrix $([\mathbf{A}] \cdot \lambda + [\mathbf{B}])$ is not equal to zero, there exists an inverse of this matrix. Then both sides of equation (4-11) can be multiplied by this invers, which yields the trivial solution that is unable to fulfil initial conditions not equal to zero. So a non-trivial solution can only be found for

$$det([\mathbf{A}] \cdot \lambda + [\mathbf{B}]) = 0 \tag{4-12}$$

This is the characteristic equation of a MDOF system, whose solutions for λ are the eigenvalues of the system. For an oscillatory system with N degrees of freedom there are $2N$ eigenvalues appearing in complex conjugate pairs. Substituting them into equation (4-11) and solving it for $\begin{Bmatrix} \lambda\{\bar{X}\} \\ \{\bar{X}\} \end{Bmatrix}$ will yield a corresponding eigenvector of dimension $2N \times 1$ for each eigenvalue λ. In case of multiple eigenvalues there may be problems to identify $2N$ linear independent eigenvectors, e.g. in case of rigid body modes. This case does not occur in Structural Health Monitoring (SHM).

The eigenvectors are collected in the so-called eigenvector or modal matrix.

$$[\mathbf{\Psi}] = \begin{bmatrix} \lambda_1\{\psi\}_1 & \lambda_2\{\psi\}_2 & \cdots & \lambda_N\{\psi\}_N & \lambda_1^*\{\psi\}_1^* & \lambda_2^*\{\psi\}_2^* & \cdots & \lambda_N^*\{\psi\}_N^* \\ \{\psi\}_1 & \{\psi\}_2 & \cdots & \{\psi\}_N & \{\psi\}_1^* & \{\psi\}_2^* & \cdots & \{\psi\}_N^* \end{bmatrix} = \begin{bmatrix} \mathbf{\Psi_u} \\ \mathbf{\Psi_m} \end{bmatrix} \tag{4-13}$$

Each column of this matrix is an eigenvector whose upper part $[\mathbf{\Psi_u}]$ also contains the corresponding eigenvalue. The vectors $\{\psi\}_r \in \mathbb{C}^{N \times 1}$ are called the mode shape vectors or simply mode shapes corresponding to mode r with the eigenvalue λ_r.

As known for eigenvectors, they are not unique but can be scaled arbitrarily and will still fulfil equation (4-11). So in order to compare mode shapes, it is necessary to normalise them in a specific way.

It is possible to obtain the modal parameters of a real structure by experimental approaches like for instance a classic experimental modal analysis (EMA), where the response of the structure is measured while exciting it with a force measured as well. Further approaches for output only measurements exist, where advantage is taken from natural excitations like wind, waves or traffic. Here the input forces are not known, but assumed to be of a certain characteristics like e.g. white noise.

It is a common approach to identify a system, i.e. to find the relationship between input and output quantities, by calculating the transfer functions based on experimentally obtained modal parameters.

In a MDOF system the relation between an excitation at DOF i and the corresponding response at DOF j can be formulated as a transfer function $G_{ij}(s)$. For N degrees of freedom this results in a transfer function matrix $[\mathbf{G}(s)]$ of the dimension N×N.

Based on differential equation (4-1) it can be found as follows. After the equation is transformed into Laplace domain, it can be written as:

$$([\mathbf{M}] \cdot s^2 + [\mathbf{C}] \cdot s + [\mathbf{K}]) \cdot \{x(s)\} = \{f(s)\} \Longleftrightarrow [\mathbf{K_{dyn}}(s)] \cdot \{x(s)\} = \{f(s)\} \tag{4-14}$$

Where s is a complex quantity. The matrix $[\mathbf{K_{dyn}}(s)]$ is called the dynamic stiffness matrix (cf. [63]). Inverting equation (4-14) yields the transfer function matrix as the inverse of the dynamic stiffness matrix.

$$\{x(s)\} = [\mathbf{K_{dyn}}(s)]^{-1} \cdot \{f(s)\} = [\mathbf{G}(s)] \cdot \{f(s)\} \tag{4-15}$$

The partial fraction decomposition of this transfer function matrix can be formulated as follows (cf. [63]).

$$[\mathbf{G}(s)] = [[\mathbf{M}] \cdot s^2 + [\mathbf{C}] \cdot s + [\mathbf{K}]]^{-1} = \sum_{r=1}^{N} \frac{[\mathbf{R}]_r}{s - \lambda_r} + \frac{[\mathbf{R}]_r^*}{s - \lambda_r^*} \tag{4-16}$$

It is possible to use the eigenvalues λ_r and the corresponding residua $[\mathbf{R}]_r \in \mathbb{C}^{N \times N}$ to calculate the transfer function matrix. Furthermore, it is possible to decompose it into its modal contributions. The residua can be obtained by calculating the dyadic products of the mode shape vectors.

$$[\mathbf{G}(s)] = \sum_{r=1}^{N} \frac{\{\psi\}_r \{\psi\}_r^T}{a_r (s - \lambda_r)} + \frac{\{\psi\}_r^* \{\psi\}_r^H}{a_r^* (s - \lambda_r^*)} \tag{4-17}$$

Where the superposed H means conjugated and transposed, also called Hermitian conjugated or adjoint. Like explained above the mode shapes are not unique but can be scaled arbitrary. But the residua are specific values, which depends on the system parameters. So the mode shapes have to be scaled in an appropriate way. For this purpose the scaling factor a_r, the so called Modal A, has been introduced. It can be obtained from the state space model with $[\mathbf{A}]$ and $[\mathbf{B}]$ according to equation (4-7) of the system by the following orthogonality condition (cf. [65]).

$$[\mathbf{\Psi}]^T [\mathbf{A}] [\mathbf{\Psi}] = \begin{bmatrix} a_1 & & & & & \\ & \ddots & & & 0 & \\ & & a_N & & & \\ & & & a_1^* & & \\ & 0 & & & \ddots & \\ & & & & & a_N^* \end{bmatrix} = [\mathbf{a}] \tag{4-18}$$

The unit of Modal A is $\left[\frac{kgm^2}{s}\right]$.

Analogously, another factor can be calculated based on matrix $[\mathbf{B}]$.

$$[\Psi]^T[\mathbf{B}][\Psi] = \begin{bmatrix} b_1 & & & & & \\ & \ddots & & & 0 & \\ & & b_N & & & \\ & & & b_1^* & & \\ & 0 & & & \ddots & \\ & & & & & b_N^* \end{bmatrix} = [\mathbf{b}] \tag{4-19}$$

This factor is called Modal B and its unit is $\left[\frac{kgm^2}{s^2}\right]$. The relationship between these two factors and the eigenvalue is given for mode r by:

$$\lambda_r = -\frac{b_r}{a_r} \tag{4-20}$$

Every single transfer function can now be calculated according to the following formula.

$$G_{ij}(s) = \sum_{r=1}^{N} \frac{{}_rR_{ij}}{s-\lambda_r} + \frac{{}_rR_{ij}^*}{s-\lambda_r^*} = \sum_{r=1}^{N} \frac{{}_r\psi_i \; {}_r\psi_j}{a_r(s-\lambda_r)} + \frac{{}_r\psi_i^* \; {}_r\psi_j^*}{a_r^*(s-\lambda_r^*)} \tag{4-21}$$

For pure imaginary $s = j\Omega$ these functions turn into the Frequency Response Functions (FRF), which describe the amplitude and the phase response of the system in the steady state.

4.2 Inverse stiffness matrix

For the static case, that means if the frequency Ω of the excitation force is zero, the complex frequency s becomes $s = 0$. Substituding this value in equation (4-16) yields:

$$[\mathbf{G}(s=\mathbf{0})] = [\mathbf{K}]^{-1} = \sum_{r=1}^{N} \frac{[\mathbf{R}]_r}{-\lambda_r} + \frac{[\mathbf{R}]_r^*}{-\lambda_r^*} = \sum_{r=1}^{N} \frac{\{\psi\}_r\{\psi\}_r^T}{-a_r\lambda_r} + \frac{\{\psi\}_r^*\{\psi\}_r^H}{-a_r^*\lambda_r^*} \tag{4-22}$$

Obviously, by using this formula the inverse stiffness matrix of the system can be calculated based on measured modal parameters. This matrix is often referred to as flexibility matrix $[\mathbf{F}]$ or even as modal flexibility matrix.

If no damping is present, i.e. $[\mathbf{C}] = [\mathbf{0}]$, the residua ${}_rR_{ij} = {}_r\psi_i^* a_r^{-1} \; {}_r\psi_j^*$ become purely imaginary values (cf. for instance [63]). Furthermore, for this case the eigenvalue are $\lambda_r = \pm i\omega_r$ and the eigenvectors are real. Now equation (4-22) can be rewritten as:

$$[\mathbf{F}] = [\mathbf{K}]^{-1} = \sum_{r=1}^{N} \frac{[\mathbf{R}]_r}{-i\omega_r} + \frac{-[\mathbf{R}]_r}{i\omega_r} \tag{4-23}$$

After inserting the residuum $[\mathbf{R}]_r = \frac{\{\psi\}_r\{\psi\}_r^T}{a_r}$ and expanding the two fractions in equation (4-23) by the conjugate denominator one obtains:

$$[\mathbf{F}] = [\mathbf{K}]^{-1} = \sum_{r=1}^{N} \frac{\{\psi\}_r \frac{2i\omega_r}{a_r}\{\psi\}_r^T}{\omega_r^2} = \sum_{r=1}^{N} \frac{\{\psi\}_r\{\psi\}_r^T}{m_r \omega_r^2} \tag{4-24}$$

$$m_r = \frac{a_r}{2i\omega_r} \tag{4-25}$$

The quantity m_r is the so-called modal mass $[kgm^2]$ corresponding to mode r. By using the modal mass as scaling factor, the mode shapes can be normalised to unit modal mass (UMM).

$$\frac{\{\psi_r\}^T[\mathbf{M}]\{\psi_r\}}{m_r} = 1 = \{\varphi_r\}^T[\mathbf{M}]\{\varphi_r\} \tag{4-26}$$

Herewith, equation (4-24) can be reformulated as follows.

$$[\mathbf{F}] = \sum_{r=1}^{N} \frac{\{\varphi\}_r\{\varphi\}_r^T}{\omega_r^2} = [\mathbf{\Phi}][\mathbf{\Omega}]^{-1}[\mathbf{\Phi}]^T \tag{4-27}$$

Where $[\mathbf{\Phi}]$ is a matrix containing the UMM mode shapes $\{\varphi_r\}$ as column vectors and $[\mathbf{\Omega}]$ is a diagonal matrix containing the corresponding squared angular eigenfrequencies.

If the modal parameters were identified experimentally, the number of identified modes M is often smaller than the number of measured DOFs N, as higher modes are more difficult to excite and to measure with precision. Hence, the sum in equation (4-27) is truncated after $r = M \leq N$. Due to the square of angular eigenfrequency in the denominator, the contribution of higher modes to the flexibility is small compared to lower modes. Therefore, adequate results for $[\mathbf{F}]$ may be obtained even with $M < N$.

Theoretically, the stiffness matrix can be obtained by just inverting the flexibility matrix. But since the flexibility matrix is calculated from the dyadic products of M mode shape vectors, a $N{\times}N$ flexibility matrix has the rank M. If $M < N$, the resulting flexibility matrix is singular and hence cannot be inverted.

4.3   Physical meaning of the modal parameters

In this chapter a brief explanation is given about how the modal parameters of a structure have to be interpreted physically. As explained in Chapter 4.1, the eigenvalues and the corresponding eigenvectors are the solutions of the general eigenvalue problem in equation (4-11) and are specific for each mode r. The eigenvalues λ_r that appear in complex conjugated pairs are of the form (cf. [64]):

$$\lambda_r = \omega_r \left(-\xi_r \pm i\sqrt{1 - \xi_r^2} \right) \tag{4-28}$$

Where ω_r is the angular eigenfrequency of the undamped system and ξ_r is the damping ratio related to the critical damping. If $\xi_r < 1$ the system is underdamped and a harmonic oscillation, whose energy will be dissipated over time, can take place. This is the interesting case for this thesis. More information about this physical quantity and the behaviour of single degree of freedom oscillators can be taken from many sources, for instance the first chapter of [64].

As can be seen from equation (4-28) the eigenvalue is a complex number that includes two pieces of information, the frequency and the damping of the oscillation of the structure in mode r. The imaginary part $\omega_r\sqrt{1 - \xi_r^2}$ is the angular eigenfrequency of the damped system ω_{dr} and the angular eigenfrequency of the undamped system ω_r itself is the absolute value of the eigenvalue. Therefore, the quantities eigenvalue and eigenfrequency must not be confused. The argument of this complex number is only defined by the damping.

As explained in Chapter 4.1, in state space formulation the eigenvectors of a structure are of the form $\left\{ \begin{array}{c} \lambda_r \{\psi\}_r \\ \{\psi\}_r \end{array} \right\} = \left\{ \begin{array}{c} \lambda_r \{\bar{X}\}_r \\ \{\bar{X}\}_r \end{array} \right\}$, i.e. the components $_r\psi_i$ of the mode shapes are the complex amplitudes $_r\bar{X}_i$ for the oscillations of each DOF i in mode r. The absolute values of these amplitudes are the maximum displacements of a DOF relative to each other DOF, while their arguments are the phase shifts between the oscillations of the DOFs. Since the eigenvectors are arbitrarily scalable, these amplitudes are only relative values. The complete free vibration response of a structure can now be formulated as (cf. [64]):

$$\{x(t)\} = \sum_{r\prime=1}^{2N} \{\psi\}_{r\prime}\bar{Q}_{r\prime}e^{\lambda_{r\prime}t} = \sum_{r=1}^{N} \{\psi\}_r\bar{Q}_r e^{\lambda_r t} + \{\psi\}_r^*\bar{Q}_r^* e^{\lambda_r^* t} \tag{4-29}$$

Where r' is the number of a column in the modal matrix as defined in equation (4-13), while r is the mode number. $\bar{Q}_r$ are the so-called modal participation factors, which are weighting factors for each mode that depend on the initial conditions. For instance, if the structure is excited by a hammer impact in general all N modes participate to the response, while if all DOFs are deflected according to a certain mode shape and then let free without initial velocity, the resulting response is exactly the corresponding mode.

If the arguments of the components in the mode shape vectors differ only by 0° or 180°, they are so-called normal modes. It means that during the oscillation in the corresponding mode, all DOFs reach the maximal displacement at the same time, the oscillations are in phase. If other relative phase shifts occur, one talks of complex modes. Normal modes are in general only obtained in the case of small or no damping or in the rather hypothetical case of proportional damping. For instance, an FE-simulation, where no attenuation was taken into account, provides normal modes. Since these mode shapes are displayed as purely real vectors, they are often called real modes, but this is not accurate because by scaling them by a complex factor the components can become complex values again and it is still the same mode shape.

In reality, damping is always present and additionally measurement errors occur, so the mode shapes are always complex ones. But for low damped systems the relative phase shifts differ only slightly from 0° or 180°. However, in order to compare measured mode shapes to simulated normal ones, a method for the extraction of real mode shapes from measured complex ones must be established. One possibility for this is suggested by Wang et al. in [65]. But in the case of weakly damped systems, the simplest possibility is to consider only the imaginary part, the real part, or the magnitude of the individual components of the measured mode shapes. However, it must be checked for each individual case which one of these approaches is appropriate, which is difficult to automate. But such automation is necessary if an optimisation algorithm will be used.

As stated in equation (4-26), except for eigenfrequencies, mode shapes and damping ratio there is another modal parameter, the so-called generalised or modal mass m_r, replacing or expressing the scaling factor of the mode shapes.

$$\{\psi_r\}^H[\mathbf{M}]\{\psi_r\} = m_r \tag{4-30}$$

Analogously, the generalised stiffness and damping can be calculated by the following formulas (4-31) and (4-32), respectively.

$$\{\psi_r\}^H[\mathbf{K}]\{\psi_r\} = k_r \tag{4-31}$$

$$\{\psi_r\}^H[\mathbf{C}]\{\psi_r\} = c_r \tag{4-32}$$

Finally, with these values the angular eigenfrequency for mode r can be calculated by the same formula as used for SDOF systems.

$$\omega_r = \sqrt{\frac{k_r}{m_r}} \tag{4-33}$$

4.4 Experimental determination of modal parameters by EMA

The modal parameters can be determined analytically by solving the general eigenvalue problem in equation (4-11), if the structural matrices $[\mathbf{M}]$, $[\mathbf{K}]$ and $[\mathbf{C}]$ are known. But in Chapter 4.1 it is shown, that the other way around is also possible. That means the transfer function matrix $[\mathbf{G}(s)]$, which is defined by the structural matrices according to equations (4-14)-(4-16) can be calculated from modal parameters (equation (4-17)). Therefore, an experimentally system identification is possible based on measured modal parameters.

In a process called experimental modal analysis (EMA), the modal parameters of a structure can be estimated based on measurements. For this purpose, the structure is excited by a force, which is measured as input signal. Different forms of excitations are used. An impulse can be generated by a hammer impact, whose spectrum includes frequencies in a certain range that depends on the stiffness of the hammer head. By using a soft hammer head vibrations at lower frequencies will be excited than with a stiffer hammer head. Alternatively, the impulse can be generated by a dropped weight. Furthermore, an electromagnetic shaker or an unbalanced mass exciter can be used to generate a defined force signal, for instance white noise or a harmonic excitation with varying frequencies. In the present thesis a so-called swept sine excitation is used were the frequency of a harmonic input signal is steadily increased with a certain sweep rate.

The response of the structure, i.e. the vibrations that are caused by the excitation, is measured for different degrees of freedom (DOFs), for instance by means of accelerometers or laser vibrometers. The measured DOFs are defined by the positions of the sensors and the

measurement directions. Alternatively, the response can be measured only for one degree of freedom but the position of the exciter is altered.

After the measurements the data is transformed from time to frequency domain by an FFT (Fast Fourier Transformation) and the spectra of the output signals are divided by the spectra of the input signals to determine the frequency response functions (FRFs) for discrete frequencies. Different formulas can be found in literature for this purpose (e.g [63,64,66]) and often not the FFT spectra directly but cross- and autopower spectra are used.

Now the modal parameters can be estimated based on the obtained FRFs. Different methods can be used for this step like for instance algorithms which calculates a best fit of an assumed analytical FRF with the modal parameters as fitting variables.

4.5   Mode shape correlation methods

How previously described, the eigenvectors $\begin{Bmatrix} \lambda_r\{\psi\}_r \\ \{\psi\}_r \end{Bmatrix}$ of a MDOF systems consists of the mode shapes $\{\psi\}_r$ and the corresponding eigenvalues λ_r, where r is the number of the mode. For a system with N degrees of freedom, N modes exist, which are summarised together with their complex conjugates in the so-called modal matrix given in (4-13). Since eigenvectors are still valid if they are scaled arbitrarily, it is mostly necessary to normalise the mode shapes before they can be compared. Several possibilities for this normalisation can be found in literature, like the previously described scaling to unit modal mass (UMM) or the scaling to the highest magnitude of the components.

Mode shapes obtained by means of an FE-simulation are often purely real, as often no damping is taken into account in the FE model. In this case, a comparison with measured complex mode shapes, e.g. in a model updating procedure, can be facilitated by extracting real mode shapes from the complex ones. One way to do this is described in [65]. Depending on the mode shapes it can be sufficient to just consider the imaginary or the real part.

Furthermore, if mode shapes obtained by a simulation shall be compared to measured ones and the simulation already uses the same kind of normalisation as the one used for the measurements, it still can happen that a simulated mode shape is turned by 180° compared to the corresponding measured one. Although it still remains the same shape, the Euclidian difference between the simulated and the measured vectors will be huge. If the parameters of the model are changed it can even happen that in one simulation run the mode shapes are

rotated by 180° and in another one they are not. That means it is difficult to compare mode shape vectors by just calculating the Euclidian norm of the difference vector.

As an alternative in literature (cf. for instance [64,66]) several so-called correlation criterions are described. Some of them are used in this thesis and therefore are briefly described here. All criterions used here have the advantage that no information about the structural matrices [**K**], [**M**] and [**C**] are necessary for the evaluation. But it shall be mentioned that some variations exists, which include the structural matrices e.g. for the purpose of weighting.

The first one is the so-called Modal Assurance Criterion (MAC), which is widely used in the research community for the correlation of mode shapes. It is defined by the following formula.

$$MAC(\{\psi_{\mathrm{meas}}\}, \{\psi_{\mathrm{sim}}\}) = \frac{|\{\psi_{\mathrm{meas}}\}^T [\mathbf{W}] \{\psi^*_{sim}\}|^2}{(\{\psi_{\mathrm{meas}}\}^T [\mathbf{W}] \{\psi^*_{meas}\})(\{\psi_{\mathrm{sim}}\}^T [\mathbf{W}] \{\psi^*_{sim}\})} \tag{4-34}$$

Here the compared vectors $\{\psi_{\mathrm{meas}}\}$ and $\{\psi_{\mathrm{sim}}\}$ are the measured and the simulated mode shape, respectively. But the MAC can be used for the comparison of arbitrary vectors. [**W**] is a weighing matrix. If the mass- or the stiffness-matrix is used to define the weighting, this criterion is called Normalised MAC or Normalised Cross Orthogonality (NCO). Since in an experimental modal analysis these matrices are typically unknown or difficult to determine with sufficient accuracy, in the following the unity matrix is used for [**W**]. This is the approach often used in the research community.

The scalar product in the numerator $\{\psi_{\mathrm{meas}}\}^T \{\psi^*_{sim}\}$ yields in general a complex number $\bar{a} \in \mathbb{C}$, while the products in the denominator yield real values $b, c \in \mathbb{R}$, since they are the squared absolute values of the mode shape vectors. With that equation (4-34) can be simplified as:

$$MAC_{unscaled} = \frac{|\bar{a}|^2}{b \cdot c} \tag{4-35}$$

Let us assume that the mode shapes are scaled by arbitrarily complex scaling factors $\bar{c}_1$ and $\bar{c}_2$. Then equation (4-34) becomes:

$$MAC_{scaled}(\{\psi_{\mathrm{meas}}\}, \{\psi_{\mathrm{sim}}\}) = \frac{|\bar{c}_1 \{\psi_{\mathrm{meas}}\}^T \bar{c}_2^* \{\psi^*_{sim}\}|^2}{(\bar{c}_1 \{\psi_{\mathrm{meas}}\}^T \bar{c}_1^* \{\psi^*_{meas}\})(\bar{c}_2 \{\psi_{\mathrm{sim}}\}^T \bar{c}_2^* \{\psi^*_{sim}\})} \tag{4-36}$$

With the same approach as for $MAC_{unscaled}$ this equation can be simplified:

$$MAC_{scaled} = \frac{|\bar{c}_1 \bar{c}_2^* \bar{a}|^2}{(|\bar{c}_1|^2 b)(|\bar{c}_2|^2 c)} = \frac{|\bar{c}_1|^2 |\bar{c}_2|^2 |\bar{a}|^2}{|\bar{c}_1|^2 |\bar{c}_2|^2 b \cdot c} = MAC_{unscaled} \quad q.e.d. \tag{4-37}$$

That means this criterion works for complex as well as for real vectors, since it has the great advantage that it is independent of the scaling of the mode shapes, which is why $\{\psi_{meas}\}$ and $\{\psi_{sim}\}$ can be arbitrarily scaled mode shapes. That also means that a phase lag between the mode shapes, like for instance a rotation in the complex plane by 180°, does not influence results. For real modes as well as complex modes the MAC provides a real value between 0 and 1, where 1 means perfect matching of both vectors and 0 means orthogonality, i.e. no match.

Because of these properties, the modal assurance criterion is highly appropriate for the realisation of an automatic correlation of mode shape pairs from measured and simulated modes. A decrease of the MAC value for these correlated pairs over time can be an indicator for changings at a structure like for instance damage.

Another criterion that is related to the MAC, is the Normalised Modal Difference (NMD), which was proposed by Mordini et al. in [44] for the comparison of quite similar mode shapes. According to the authors, it is much more sensitive than that MAC to the difference of similar vectors but less useful for uncorrelated ones. It is described in more detail in [64]. The physical meaning of the NMD is explained there as the average fraction of difference of all DOFs between the two compared modes. So if the NMD-value is zero, the modes match perfectly. The NMD can be calculated based on the MAC as follows.

$$NMD = \sqrt{\frac{1 - MAC}{MAC}} \tag{4-38}$$

A third correlation criterion that can be found in [63], [64], as well as [66] is the Modal Scale Factor (MSF). It can be defined in two different ways, depending on which mode shapes are used as reference.

$$MSF(\{\psi_{meas}\}, \{\psi_{sim}\}) = \frac{|\{\psi_{meas}\}^T \{\psi_{sim}^*\}|}{\{\psi_{sim}\}^T \{\psi_{sim}^*\}} \tag{4-39}$$

$$MSF(\{\psi_{\text{sim}}\},\{\psi_{\text{meas}}\}) = \frac{|\{\psi_{\text{sim}}\}^T\{\psi_{meas}^*\}|}{\{\psi_{\text{meas}}\}^T\{\psi_{meas}^*\}} \tag{4-40}$$

If the measured and the simulated mode shape vectors only differs by an arbitrary scalar factor $\bar{c} \in \mathbb{C}$ ($\{\psi_{\text{sim}}\} = \bar{c}\{\psi_{\text{meas}}\}$), the resulting MSF values are:

$$MSF(\{\psi_{\text{meas}}\},\{\psi_{\text{sim}}\}) = \frac{|\{\psi_{\text{meas}}\}^T\bar{c}^*\{\psi_{meas}^*\}|}{\bar{c}\{\psi_{\text{meas}}\}^T\bar{c}^*\{\psi_{meas}^*\}} = \frac{1}{|\bar{c}|} \tag{4-41}$$

$$MSF(\{\psi_{\text{sim}}\},\{\psi_{\text{meas}}\}) = \frac{|\bar{c}\{\psi_{\text{meas}}\}^T\{\psi_{meas}^*\}|}{\{\psi_{\text{meas}}\}^T\{\psi_{meas}^*\}} = |\bar{c}| \tag{4-42}$$

In literature the physical meaning of MSF and MAC is described as follows. In order to compare two vectors, like for instance mode shapes, the components of one vector can be plotted vs. the components of the second vector. Afterwards a linear regression line can be calculated. The MSF is the slope of this line, while the MAC provides the degree of correlation. If the MAC value is equal to zero, the MSF value has no meaning because there is no linear relationship. If the mode shapes to be compared are normalised in the same way, e.g. to unit model mass, a MSF-value near 1 means a good correlation.

MAC, NMD and MSF are global correlation criterions, i.e. they do not provide any information about the location of the differences between compared mode shapes. Hence, if they are used as damage indicators, the damage can be detected but not localised. For this purpose, other criterions exists, like for instance the Coordinate Modal Assurance Criterion (COMAC) that is also described in [64] and [66]. Instead of providing global information about differences between two mode shapes, it compares the shapes at the individual DOFs, averaged over several correlated mode shape pairs (CMP). Based on a set of n_{CMP} mode shape pairs, the COMAC value for every DOF i can be calculated by the following formula.

$$COMAC(i) = \frac{\left(\sum_{j=1}^{n_{CMP}}|\psi_{sim}(i,j)\psi_{meas}^*(i,j)|\right)^2}{\sum_{j=1}^{n_{CMP}}|\psi_{sim}(i,j)|^2 \sum_{j=1}^{n_{CMP}}|\psi_{meas}(i,j)|^2} \tag{4-43}$$

This correlation technique is also described in [63], where the authors state that, in opposition to the MAC, the COMAC is very sensitive to the scaling of the mode shapes. That means, for the calculation of the COMAC, the same normalisation must be used for all mode shapes.

4.6 Optimisation and model updating

The basic idea of model updating is to minimise the deviation between simulated results and measured values. For this purpose, a mathematical model, usually a numerical finite element model, is updated by varying a set of predefined parameters. In order to measure the deviation between model and reality, a so called objective function depending on the chosen updating parameters is defined, which yields an objective value that has to be minimised. The simulated values depend on the updating parameters, while the measurements can be carried out at different points in time and thus reflect different states of the structure, so the model can be adapted to these different states.

In model updating, an optimisation problem is solved, which can be formulated mathematically (for detailed information cf. Nocedal et al. (2006) [67]).

$$\underset{\{p\}\in\mathbb{R}^n}{\text{Min}} f(\{p\}) \quad subject\ to \quad \begin{matrix} c_i(\{p\}) = 0 \\ c_j(\{p\}) \geq 0 \end{matrix} \tag{4-44}$$

The function $f(\{p\})$ with $\{p\} \in \mathbb{R}^n$ is the objective function depending on a set of n unknown or uncertain parameters p. The vector $\{p\}$ must satisfy the equality conditions c_i as well as the inequality conditions c_j.

For the purpose of damage detection the idea is that changes of the structure, especially local stiffness reductions, are a hint to damage. Therefore, here the aim of the model updating is to localise and quantify stiffness reduction.

In the first step it must be decided, which parameters will be used in the model to simulate damage. For instance to model a local reduction of the bending stiffness EJ, where E is the Young's modulus of the material and J is the area moment of inertia of the cross-section, either E or J can be reduced. That means either material properties of certain elements or geometrical properties at a certain position can be used as parameter $\{p\}$.

After the used parameters are defined, an appropriate FE-model must be created. Not only the model must be parametrised, it must also be possible to determine with sufficient accuracy the quantities, which have been measured in reality, too. For instance, these can be static displacements of nodes at the positions, where displacement sensors were located in reality or the measured and the simulated eigenfrequencies.

In the next step, the objective function must be defined that shall be used to compare the measured physical quantities and the simulated ones. In the following, three possibilities are

proposed to compare scalar variables (e.g. displacements or eigenfrequencies), vector quantities (e.g. mode shapes) or matrices (e.g. modal flexibility matrices). Since the measured values can be obtained by different measuring methods, the objective function for model updating is a good possibility to combine the results of static and dynamic measurements.

If the quantities to be compared are scalar quantities, a method similar to the weighted least squares technique, as suggested by Link 1999 [35], may be used.

$$
\begin{aligned}
f_{scalar}(\{p\}) \quad &= \|[W](\{x_{meas}\} - \{x_{sim}(\{p\})\})\|_2 \\
&= \sqrt{\sum_{i=1}^{k}\left(W_{ii}|\ _i x_{meas} -\ _i x_{sim}\{p\}|\right)^2}
\end{aligned}
\qquad (4\text{-}45)
$$

Where k is the number of measured values and $[W]$ is a diagonal weighting matrix.

At first, the difference between the measured value and the result of the FE simulation is calculated for any scalar value. This difference is weighted by the factor W_{ii} and subsequently squared. The weighted error squares are summed. The objective value results as the square root of this sum. In other words, the measured and simulated values are combined in the vectors $\{x_{meas}\}$ and $\{x_{sim}\}$, respectively, and then the Euclidean norm of the weighted difference vector is determined (cf. Appendix A.1 for an explanation of the used norms). The simulated values depend on the selected parameters $\{p\}$, while the measurements can be carried out at different points in time, thus reflecting different states of the structure. As long as all the measured and simulated quantities are not complex but real numbers, the absolute values in equation (4-45) can be omitted.

The weighting factors W_{ii} can be defined as follows. Since measurements are always subject to errors, measured values, which can be determined with lower accuracy, should have a smaller influence on the objective value than more accurate measurements. In order to achieve this, it is proposed here to divide this difference between measurement and simulation by the accuracy of the respective measurement. In the ideal case, a statistical value such as the standard deviation should be used, as for instance proposed by Schlune et al. 2009 [45]. Since the accuracy also has the same unit as the measured value, one now also obtains a unified value. Only in this way it is possible to add deviations of different physical quantities, such as eigenfrequencies and displacements. The value of the objective function is then also unified. Furthermore, it is proposed here that the differences should be divided by the total number of measurements k in order to avoid the objective value being increased only because

more measurements have been included in its calculation. This is especially important if objective functions containing different physical quantities, are added in a complete objective function, e.g. the deviation of the static deflection to the deviation of the mode shapes. The differences of the static deflection and the differences of the mode shapes must be divided by the number of distance sensors and considered degrees of freedom, respectively. Otherwise, the contribution to the complete objective function, for which more measured values were used, prevails.

Instead of the L2-norm (Euclidian norm), as in equation (4-45), it is also proposed to use other norms for the definition of the objective function, e.g. the L1-norm, which is in fact the sum of the absolute values of the components of a vector. In Chapter 8.3 the objective functions actually used are explained in more detail and in Chapter 8.6 the results when using the L1-norm are compared to the ones obtained with the L2-norm.

An objective function based on the L1-norm will be defined as follows.

$$f_{scalar}(\{p\}) = \|[W](\{x_{meas}\} - \{x_{sim}(\{p\})\})\|_1 = \sum_{i=1}^{k} W_{ii} \left| {}_i x_{meas} - {}_i x_{sim}\{p\} \right| \tag{4-46}$$

Thus the objective value will be the weighted sum of the absolute values of the difference vector's components. In general, the objective values determined with this equation are greater than the target values according to equation (4-45), since here is no square root. Therefore, the objective function according to equation (4-46) is more sensitive to changes in the parameters.

Like already mentioned the measured values can be obtained by static or dynamic measurements. However, if vibration parameters are used, some challenges arise which are not important for static measurements. For the comparison of dynamic properties, first the measured modes and the simulated ones must be correlated. The particular challenge is here, that when changing the model by modifying the updating parameters, the number and order of the simulated modes in the considered frequency range can change. Therefore, the correlation made for the reference state of the model, i.e. when no damage is simulated, need not to be valid for the following simulations with different parameters. Therefore, it is advantageous to implement an automatic mode correlation. Therefore, correlation techniques like the ones described in Chapter 4.5 may be used. Especially, the Modal Assurance Criterion (MAC) as given in equation (4-34) is highly appropriate for this task.

This criterion can be used to identify automatically the matching mode pairs. The approach calculates the MAC-value between all measured and simulated modes and the results are saved as a matrix. Then the highest MAC-values are searched in order to define the correlated mode pairs.
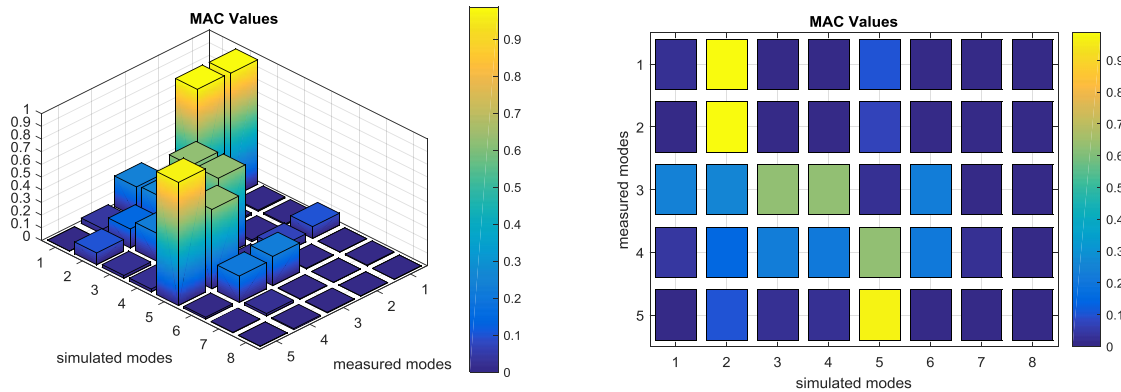
Figure 4.2: Example for a correlation of measured modes with simulated ones by means of MAC

Figure 4.2 shows an example for this correlation technique. Here 5 modes were identified by an experimental modal analysis (EMA) and 8 modes were simulated by an FE-model of the structure. The second simulated mode shape can be correlated with the first as well as the second mode that were identified from measured data. This is because both measured modes have a similar shape. The same applies to the third measured mode, where 2 matching simulated modes can be found. In such cases it must be defined in the automatic correlation, which possibilities shall be chosen. In this example only simulated mode 5 can be unambiguously correlated with the fifth measured mode. Here, measured mode 4 was omitted from the further evaluations, because it was not well identified and so no similar mode shape was found by the simulation, meaning that all mode pairs with this mode have rather low MAC values. The simulated modes 1, 6, 7 and 8 were not identified by the EMA. That can happen, if they were not well excited or if the sensors did not measure the DOFs that were oscillating in these modes. Apart from this, it can also indicate modelling errors. The example shows that although it is theoretically simple to implement an automatic correlation algorithm based on the MAC, but some issues have to be considered.

After the correlated mode shape pairs are defined, the dynamic properties can be compared, i.e. objective functions must be defined. Since the eigenfrequencies are scalar values the procedures described above can be used. Actually, for vector quantities, such as mode shapes, the same methods could be used. But it was already discussed in Chapter 4.5, why this is

difficult for mode shape vectors. Alternatively, it is more appropriate to use again the Modal Assurance Criterion (MAC) to define the objective function. The MAC-value is calculated according to equation (4-34) and the deviation of the mode shapes can be defined as 1-MAC. Now the objective function can be formulated as:

$$f_{shapes}(\{p\}) = \|[W]\{1 - MAC(\{p\})\}\|_2 = \sqrt{\sum_{i=1}^{k} \left(W_{ii}(1 - MAC_i(\{p\})) \right)^2} \qquad (4\text{-}47)$$

Where k is the number of measured modes. Of course, here also exists the possibility to use the L1-norm.

If the correlation between the measured and the simulated modes is quite good, i.e. the MAC-values are near 1, an alternative objective function can be defined based on the NMD values (cf. equation (4-38)) as:

$$f_{shapes}(\{p\}) = \|[W]\{NMD(\{p\})\}\|_2 = \sqrt{\sum_{i=1}^{k} \left(W_{ii}(NMD_i(\{p\})) \right)^2} \qquad (4\text{-}48)$$

Instead of considering the eigenfrequencies as scalar values and the mode shapes individually, the modal parameters can also be summarised by calculating the flexibility matrix according to equation (4-24). It applies to undamped or proportionally damped systems, whereby proportional attenuation can be assumed for weakly damped systems such as the bridges considered here.

How suggested by Jaishi und Ren (2006) [41], the Frobenius norm can be used to calculate the deviations between measurement and simulation. This norm is defined for a matrix of dimension $N \times M$ as:

$$\|[\mathbf{A}]\|_F = \sum_{i=1}^{N} \sum_{j=1}^{M} |a_{ij}|^2 \qquad (4\text{-}49)$$

This allows calculating the Frobenius norm of a matrix, which contains the differences between the components of the measured and the simulated flexibility matrix.

$$f_{flex}(\{p\}) = W \cdot \|[\mathbf{F_{meas}}] - [\mathbf{F_{sim}}]\|_F = \frac{1}{N^2} \cdot \frac{1}{\Delta} \cdot \sum_{i=1}^{N} \sum_{j=1}^{N} \left| \left(_{ij}f_{meas} - _{ij}f_{sim}(\{p\}) \right) \right|^2 \qquad (4\text{-}50)$$

where W is a weighting factor. It is proposed here to define the weighting by considering the number of measured degrees of freedom N and the accuracy of the calculated flexibility Δ.

For the algorithm that minimises the objective function, there are many possibilities. For example, the trust region Newton method, also used by Teughels (2002) [36], as described in [67]. Promising as well is the NLPQL algorithm (Non Linear Programming by Quadratic Lagrangian) published by Schittkowski (1986) [68].

After the model is finished it has to be validated. That means the simulated results of the model without damage must fit to the measurements taken from a reference state of the structure. Later measurements are compared to this reference state in order to find changes, which can be caused by damage. Hence, the measurements must be repeatable and therefore well documented. Ideally, the reference measurements were taken from the newly build bridge. The model updating procedure can already be used for this validation (like for instance in [39]). But the validation can also mean to use engineering knowledge to change properties of the model independent from the updating parameters with the aim to improve the consistency between measurement and simulation.

With a parametrised and validated model of the reference state, damage assessment can be performed in distinct time intervals. First measurements must be performed in the same way as the reference measurements. Now the model can be updated by searching for an optimal parameter set that minimises the objective function or the deviation between simulation and measurement. Afterwards, the updated model is compared to the reference model in order to detect, localise and quantify damage. For instance the stiffness matrices of the two models can be compared. If damage is present at the real bridge, it can be expected that the simulation results fit best to the new measurements, if the stiffness of the model was reduced at the correct locations of damage.

5 IN-SITU TESTS AT A PRESTRESSED BRIDGE BEAM

5.1 Initial situation and test setup

In autumn 2013 a new steel bridge was inaugurated, which crosses the river Mosel between Grevenmacher (Luxembourg) and Wellen (Germany). It replaces a bridge built in the years 1953 to 1955 that was made of prestressed concrete. This former bridge was demolished due to safety concerns.

The old bridge consisted of 5 spans, where each span was composed of 5 adjoining concrete beams, which carried the driving lane. These beams were prestressed by internal steel tendons in longitudinal direction. Furthermore, the individual beams were connected to each other by transverse tendons in a distance of $7.5\,m$, also imbedded in concrete. These connections are here referred to as transverse beams. Further transverse tendons were imbedded in the top flange.

Two of these beams, with a length of $46\,m$ and a mass of approximately $120\,t$ each, were shipped to the nearby port of Mertert. Their 19 tendons in longitudinal direction were intact, while the transverse tendons had lost their prestress, because they were cut during the demolition of the bridge. These beams were used to test different methods for damage detection and localisation.

During the demolition of the bridge and the subsequent transport, both beams were a little bit damaged, especially on the top flange. The centre bar, in which the longitudinal tendons were located, remained visibly intact. Figure 5.1 gives an impression of the condition of the beams at the beginning of the experiments. One can also see the seven transverse beams and some of the transverse tendons.

The two beams were still connected by some of the transverse beams, but these were finally cut. One of the beams was then used for the further experiments, while the other one was cut into parts and used to load the structure.
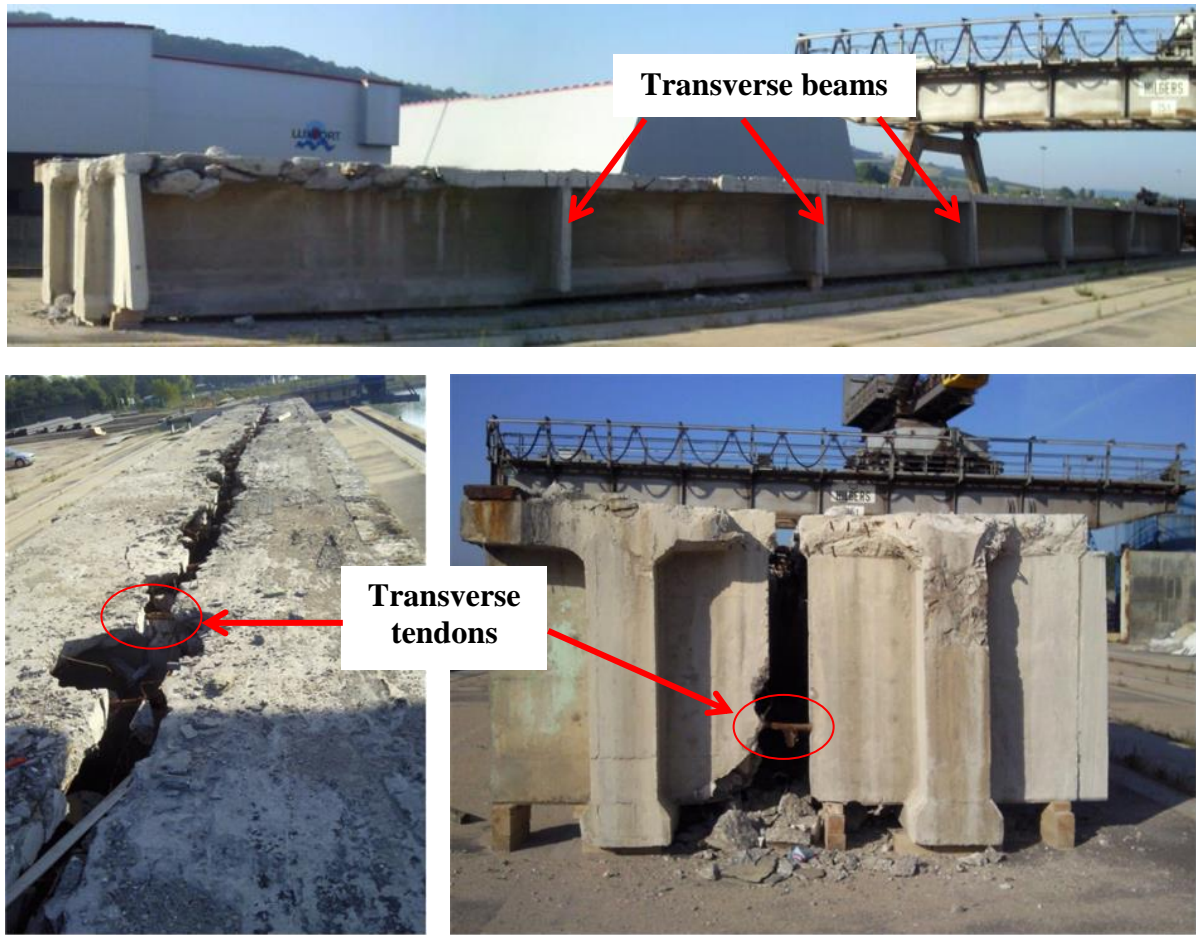
Figure 5.1: Condition of the concrete beams at 21st of August 2013 after their transport to the port of Mertert

Specimens have been taken from the beams in order to determine the material properties of the concrete. In Table 5.1 the measured properties are summarised.

| a) Preparation for measurement of Young's modulus and Poisson's ratio | b) After testing of compression strength | c) After testing of splitting tensile strength |

Figure 5.2: Concrete specimens

Table 5.1: Material properties of tested concrete specimens

Specimen No.	Length l [mm]	Diameter d [mm]	Mass m [kg]	Density ρ [kg/m^3]	Young's Modulus E [MPa]	Poisson's ratio ν	compression strength f_d [MPa]	splitting tensile strength f_{sz} [MPa]
1	200	104.0	4.14	2439	42670	0.12	91	--
2	203	104.0	4.18	2426	--	--	--	5.9
3	204	104.1	4.17	2408	37130	0.14	67	--
4	202	103.9	4.16	2431	39180	--	69	--
5	203	104.0	4.29	2483	--	--	--	4.0
6	203	104.1	4.27	2474	43290	0.13	75	--
7	204	104.1	4.16	2399	--	--	--	5.8
mean value				2437	40568	0.13	76	5.2
standard deviation				31	2920	0.01	11	1.0

The actual prestress in the steel tendons was measured using strain gauges. For this purpose some of the tendons were laid bare and subsequently the gauges were glued onto one of the 12 fibres of a tendon. Then this single fibre was cut, while the rest of the tendon remained undamaged. The strain was measured during the cutting and the resulting data is shown in Figure 5.4. In addition the length of gap was callipered manually. This procedure was performed on two fibres of two different tendons.

Figure 5.3: resistance strain gauges on the tendons
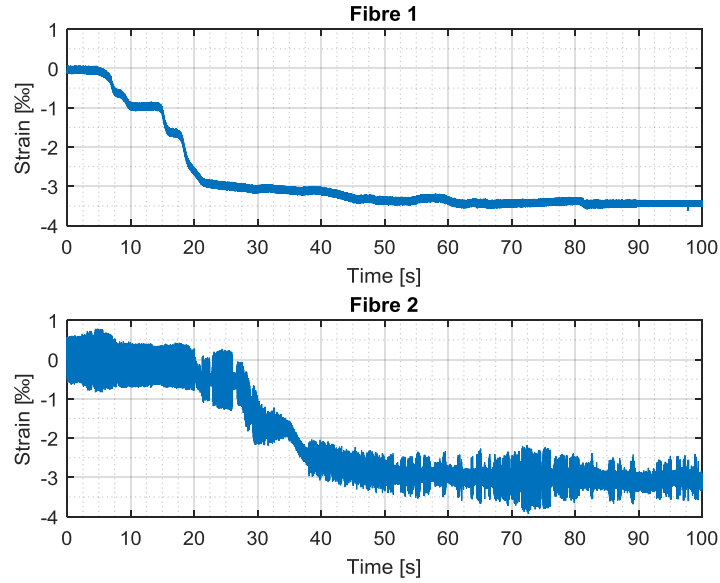
Figure 5.4: Strain measurements at two different fibres during cutting

Table 5.2: Results of strain measurements – decrease in length and in strain

	M1	**M2**	**M3**	**M4**	**Average**
Δl [mm]	-2.00	-2.40	-2.10	-2.50	-2.25
Δε [‰]	-3.00	-3.50			-3.25

In average a strain of $\varepsilon = 3.25\,‰$ and a decrease in length of $\Delta l = 2.25mm$ were determined. Taking into account a Young's modulus of $E = 2 \cdot 10^5 MPa$ a prestress of $\sigma_{ps} = 650MPa$ can be calculated.

$$\sigma_{ps} = E \cdot \varepsilon \tag{5-1}$$

$$= 2 \cdot 10^5 MPa \cdot 3.25 \cdot 10^{-3} = 650MPa$$

The back anchoring length l_0 can also be calculated as follows:

$$\varepsilon = \frac{\Delta l}{l_0}$$

$$\Leftrightarrow l_0 = \frac{\Delta l}{\varepsilon} \tag{5-2}$$

$$= \frac{2.25mm}{3.25 \cdot 10^{-3}} = 0.69m$$

The latter means that approximately $0.7\,m$ of the tendon was stress relieved before it was anchored again by friction. Hence, approximately $35\,cm$ from the cutting line the tendons may be considered intact.

A test setup was mounted in the port of Mertert for a few months. The basic idea was to simulate aging of the beam by inducing artificial damage of increasing severity. 5 different damage scenarios (DS) were realised from DS#0 – healthy state to DS#4 – heavily damaged. In each damage scenario, static and dynamic measurements were performed and the collected data were examined in order to test different approaches of damage detection and localisation.

These types of tests are often performed in laboratory by using small models. There are two problems arising from this approach. First, it is not guaranteed that the behaviour of a scaled model is the same as of the real structure. But even if the results of the laboratory tests can be applied to reality, the second problem is that a laboratory is mostly a controlled environment without significant changes in temperature, air humidity, solar radiation and soil condition. But real structures are always exposed to such environmental changes, so their physical properties change over time. These changes due to environmental influences are superposed to the changes due to damage. Therefore, it is more difficult to detect damage based on measured physical properties of real structures than in the laboratory. This is the main reason why here a part of a real bridge was used and a test setup was built up outdoor. An additional objective was to examine the influence of environmental factors, especially temperature, and to find possibilities to compensate these influences.

The behaviour of a separated bridge beam without asphalt layer is not the same as it was at the original bridge, but the intention was to reproduce the conditions during the lifetime of the bridge as far as possible in the test setup. First of all, the beam was supported by a fixed and a sliding bearing at its ends. The sliding bearing was realised with two steel plates, where grease was applied between them. Afterwards, the tested beam was loaded with a supplemental mass to simulate the additional dead load, which the beam had to sustain during the lifetime of the bridge. For this purpose a part of the second beam was separated with a length of $12\,m$ and a mass of about $30\,t$. This piece was mounted on the top flange of the tested beam.

**a) Sliding bearing, realised
with two steel plates**

Grease
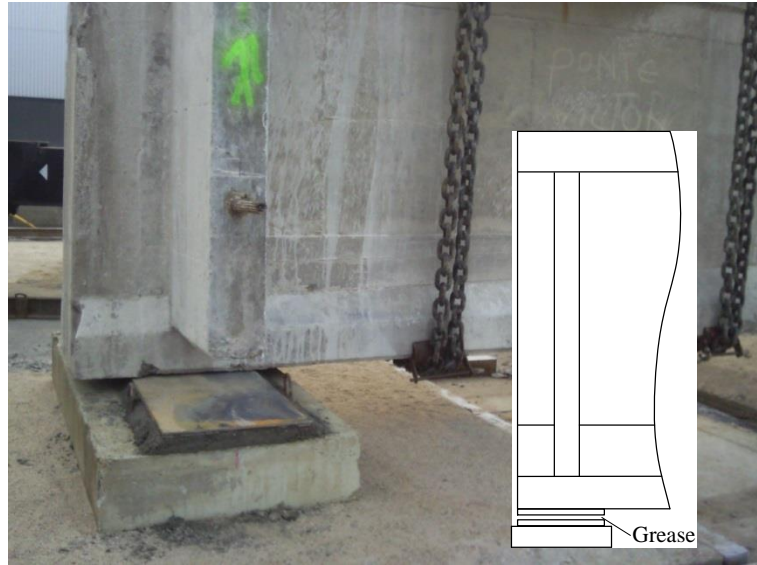
**b) Positioning of the beam
onto the bearings**

c) Finished fixed bearing

d) Finished sliding bearing

Figure 5.5: Realisation of the bearings for the test beam in the port of Mertert

**2 live loads
for static tests
(13 t each)**

**Additional
Dead load (30 t)**

**Sliding
bearing**

**Electro-magnetic
shaker (1 t)**

**Shaker control and
data acquisition**
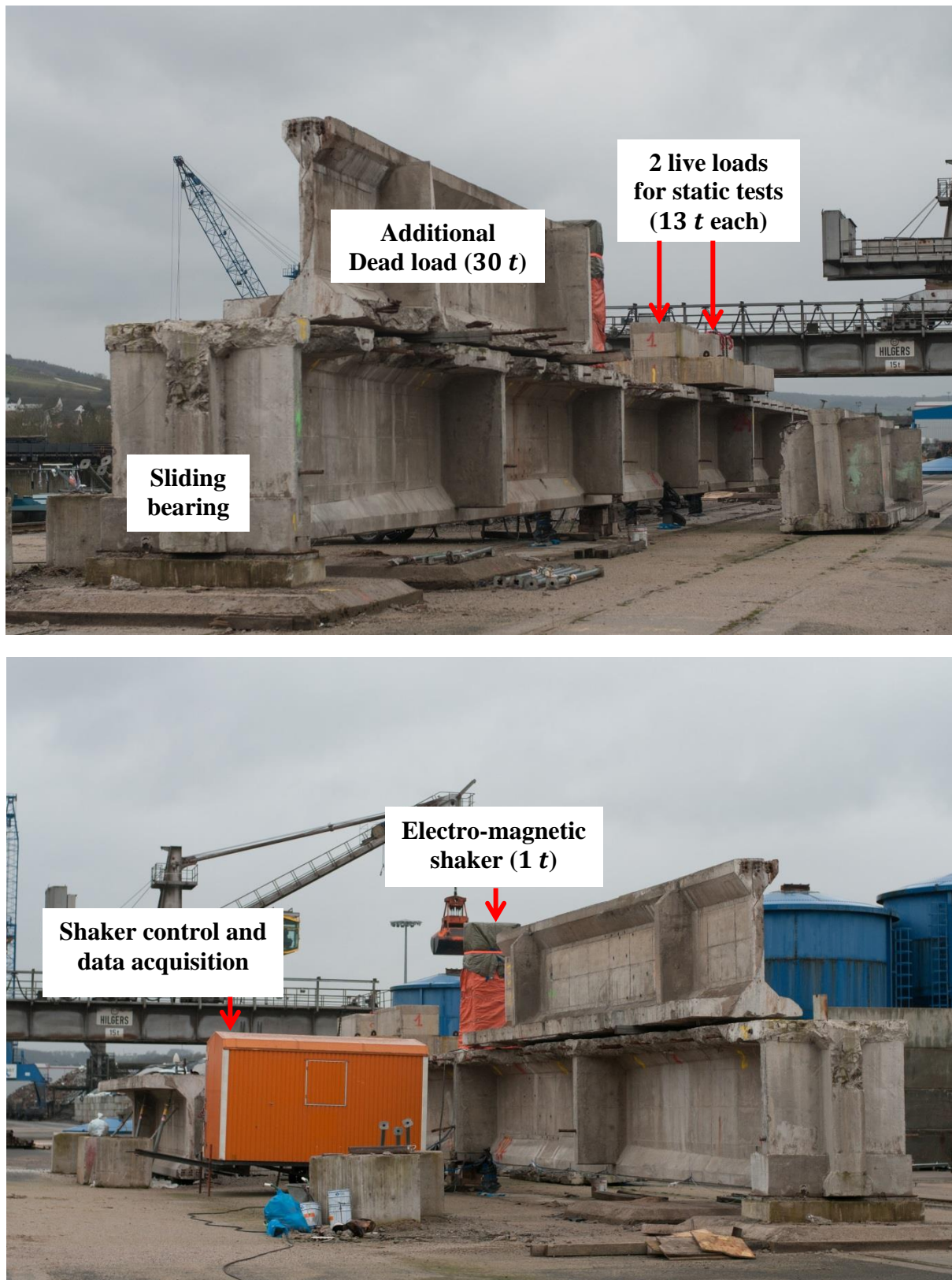
Figure 5.6: Test setup at the port of Mertert

Afterwards, the test setup was equipped with sensors for temperature and displacement as well as with accelerometers.

a) Accelerometer

b) Temperature sensor

c) Displacement sensors SV1 and SV8

d) Vertical displacement sensor

e) Horizontal displacement sensor SV7

Figure 5.7: Sensors at the test setup in the port of Mertert
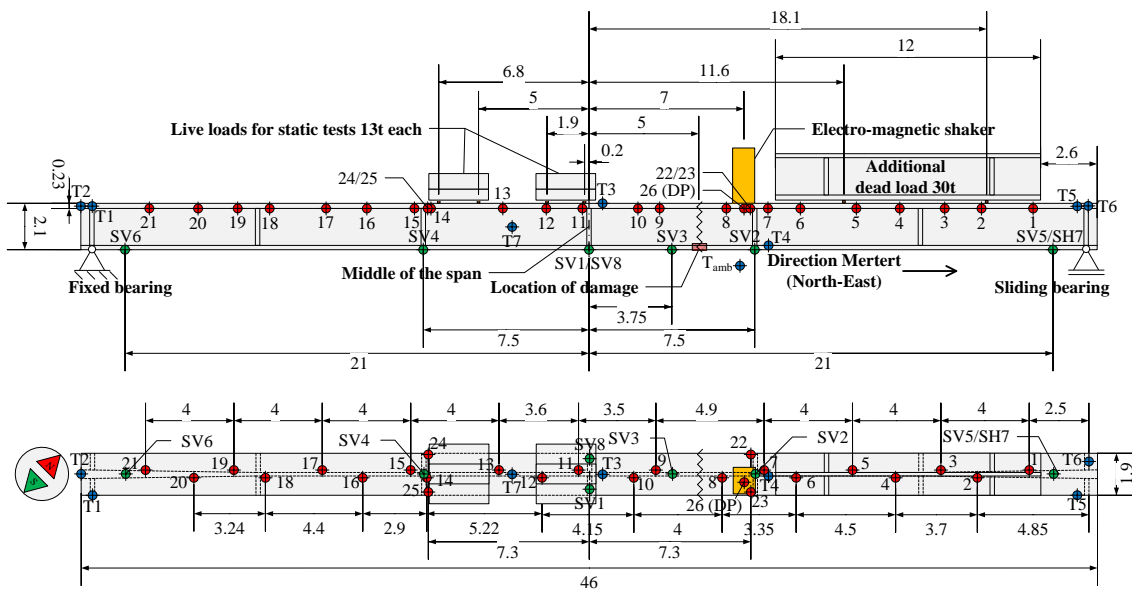
Figure 5.8: Test setup with sensors; red: accelerometers; green: displacement sensors; blue: temperature sensors;
In the following the upper view is referred to as "south side", while the opposite side is called "north side"
(unit of dimensions: [m]).

In the following Chapters 5.2 and 5.3 the damage scenarios and the performed static and dynamic tests are explained in detail. Chapters 6, 7 and 8 also relate to the test setup, which was described here. At first, in Chapter 6 an approach to compensate the influence of temperature fluctuations on the measured displacements is described. Then in Chapter 7 different commonly known damage indicators are evaluated in order to test if the artificially introduced damage could be detected by them. Finally, in Chapter 8 a model updating approach for damage localisation based on an FE-model of the test setup is explained.

5.2 Static tests

During the whole test period the deflection of the beam and the temperature at different locations were permanently monitored with a sampling rate of one per minute. These measurements were synchronised, so for every measured deflection, a corresponding temperature distribution can be defined.

The vertical deflection was measured by seven inductive displacement sensors, labelled SV1…SV6 and SV8, which measured the vertical movement of the lower side of the beam against the soil that was assumed to be fixed. This was verified by measurements with an independent optical system, which revealed that the vertical displacement of the bearings during the performed static loading tests was less than $0.29\,mm$. A description of these measurements can be found in [69]. An additional sensor (SH7) was mounted to check horizontal displacement of the sliding bearing. Sensors SV1 and SV8 were mounted at the same position along the axis of the beam, but on opposite sides of the bottom flange, so it is possible to notice a rotation of the beam along its axis. The temperature sensors T1-T7 were embedded at least $5\,cm$ inside the concrete, while T_{amb} measured the ambient air temperature in the shadow.

Artificial damage was introduced by cutting tendons at the damage location $5\,m$ off the centre, as marked in Figure 5.8. Figure 5.9 shows the lower part of the cross-section at this location with the positions of the tendons. Fully cut cables are marked by a cross, while partially cut ones are marked by a half-filled circle. The damage was always introduced symmetrically on both sides of the beam. In DS#4, additionally 6 tendons were only partly cut. Figure 5.10 shows a photographic picture of the cut tendons during the last scenario DS#4. The tendons are numbered in the same order as in the official plans of the former bridge.
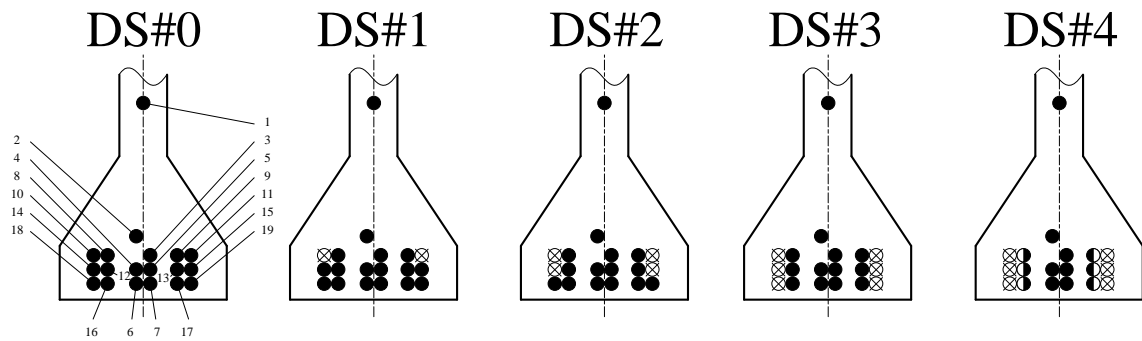
Figure 5.9: Damage scenarios
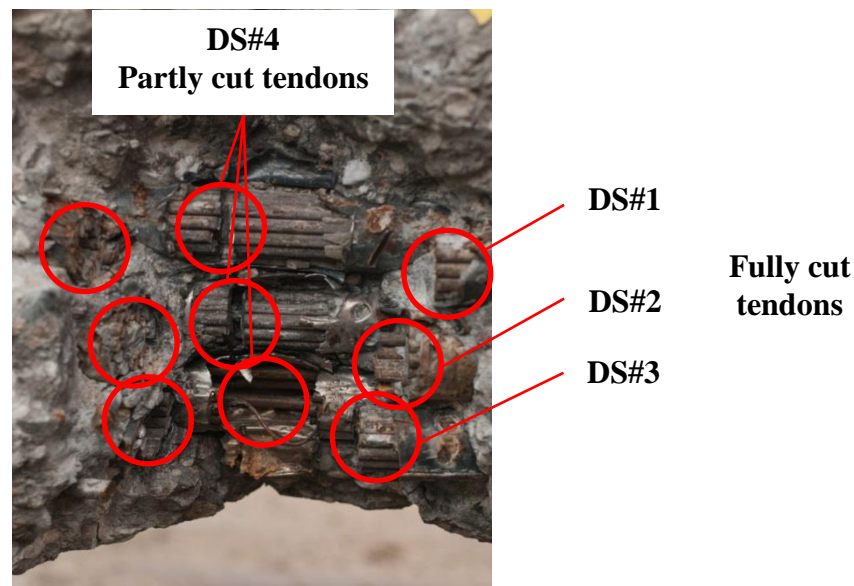
Figure 5.10: Cut tendons in DS#4, marked by red circles, photographed from one side of the beam

One effect of the prestress is that it compensates tensile stresses while the beam is bended due to a loading. The effect is illustrated in Figure 5.11, which shows the composite stress for this case. This is advantageous since the tensile strength of concrete is far less than its compressive strength. Thus, the cutting of the tendons leads to higher tensile stresses in the beam than in the healthy state while it is loaded. If these exceed the tensile strength, there will be vertical cracks.
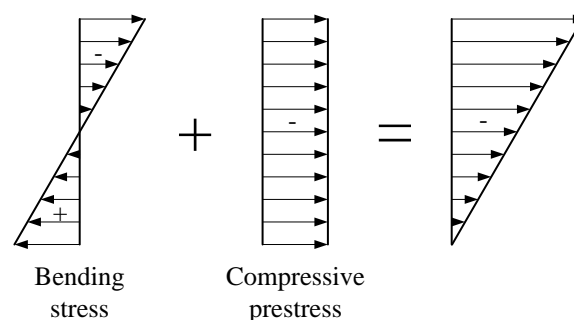
Figure 5.11: Composite stress in a prestressed beam while loaded by a bending moment

Static load tests were performed by loading the beam with additional loads of about $2 \cdot 13 = 26\,t$ to simulate live load due to traffic (cf. Figure 5.12). Each loading lasted at least 24 hours.

Figure 5.12: Loading of the prestressed concrete beam for static test

During these static tests, cracks occurred around the damage location. The formation of the cracks on both sides of the beam is shown in Figure 5.13. During the first 2 damage scenarios, i.e. DS#1 and DS#2, only horizontal cracks appeared due to the back-anchoring of the severed tendons. Such cracks have only a small impact on the bending stiffness of the beam, because the supporting cross-section is not considerably reduced. Vertical cracks appeared from DS#3.

south side

shaker

Middle of
the span

cutting
line

12   10   8   26 (DP) 23   6

1.16   1.5   1.17   1.1

Direction Mertert
(North-East)

1.12   1.18

2.13   1.62

3.16   2.32

north side

shaker

cutting
line

Middle of
the span

7   22   9   11

0.815   0.37   1.23   1.11   0.29

Direction Mertert
(North-East)

1.68   2.39

1.88   2.5

2.36   3.45

2.435   3.655

— 04.02.14 DS#1 unloaded (after loading 31.01-03.02) just before DS#2
— 06.02.14 DS#2 unloaded (after loading 04.02-05.02) just before DS#3
— 10.02.14 DS#3 loaded (since 06.02) one day before DS#4
— 19.02.14 DS#4 loaded (since 18.02) last day

Figure 5.13: Formation of cracks during the test period [dimensions in meter]

a) South side

b) North side

Figure 5.14: Crack pattern in DS#4

Chapter 5: In-situ tests at a prestressed bridge beam

In order to have an idea of the reaction forces on the bearings of the test setup, they were calculated manually. For this purpose, an equivalent static system was defined and drawn in Figure 5.15.
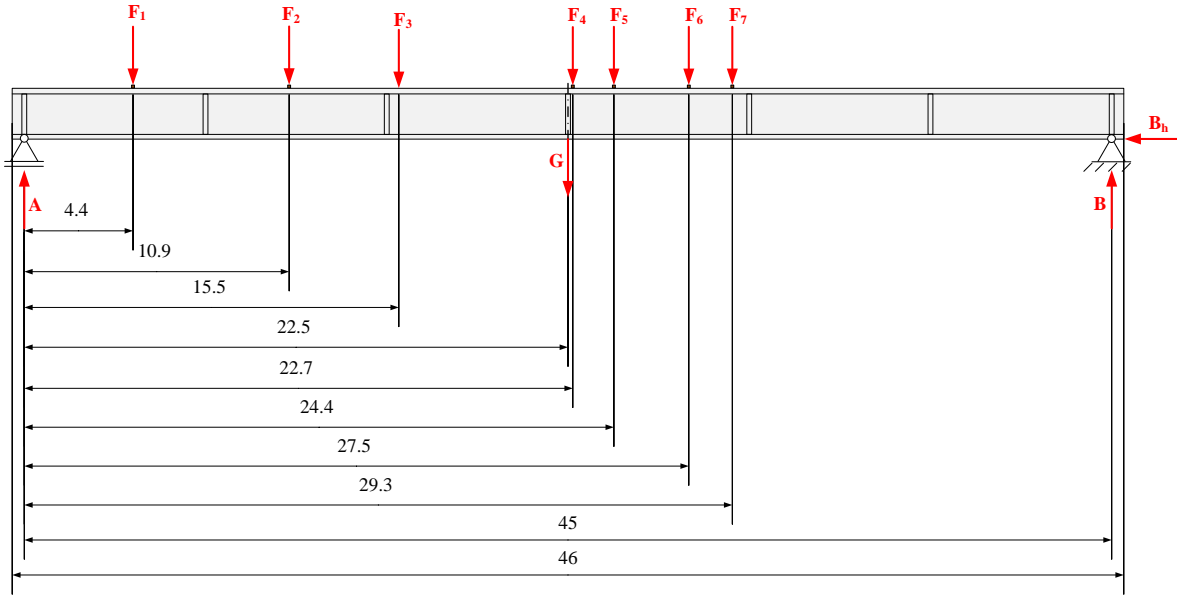
Figure 5.15: Test setup with forces due to gravity and bearing reactions (dimensions in [m])

F_1 and F_2 are forces, which came from the $30\ t$ additional dead load that permanently stayed on top of the tested beam and was supported by wooden beams at the locations stated in Figure 5.15. They were calculated firstly as $F_1 = 115\ kN$ and $F_2 = 185\ kN$.

$F_3 = 10\ kN$ is the weight of the electro-magnetic shaker that was used for experimental modal analysis. It stayed on the beam for the whole test period.

F_4 to F_7 are forces resulting from the two additional live loads of each $13\ t$ for static loading tests, transmitted to the beam by 4 wood supports. These forces all had the same magnitude of $65\ kN$.

At last for the calculation of reaction forces, a single force $G = 1200\ kN$ in the middle of the span presents the weight of the tested beam.

Since all external forces took effect in vertical direction, the horizontal reaction force B_h is equal to zero. The vertical bearing reactions were calculated as $A = 960{,}42\ kN$ and $B = 809{,}58\ kN$ while the application of every external force. When the live loads were removed, the bearing reactions resulted to $A = 850{,}50\ kN$ and $B = 659{,}50\ kN$.

Furthermore, the downward displacement of the tested beam in the middle of the span between the two bearings due to the additional live loads, can be calculated manually and be

compared to results from FE-simulations. Again, the loads were assumed as single forces as shown in Figure 5.15 (F_4 to F_7). The cross-section of the beam in the middle of the span is shown in Figure 5.16 together with its physical properties. The centre bar of the beam became wider near its ends, but for this calculation the cross-section is assumed to be constant, because the intention is just to estimate the displacement.
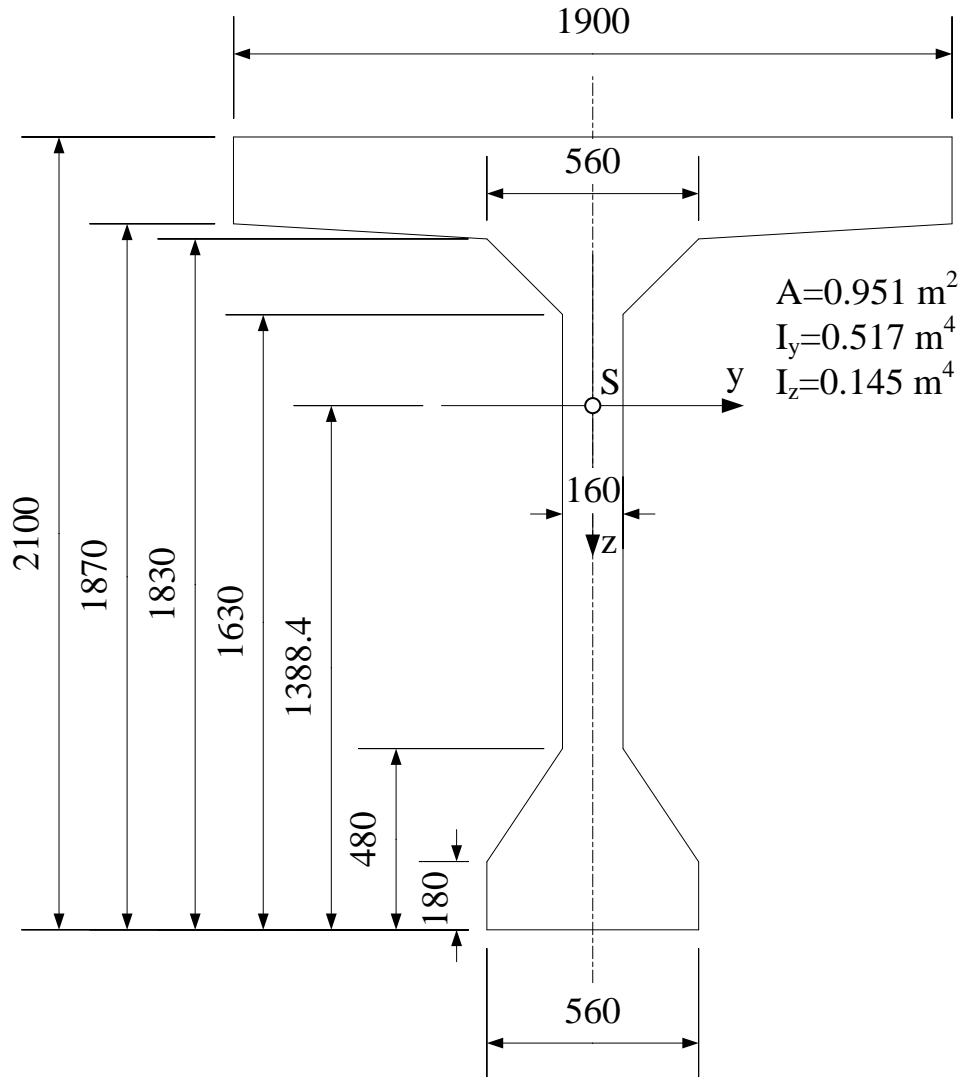
Figure 5.16: Cross-section of the beam in Mertert, shown in the middle of the span (dimensions in [mm])

A linear behaviour was assumed, so the deflections due to each of the four forces can be calculated separately and summed afterwards. For the present loading case shown schematically in Figure 5.17, the deflection along the beam's axis due to a single force can be calculated according to [70] by the following equations (5-3) and (5-4).
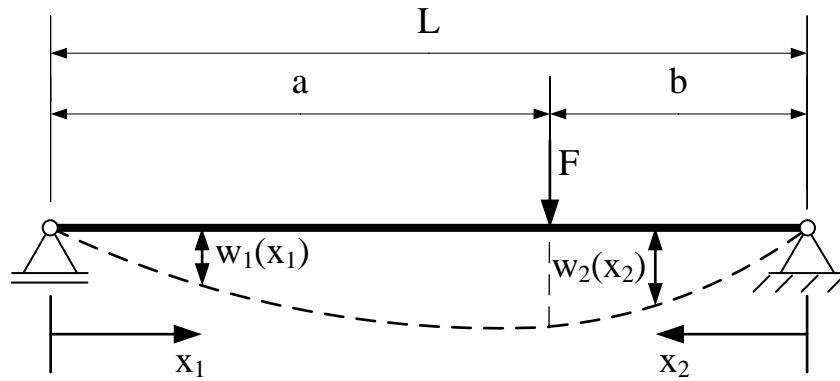
Figure 5.17: Deflection of a simple beam due to a single force

$$w_1(x_1) = \frac{FL^3}{6EI} \frac{a}{L} \left(\frac{b}{L}\right)^2 \frac{x_1}{L} \left(1 + \frac{L}{b} - \frac{x_1^2}{ab}\right) \quad , x_1 \le a \tag{5-3}$$

$$w_2(x_2) = \frac{FL^3}{6EI} \frac{b}{L} \left(\frac{a}{L}\right)^2 \frac{x_2}{L} \left(1 + \frac{L}{a} - \frac{x_2^2}{ab}\right) \quad , x_2 \le b \tag{5-4}$$

where EI is the bending stiffness of the beam. For the Young's modulus E, the mean value was used, which was determined by the material tests whose results are shown in Table 5.1, i.e. $40568\ MPa$. For the axial area moment of inertia, the value of I_y shown in Figure 5.16 was used.

A vertical displacement of $22.34\ mm$ is then calculated in the middle of the span, i.e. at the position of displacement sensors SV1 and SV8, due to the additional live loads in the healthy state DS#0.

Figures 5.18 and 5.19 show the measured displacement of all sensors from 23/01/2014 until the end of the measurements on 19/02/2014 including all different damage scenarios DS#0 (undamaged) to DS#4, separated by vertical red lines. Furthermore, the static tests as well as the periods between them are denominated after the following abbreviations.

#x-L: Loading in damage state x

#x-UL: Unloading in damage state x

While "loading" means the test loads were placed on top of the beam, "unloading" means, that they were not present.
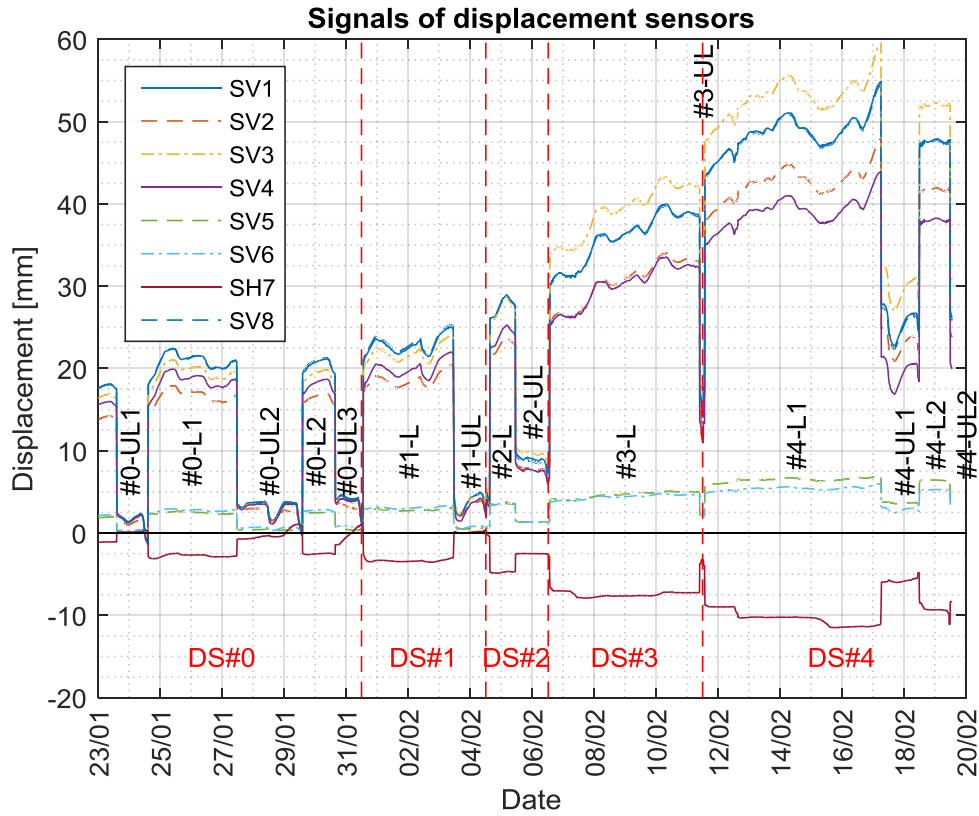
Figure 5.18: Signals of displacement sensors
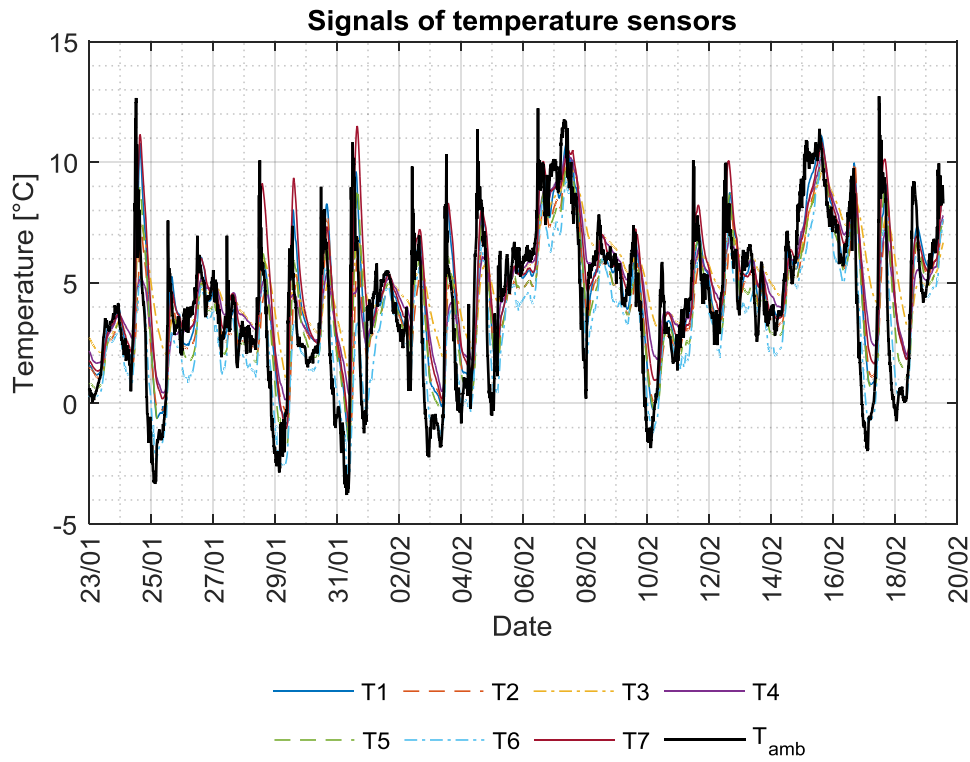
Figure 5.19: Signals of temperature sensors

An increase measured by a vertical displacement sensor means downward movement. The red signal with mostly negative values SH7 shows the horizontal movement of the beam at the sliding bearing. If this signal increases, the end of the beam moves away from the sliding bearing in direction of the fixed bearing, i.e. to the left in the view shown in Figure 5.8. If the beam is loaded with the test live loads, it inclines over the sliding bearing. As a result of this inclination, the lower part of the beam, where the sensor is located, moves towards the bearing, so the signal decreases as it can be seen in Figure 5.18.

Furthermore, it can be observed that after the removal of the load the signals did not always return to the values before the loading test, i.e. the beam did not return to its former state. Before this effect is explained, some terms used in this thesis must be defined.
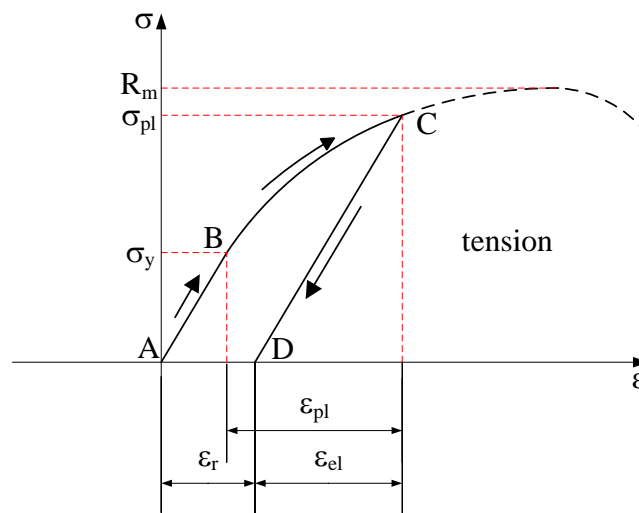
Figure 5.20: Qualitative stress-strain diagram determined in tensile test according to [71]

Figure 5.20 shows a qualitative stress-strain diagram determined in tensile test according to Issler et al. (2003) [71]. As long as the yield stress σ_y is not exceeded (point B), the part will return to its former state after the removal of the load, i.e. only elastic deformation occurs. Further loading, e.g. up to point C, leads to additional plastic strain ε_{pl} and the material behaviour becomes non-linear. Now after the removal of the load (point D) the strain is reduced by the elastic contribution ε_{el} and there will be a remaining strain ε_r. Accordingly, these terms can be defined for concrete under uniaxial compressive load as follows.
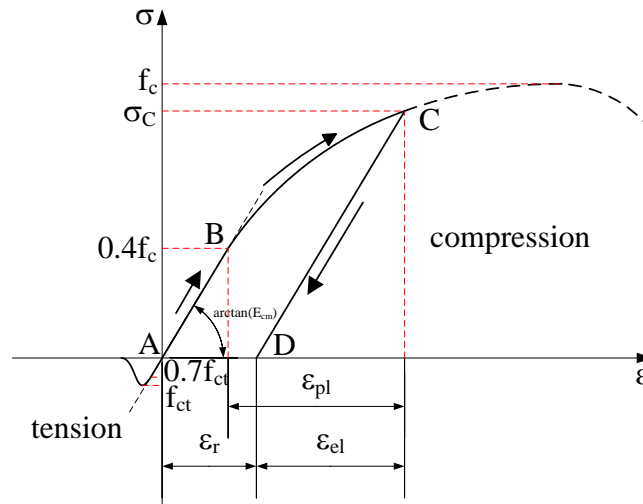
Figure 5.21: Qualitative stress-strain diagram for pure concrete under uniaxial load (cf. [2])

Bungard stated in his doctoral thesis [2] that the material behaviour of concrete under uniaxial compression can be assumed as linear elastic up to 40% of the compressive strength f_c as well as under uniaxial tension up to 70% of the tensile strength f_{ct}. Figure 5.21 shows a qualitative stress-strain diagram for concrete. The Young's modulus of concrete in the linear-elastic range can be defined as the slope of a secant through the origin (point A) and point B and is then referred to as secant Young's modulus E_{cm}.

As long as the stress is in the range between $0.7f_{ct}$ and $0.4f_c$, the strain decreases to zero after the load has been removed, i.e. it returns to point A. If the stress exceeds the linear elastic range, the stress-strain relationship of concrete becomes nonlinear, so plastic strain ε_{pl} occur and when the load is removed, a permanent strain ε_r remains.

It can be summarized that if the relationship between stress and resulting strain is non-linear, plastic deformation occurs, which leads to remaining deformations after the removal of the load.

Waltering performed for his doctoral thesis [1] static loading tests of a reinforced concrete beam in laboratory. The beam with a length of $6\,m$ was supported by a hinge and roller bearing as shown in Figure 5.22.
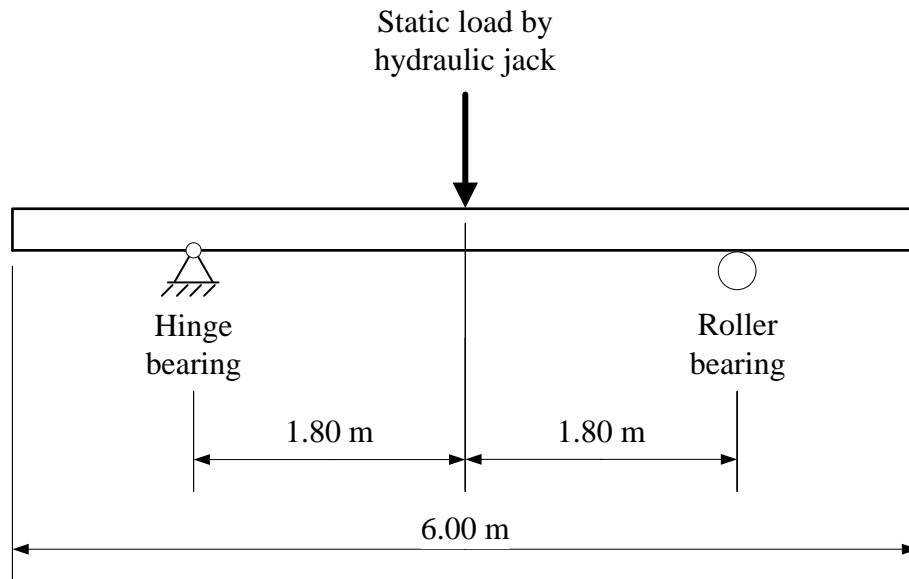
Figure 5.22: Experimental setup with reinforced concrete beam (cf. [1])

A hydraulic jack was used to apply static loads. Several load steps were performed with increasing magnitude of the applied force and between the load steps the load was relieved. Figure 5.23 shows a force-displacement diagram for load steps #2-#6, where the applied force is plotted over the deformation in the middle of the span.
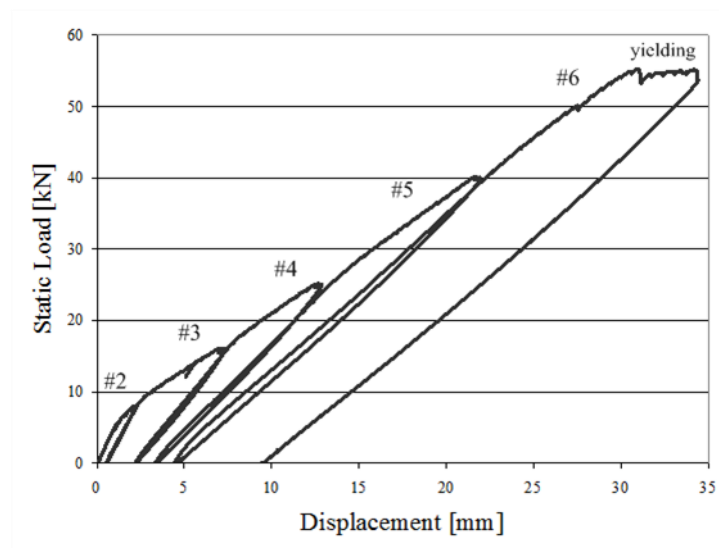
Figure 5.23: Force-displacement diagram for gradually damaged reinforced concrete beam [1]

Four main effects can be observed. When loading the beam, the relationship between force and displacement is quite linear up to a certain load. But then the slope of the curve decreased, while the load was further increased. This non-linearity is explained in [1] by the formation of cracks. Secondly, after the removal of the load, the beam did not return to its initial state i.e. a deformation remained. The third effect is that the slopes of the curves

decreased in every load step compared to the former steps, since the stiffness of the beam was reduced due to the cracks. Finally, in the last load step #6 a yielding of the beam can be clearly observed, i.e. the displacement increased while the force stayed on the same level.

Similar effects can be observed in the courses of the measured displacements in Figure 5.18. Already before the 23rd of January 2014, when the graph in Figure 5.18 begins, the beam was loaded for several times. Therefore, in the undamaged state DS#0 only small or nearly no remaining deformations can be seen in Figure 5.18. The beam already reached a steady state, i.e. it occurred almost no further cracks when the beam was loaded. Since the first artificial damage was introduced in scenario DS#1, the vertical deflection increased over time while the static tests, i.e. while the beam was loaded with the additional live loads, although the load stayed the same. The effect is still weak in DS#1 but can be clearly seen in the following damage scenarios and can be explained by the formation of cracks. After the removal of the load the beam did not return to the deflection before the test but a residual deformation remained. In DS#4 2 consecutive static load tests were performed without introducing damage between them. While plastic strain occurred during the first loading #4-L1, which led to remaining deformations, the deformations after the second loading #4-L2 were nearly the same as before this loading, so the beam reached again a steady state. The increasing remaining deformation of the beam is referred to in the following as "sagging".

Especially, as revealed by data from 30/01/14 18:00 to 31/01/14 12:00, a stick-slip effect occurred caused by the friction between the steel plates of the sliding bearing. The specified period is shown in detail in Figure 5.24.

a) **Vertical displacements**

b) **horizontal displacements**

c) **Temperatures**

d) **Concrete temperature measured by T4**
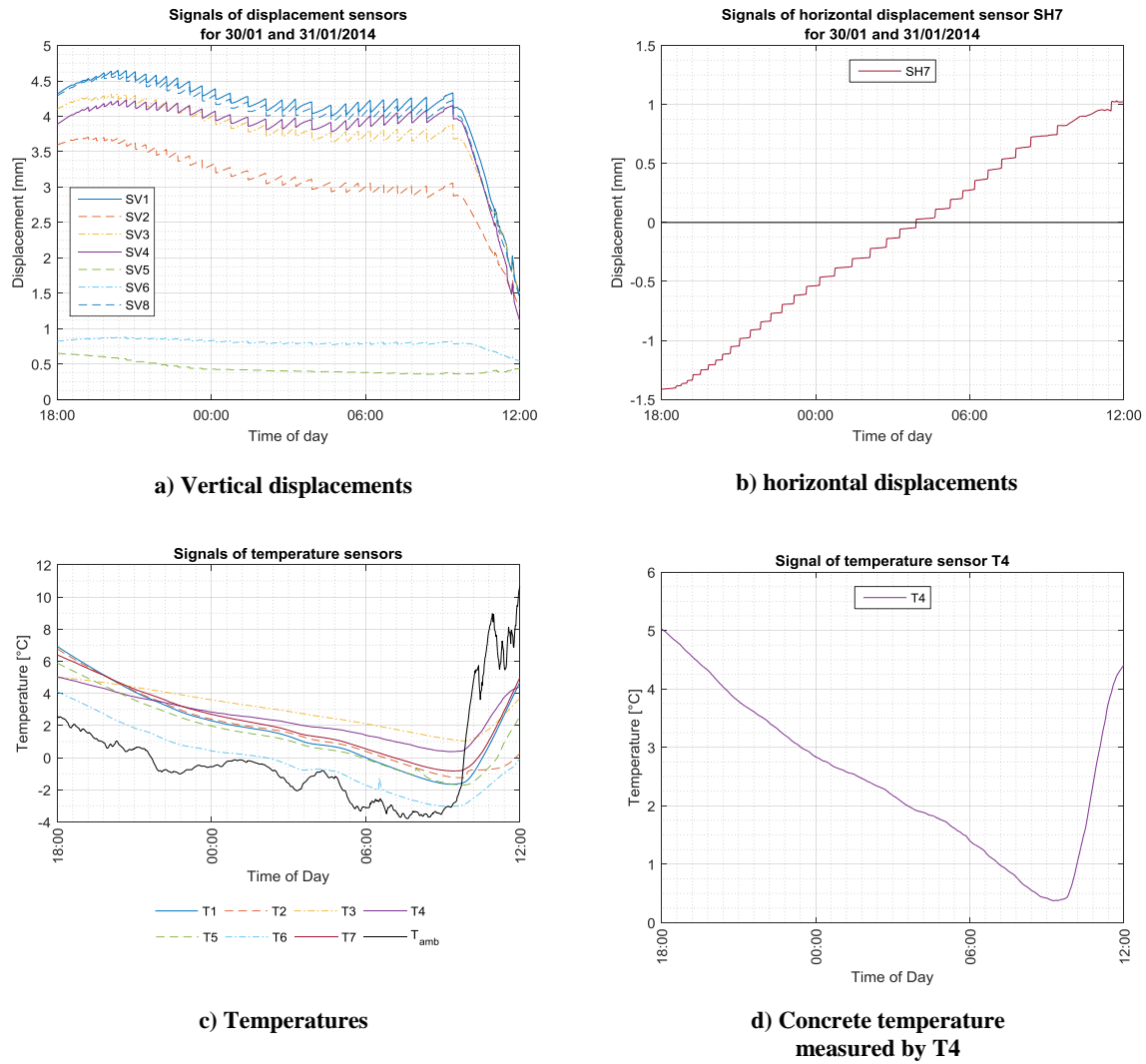
Figure 5.24: Displacements with stick-slip effect

After the removal of the live loads earlier on 30/01, the deflection of the beam had a tendency upwards and involved the end on sliding bearing get closer to the fixed bearing due to the decrease of the inclination. Therefore, as shown in Figure 5.18, the signal of SH7 rose abruptly at the moment of unloading and the signals of the vertical displacement sensors fell at the same time. However, some time after the removal of the loads, signal SH7 further increased and steps can be seen in the course of this signal (cf. Figure 5.24b). For an explanation of this behaviour, the course of the measured concrete temperatures T1-T7 in the same time period is considered (cf. Figure 5.24c), which shows an overall decrease of the concrete temperatures. This would result in a contraction of the beam but it was constrained by the static friction between the steel plates of the sliding bearing. Therefore, an increasing axial force is caused in the beam until it exceeds the static friction. Then the beam moved on the sliding bearing until the axial force was again lower than the sliding friction and this procedure repeated while the temperature further decreased.

The magnitude of the axial force, which was necessary to exceed the static friction, can be estimated by considering the temperature differences between two successive movements on the sliding bearing. The axial force, which is created by constrained heat expansion or contraction due to a certain change in concrete temperature ΔT can be calculated by the following equation [70]:

$$F = EA \cdot \alpha_T \cdot \Delta T \tag{5-5}$$

Where EA is the axial rigidity of the beam and α_T is the coefficient of thermal expansion. For the Young's modulus E again the value from Table 5.1, i.e. $40568\ MPa$, was used, furthermore cross-sectional area $A = 0.951 m^2$ and $\alpha_T = 10^{-5} K^{-1}$. The difference of the temperatures, at the moment when the horizontal movement stops and where it start again was determined from the signal of sensor T4 and averaged for 20 steps in Figure 5.24b. The result is $\Delta T = \frac{1}{20}(0.56°C - 3.65°C) = -0.15\ °C$. The used values are illustrated in Figure 5.25.
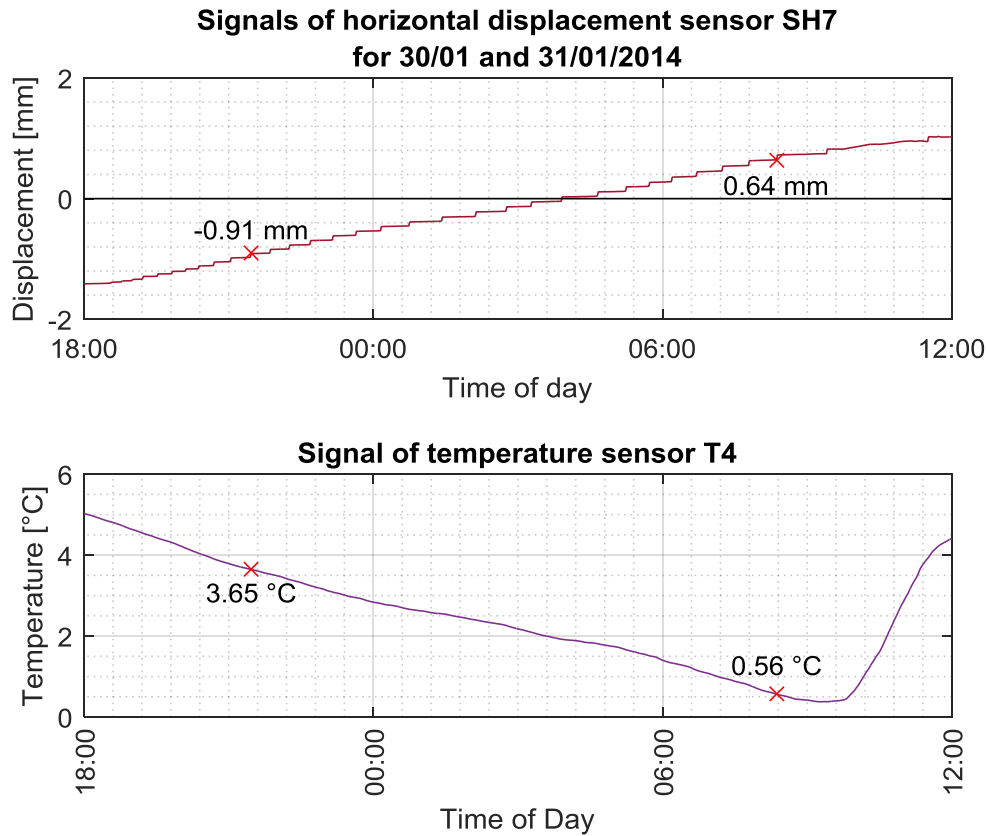
Figure 5.25: Determination of temperature difference ΔT

By substituting these values in equation (5-5), an axial force due to heat contraction of $F_{ax} = 59500 \, N$ can be estimated. This is the difference between the static and the sliding friction.

Furthermore, a serrated course of the signals of the vertical displacement sensors can be seen in Figure 5.24a. This is caused by an increasing downward deflection of the beam while the axial force calculated above built up, followed by an abrupt upwards movement at the moment when the sliding bearing started to move. The axial force caused a bending moment, because it occurred at the bottom flange of the beam and its line of action did not go through the centre of gravity of the cross-section. This bending moment is equal to the product of the force and the distance of the centre of gravity from the bottom of the beam $e_z = 1.39 \, m$ that can be seen in Figure 5.16. According to [70] the displacement in the middle of the span due to this moment can be calculated by the following formula.

$$w\left(\frac{L}{2}\right) = \frac{M_b L^2}{16EI} = \frac{F_{ax} \cdot e_z \cdot L^2}{16EI} \tag{5-6}$$

For the bending stiffness EI and the length L again the same values must be used as in the above calculation of the deflection of the beam due to a single force. This yields a displacement of $w\left(\frac{L}{2}\right) = 0.52 \, mm$. This should be the height of the "saw teeth" that can be seen in the course of the signal SV1 in Figure 5.24a. They are slightly smaller, but the order of magnitude fits and the above calculation must be considered as estimation.

At the end of the considered time period the temperature rose relatively swift and the beam is again bended upwards. In Figure 5.18, this movement can often be observed in the middle of the days, when the temperatures rose. The effect occurred as well in periods when the beam was loaded, as can be seen in Figure 5.26. Since always an upwards movement of the beam was observed at points in time when the beam was artificially damaged by cutting tendons, the question arose, if this movement was introduced by the damaging. But the damaging always took place around noon, so it is more logical to assume that the movement occurred due the above explained temperature effect.

Until this point, the bending of the beam due to changes in its overall temperature was discussed, which can be explained by the stick-slip effect that occurred because the sliding bearing was not ideal. But even if the sliding is not blocked, a bending can still occur caused by a temperature gradient between the upper and lower parts of the beam. In order to explain

this effect, the behaviour of the beam during the course of the day 25/01/14 is discussed in the following. During this day, the beam was loaded with the additional live loads.

A detailed diagram for this day is presented in Figure 5.26, where the measured temperatures are shown in comparison to the displacement of the beam in the centre of the span, i.e. at sensor position SV1.
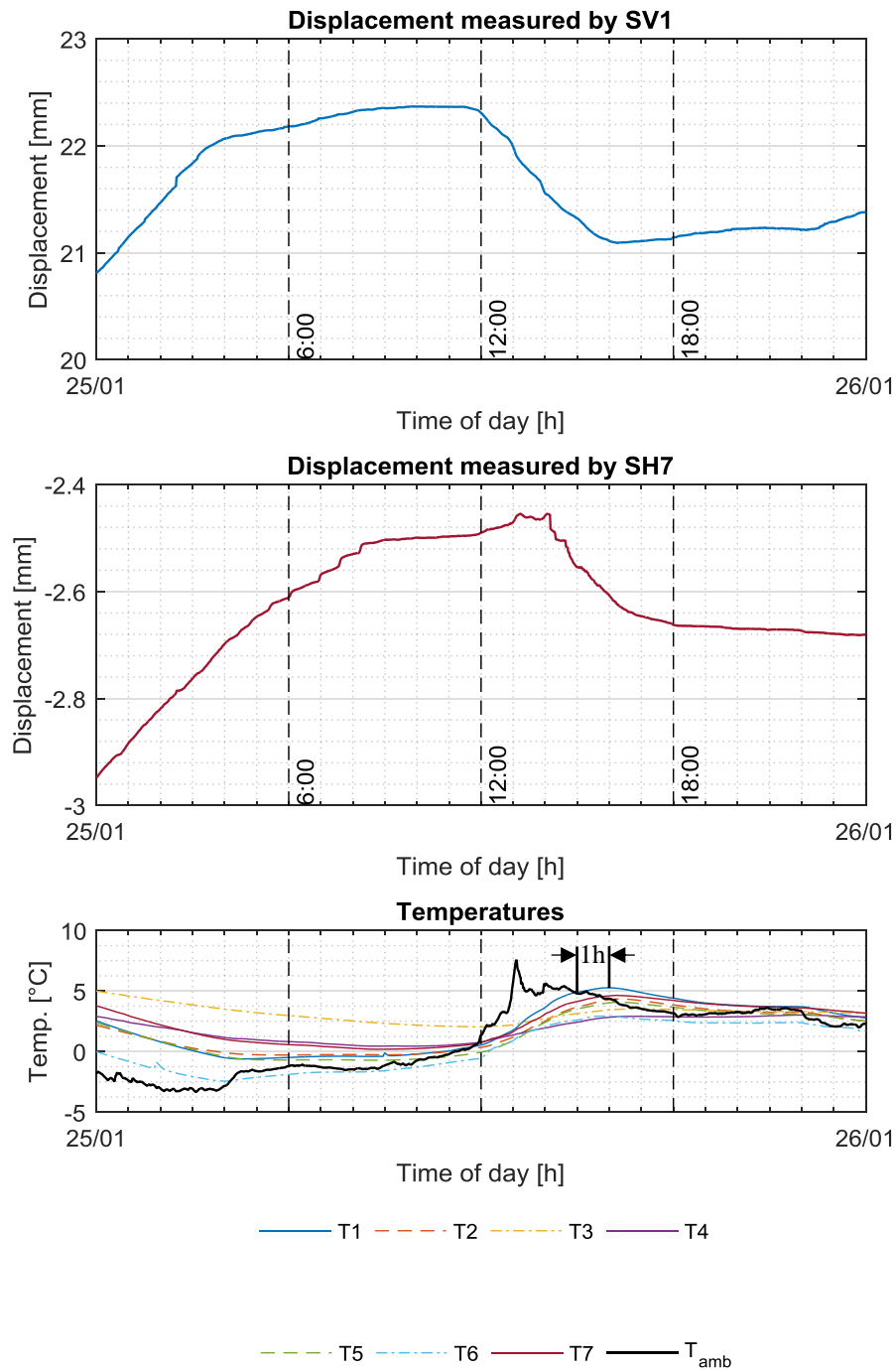
Figure 5.26: Effect of temperature on the deformation of the beam during the day

63

First of all, as expected, the heating of the concrete shows low-pass behaviour, caused by its heat capacity. Therefore, the variations of the temperatures measured inside the concrete (T1-T7) are smoother than the change of the ambient temperature. Additionally, between noon and 18o'clock a phase shift of about 1 hour can be determined. If the change in ambient temperature is slower, the phase shift is less.

From midnight until noon, the displacement at the position of SV1 rises, i.e. the beam bends downwards. But afterwards, a movement in the opposite direction may occur. The reversal of movement cannot be explained by the loading, since it did not change over the whole day. Instead, the hypothesis is that this movement was caused by temperature fluctuations. While no considerable stick-slip effect was observed, it can be assumed that the sliding bearing was not blocked. It is believed that the temperature difference between the upper and lower parts of the beam caused the deflection. In order to test the hypothesis and to explain the effect, a demonstration is performed below.

Let us consider a simple beam supported by a fixed and a sliding bearing. As long as the temperature changes uniformly over the whole beam, it will expand or contract unhindered thanks to the sliding bearing. No stresses or deflections occur due to the temperature change but only the length of the beam changes to the value L_0 at temperature T_0. Now let us assume, that the temperature of the upper part T_1 becomes higher than the temperature of the lower part, which remains T_0. As a result, the upper region of the beam expands further by the length ΔL. The cross-section inclines by the angle β and the beam bends upwards.
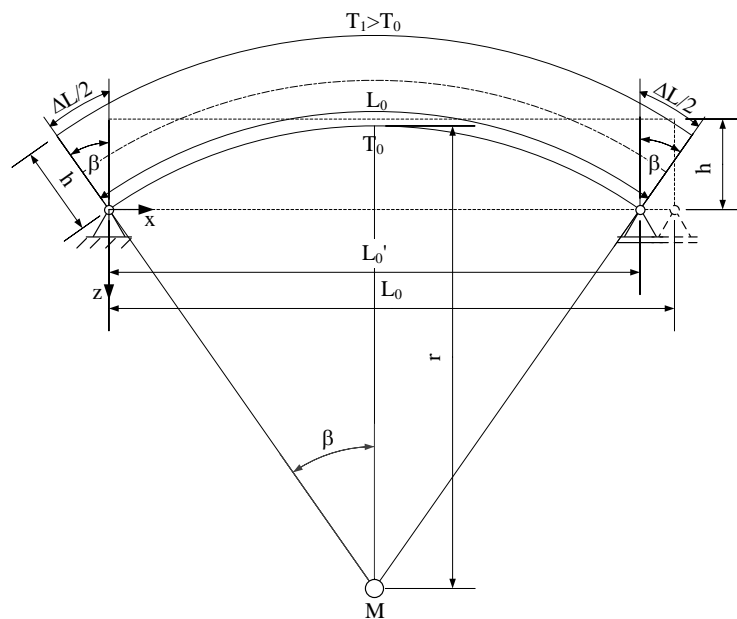
Figure 5.27: Deflection caused by temperature gradient

Considering Figure 5.27, two equations for β can be formulated.

$$\beta = \frac{180° \cdot \frac{L_0}{2}}{\pi r} \tag{5-7}$$

$$\beta = \frac{180° \cdot \frac{\Delta L}{2}}{\pi h} \tag{5-8}$$

Furthermore, with $\Delta T = T_1 - T_0$ the strain due to heat expansion can be formulated as follows and ΔL can be determined.

$$\varepsilon = \frac{\Delta L}{L_0} = \alpha_T \cdot \Delta T \iff \Delta L = L_0 \cdot \alpha_T \cdot \Delta T \tag{5-9}$$

where α_T is the coefficient of thermal expansion. Equating the two formulas for β and substituting the expression for ΔL yields the following equation for the radius r of curvature.

$$r = \frac{L_0 h}{\Delta L} = \frac{h}{\alpha_T \cdot \Delta T} \tag{5-10}$$

The curvature is the inverse of the radius r and considered as constant. By integration, an expression for the displacement z can be deduced as a function of coordinate x, which is measured in the direction of the beam's axis.

$$z''(x) = \frac{1}{r} = \frac{\alpha_T \cdot \Delta T}{h} = constant \tag{5-11}$$

$$z'(x) = \frac{\alpha_T \cdot \Delta T}{h} \cdot x + C_1 \tag{5-12}$$

$$z(x) = \frac{\alpha_T \cdot \Delta T}{2h} \cdot x^2 + C_1 x + C_2 \tag{5-13}$$

The constants in equation (5-13) can be determined by the boundary conditions.

$$z(x = 0) = 0 \implies C_2 = 0 \tag{5-14}$$

$$z(x = L_0) = 0 \implies C_1 = -\frac{L_0 \cdot \alpha_T \cdot \Delta T}{2h} \tag{5-15}$$

This yields the following equation for $z(x)$.

$$z(x) = \frac{\alpha_T \cdot \Delta T}{2h} \cdot x^2 - \frac{L_0 \cdot \alpha_T \cdot \Delta T}{2h} x \tag{5-16}$$

Inserting for the position $x = \frac{L_0}{2}$ yields:

$$z\left(\frac{L_0}{2}\right) = -\frac{L_0^2 \cdot \alpha_T}{8h} \cdot \Delta T \tag{5-17}$$

Hence, the displacement of the beam in the middle of the span is proportional to the temperature difference ΔT.

Now the following values for α_T, h and L_0, will be used, for reflecting the test setup in the port of Mertert described in Chapter 5.1.

$$\alpha_T = 10^{-5} \, K^{-1}$$
$$h = 2100 \, mm$$
$$L_0 = 46000 \, mm$$

The maximum value of displacement z was determined in the middle of the beam, i.e. at $x = \frac{L_0}{2}$. With the above values one obtains:

$$z\left(\frac{L_0}{2}\right) = -1.26 \frac{mm}{K} \cdot \Delta T \tag{5-18}$$

Table 5.3 shows the deformation for different values of ΔT.

Table 5.3: Deformation of a beam due to temperature difference ΔT between the top and the bottom

ΔT [K]	1	2	3	4	5
z(L$_0$/2) [mm]	-1.26	-2.52	-3.78	-5.04	-6.30
r [mm]	2.10E+08	1.05E+08	7.00E+07	5.25E+07	4.20E+07
β [°]	6.28E-03	1.26E-02	1.88E-02	2.51E-02	3.14E-02
L$_0$-L$_0$' [mm]	9.20E-05	3.68E-04	8.28E-04	1.47E-03	2.30E-03

As shown in Figure 5.8, the temperature T4 was measured near the bottom of the beam, while all other concrete temperatures were measured in the top flange or in the middle of the centre bar (T7). During the morning of the 25th of January 2014 (cf. Figure 5.26), T4 is higher than the other concrete temperatures, except T3. The differences varied between 0 to $1°C$. According to the above example, this should yield a displacement of about $1.25 \, mm$. This fits the displacement in Figure 5.26 due to temperature fluctuations during the morning. The beam bended downwards, since the top flange was colder than the lower part of the centre bar. On the afternoon the temperature T4 fell below most other concrete temperatures, so the beam bended in the opposite direction. Furthermore, T4 rose again over the other

temperatures during the afternoon and the evening, thus the beam trended again to bend downwards.

The values, which were calculated for z at $\frac{L_0}{2}$, match approximately the deformation due to temperature fluctuations, which were observed during the tests in the port of Mertert. This shows that the change in deflection due to temperature came mainly from the temperature difference between the lower and upper parts of the beam. More exactly, it can be concluded that the deformations of the beam that occurred due to the temperature difference between top and bottom flange were one order of magnitude higher as the deformation due to fluctuations of the bottom temperature T4 itself.

During the deformation due to ΔT the horizontal distance between the bearings changes from L_0 to $L_0{}'$. But for a beam with a length of $46\,m$ the difference between L_0 and $L_0{}'$ is negligible, so deformation due to ΔT can also take place, while the sliding bearing is fixed, that means at the same time when deformation due to fluctuations of T4 occurred. Therefore, it has to be expected that both effects are superposed in the measurement data.

5.3 Dynamic tests

In the dynamic tests the modal parameters of the test setup (eigenfrequencies, damping, mode shapes and modal mass) were detected by Experimental Modal Analysis (EMA). The structure was excited with an electromagnetic shaker type "Tira" positioned on the top of the beam (cf. Figures 5.6 and 5.8). A detailed description of this shaker can be found in [58]. A swept sine excitation was used with a sweep rate of $0.02\frac{Hz}{s}$. The force amplitude of this shaker is adjustable and tests with different force amplitudes were performed but for the most tests the amplitude $2000\,N$ was used. Here, the intention was not to examine the dependency of the dynamic parameters on the amplitude of the excitation but to perform the same measurement several times in the different damage scenarios DS#0 to DS#4. During the tests the excitation force was measured by 3 force transducers that were positioned between the shaker and the beam. As input signal the sum of the three force signals was calculated. The response of the structure was measured by 26 accelerometers type PCB393B04, whose positions can be seen in Figure 5.8. One of the accelerometers was positioned under the shaker as driving point (DP). The signals were recorded by a data acquisition system (DAQ) at a sampling rate of $2500\,Hz$. After the conclusion of the tests the gathered data was examined with modal analysis software to obtain the modal parameters. Figures 5.28 and

5.29 show the input signal and the response of the system, which were measured at the driving point for a measurement at 31/01/14 11:28:18.
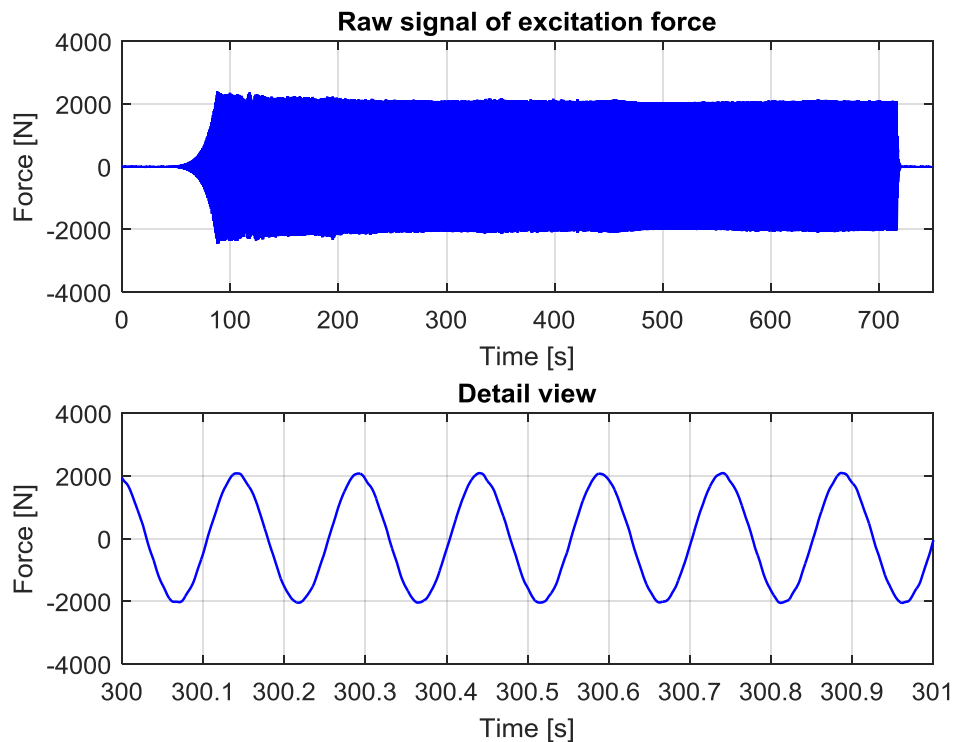
Figure 5.28: Excitation force as sum of the signals measured by three force transducers
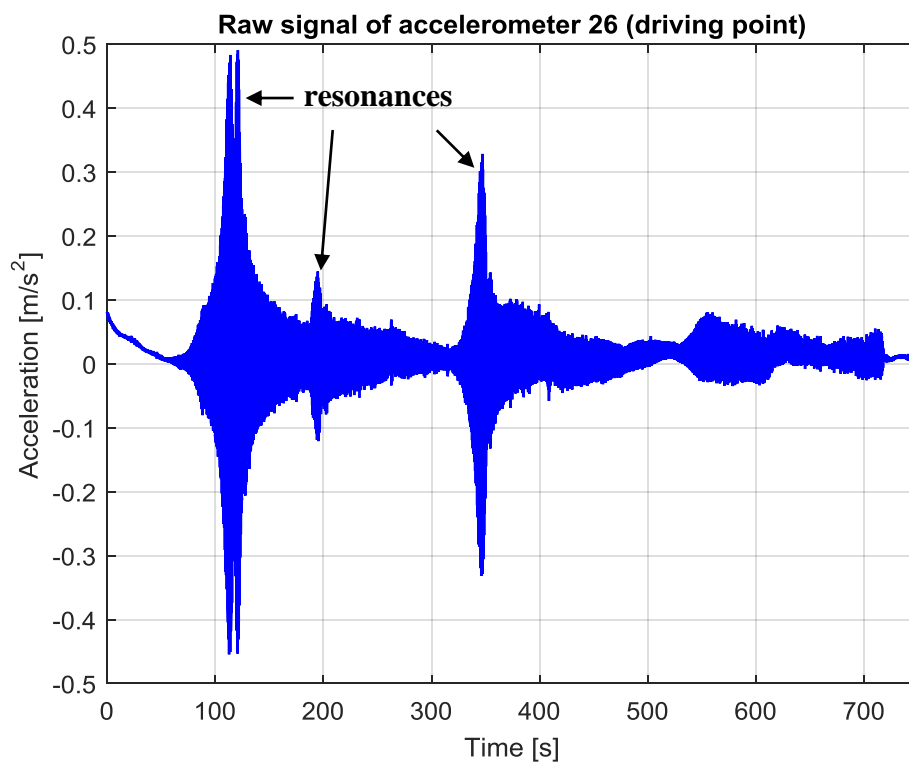
Figure 5.29: Acceleration measured during a dynamic test at the driving point

The considered frequency range started at $2.5\,Hz$, because the shaker wasn't capable of generating the necessary force amplitude at lower frequencies. In the evaluation described in the following, a frequency range from $2.5\,Hz$ to $10\,Hz$ is considered. For practical reasons it was difficult to handle the large data files, which result from the measurements with sampling rate $2500\,Hz$, and here this high sampling rate was not necessary, because the highest considered frequency is only $10\,Hz$. Hence, the data was reduced before the further evaluation. Before the reduction in order to avoid the aliasing, the frequencies over $125\,Hz$ were filtered from the data. For this purpose a digital low pass filter was created and the Matlab function 'filtfilt' was used that filters the data without causing a phase shift. The input data pass through the filter in forward and reverse direction, whereby the phase shift is compensated. In Figure 5.30 the resulting output of the filter is drawn in comparison to the original raw signal for one accelerometer. It can be seen that the course of the filtered signal is smoother, since the high frequencies were removed and that no phase shift occurred. After the filtering the sampling rate was reduced by factor 10 to $250\,Hz$ by using only every tenth sample of the filtered signal for the further evaluation.
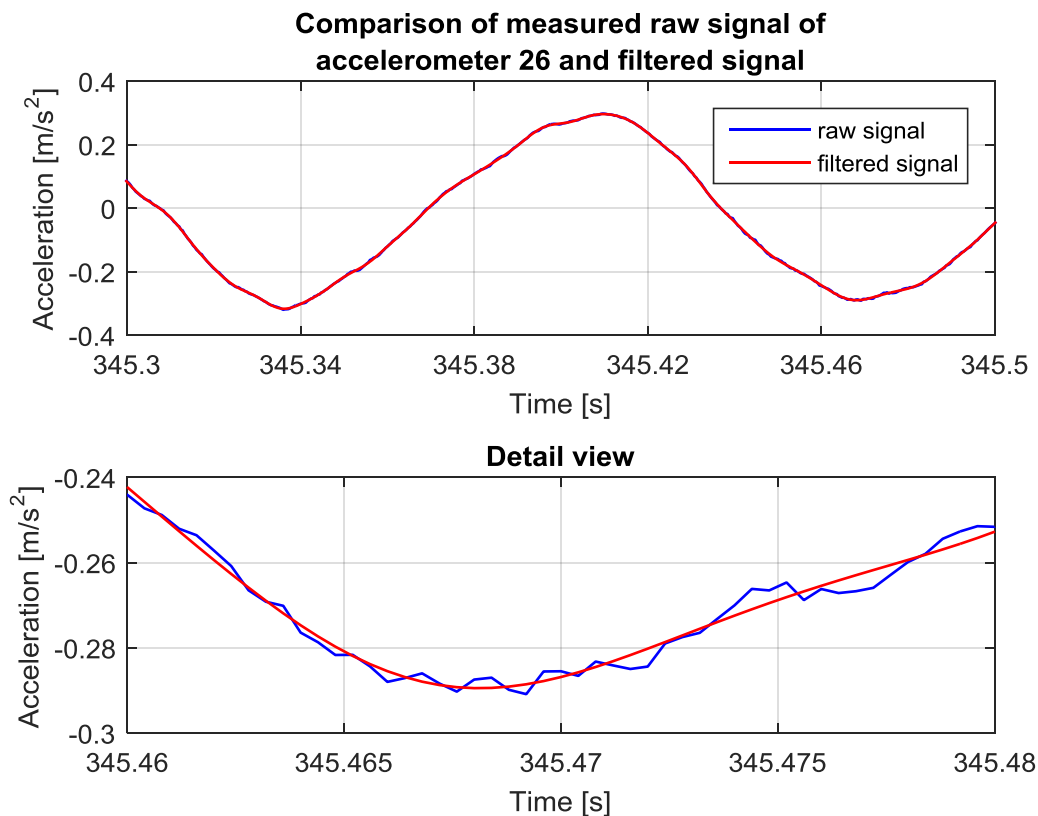
Figure 5.30: Raw and filtered signal of accelerometer 26 (driving point)

The data, which was filtered and reduced as described above, were now imported to the software ME'scope, which was used to calculate discrete values of the frequency response functions (FRFs) for every DOF with regard to the input force that took effect at the driving point. For this purpose first the Fourier spectra of the input and response signals are calculated by performing a Fast Fourier Transformation (FFT). Then the crosspower spectra of the input and the outputs are divided by the autopower spectra of the input.

$$[FRF] = [\{X_{res}(f)\}\{X_F(f)\}^H][\{X_F(f)\}\{X_F(f)\}^H]^{-1} \tag{5-19}$$

Where $\{X_{res}(f)\}$ and $\{X_F(f)\}$ are the Fourier transform of the response and the input force signals, respectively, given as discrete values for certain frequencies. The superposed H denotes the conjugate transposed. The operation yields a matrix with discrete values of the FRFs. At first, the FRFs were calculated for several parts of the signals with duration 100s. This yielded a frequency resolution of the resulting FRFs of 0.01 Hz. The used individual signal parts overlapped by 66% and were multiplied with a Hanning window in order to avoid the leakage effect due to a non-periodic signal. This effect is well-known in the field of signal analysis and means that the energy contribution at a signal that belongs to a certain frequency is spread over a frequency range, which distorts the spectra. It occurs if the input of a FFT is non-periodic. The Hanning window forces the signal to become zero at the beginning and the end, whereby a periodic signal is created artificially. The disadvantage is that a damping is added to the signal.

However, in order to obtain one FRF for every DOF, it was averaged over all the separate signal parts. By doing this, noise is reduced, if all FRFs used for the averaging are the same. The procedure so far yielded discrete values of the FRFs, whose magnitude is plotted in Figures 5.31 and 5.32 for one measurement in the healthy state of the beam. Four resonance frequencies can clearly be identified by peaks in the FRFs.
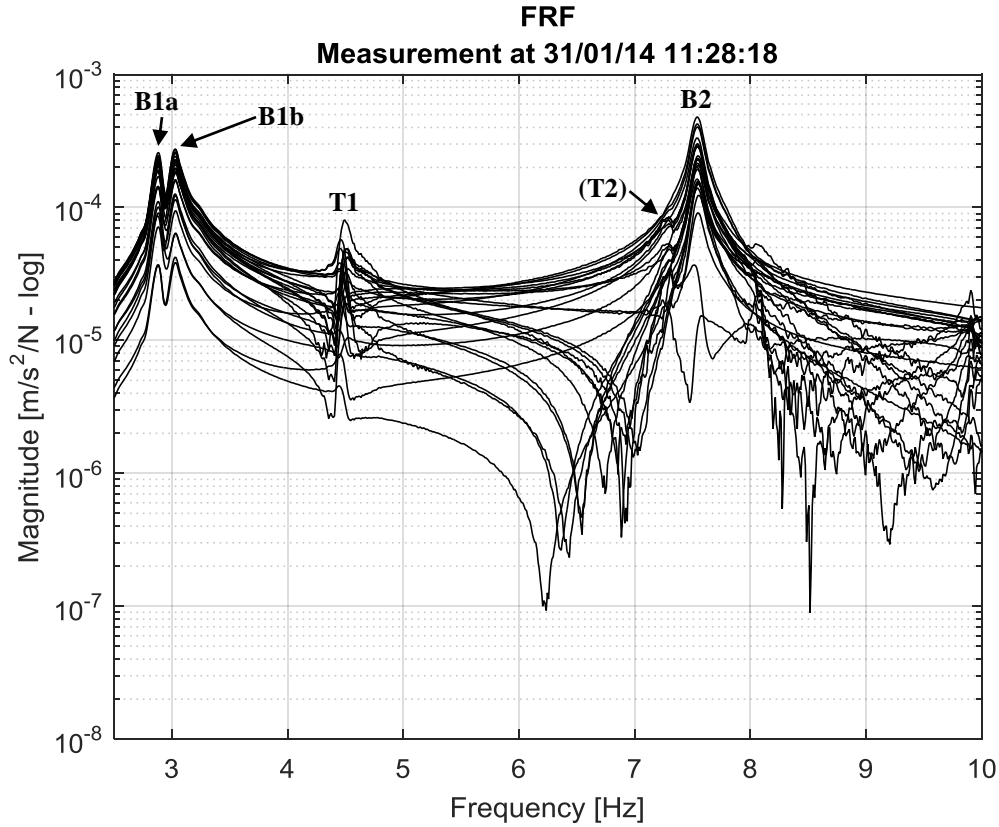
Figure 5.31: FRFs measured for the bridge beam in Mertert in DS#0
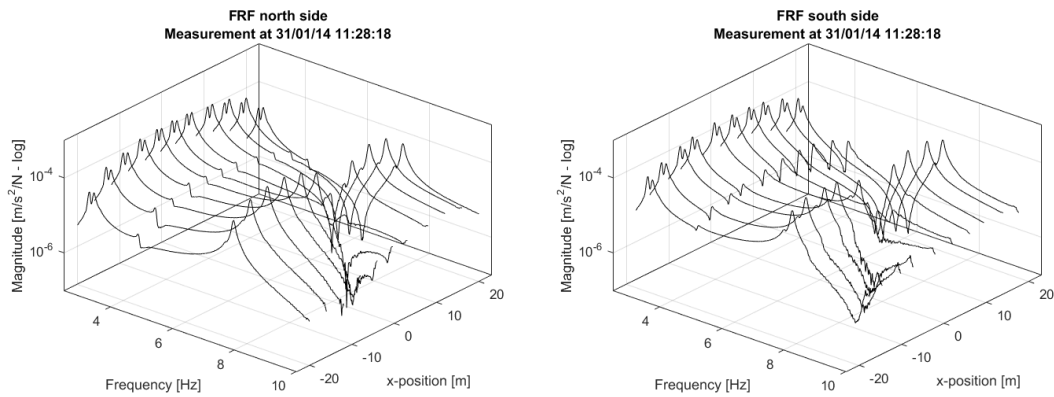
Figure 5.32: FRFs measured for the bridge beam in Mertert in DS#0

Now the FRFs were exported to OROS, where estimates of the modal parameters were obtained by the method 'EMA Broadband', which uses the Polyreference Least Squares Complex Frequency (p-LSCF) algorithm, which is described in Guillaume et al. (2003) [72].

In the following the results are shown for the measurement in the healthy state of the beam that was also used for the plots of the FRFs.

Table 5.4: Modes identified in the measurement at 31/01/14 11:28:18

Mode	Eigenfrequency [Hz]	Damping [%]	Modal A [kgm²/s]	Modal B [kgm²/s²]
B1a	2,88	0,786	-1.81e+05 - 6.55e+05i	-1.19e+07 +3.18e+06i
B1b	3,03	1,939	6.57e+04 - 2.69e+05i	-5.10e+06 - 1.35e+06i
T1	4,48	1,540	1.32e+05 - 4.84e+06i	-1.36e+08 - 5.82e+06i
T2	7,29	0,580	3.21e+06 - 8.38e+06i	3.85e+08 - 1.45e+08i
B2	7,54	0,684	-4.61e+04 - 6.74e+05i	-3.20e+07 + 1.96e+06i
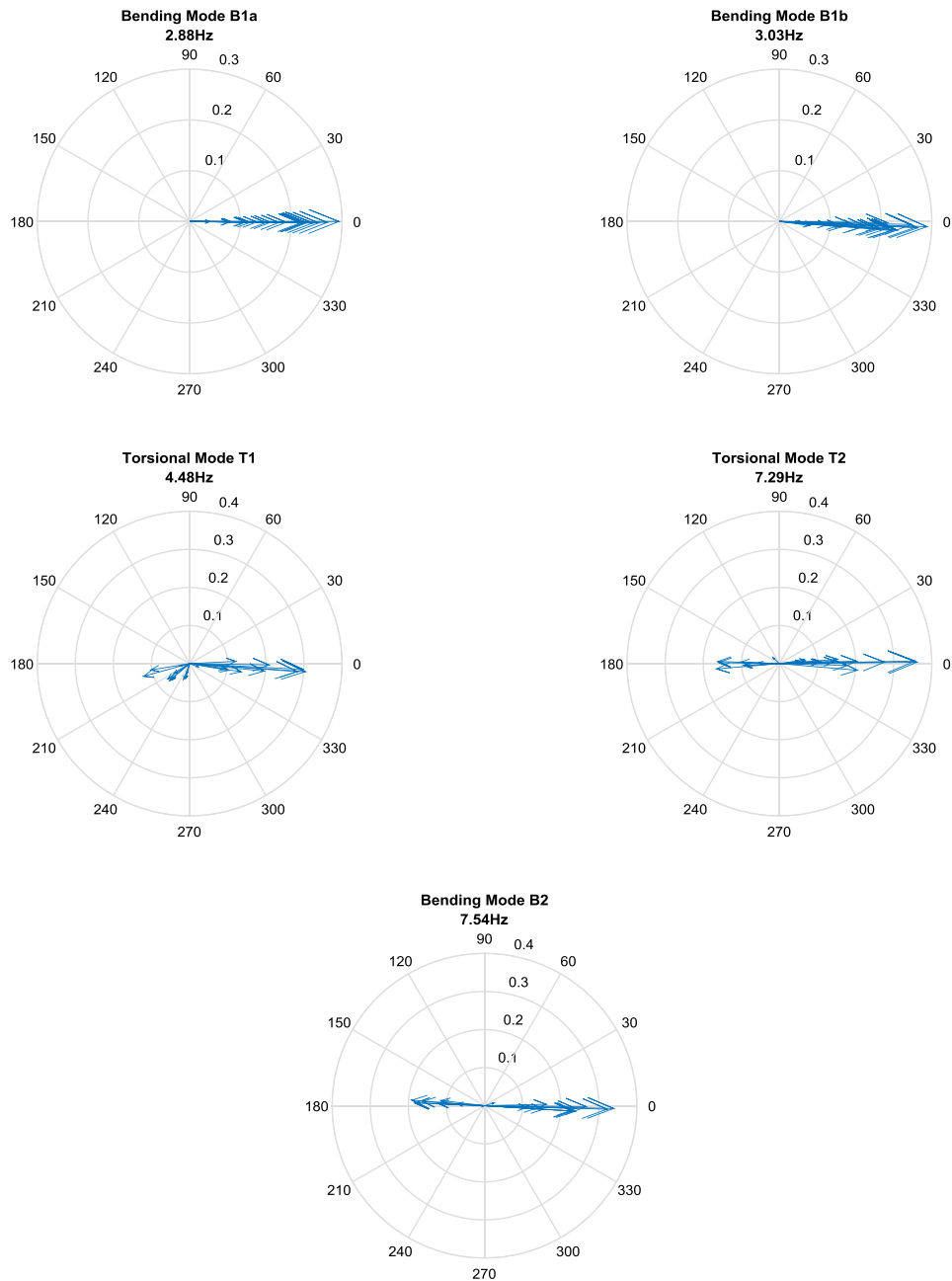
Figure 5.33: Not normalised mode shape components as calculated by OROS plotted in the Gaussian plane as compass plots
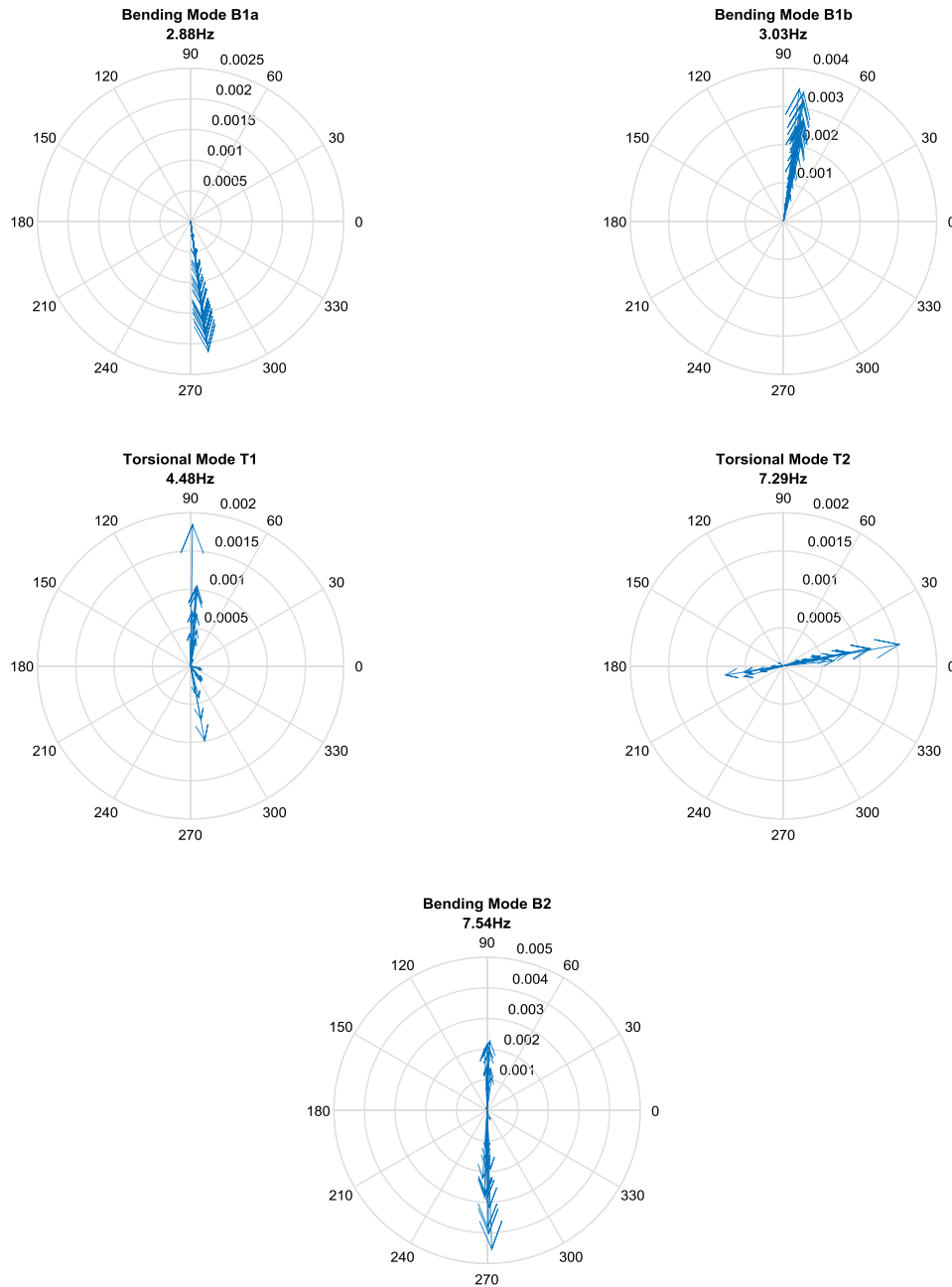
Figure 5.34: Mode shape components scaled to unit modal mass plotted in the Gaussian plane as compass plots

As it can be seen in Figure 5.34, the mode shapes normalised to unit modal mass are nearly purely imaginary. An exception is torsional mode T2, which is a hint, that for this mode the modal mass was not well identified. Furthermore, this mode was not very distinct in the FRFs (cf. Figure 5.32). For these reasons, this mode was omitted in the further evaluations.
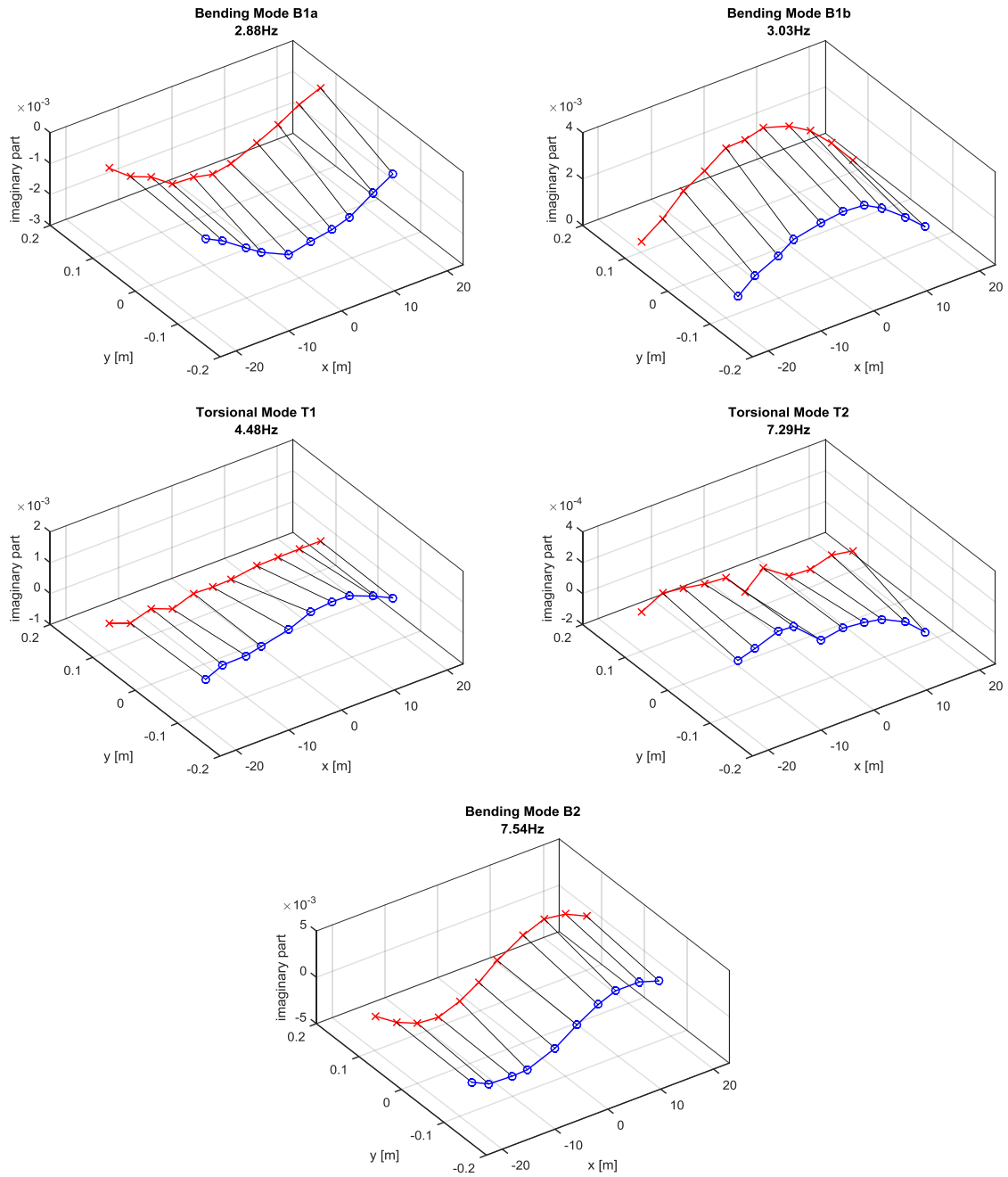
Figure 5.35: Identified mode shapes scaled to unit modal mass (UMM); The imaginary part of the components was used for these plots. The x- and y-axis are the coordinates of the accelerometers at the beam (red: north side, blue: south side).

At first, these dynamic tests were performed on the undamaged beam, i.e. on the beam as it was after the bridge had been demolished and the transport had been carried out. This state was defined as the reference state (DS#0). Subsequently, defined damages were introduced by cutting some of the tendons to realise damage scenario DS#1 to DS#4 as specified in Chapter 5.2. These artificial damages simulated an aging process with increasing damage. The tests were repeated in every damage scenario. The gathered data was used in several evaluations, which are described in the following chapters. The aim was to test, if the

measured modal parameters can be used for the detection of the damage introduced in DS#1 to DS#4. Finally, some of the measurements were chosen to be used in a model updating procedure that is described in Chapter 8.

5.4 Conclusion

During the entire test period, and especially after artificially damage was introduced, the prestressed concrete showed an increasing permanent deformation. After a loss of prestress, it takes some time until the beam has reached a new steady state. This is because, the application of a load leads to the formation of cracks, which still grow for some time. In contrast to the damage scenarios DS#1 to DS#3, 2 static load tests were performed in the last scenario. Here it was found that the permanent deformation of the beam after the second test was significantly lower than after the first one.

Furthermore, the deflection was strongly influenced by temperature fluctuations. In order to separate this influence from the effects of damage on the deformations, a method for temperature compensation is proposed in the next chapter.

By experimental modal analysis, 3 bending modes and 1 torsional mode in the frequency range $2.5 - 10\,Hz$ were clearly identified. Some of the FRFs showed an additional peak (marked in Figure 5.31 as T2), which was identified by the modal analysis software as a further torsional mode. But the quality of the identification for this mode was quite bad, so it was omitted in the further evaluation. The frequencies of the first two modes were similar, as they are highly coupled modes. The torsional mode shape T1 was very discontinuous, which indicated that it was not well identified. This was most likely due to the fact that most of the acceleration sensors were placed too close to the centre bar of the beam in order to detect the torsion well. Originally, this positioning had been chosen because of the damage that was present on the top flange from the beginning. Only four of the 26 accelerometers in total were mounted near the edges of the top flange.

6   TEMPERATURE COMPENSATION

As discussed in Chapter 5.2, the courses of the static displacements are overlaid by deformations caused by temperature fluctuations as can be seen in Figure 5.26. This up-down movement caused by temperature fluctuation during the course of a day is unavoidable, although the measurements were performed in winter with mostly cloudy sky. It is evident that the temperature gradients within a structure strongly increase in summer as a result of higher solar irradiation. Hence, the effect of temperature fluctuations on the deformations also increases. However, it is useful to compensate it, as it has nothing to do with the artificially introduced damage during the tests.

In [69], a compensation procedure was described and illustrated by data measured in the port of Mertert. It is briefly explained here.

In Chapter 5.2 it was shown that fluctuations of the overall temperature of the concrete beam can cause deflection, if the sliding bearing is blocked. Therefore, in Figures 6.1 and 6.2, the displacements measured by SV1 and SH7, respectively, during all loadings (L) are plotted vs. the bottom flange temperature T4.

In Figure 5.18, the sensors were set to zero at the starting of reference state DS#0, following an offset of sensors. The data considered here are taken before the offset. However, this does not affect the procedure for temperature compensation.

Like elucidated in Chapter 5.2, the horizontal movements of the beam at the sliding bearing are rather small or even zero, if the deformations are only caused by temperature fluctuations. Therefore, only data, which was taken during such periods, provide information that is useful for temperature compensation.

Magenta points present the full data set, from which a selection is performed for each period when only small or no horizontal movement at the sliding bearing occurred, which can be clearly observed in Figure 6.2. These selected data are marked by dark blue lines and used for temperature compensation. Since the sliding bearing was not ideal, a stick-slip effect exists, i.e. there are several distinct periods separated by slips of this bearing even during the same loading. For instance, there are three periods with only small horizontal movement during loading #4-L1.
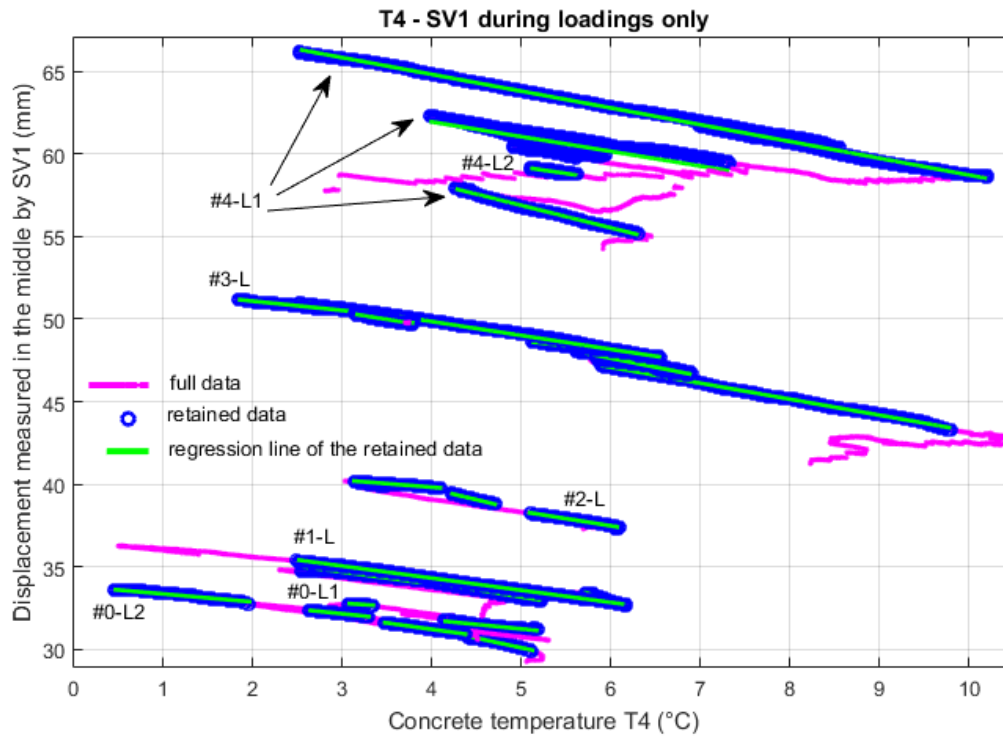
Figure 6.1: Vertical displacement in the middle of the beam (SV1) vs. temperature T4 [69]
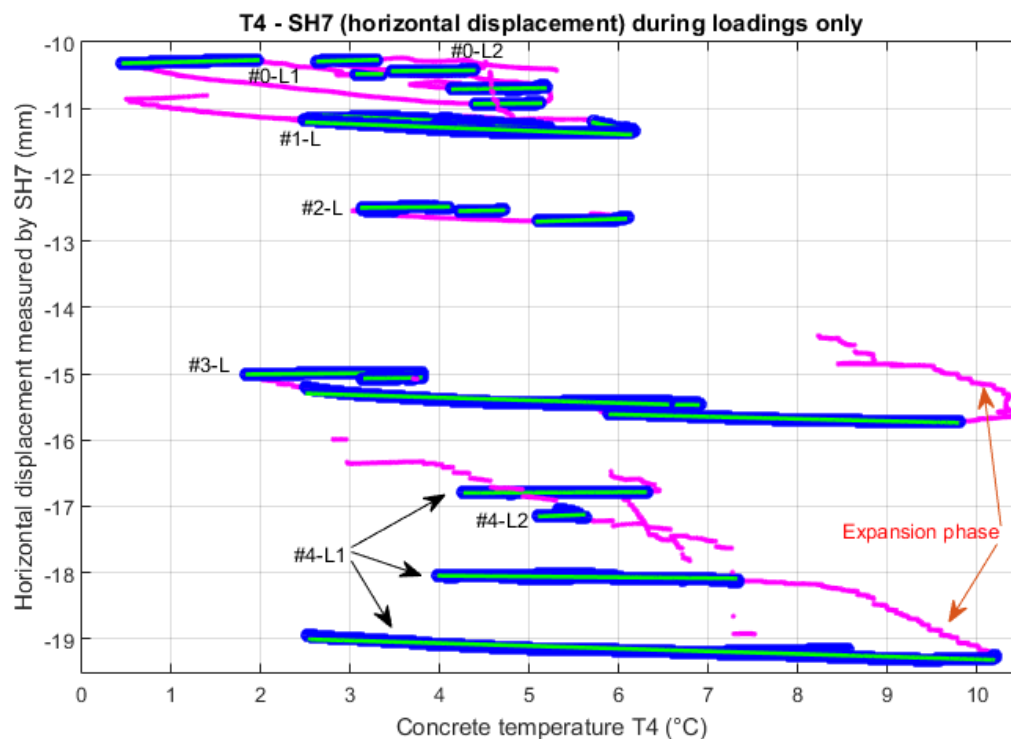
Figure 6.2: Horizontal displacement at the sliding bearing (SH7) vs. temperature T4 [69]

Only for the selected data, a linear regression line was assessed and presented in green for each period. Figure 6.3 facilitates the observation by separating each loading.
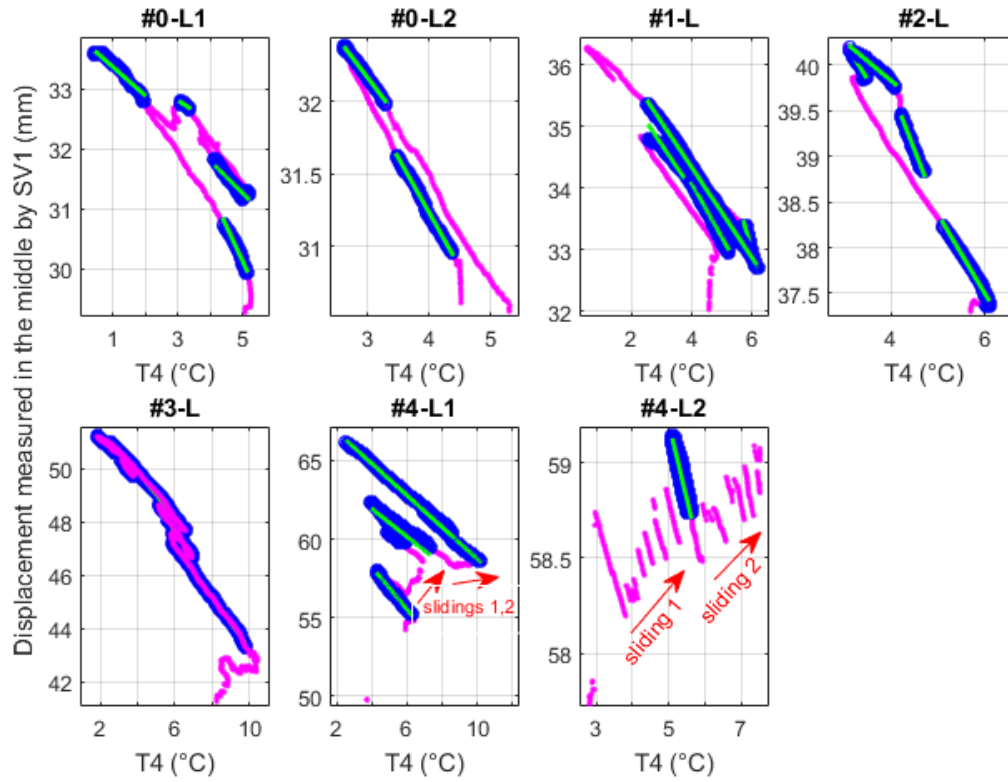
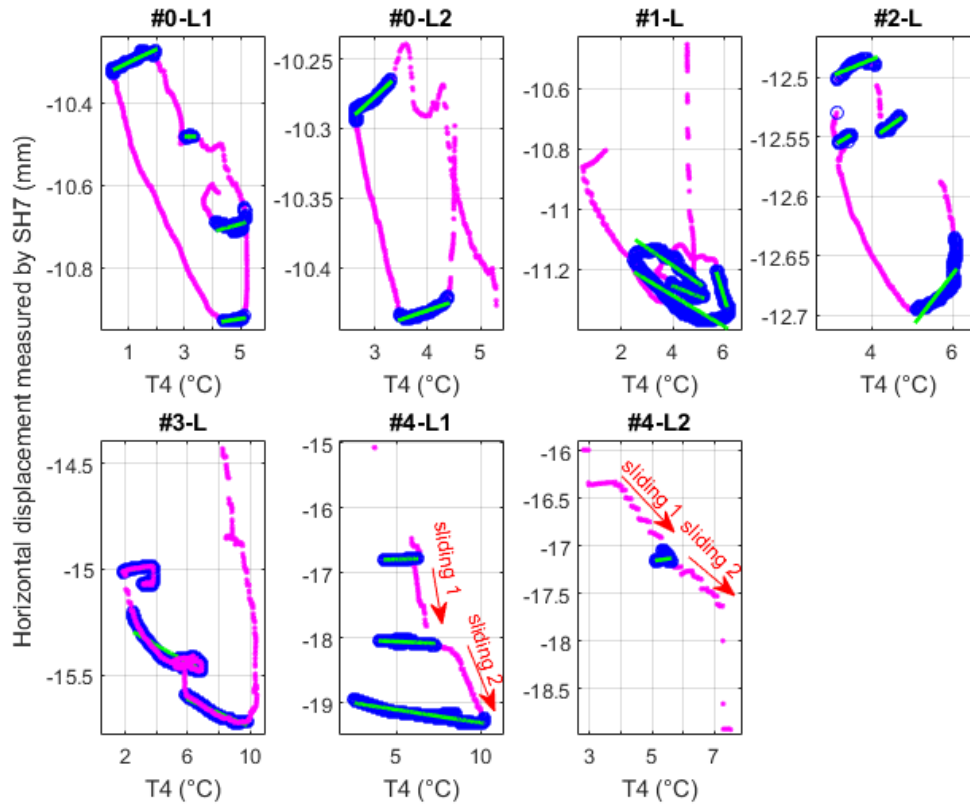**Figure 6.3: Detailed plots of vertical displacement SV1 vs. T4 for each loading [69]**

Figure 6.4: Detailed plots of vertical displacement SH7 vs. T4 for each loading [69]

The above figures show that the regression lines match quite well with the selected data, i.e. the variance is low. The assumption of a linear relationship between vertical displacement SV1 and concrete temperature T4 is obviously appropriate. Additionally, most of the regression lines are quite parallel. Especially for the vertical displacement, the trend is clear: a higher temperature T4 corresponds to a less displacement, i.e. the beam moved upwards and vice versa.

Furthermore, it was shown in Chapter 5.2 that even with an ideal sliding bearing, deflection can be produced by temperature fluctuations. In this case they are caused by temperature gradients in the beam, like for instance a difference between the temperature in the top and the bottom surface. Therefore, similar plots as in Figure 6.3 were created for SV1 and $\Delta T = T6 - T4$, where T4 and T6 present the temperature of the bottom flange and the top flange accordingly.
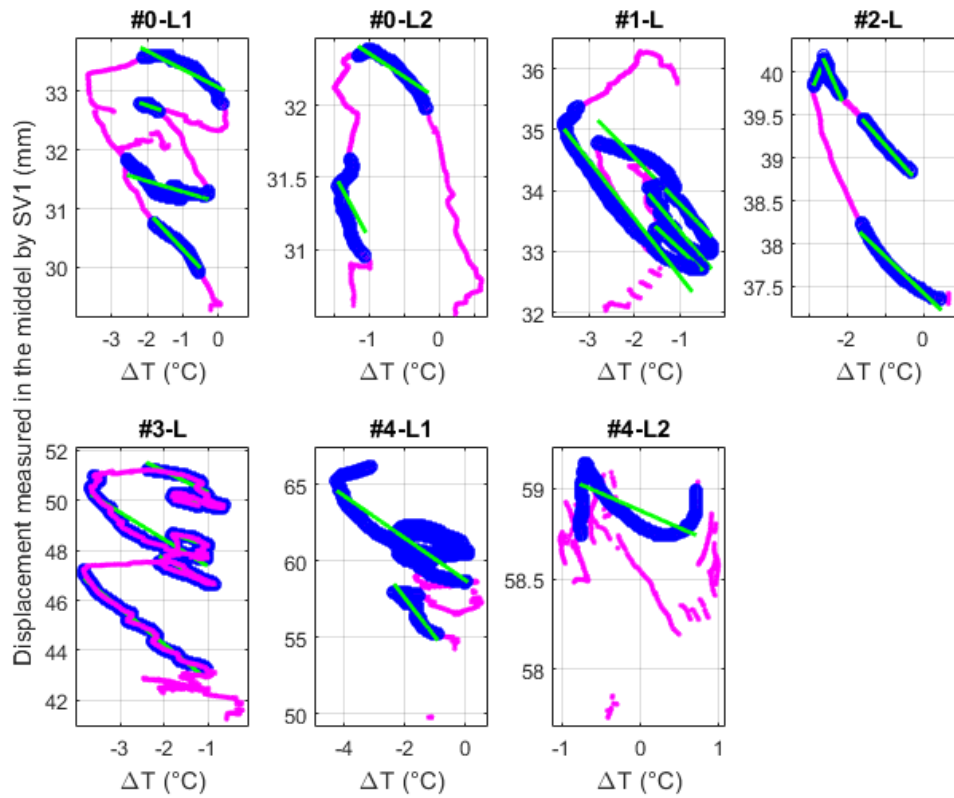
Figure 6.5: Detailed plots of deformation SV1 vs. $\Delta T = T6 - T4$ for each loading [69]

The temperature difference ΔT is mostly negative, which means that the top temperature T6 is less than the bottom temperature T4. As analysed in Chapter 5.2, a negative ΔT leads to a downward deflection, while a positive ΔT results in an upward bending. So it can be resumed that an increase of ΔT accompanies a decrease of deflection of the beam. In comparison to

SV1 vs. T4, the linear relationship in SV1 vs. ΔT is less pronounced with more varied slopes of the regression lines. That means the correlation between SV1 and T4 is stronger and so it is more appropriate as basis for temperature compensation.

The compensation consists in performing a projection of data following a pre-defined direction and a reference temperature. Since the regression lines are quite parallel, a common slope can be chosen as a representative direction. Since the measurements were taken in winter when the ambient temperature was quite low, a reference temperature of 5°C was chosen. Figure 6.6 gives an example that two data points X1 and X2 measured at different temperatures are mapped onto the reference temperature and result in two derived points Y1 and Y2.

a) SV1 over T4   b) SV1 over time
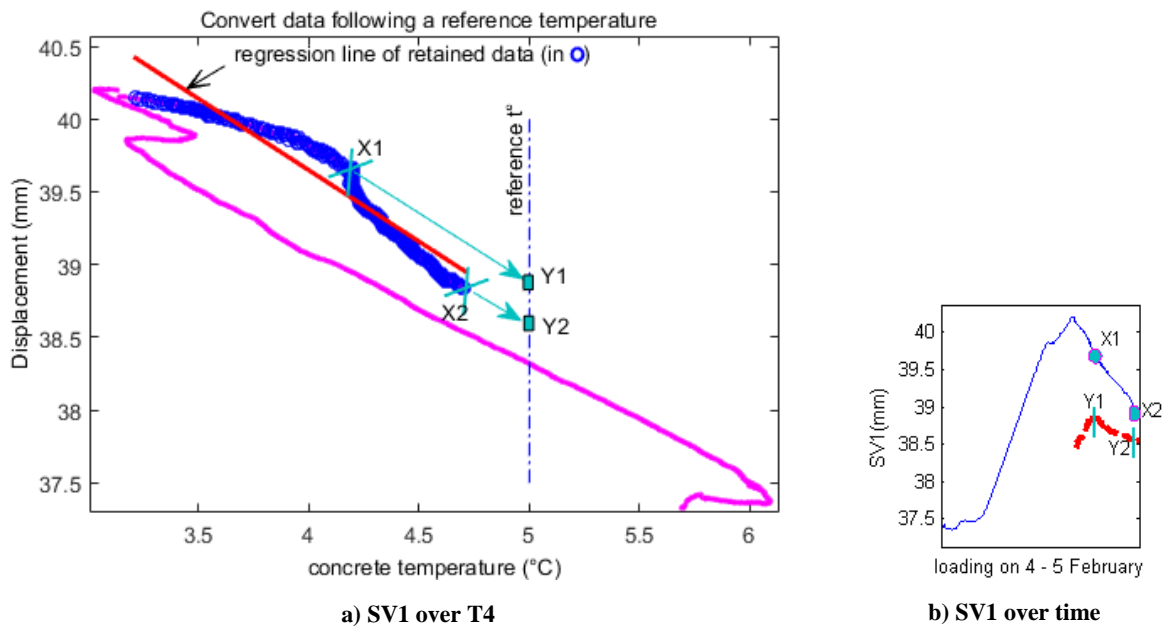
Figure 6.6: Example of temperature compensation: 2 points X1 and X2 are projected through the slope of the regression line to the reference temperature, which yields two new points Y1 and Y2 [69]

This mapping was performed for selected data points with inconsiderable movement at the sliding bearing (that Figure 6.3 shows for loading cases) and presented in Figure 6.7.
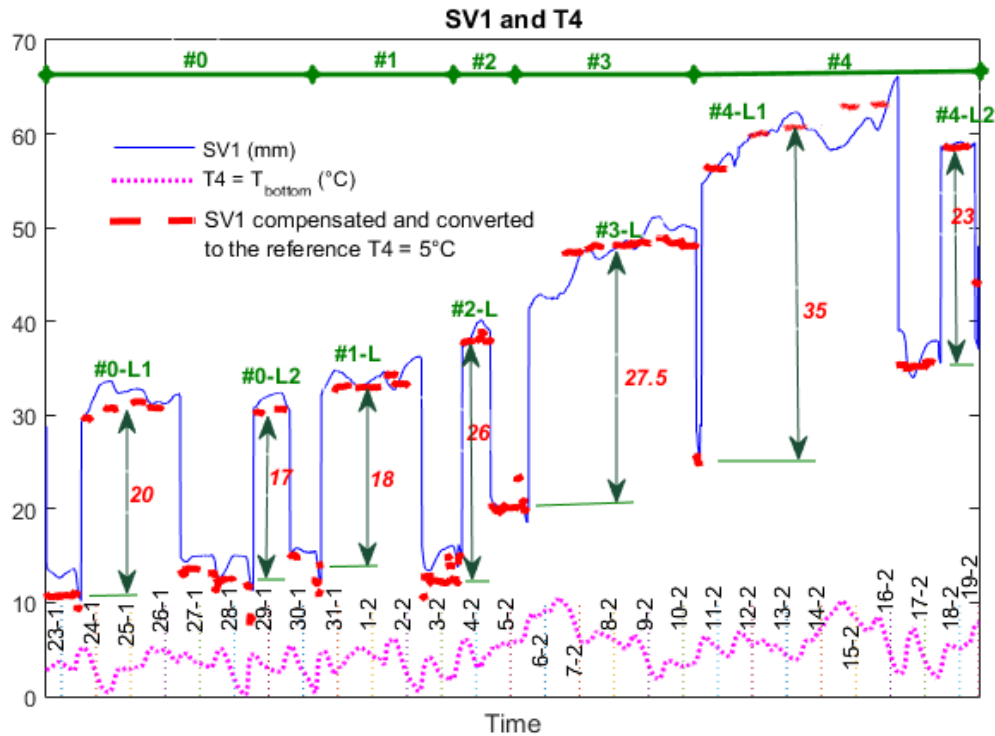
Figure 6.7: Measured signal SV1 (blue) and compensated values for selected data (red) [69]

The compensated data show less variation and should be more appropriate than the raw data for model updating and damage detection in the following steps.

It is possible to use the described procedure for temperature compensation for other quantities, like for instance the eigenfrequencies, too. Changes of the Young's moduli due to temperature fluctuation cause stiffness changes and hence changes of the eigenfrequencies of a structure. For most bridges changes in the asphalt temperature have a high impact on the eigenfrequencies, since the Young's modulus of asphalt shows a high dependency on temperature. In the test setup, which was examined in the present thesis, the asphalt layer was already removed from the top of the prestressed concrete beam, hence a temperature compensation of the eigenfrequencies was omitted.

7 EVALUATION OF DAMAGE INDICATORS

7.1 Static deflection

Already from the raw data shown in Figures 5.18 and 5.19, increasing damages are detectable. In DS#0, the maximum displacement occurs in the middle of the span between the two bearings at the positions of sensors SV1 and SV8. With increasing damages, the displacement at point SV3 approaches the value in the middle and even exceeds this value from DS#3 on. It allows localising the damage, since SV3 was the nearest sensor to the damage location. The point of maximal displacement shifted towards the damage.

Furthermore, as already mentioned in Chapter 5.2 a sagging, i.e. a steady downwards movement of the beam due to increasing permanent deformation, of the beam is observed in Figures 5.18 and 5.19. Especially from #2-UL to #4-UL1, it shows clearly, that the beam did not return to its former state after removal of the load. To a smaller extent, these remaining deformations already occurred in the healthy state as well as DS#1. They can be explained by the formation of cracks in the concrete and small plastic deformations of the reinforcements during the loading of the beam. Furthermore, while the deflection in #0-L1 and #0-L2, i.e. without the presence of damage, stays more or less at the same level, it increases in #1-L to #4-L1, while the beam is loaded. The effect of plastic deformations increased after the cutting of tendons and led to progressive irreversible deformations. In the last static loading test #4-L2 the irreversible deformation already occurred in the previous loading and so the beam had reached a new steady state.

In the following, the displacements which occurred during the load tests (stages designated with "L") and between them (stages designated with "U"), are examined more in detail. As it is observed in Figure 5.18, these displacements were not constant over time. Besides the above mentioned effects, the displacements were also dependent on temperature fluctuations as elucidated in Chapter 5.2. In order to show the deflection along the longitudinal axis of the beam, a 'representative' value was determined for each of these stages and each sensor. Then these values were used as nodes for a cubic spline interpolation. Afterwards, the first and second derivatives of the splines were also calculated. At first, it will be described here, how the representative values were chosen.

Since the up and down movements of the beam due to temperature fluctuations are not related to damage, only temperature compensated displacements are evaluated. They were determined by means of the procedure that has been described in Chapter 6. For the temperature compensation, the full data set of measured displacements was subdivided into parts, which were serially numbered. Only for some manually selected parts, the temperature compensation was performed. The main selection criterion was that there were only small movement at the sliding bearing like elucidated in Chapter 6. As an example, Figure 7.1 shows temperature compensated displacements for unloading #0-UL2 and sensor SV3. Due to the mentioned selection process the parts 3 and 8 are missing in Figure 7.1.
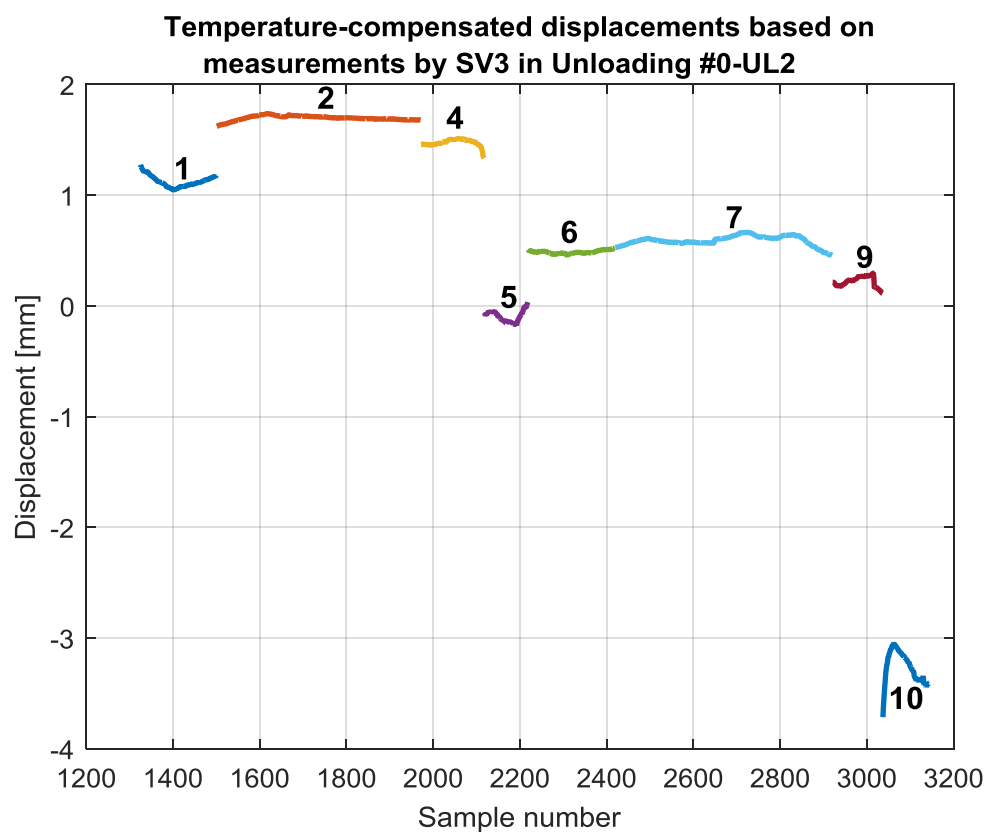
Figure 7.1: Detailed view of the temperature-compensated displacements in unloading #0-UL2

It can be seen in Figure 7.1 that in spite of the temperature compensation, there are still important variations. Especially, the values in part 10 are much smaller as in the previous parts. This is a decrease of the deflection, which occurred when the temperatures rose around noon as it was explained in Chapter 5.2. Hence, in order to determine one representative value, it was firstly necessary to choose manually parts for which the temperature-compensated values were quite consistent. If several parts corresponded to this criterion, preference was given to the ones that were measured later, because for these parts, the beam had more time to settle down. For instance, here parts 6 and 7 were selected. Finally, as

representative value for the temperature-compensated displacement, the mean value of the selected data was calculated. This procedure was repeated for all displacement sensors and every loading and unloading.

At first, the absolute displacements against a base line were considered. Already before the temperature compensation, the signals of all sensors were set to zero at a certain point in time (22/01/2014 11:59:00). Therefore, the representative displacement values for stage #0-UL1, which were determined as described above, were very close to zero. For the following representations, these displacements have been used as a reference, i.e. by subtracting from all determined displacements for all sensors the corresponding values in stage #0-UL1, the deflection in #0-UL1 was defined as the base line. The result is shown in Figure 7.2. The solid lines represent the loadings and the dashed lines the unloadings. For comparability, the plot of the sensors signals in Figure 5.18 uses the same baseline. In the following plots, the damage location is shown by grey shading.
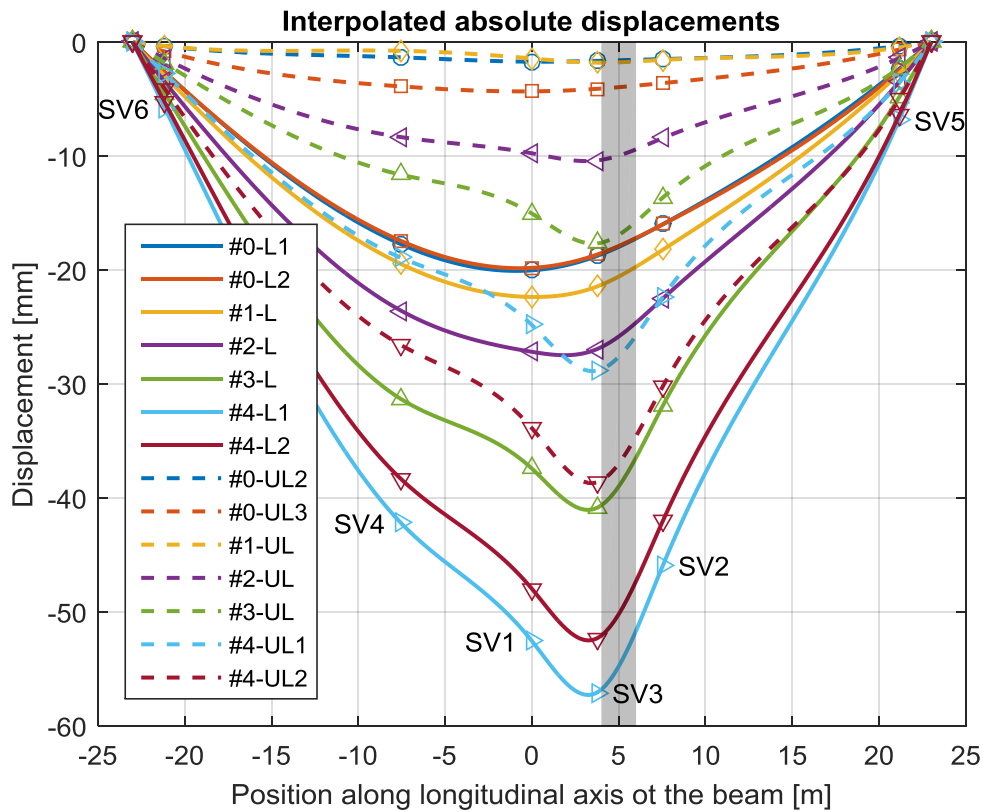
Figure 7.2: Interpolated absolute deformations of the beam derived from temperature compensated measurements; The markers show the actually measured values and the damage location is shown by grey shading.

As expected, the deflection during load tests was increasing with increasing damage. In the undamaged state #0-L1 and #0-L2, the deformations were still approximately equal. However, after cutting 2 tendons, it already increased in #1-L. This trend was kept with

increasing damage until stage #4-L2, where the deflection is again lower than in #4-L1. It is necessary to reveal that DS#4 is the only damage scenario except the reference state DS#0, in which two load tests were performed. Between these two static loadings no further tendons were cut. Therefore, the plastic deformations after introducing the artificial damage in DS#4 occurred mainly during the first loading. So, it was expected that the absolute deflection in the second loading test would be approximately the same as it was at the end of the previous test.

The same applies to the deflection after the load tests, i.e. in #4-UL1 and #4-UL2. Since how mentioned above, the plastic deformations were largely completed before the start of the second loading test, mainly elastic deformations took place here, which would have to go back completely after the unloading. The curve for #4-UL2 in Figure 7.2 seems to contradict this, because it looks as if new significant permanent deformations had occurred since it is far lower than the curve for #4-UL1. Actually, there is not much time left between the unloading after #4-L2 and the shutdown of the data acquisition system. Too few data were collected to perform good temperature compensation in #4-UL2. In Figure 6.7 it can be seen that the temperature compensated displacements for the last unloading #4-UL2 are much higher than the measured values, so they have to be considered as not accurate or as outliers. However, in the raw data in Figure 5.18, it can be seen that the measured deformations after the last removal of the load actually return approximately to the values before #4-L2.

The analysis of the raw data showed already that the maximum of deflection shifts towards the damage location with increasing damage. Correspondingly, Figure 7.2 shows the same effect. Before #2-L, the displacement at SV3 is less than at SV1. The maximum of the deformation is therefore still close to the middle of the span. In #2-L, the displacements at the two positions are approximately equal and from DS#3 the value in SV3 exceeds SV1. Consequently, the course of the deflection curve also changes considerably. So, it is expected that its derivatives should be useful for the detection.

The derivatives can be calculated directly from the cubic splines interpolated in the last step. The first derivative is the slope of the deflection curve and the second derivative is proportional to the bending moment M_y.

$$w' = \tan(-\varphi_y) \qquad (7\text{-}1)$$

$$w'' = -\frac{M_y}{EI_y} \tag{7-2}$$

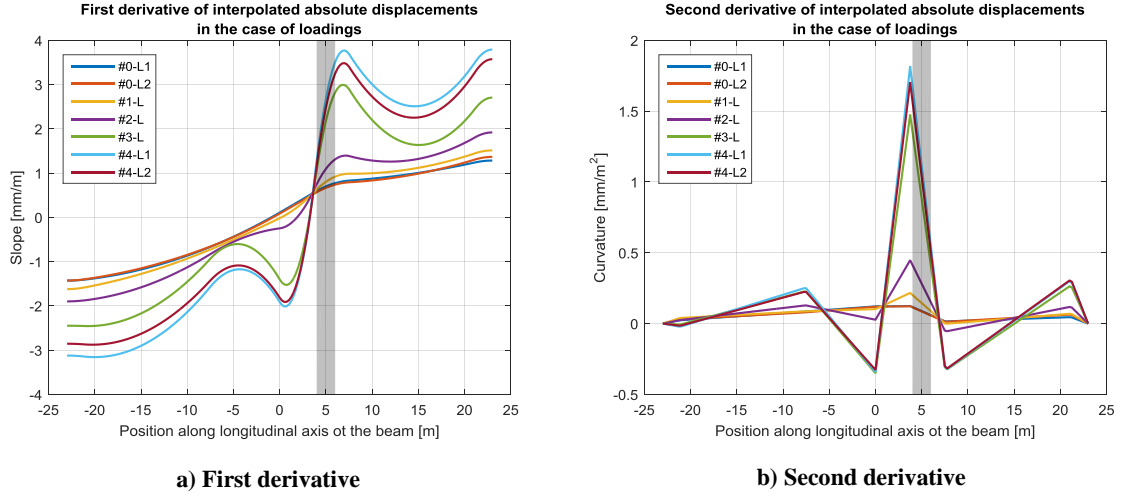where φ_y is the angle of inclination and EI_y is the bending stiffness.

a) First derivative   b) Second derivative

Figure 7.3: Derivatives of the interpolated absolute displacements in the case of loadings
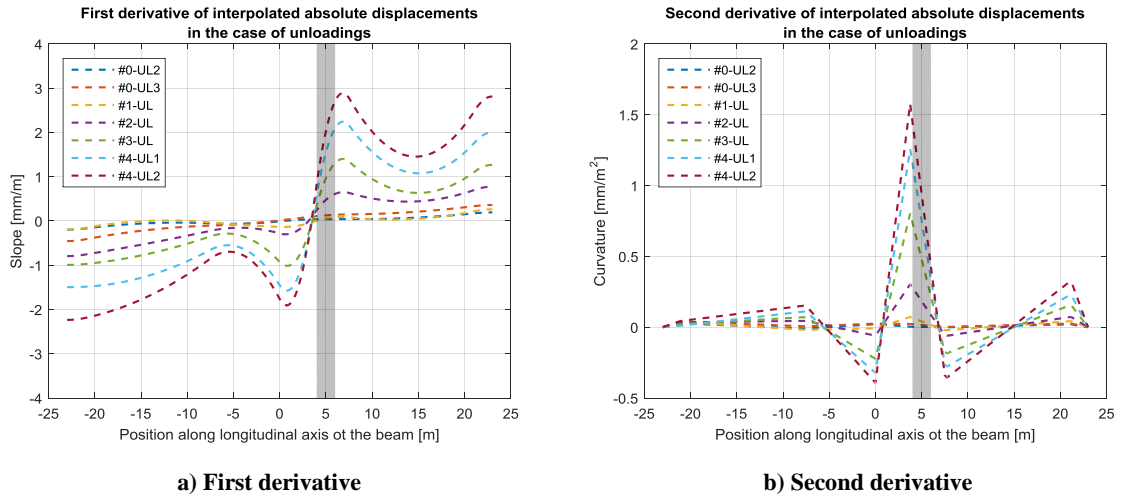

a) First derivative   b) Second derivative

Figure 7.4: Derivatives of the interpolated absolute displacements in the case of unloadings

Figures 7.3 and 7.4 show that the derivatives allow to detect and localise clearly the damage. The first derivative, i.e. the slope of a deflection line, shows an S-shaped curve in the vicinity of the damage, which becomes more significant with increasing damage. The curves for #4-L1 and #4-L2 are quite similar, because no additional damage was introduced between the two static tests. However, the damage could still be clearly localised by considering this curve. The curvature of the curves, i.e. the second derivative, even shows a significant peak at the damage position. An assessment of the severity of the damage is possible, considering the height of the peak.

Now, the deflections, which result purely from the load with the additional live loads of $2 \times 13\,t$, will be considered. For this purpose, the difference between the deformations directly before and during a loading was calculated. The curves also include plastic deformations, which occurred during the load tests. As before for the absolute deflections, the first and second derivatives were calculated based on a cubic spline interpolation. Again the location of artificial damage is shown by grey shading in the following plots.
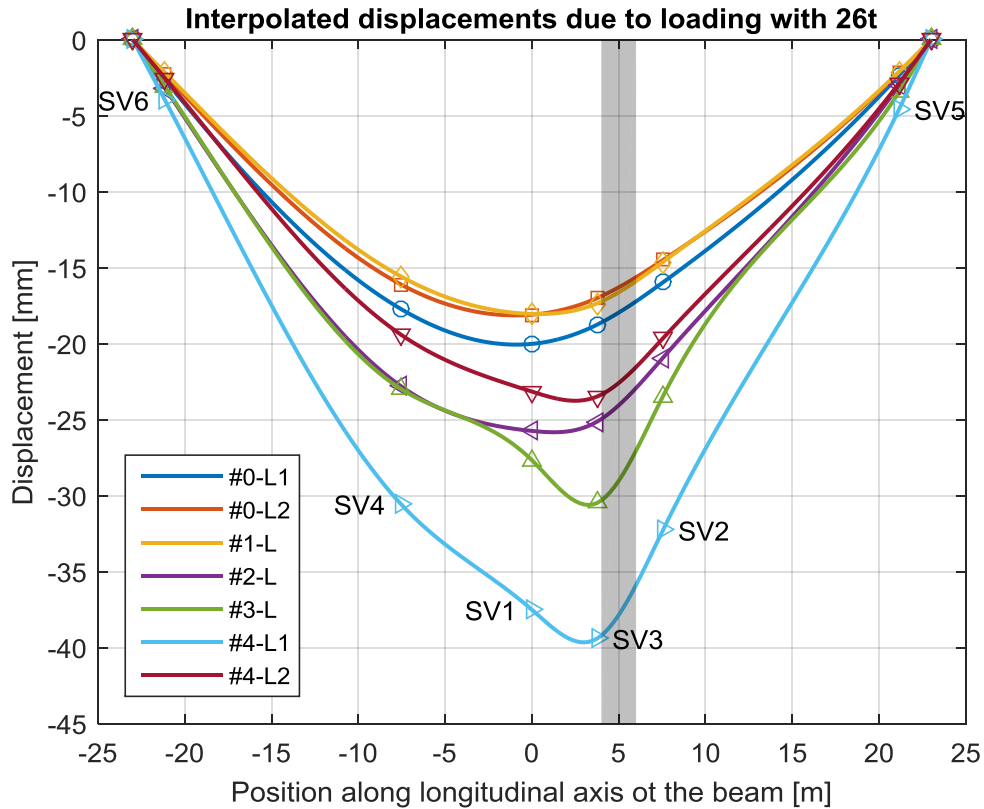
Figure 7.5: Cubic spline interpolated displacements due to live loads derived from temperature compensated measurements; The damage location is shown by grey shading.
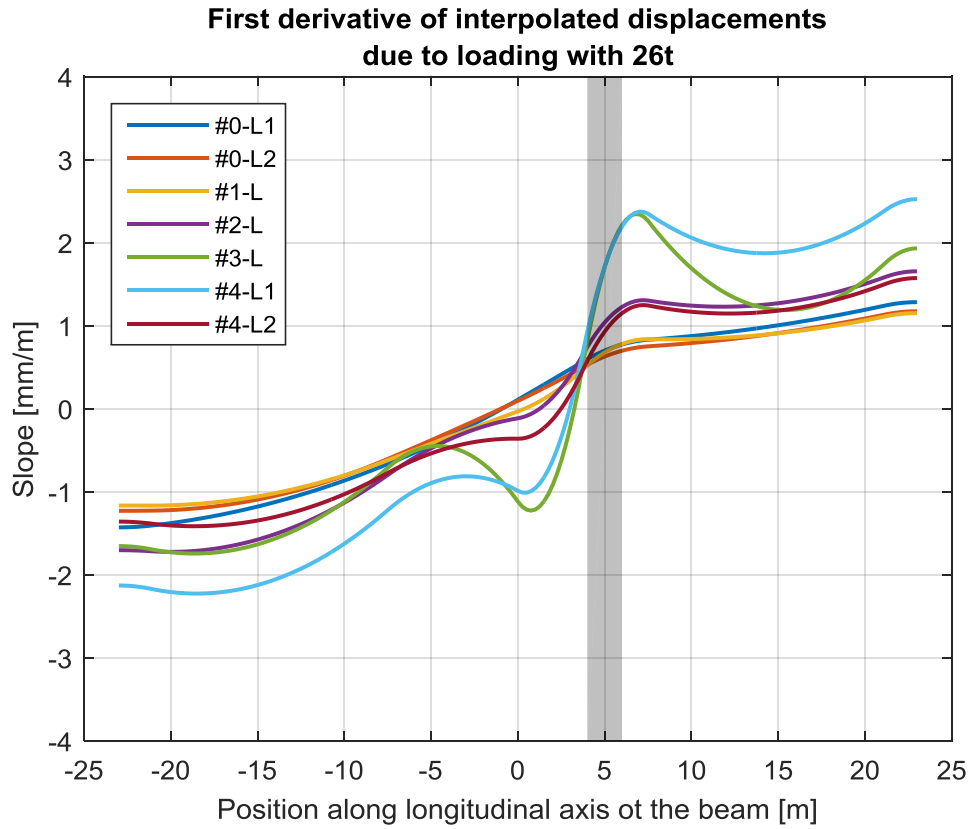
Figure 7.6: First derivative of the interpolated displacements due to live loads
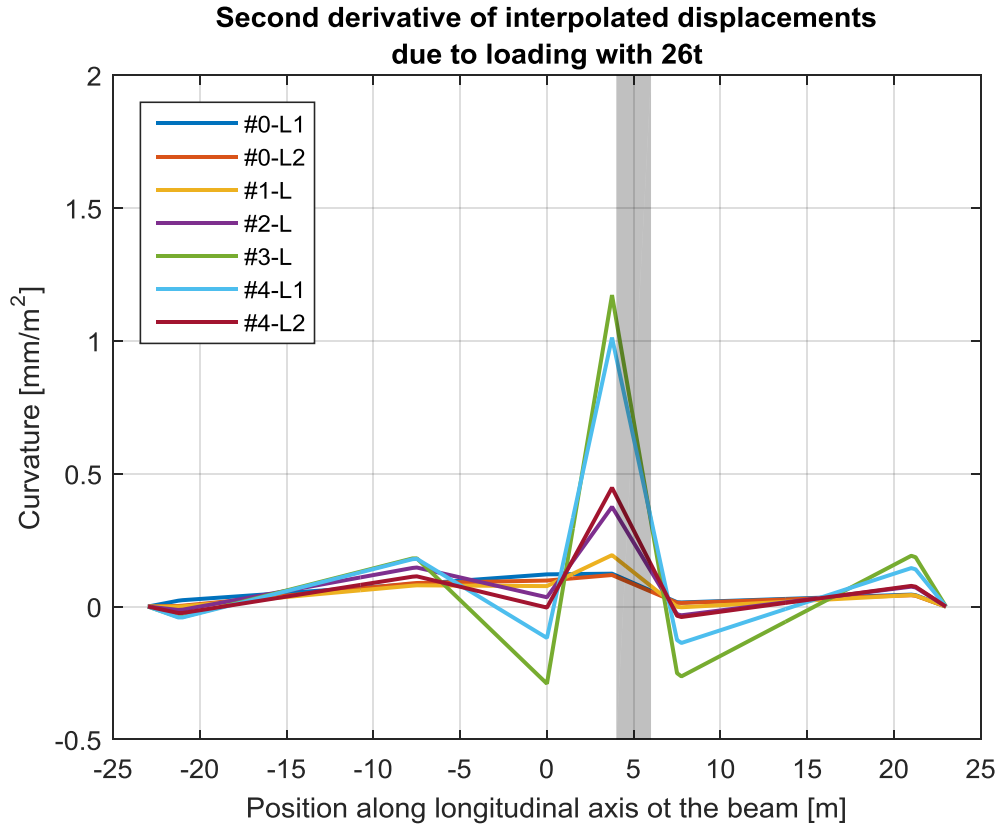
Figure 7.7: Second derivative of the interpolated displacements due to live loads

The deformations in the first load test #0-L1 are somewhat larger than in the second test, which can be explained by the fact that micro cracks occurred due to the load and that it might also lead to settlement effects in the bearings. Therefore, remaining deformations occurred here, which were already present before #0-L2. However, even before the series of measurements presented here, loads of the test setup with the additional live loads had taken place several times to minimise this effect. Nevertheless, the deflection in #1-L is again at similar level as in #0-L2. The damage introduced in DS#1 was still too small to be recognised. Moreover, as at the beginning, the maximum of the deflection is still in the middle of the beam at SV1. However, for #2-L, the damage can be detected clearly by the increase in the deformations and the approximation of the value for SV3 to that for SV1. From #3-L, i.e. DS#3, the maximum of the curves is actually at SV3, i.e. closer to the damage location. For #4-L2, a considerable reduction of deformations is observed with respect to #4-L1, which can be explained by the fact that permanent deformations due to loading had remained from #4-L1 and did no longer occur in #4-L2. However, the maximum value remains at SV3.

As for the absolute displacements, the damage can be easily detected by means of the derivatives of the interpolated displacements due to the additional loads. As in case of dead load only, the first derivative shows an S-shaped curve in the vicinity of the damage, which becomes more significant with increasing damage. Only at #4-L2, the effect decreases due to the reason mentioned in the last paragraph. The second derivative also shows a peak at the damage position.

7.2   Eigenfrequencies

Eigenfrequencies are the absolute values of the eigenvalues determined by solving equation (4-12). The matrices $[\mathbf{A}]$ and $[\mathbf{B}]$ of this equation contain the structural matrices of the MDOF system, including the stiffness matrix. If components of this matrix decrease, the magnitudes of the eigenvalues reduce generally, too. Furthermore, the angular eigenfrequencies can be calculated from the generalised stiffness and the modal mass according to equation (4-33), where if the mass is constant then $\omega_r \sim \sqrt{k_r}$. Therefore, a decrease in the stiffness, e.g. due to damage, leads to a decrease in eigenfrequencies. Furthermore, the loss of prestress due to damaged tendons also reduces eigenfrequencies. This results from the following equation for the calculation of the eigenfrequencies of a pretensioned, simply supported beam (cf. [73]).

$$\omega_n = \sqrt{\frac{EJ(n\pi)^4}{\mu l^4} + \frac{N(n\pi)^2}{\mu l^2}} \qquad\qquad (7\text{-}3)$$

ω_n: n-th angular eigenfrequency

EJ: flexural rigidity

l: span length (distance of the bearings)

μ: mass distribution

N: normal force (e.g. due to prestress)

This equation states, inter alia, when the pretension force N decreases, the angular eigenfrequencies decrease as well.

The simplest way to use dynamic parameters for damage detection is therefore to monitor the eigenfrequencies. Since these are properties of the whole system and are not linked to a certain degree of freedom, the reduction in eigenfrequencies is a global damage indicator. That means it provides only the possibility to detect the presence of stiffness losses, but not to localise them. In Figure 7.8, the eigenfrequencies of the beam in Mertert are shown for 4 modes during the test period. A clear decrease of all eigenfrequencies is observed, as the stiffness of the beam decreases more and more due to the damages from DS#1 to DS#4. But at the transition between DS#1 to DS#2 a small increase can be seen, which has to be considered as measurement error or environmental effect.

a) Bending mode B1a

b) Bending mode B1b

c) Torsional mode T1

d) Bending mode B2
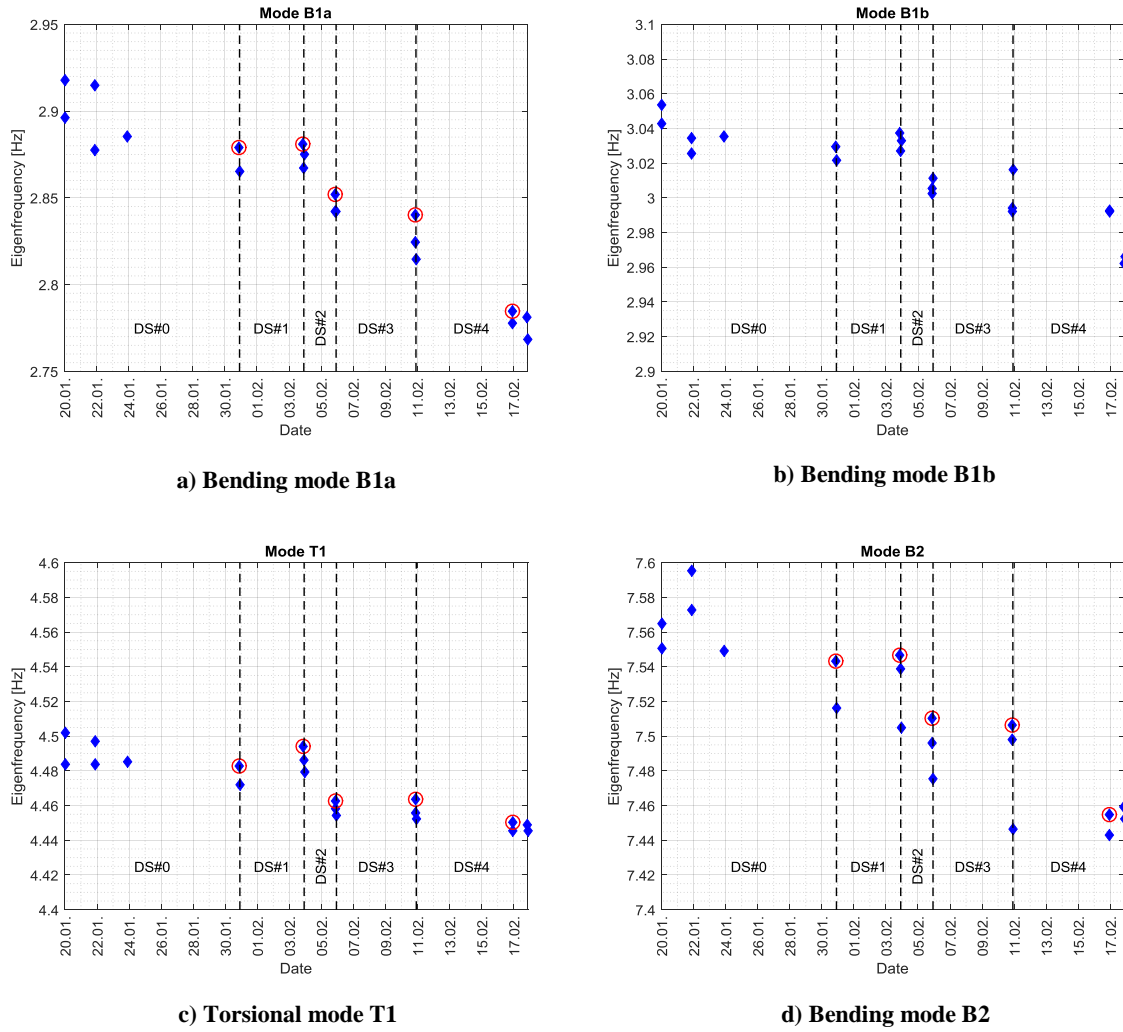
Figure 7.8: Eigenfrequencies vs. time during the tests in the port of Mertert; Measurements used for model updating (cf. Chapter 8) are marked with a red circle

7.3 Mode shapes

7.3.1 Visual comparison of mode shapes

For the beam tested in Mertert, four modes were well identified in the frequency range $2.5 - 15\ Hz$. For the evaluation in this chapter, one dynamic measurement was selected for any of the 5 damage scenarios DS#0 to DS#4 as listed in Table 7.1. The resulting modes for the reference state DS#0 are listed in Table 7.2.

Table 7.1: Dynamic measurements selected for evaluation

DS#	Date	Time (local UTC+1)
0	31/01/2014	11:28:18
1	04/02/2014	11:00:26
2	06/02/2014	11:10:09
3	11/02/2014	10:56:52
4	17/02/2014	12:03:24

Table 7.2: Modes identified in DS#0 (Measurement at 31/01/2014 11:28:18)

Eigenfrequ. [Hz]	Abbreviation	Description
2.88	B1a	Bending mode
3.03	B1b	Bending mode
4.48	T1	Torsional mode
7.54	B2	Bending mode

After scaling the mode shapes to unit modal mass (UMM), their components became nearly pure imaginary, as it shown in Figure 7.9. Here the complex components of the mode shape vectors were plotted as pointers in polar coordinates, whose length is the magnitude of the complex numbers and whose angle to the horizontal axis is the argument. The different modes are marked by different colours. One can see that for all components the real part is small compared to the imaginary part. Therefore, for the following drawings of the mode shapes and their derivatives, only the imaginary part was considered, in order to avoid travelling phase pattern.
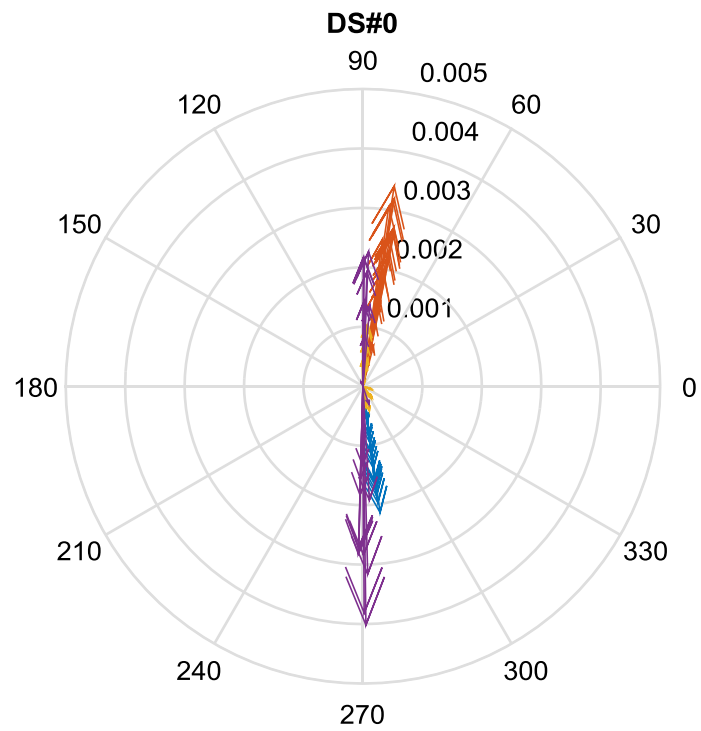
Figure 7.9: Complex components of UMM-mode shapes in DS#0, plotted as pointers in the Gaussian plane
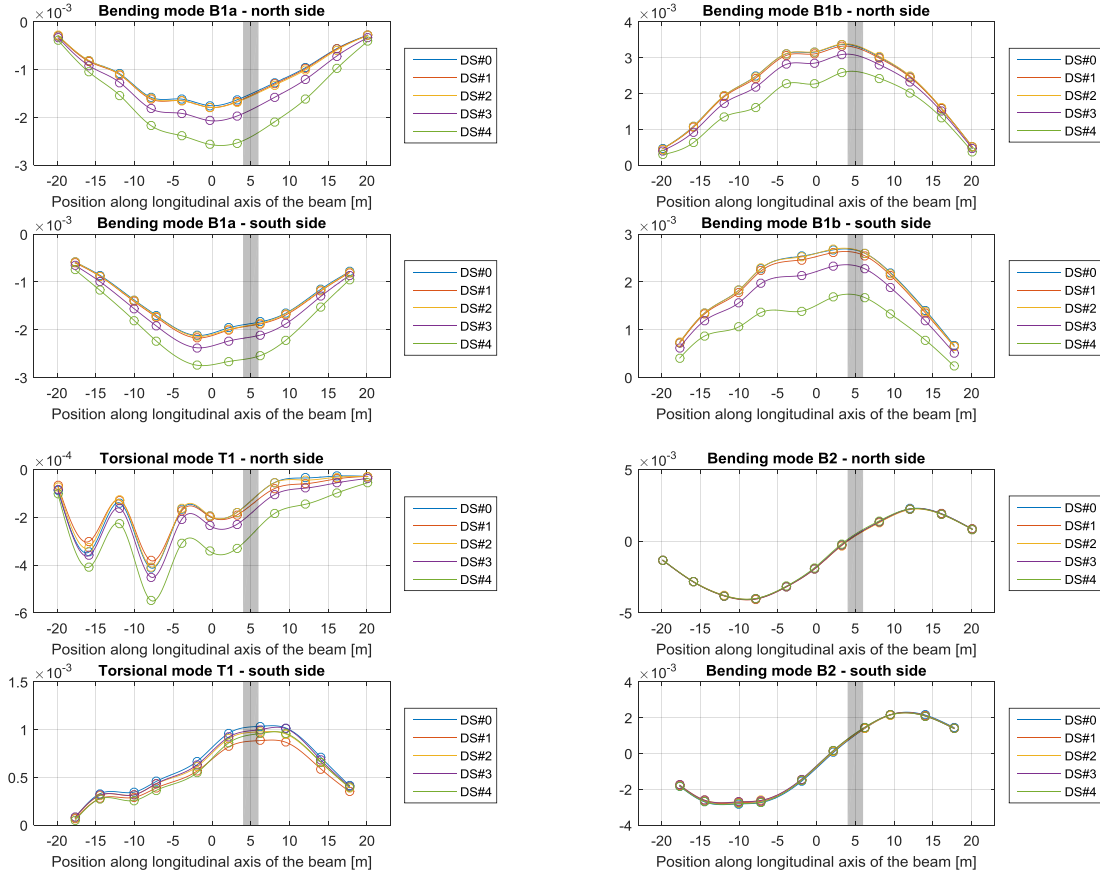
Figure 7.10: Cubic spline interpolated UMM-mode shapes separated in the north and the south side of the beam for each damage scenario; The markers show the actually measured values, which are the imaginary parts of the mode shape components. The damage location is marked by grey shading.

First of all, it is necessary to mention that B1a and B1b were coupled modes, because their frequencies and shapes are quite similar. Furthermore, it can be deduced from Figure 7.10 that the shapes for mode T1 were not well identified. A reason for this bad identification could be that most of the accelerometers were located too near to the web of the beam that did not facilitate a clear identification of torsional modes. For DS#0-DS#2, all mode shapes show very small differences, so it is difficult to recognise the damage until DS#2. Actually, the shapes of B2 show no visible changes for different damage scenarios. Only from DS#3 onwards really significant differences in the shapes can be seen. In this damage scenario vertical cracks occurred for the first time during the static loading. The severity of the damage can be assessed qualitatively from the magnitude of the changes but a localisation of the damage is not possible.

In the next step, the first and second derivatives of the mode shapes were determined by the procedure used in Chapter 7.1 for the static deflections. First a cubic spline interpolation was

performed using the measured values as anchor points and subsequently the slopes and curvatures of these splines were calculated.
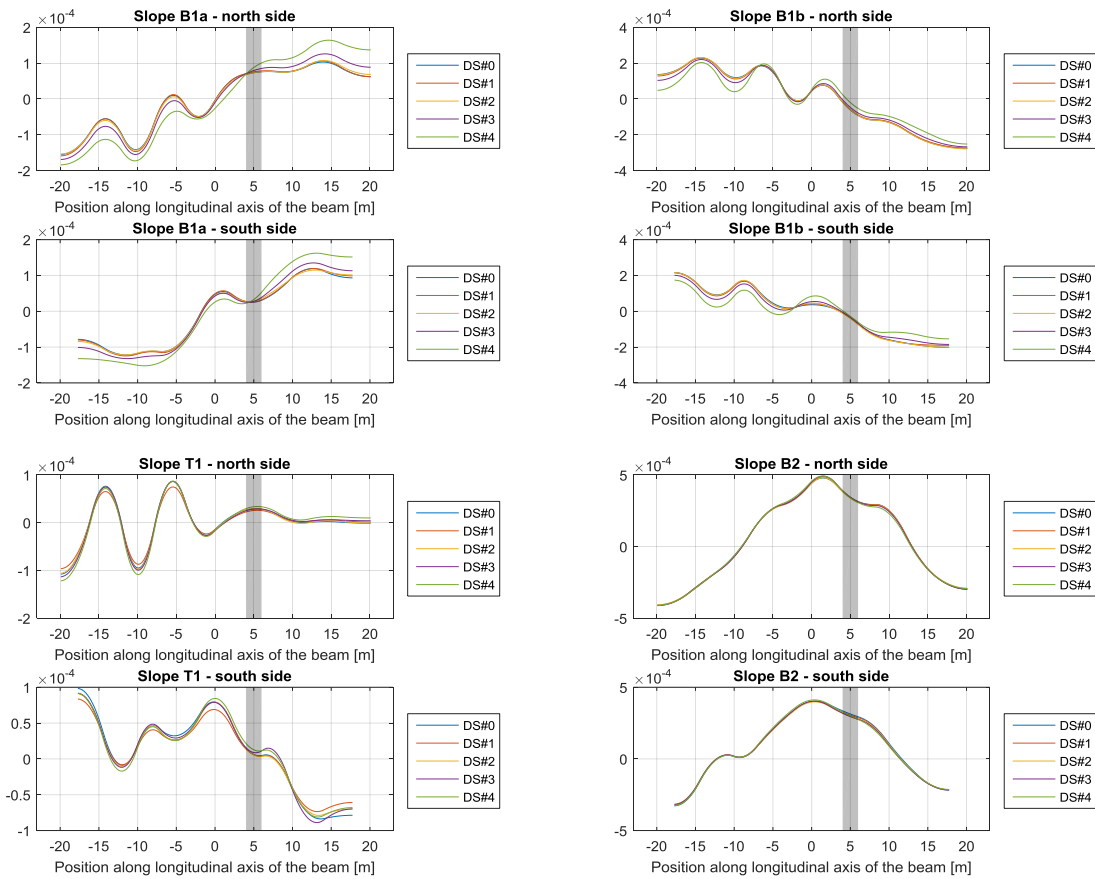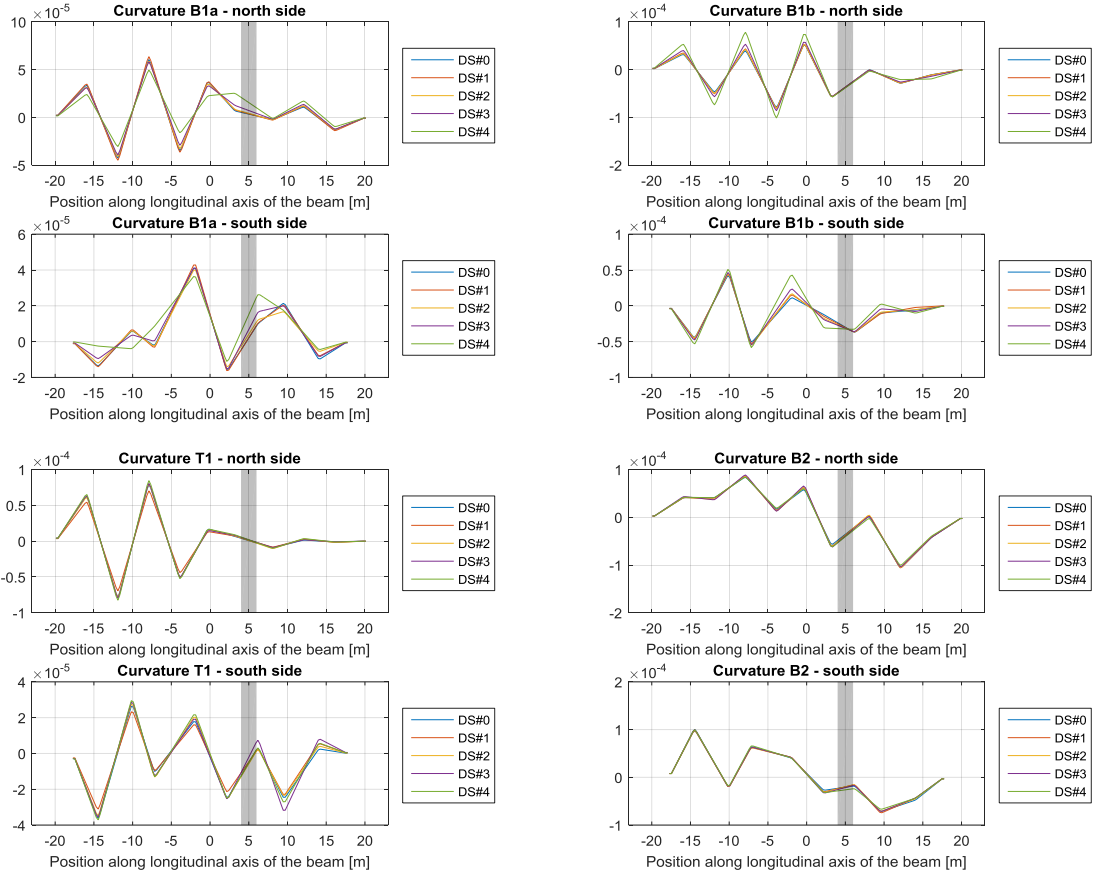

Figure 7.11: First numerical derivative (slope) of the UMM-mode shapes separated in the north and the south side of the beam for each damage scenario; The damage location is marked by grey shading.

The result of damage detection using the slopes is quite similar as for the mode shapes themselves. From DS#3 on, when first vertical cracks appeared, significant changes can be seen in the first derivatives. The changes are larger for DS#4 than for DS#3, which shows the more severe damage in DS#4. Since the mode shapes of B2 are already quite similar for all damage scenarios, of course the slopes show no changes, too.

The curvature does not give more interesting information on behalf of damage detection. A real significant change can only be seen for DS#4 and the differences do not occur at damage location.

Figure 7.12: Second numerical derivative (curvature) of the UMM-mode shapes separated in the north and the south side of the beam for each damage scenario; The damage location is marked by grey shading.

7.3.2 Comparison of mode shapes by correlation methods

Correlation methods for comparing mode shapes as described in Chapter 4.5 are also considered. While the explanations in Chapter 4.5 refer to the comparison of measured to simulated mode shapes, measured mode shapes are compared with a reference measurement in the following.

First the Modal Assurance Criterion (MAC) and the Normalised Modal Difference (NMD) according to equation and (4-34) and (4-38), respectively, will be used.

When comparing mode shapes, the MAC provides values between 0 and 1 where 1 means perfect matching, while for the NMD lower values shows better match. In opposition to the MAC, the NMD is not limited by 1.

20 dynamic tests covering the entire time period, in which the test setup was built up, were chosen from all performed tests. The changing in the measured mode shapes over time is monitored by calculating the MAC and the NMD values between all later measurements and the first one that was taken in the undamaged state DS#0, i.e. 19 out of 20 measurements

were compared to the first one. The modes listed in Table 7.2 were evaluated for this comparison.

Figure 7.13 shows the development of the MAC- and the NMD-value, while the test beam was stepwise artificially damaged in the scenarios DS#1 to DS#4. Since the properties, especially stiffness, of the structure change, it can be assumed that there are also changes in the mode shapes, so the MAC values should decrease, while the NMD-values should increase. The calculated correlation values are shown in a scatter diagram, i.e. as individual points. Linear regression lines were added for every mode, for a better visibility of the trend.
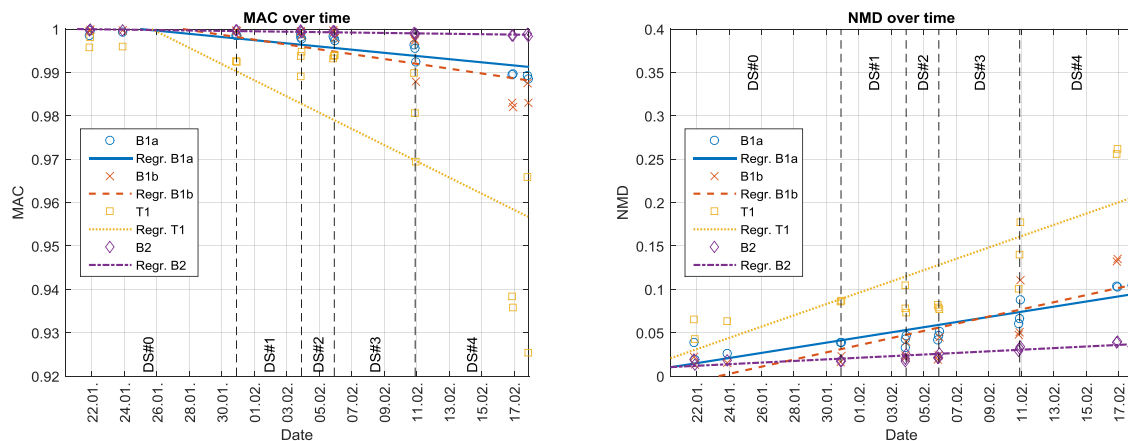
Figure 7.13: MAC- and NMD-values of 4 measured modes

As expected, it can be noticed that the MAC values decrease over time. The regression line for the torsional mode T1 shows the highest slope, but the variance of the determined values is very high for this mode. The bending mode B2 shows the lowest change in the MAC-values. This fits the result in Chapter 7.3.1, where this mode shape does not show any changes in the different damage states. As already revealed, it resides in the fact that the damage was located too near to a node of the mode shape B2 to be reflected in the shape.

Similar conclusions can be drawn for the NMD-values. Here even the values for mode B2 show a clear increasing trend similar to the other modes. This supports the assertion of Mordini et al. in [44] that the NMD-value is more sensitive than the MAC-value for changes in highly correlated mode shapes, i.e. quite similar ones.

As mentioned in Chapter 4.5, the MAC together with the Modal Scale Factor (MSF) describe a linear relationship between the compared mode shapes. Hence, in order to complete the comparison the MSF should be considered, too. Therefore, the same evaluation as described for MAC and NMD was performed for the MSF. Beforehand, all mode shapes were

normalised to unit modal mass, so a MSF-value of 1 means a good correlation. Therefore, in the following diagrams the difference MSF-1 is plotted.
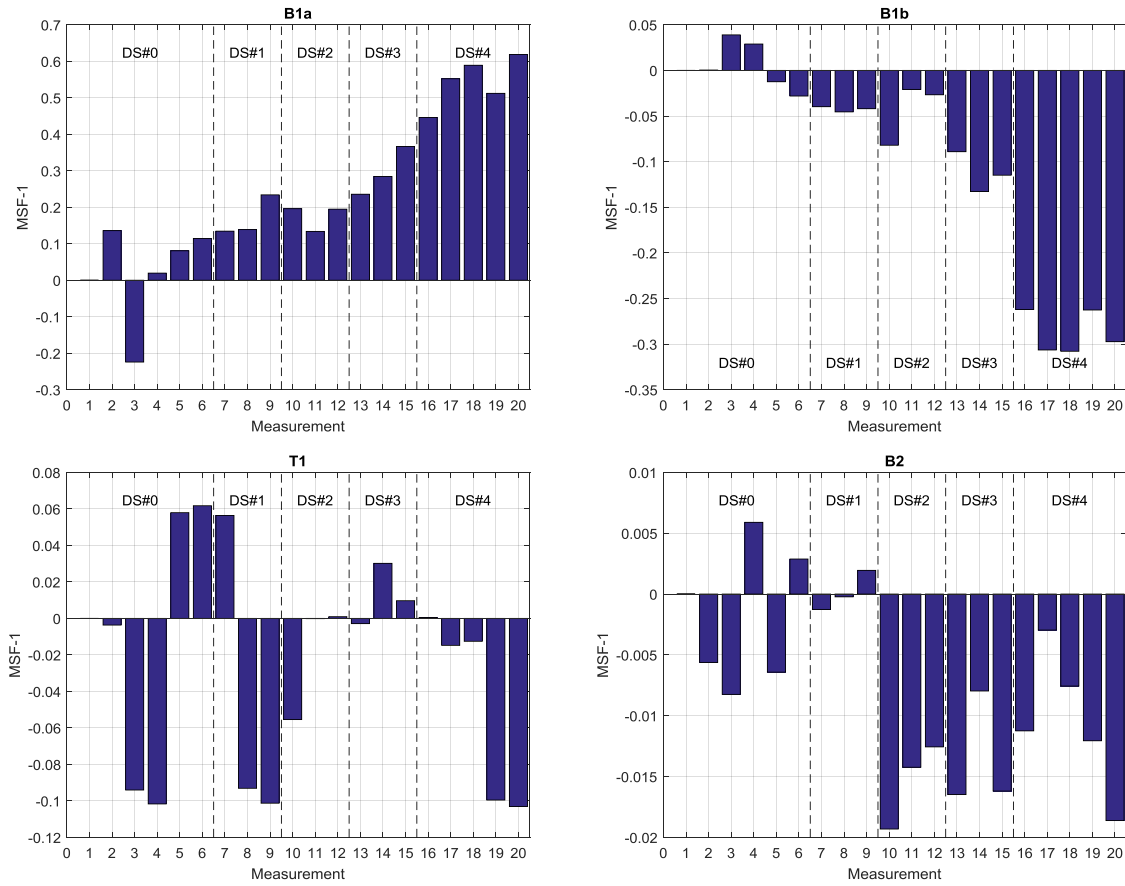

Figure 7.14: MSF values for 20 measurements using the first one as reference

For the bending modes B1a and B1b the differences of the MSF values to 1 clearly increase while the beam is more and more damaged. With these results it would have been possible to detect the change of the structure due to the damage. Only the torsional mode T1 does not show distinct trend. But this was expected, since the shapes for mode T1 were not well identified (cf. Figure 7.10). For the higher bending mode B2 a clear change in the mode shapes can be detected from DS#2 on, but a quantification of the damage is not possible. Furthermore, the absolute values of MSF-1 for B2 are one order of magnitude smaller as the ones for B1a and B1b. This corresponds to Figure 7.10, where no visible difference can be seen in the B2 mode shapes in the different damage scenarios.

Although the authors in [64] state, that the method shall be used in a free-free setup, the Coordinate Modal Assurance Criterion (COMAC) according to equation (4-43) is here evaluated, for the purpose of damage localisation. For the sake of clarity, not all 20 measurements were considered here as in the evaluation of MAC, NMD and MSF, but one

measurement was selected for each damage scenario. The same measurements were used as already in Chapter 7.3.1 for the visual comparison, which are listed in Table 7.1. The measurement chosen for DS#0 was used as reference. Beforehand, all mode shapes were normalised by scaling to unit modal mass, since the COMAC is sensitive to the normalisation.
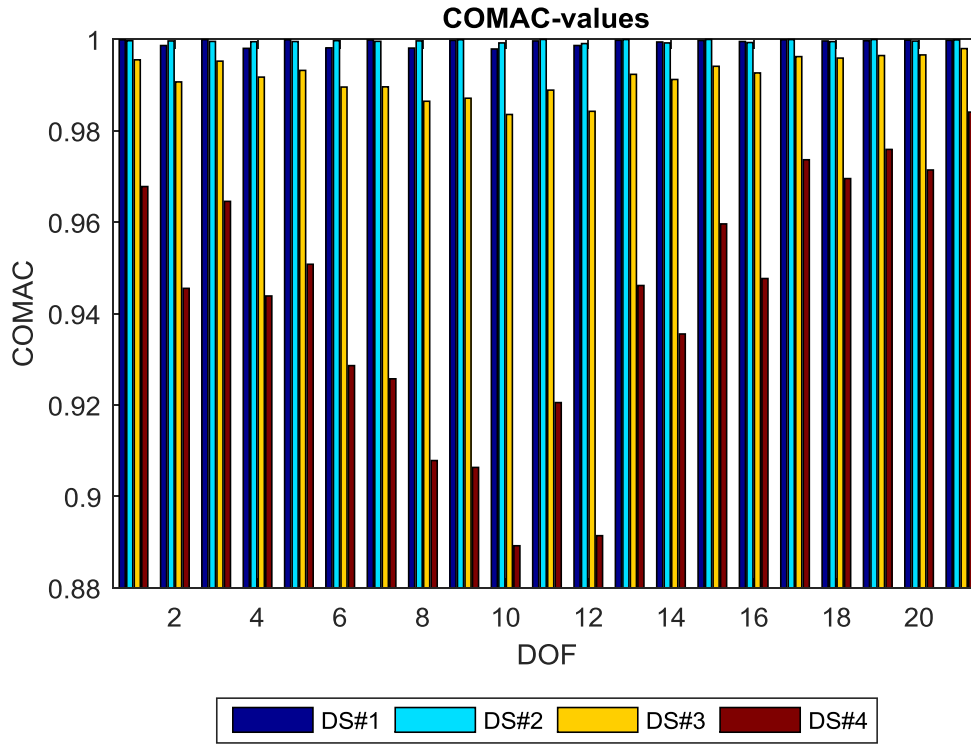

Figure 7.15: COMAC for damage scenarios DS#1-DS#4 based on modes B1a, B1b, T1 and B2

The result in Figure 7.15 shows the highest decrease in the COMAC value from DS#1 to DS#4 in DOF 10, while the damage was located between DOFs 8 and 9. Based on only the information from the COMAC, the damage can be located between DOF 8 to DOF 12, which is a range of about $8\ m$. The damage can be localised from DS#3 on, in which first vertical cracks appeared.

7.4 Flexibility

As it was described in Chapter 4.2, it is possible to calculate the inverse stiffness matrix, also called flexibility matrix, based on the dynamic properties of the system. These properties can be obtained by an experimental modal analysis explained in Chapter 4.4. If N DOF were measured, a $N \times N$ flexibility matrix $[\mathbf{F}]$ will be obtained. Each component F_{ij} of this matrix

is the displacement at DOF i if a unit force is applied to DOF j and vice versa. A complete modal model of a N-DOF system consists of N modes, but as elucidated in Chapter 4.2 it is possible to obtain adequate results for $[\mathbf{F}]$ even with a lower number of modes. But in this case the resulting matrix will be singular and hence the stiffness matrix cannot be calculated by an inversion. In most cases it is not possible to obtain all necessary modes by experimental measurements. Since damage detection can be performed by searching for stiffness reductions, the stiffness matrix would be highly appropriate for this purpose. Theoretically, it would be possible to obtain a stiffness matrix by including fewer DOFs in the calculation. But this would reduce the local resolution for the damage localisation.

Alternatively, the article by Schommer, Mahowald et al. (2017) [74] investigates the applicability of a dynamically measured flexibility matrix for the localisation of damage in concrete bridges. The method is there initially tested theoretically using FE models. Subsequently, measurements on real bridges, carried out by Jean Mahowald in the course of his dissertation (2013) [3], are used. The approach thus corresponds to the approach of Pandey and Biswas in [13] and [14], with the difference that here the method was validated with in-situ measured data at real bridges under real environmental conditions. It was shown in [74] that, depending on for instance the bearing conditions and the location of the damage, it is possible to directly use the flexibility matrix for damage detection.

Here it was tested, if this approach also works based on the measurements at the beam in the port of Mertert. The beam's flexibility was calculated for the different damage scenarios. As for the previously described evaluations, the measurements, which are listed in Table 7.1, are considered again. The flexibility was calculated based on the identified modes given in Table 7.2. The performed modal analysis yielded the mode shapes together with the appropriate scaling factors Modal A and Modal B. Hence, for the calculation of the flexibility matrix the general formula given as equation (4-22) was used. Here, the eigenvalues were not provided directly as results of the modal analysis, but could be calculated according to equation (4-20) based on Modal A and B.

At first in Figure 7.16, the flexibility matrix calculated for the first considered measurement in DS#0 is plotted. During the calculation, the order of the DOFs was altered in way that the sensors, which were located at the north side, are separated from the ones at the south side. Therefore, the DOF-axes show first the uneven DOF numbers and the even ones. Figure 7.16a shows the matrix as 3D surface plot, while Figure 7.16b shows the diagonal elements as well as the contributions by the different considered modes. As magnitude of the

eigenvalue, the eigenfrequency appears in the denominator in equation (4-22). Hence, as higher the eigenfrequency as lower is the contribution of the corresponding mode to the flexibility matrix. Here the contribution of B2 and T1 is already lower as the contribution of B1a and B1b.
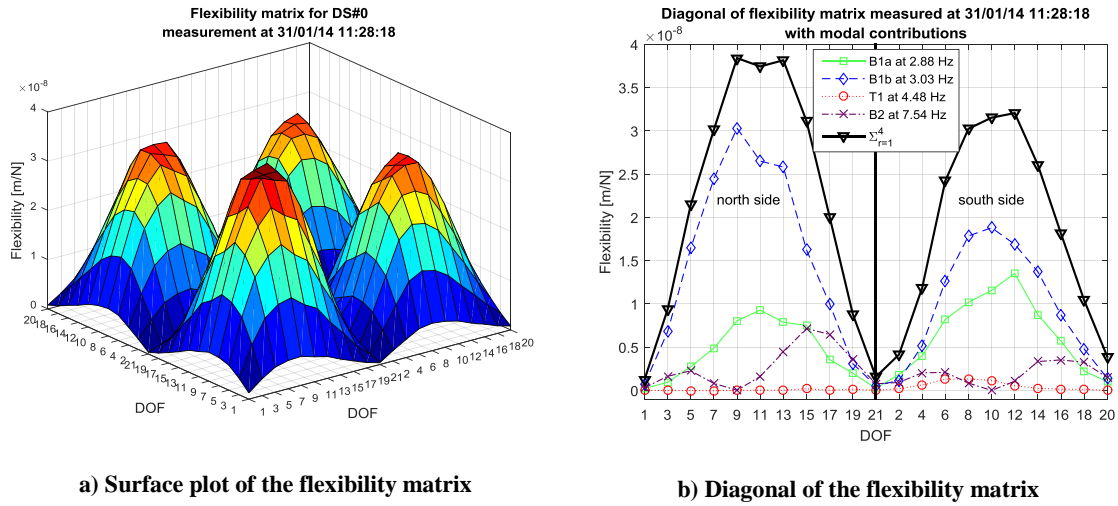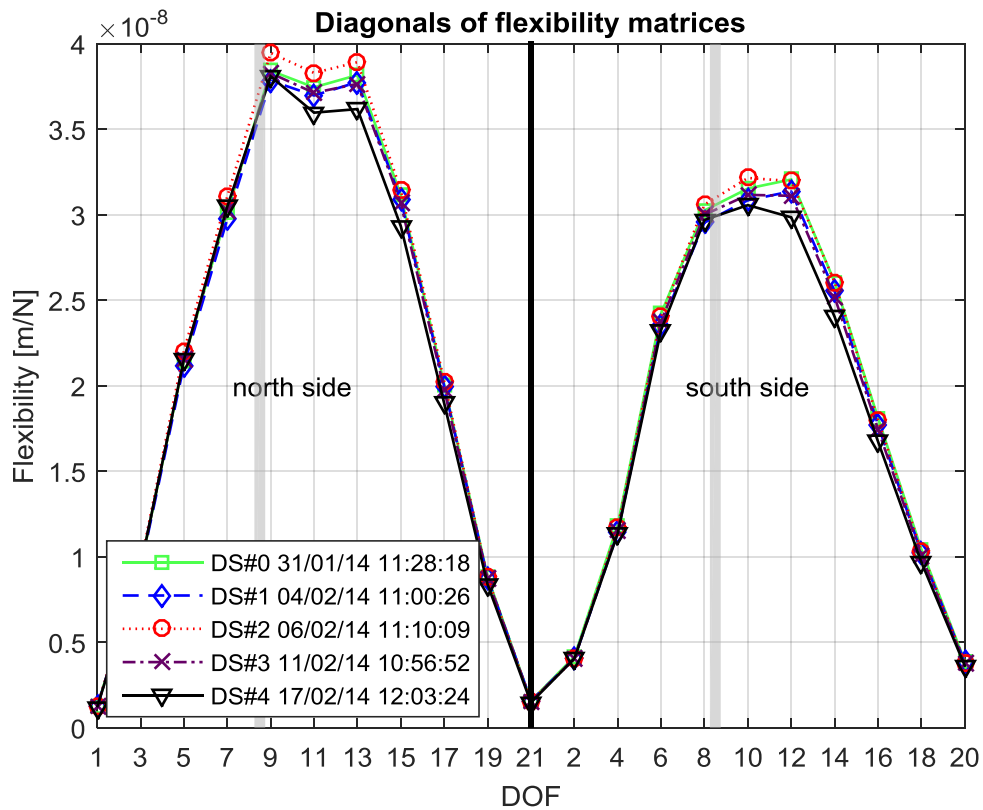

a) Surface plot of the flexibility matrix

b) Diagonal of the flexibility matrix

Figure 7.16: Flexibility matrix for DS#0

Figure 7.17: Diagonals of flexibility matrices for the damage scenarios DS#0 to DS#4

Now, in order to compare the flexibility in the damaged states DS#1 to DS#4 to the flexibility in the healthy state DS#0, the absolute as well as the relative differences of the individual matrix components F_{ij} were calculated according to the following equations (7-4) and (7-5).

$$abs\Delta_{ij} = {}_{ij}F_{damaged} - {}_{ij}F_{undamaged} \tag{7-4}$$

$$rel\Delta_{ij} = \frac{{}_{ij}F_{damaged} - {}_{ij}F_{undamaged}}{{}_{ij}F_{undamaged}} \cdot 100\% \tag{7-5}$$

The flexibility for DOFs near the bearings is very low compared to the other DOFs. The relative difference for these DOFs becomes very high due to the division by a small value. During the calculation of the relative differences, these high values were filtered out by omitting components of the flexibility matrices, which absolute values were lower than 5% of the highest occurring flexibility in the matrix.

In order to visualise the results, the diagonal elements of the difference matrices were plotted in Figure 7.18. As can be seen in Figure 5.8, the artificial damage was located between DOFs 8 and 9. This position is marked in the following diagrams by grey shading.

a) absolute differences   b) relative differences
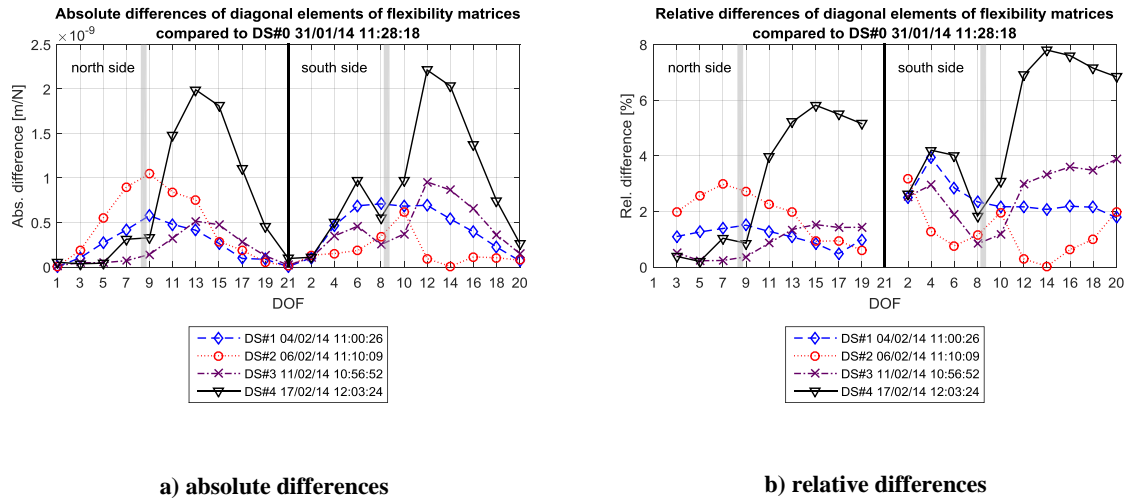
Figure 7.18: relative and absolute differences of the diagonal elements of the flexibility matrices in the different damage scenarios

The idea is now to locate the damage by searching for high differences in the flexibility. At the north side this works for DS#1 and DS#2 with the relative as well as the absolute differences. At the south side it works only for DS#1. For the other cases the maxima of the curves appear at different locations. Furthermore, the calculated differences in DS#1 and DS#2 are already as high or even higher as the ones in DS#3. Hence, the severity of the

damage cannot be assessed. Unfortunately, the conclusion is here, that the approach does not really work for the case at hand.

7.5 Conclusion

During the usual static load testing on bridges the deflection of a bridge is measured before, during and after the load, typically with optical measuring methods (levelling). The test weight and its distribution on the bridge are known. The deflection due to the load can then be determined from the difference between the measurements in the loaded and the unloaded state. The absolute deformations which also occur over longer periods compared to a fixed reference point are usually not determined nowadays. This is mainly because it is difficult to define such a fixed reference point, especially for bridges, which cross waters.

In the present test setup, the static displacements were measured with respect to the soil, which was assumed as rigid. Therefore, it was not only possible to detect the deflection due to the test loads, but also the absolute deformations. These deformations became larger during the test period. The increasing downward movement of the beam caused purely by its own weight, the additional dead load and the weight of the shaker, so when the tests loads were removed, are referred in the present thesis as the sagging of the beam. The deformation due the test load in loading #4-L2 is much lower than in the preceding loading #4-L1. This is because the deformations, in #4-L1 includes plastic deformations, which are no longer present in the following loading in the same damage scenario. The plots of the deformation curves as well as their slopes and curvatures indicate clearly the location of the damage. Even an assessment of the severity of the damage is possible to a certain extent.

Furthermore, the decrease of the eigenfrequencies with increasing damage was clearly evident, although some measurements show a small increase. The latter was explained by the standard deviation of the measurements.

All dynamic measurements were carried out in the unloaded state, when the test load of 26 t was removed. That's why any cracks that occurred during the static tests had been partially or completely closed by the prestress. Only from DS#3 onward, where already 6 tendons had been cut, visible vertical cracks appeared which remained open even after the unloading. Accordingly, only from this point in time, significant differences in the mode shapes and their derivatives can be observed. The visually detected differences for the lower damage levels must be attributed to measurement inaccuracies. The shape of bending mode B2 seems not to be influenced by the damage. A possible explanation is that the damage was located too close

to the node of this mode shape to be detected. Peaks or steps in the course of the derivatives in the vicinity of the damage location cannot be determined. Obviously, a localisation of the damage is here not possible. One conclusion is that the accuracy of the measured mode shapes was insufficient for the purpose of damage detection.

When evaluating the MAC and NMD values, a clear change over time can be observed allowing damage detection. If considering B1a and B1b the same can be said for the MSF values, while this criterion worked not well for T1 and B2. Since these criterions provide only global information, i.e. only one number over all DOFs, a localisation is not possible.

In opposition, by the COMAC that provides information for individual DOFs, the damage can be localised within a range of 8 m, but only after the appearance of visible vertical cracks.

Although the evaluation of the modal flexibility allows damage detection for some other bridges (cf. for instance [74]), here the results were inconclusive. This is explained by the insufficient accuracy of the identified mode shapes.

8 MODEL UPDATING

8.1 Objective

In a real bridge, tendons can fail in the course of time for example due to corrosion or fatigue, resulting in a loss of prestress. In Chapter 5.1, a test setup for performing measurements on a prestressed concrete beam is described. This beam was artificially damaged with pre-defined scenarios in order to simulate an aging process with the failure of several tendons. Actually, 5 damage scenarios DS#0 to DS#4 were realised, all including static load tests as well as dynamic measurements. DS#0 represents the undamaged reference state. The reduction of prestress due to damaged tendons leads to higher tensile stresses in the cross-section during loading, as it was explained in Chapter 5.2. Starting at the excess of the tensile strength of the concrete, vertical cracks occurred in the beam. First visible vertical cracks appeared in DS#3 during the static tests, in which 6 tendons had been cut. The application for the considered prestressed concrete beam is resumed below.

In the present chapter, a model updating procedure based on a parameterised FE model of the test setup is described, with the aim of detecting the damage based on the collected measurement data. The approach corresponds to the procedure described in Chapter 4.6.

At first, it is necessary to define what parameters should be used and then to implement them in an FE model, in order to simulate the damage. Ideally, these parameters have physical meaning that can be interpreted accordingly. Based on these, a correspondingly parameterised FE model can be created. This model must match as far as possible to the test setup in the undamaged state. This means that it must be validated by the data measured in the initial state DS#0, i.e. the simulation results must match the real measurements as much as possible.

Secondly, at least one objective function is defined, which provides a value that stands for the deviation between measurement and simulation. This function depends on the selected parameters. The smaller the objective value, the better the correlation. In the subsequent model updating, the parameters are set in a way that the simulation results match the measurements in every damage scenarios. This setting can be carried out by an optimisation algorithm or less automatically, e.g. by means of a parameter study.

Afterwards, the updated models are compared to the reference model to identify structural change. Either the parameters' values themselves or properties of the model, which have been influenced by them, can be compared. For instance the stiffness matrices of the models can be compared as damage in a bridge usually relates to a local stiffness decrease. Theoretically, after the model updating, simulated results should be in good agreement with measured results, if the stiffness in the model was reduced at the same degrees of freedom and to the same extent. A decrease in individual components of the stiffness matrix for the updated model can thus be an indication of damage in the real structure.

8.2   FE-model and parametrisation

The idea pursued here is to use model updating to search for local stiffness reductions in the investigated beam. Therefore, the parameters should simulate such stiffness reductions in the model.

The vertical cracks, which appeared during a static loading, reduced the bending stiffness EJ of the beam because the supporting cross-section was reduced, i.e. in reality the area moment of inertia of the cross-section J decreased. In an FE model, it is usually more convenient to locally reduce bending stiffness by simply reducing the Young's modulus E of individual elements, i.e. the material properties are modified instead the properties of the cross-section. The approach that first comes to mind would be to parameterise the Young's modulus of each individual element. Except for very simple models, this leads to a vast number of parameters, to be optimised, so that a model updating can no longer be reasonably performed. Regardless of whether a parameter study or an optimisation algorithm is used to solve this task, the computing effort would be far too high and a practical use of the method would be unthinkable.

Two approaches were used to reduce the number of parameters. Firstly, elements were combined into groups whose Young's modulus was uniformly changed. In order to allow a meaningful definition of these groups, a mapped mesh was created for the FE model.

An approach proposed by Teughels et al. [36] was applied to further reduce the number of parameters. "Damage elements" can be created by combining several of the aforementioned element groups. Young's modulus of these damage elements along the longitudinal axis of the beam is defined and is called "damage function". This function is defined by only a few parameters which are then used for model updating, based on an FE-model of the test setup. This approach is better understood with the actual model, which hence will first be described.

The model was created within the software ANSYS (ANalysis SYStem 17.0). The possibility to use scripts in APDL (Ansys Parametric Design Language) to control the system was extensively taken advantage of. As the name of this programming language indicates, its main purpose is to create parametric models corresponding to the task. Furthermore, these scripts allow to extract and to store certain results after a simulation run, as well as to implement batch processing in order to carry out automatically a large number of simulations. Therefore, a variant of the system often referred to as ANSYS Classic, which can be controlled completely via APDL, was used. This approach provides the possibility to control the model design very precisely, for instance on the type of elements used for the meshing of the geometry and on their properties.

Of course in reality, there are always nonlinearities which were investigated, for example in prestressed concrete bridges by Waltering [1]. The intention here is to use an FE model that is purely linear for an approximation, i.e. whose stiffness matrix does not depend on deformation or other variables, such as temperature. This was mainly due to the fact that the computation time for a simulation should be kept as low as possible, because the optimisation was believed to require an important number of simulation runs. Hence only linear-elastic material models were used in this study. Furthermore, when using contact conditions their properties were defined in a way that no nonlinearities were caused in the model. For instance, if contact elements were used, the option "always bonded" was set, i.e. the elements are fixed to each other so linearity is maintained.

A volume model of the test setup was created, with mainly so-called solid elements. Table 8.1 lists all types of elements used in the model. Column 'Type' corresponds to the designation in ANSYS and 'Type No.' is the numbering assigned in the model.

Table 8.1: Types of elements used for the FE-model in ANSYS

Type No.	Type	Description	Number nodes	Usage	important Options
1	SHELL281	Structural Shell	8	2D Elements for mapped meshing of areas and subsequent extrusion to a 3D mesh	
2	SOLID186	Structural Solid	20	Hexahedral elements for mapped meshing	Sometimes used as tetrahedral- or as pyramid-shaped elements
3	BEAM188	Beam	2	Beam elements for the tendons	Timoshenko beam theory
4	CONTA174	Surface-to-Surface Contact	8	Contact definitions	MPC algorithm, Bonded (always)
5	TARGE170	Target Segment	up to 8	used as target segments for CONTA174 elements	
6	BEAM188	Beam	2	Dummy-Beams to connect the tendons to the concrete	Timoshenko beam theory
8	MASS21	Structural Mass	1	point mass for shaker	
9	SOLID285	Tetrahedral Structural Solid	4	Solid elements without midside nodes; Originally intended for free meshes in less important areas, but in later versions replaced by tetrahedral form of type 2	
10	CONTA174	Surface-to-Surface Contact	8	Contact definitions (to be able to set different contact definitions in different areas)	MPC algorithm, Bonded (always)
11	SOLID185	Structural Solid	8	same as Type No. 2 but lower order element for less important areas	
12	SHELL181	Structural Shell	4	2D Elements for mapped meshing of areas without midside nodes	
14	LINK11	Linear Actuator	2	intended for springs at the bearings but not used in the final version	
15	MPC184-Revolute	Multipoint Constraint Element, Revolute Joint	2	to model a revolute joint at the sliding bearing	
16	MPC184-Planar	Multipoint Constraint Element, Planar Joint	2	to model a planar joint at the sliding bearing	

Local stiffness losses due to cracks can be stimulated by reducing the bending stiffness along the length of the beam. Therefore, the Young's modulus of groups of adjacent elements can be updated. The idea was to dismantle the beam into narrow "slices", whose stiffness is then reduced uniformly. This can be considerably facilitated by using a mapped mesh. Some geometric conditions must be met that allow creating a mapped mesh successfully. Therefore, a considerable effort was put to make this type of meshing possible, inter alia the definition of geometry directly in ANSYS, rather than using a CAD model.

a) Free mesh of tetrahedral elements (SOLID187)	**b) Mapped mesh of hexahedral elements (SOLID186)**
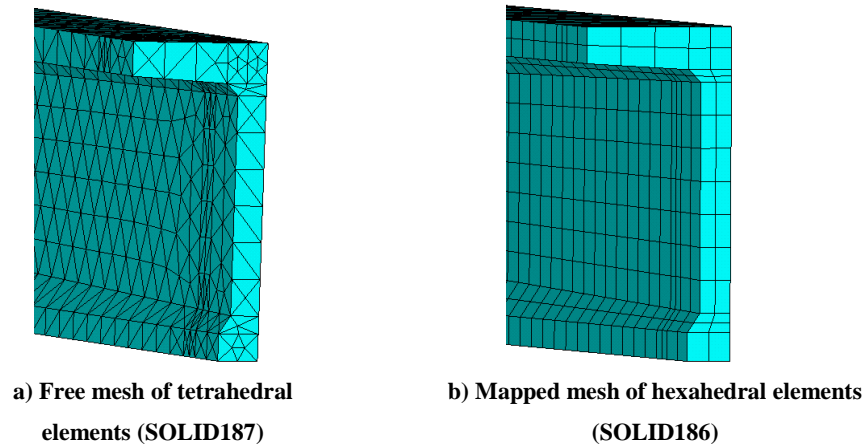
Figure 8.1: Comparison between free mesh and mapped mesh

By using hexahedral "brick" elements for the meshing of the beam, it became possible to define slices of the beam that consists of one layer of elements. For any slice, a material was defined and assigned to the corresponding slice. At the beginning, the properties of these materials were all the same, but during the model updating the Young's moduli were modified. A further advantage of the mapped mesh is that it also reduces the number of elements compared to a free mesh and avoids distorted elements, i.e. the quality of the mesh increases.

Figure 8.2 shows the meshing of the model with solid elements, detailed for the end with the sliding bearing. In this illustration, different materials are presented by different colours, i.e. areas for which the material properties could be set individually. Thus, in this model, the test beam was divided into 227 individual "slices". Although the colours repeat all 11 slices, each slice actually has its own material.
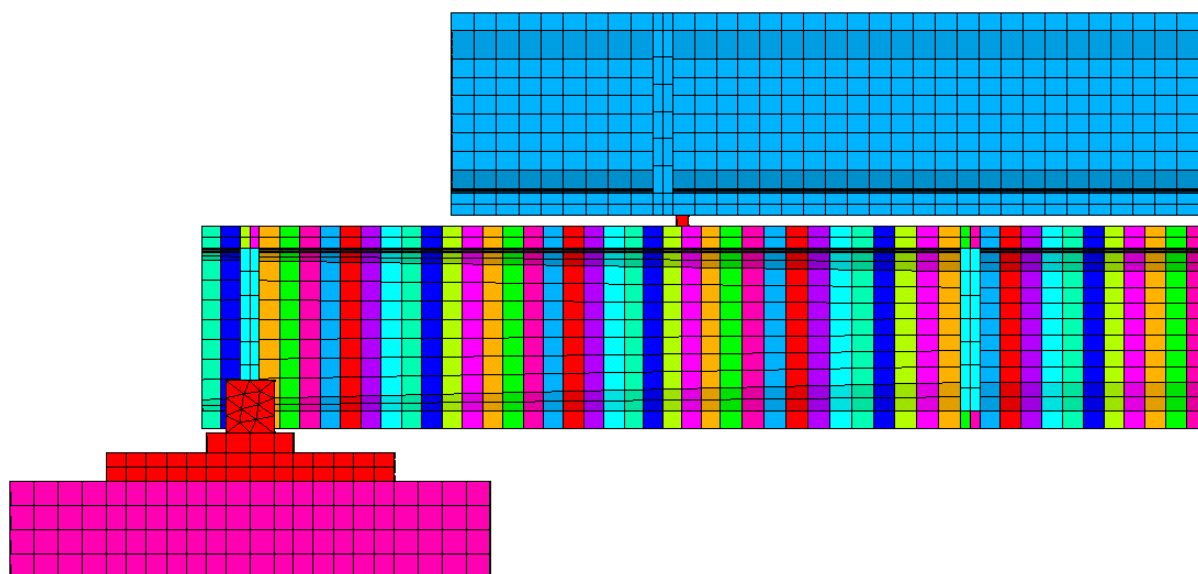
Figure 8.2: FE-model of the test setup with mapped mesh; The colours show different materials

Figure 8.3 shows the meshed cross-sections of two characteristic slices. In the middle of the beam, the centre bar is slimmer than at the ends. Despite this change in the cross-section, the number of divisions along the edges remains the same. The used coordinate system can also be seen on the lower edge. The x-direction points in the direction of the axis of the beam from the fixed to the sliding bearing and the z-direction upwards. The origin is located in the middle of the span between the bearings.

a) Cross-section at the end with the
sliding bearing

b) Cross-section near the middle of
the span between the bearings
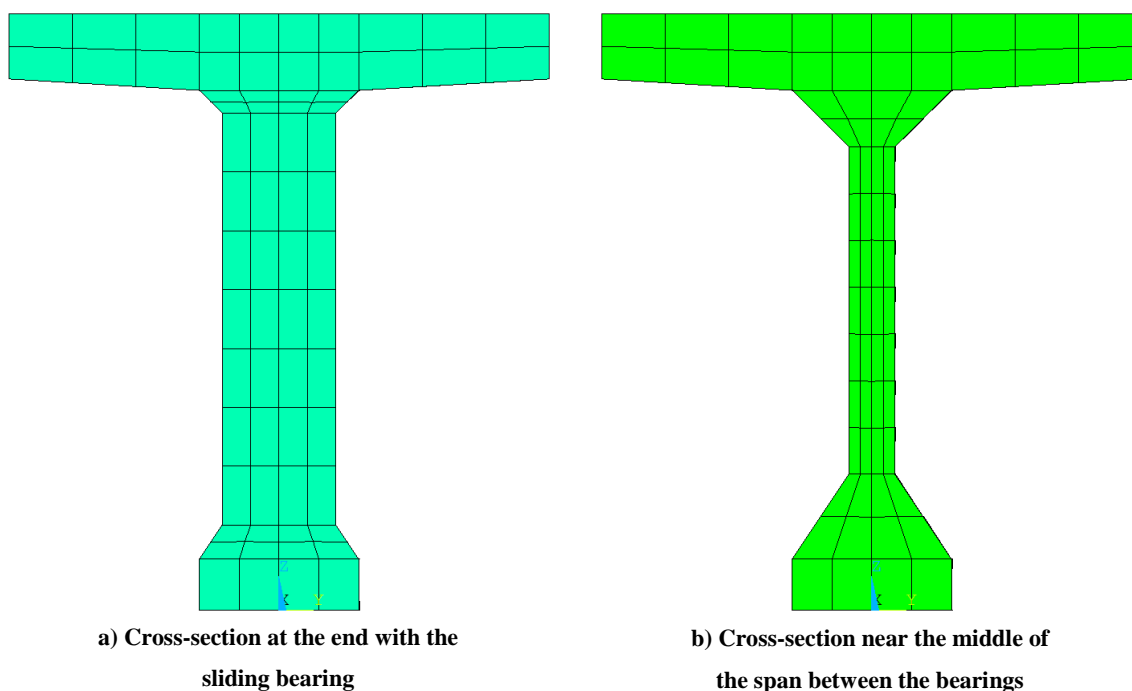
Figure 8.3: Meshed cross-section of the test beam at two different locations

Material properties used for the FE-model are summarised in Table 8.2. As in Table 8.1, the first column shows the numbers given to the materials in ANSYS. Some of the Young's

moduli were set by variables, to be able to change them easily for test purposes as well as parametrisation.

Table 8.2: Material properties used for the FE-model in ANSYS

Mat. No.	Young's modulus [MPa]	Poisson ratio	Density [kg/m³]	Material	Description
1	30000	0.13	2500	Concrete	Concrete for parts of the model, where the Young's model will not be changed during model updating
2	200000	0.3	7850	Steel	Tendons
3	10000	0.2	470	Wood	Wood beams under the loads
4	200000	0.3	0	Dummy	Beams to connect the tendons to the concrete
5 to nsec+4	30000 initially	0.13	2500	Concrete	Concrete for elements, whose Young's modulus will be changed to simulate local stiffness losses; The variable "nsec" is the number of element groups to be modified.
234	20000	0.13	2500	"Fresh" concrete	Material properties used for the newly created bearings and fundations of the test setup
235	30000	0.13	2500	Concrete	Concrete used for the additional dead load on the top of the beam to be able to modify it independently
236	3000	0.13	2500	Soil	Material used for simulated parts of the soil under the test setup

As it can be seen in the previous table, the used Young's modulus for concrete is lower as the one determined by material tests, where $40568\ MPa$ was measured (cf. Table 5.1). During the development of the model, it was found that the simulated deflections fit better to the experimentally determined ones, if the Young's modulus in the model is lowered to $30000\ MPa$. This was explained by the fact that the performed static tests were bending tests at a reinforced and prestressed concrete beam, which induced bending stress with tension on one side and compression on the other side of the beam's cross-section. Since the tensile strength of concrete is very low, this led to micro cracks at the tension side, which reduced its stiffness compared to a specimen in a pure compression test. This effect can be simulated by using a reduced Young's modulus.

The inner tendons were also simulated, which were meshed with beam elements. In reality, each tendon consists of 12 individual round bars with a diameter of 7 mm. They are arranged in a circle and are loosely held in position by a spiral spring. The cables are surrounded by a thin metal sleeve. After the cables were pre-tensioned, they were injected with mortar to

create a stiff and complete contact with the surrounding concrete and to prevent the ingress of water and thus corrosion.
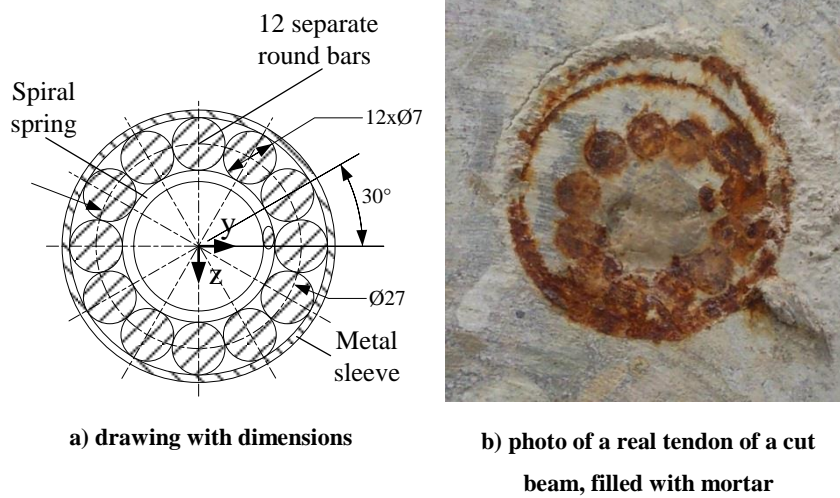

a) drawing with dimensions

b) photo of a real tendon of a cut beam, filled with mortar

Figure 8.4: Cross-section of the tendons

The question arose in which way the cross-section of the tendons should be modelled. In order to keep the number of individual elements small, the actual cable, which consisted of 12 individual round bars (cf. Figure 8.4), can be approximated by a thin walled substitute pipe. The inner and outer diameters of the annular cross-section may be chosen such that it has the same area and axial area moment of inertia as the cross-section of the ensemble of round bars. It was assumed here that the round bars do not move relatively to each other due to the injected mortar. The Steiner ratios of moments of inertia were calculated accordingly. In the following the dimensions of the annular cross-section are calculated.

The dimensions of the real tendons as indicated in the above Figure 8.4 were:

$d = 7mm = 0.007m$ Diameter of an individual round bar

$d_m = 27mm = 0.027m$ Mean diameter of a tendon

Total cross-sectional area of the 12 round bars:

$$A = 12 \cdot \frac{d^2}{4}\pi = 12 \cdot \frac{0.007^2 m^2}{4}\pi = 4.618 \cdot 10^{-4} m^2$$

Axial area moment of inertia of the round bars' cross-section:

$$I_y = I_z = 12 \cdot \frac{\pi d^4}{64} + \frac{d^2}{4}\pi \cdot \left(4 \cdot \left(\frac{d_m}{2} \cdot sin(30°) \right)^2 + 4 \cdot \left(\frac{d_m}{2} \cdot sin(60°) \right)^2 + 2 \cdot \left(\frac{d_m}{2} \right)^2 \right)$$

$$= \frac{1}{8}\pi d^2 \cdot \left(\frac{3}{2}d^2 + 3d_m^2 \right) = 4.35 \cdot 10^{-8} m^4$$

The axial area moment of inertia I_{yp} and the area of the cross-section A_p of the thin walled substitute pipe are:

$$I_{yp} = \frac{\pi}{64} \cdot (d_a^4 - d_i^4) = I_y \tag{8-1}$$

$$A_p = \frac{\pi}{4} \cdot (d_a^2 - d_i^2) = A \tag{8-2}$$

Solving (8-1) for d_a:

$$d_a = \sqrt[4]{\frac{64 I_y}{\pi} + d_i^4} \tag{8-3}$$

Substituting equation (8-3) in (8-2) yields:

$$d_i = \sqrt{\frac{8 I_y}{A} - \frac{2A}{\pi}} = 0.02144m = \underline{21.4mm}$$

Substituting this value in (8-3) yields:

$$d_a = 0.03236m = \underline{32.4mm}$$

Thus, an annular cross-section with the inner diameter d_i and the outer diameter d_a, as calculated above, was chosen for the tendons in the FE model.

In the next step the interconnection between the tendons and the surrounding concrete was modelled in a simple and linear manner. Several different possibilities were extensively tested in ANSYS Classic as well as in the newer version ANSYS Workbench. Attempts were carried out to find a compromise between computing effort and realistic representation.

Finally, node-to-node connections were created by inserting additional dummy beam elements in order to connect the tendons to the surrounding concrete elements. These additional elements had the material properties of steel like the tendons, but a density of zero, so that they add no mass to the system. Since the used solid elements had only 3 translational degrees of freedom at each node, the rotational degrees of freedom of the beam elements remain free in such a connection. This was resolved here by connecting each node of the tendons to the 3 nearest neighbouring nodes of the concrete elements. By this multiple connection, moments can be transmitted between the connected elements.
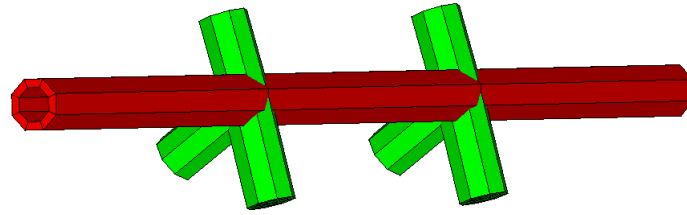
Figure 8.5: Part of a tendon (red) with additional dummy beam elements (green) connecting it to the concrete
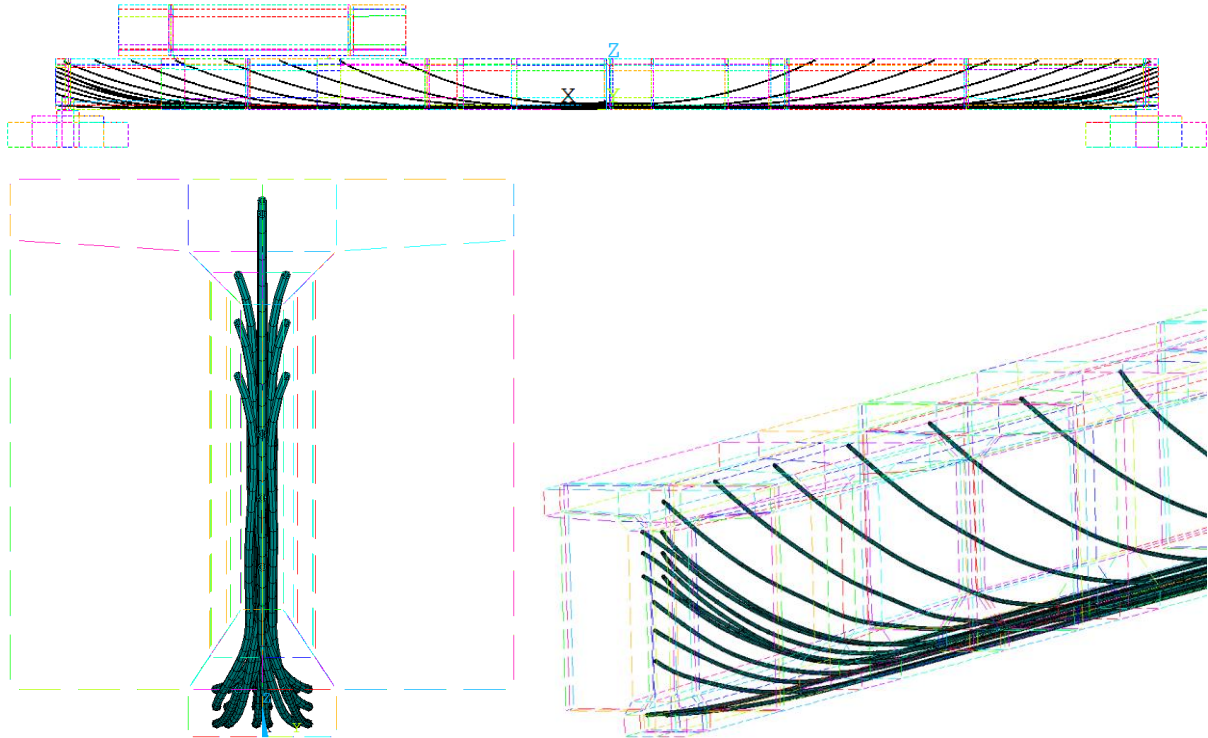
Figure 8.6: Internal tendons inside the test beam

After completion of the FE mesh for the test beam, the permanent additional dead load was also modelled. This was at site cut from the second beam in the port of Mertert and then placed on top of the test beam. Basically, the same procedure was used in ANSYS. The FE mesh of the test beam with its underlying geometry was first replicated and then parts that were not necessary for the additional load were deleted. After some further modifications, the resulting mesh was positioned over the top flange of the main beam, as presented in Figure 8.7.
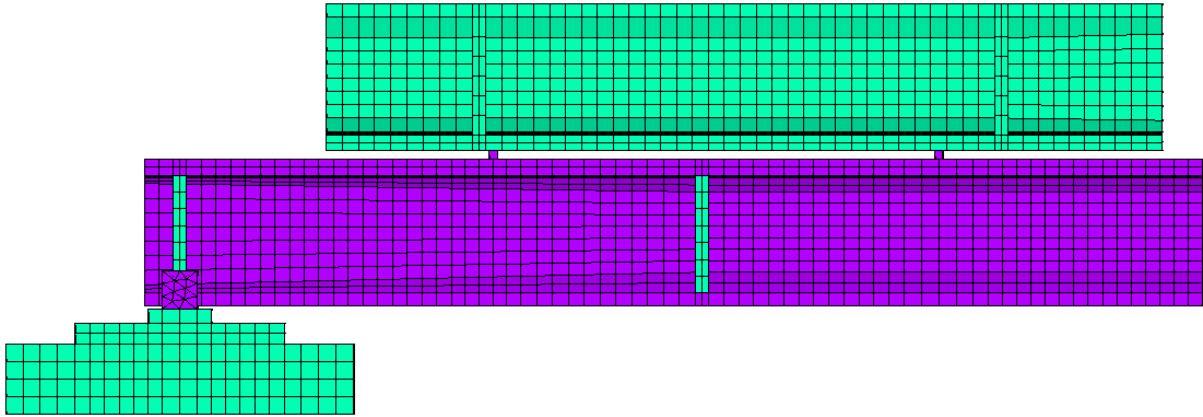
Figure 8.7: Types of used solid elements marked by different colours

For centre bar as well as top and bottom flange of the test beam, elements with intermediate nodes were used (SOLID186). Although the use of elements without intermediate nodes would significantly reduce the computing effort, the accuracy of the calculation suffers too much from the reduction of the node number, which has been thoroughly tested before. As a compromise, elements without intermediate nodes (SOLID185) were used only for less important parts. They include the transverse beams, the permanent additional load and the foundations.

In reality, the additional load was supported by wooden beams, which were also modelled here. The connection between the concrete beams and the wooden beams was realised by surface contact elements (CONTA174 and TARGE170). However, in order to avoid nonlinearities due to contact conditions, the condition "always bonded" was set here so that no relative displacement between the connected bodies was possible. This was sufficiently accurate, because during the real measurements no relative movement took place between the wood and the concrete beams due to the high friction forces. In addition, the beams could not lift, since the accelerations that were captured during the dynamic measurements were always by far smaller than $1g$ with typical peak values of about $\pm0.05g$.

Since the wooden beams were only a small part of the overall model, the wood was not defined as an orthotropic material but as isotropic. The connection between wooden beams and concrete beams can be seen in Figure 8.8, where the different element types are differently coloured.
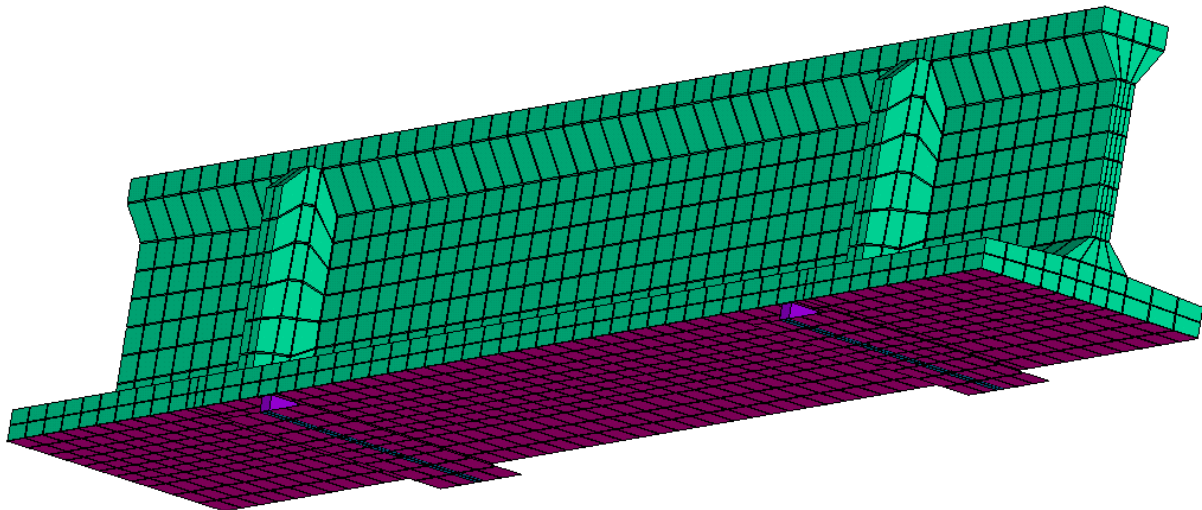
Figure 8.8: Connection between additional dead load and test beam by surface contact elements

Finally, the bearings of the beam had to be modelled. Defining the boundary conditions, they naturally have very strong influence on eigenfrequencies and mode shapes. Therefore, a lot of time was invested here to find a modelling that exactly reflects the real situation. It had proved to be insufficient to block only certain degrees of freedom of some nodes.

The test setup was equipped with a fixed and a sliding bearing, which however had not the behaviour of ideal bearings. On the fixed bearing, the beam was surrounded by concrete for a length of about half a meter. Hence, it is not only supported at one point, but at a certain area. Since the concrete of the bearings is not completely rigid, a rotation around the transverse axis was possible but not completely free. The sliding bearing was realised by two steel plates between the concrete with grease to reduce the friction. Despite the grease, there was a stick-slip effect as described in Chapter 5.2. Horizontal movement of the sliding bearing was only possible when the normal forces occurred in the axial direction exceeded the static friction between the steel plates and until the normal forces had been reduced by the expansion of the beam to a level below the sliding friction (cf. Figure 5.24b). In the static and dynamic tests, the loadings were applied only in the vertical direction, i.e. no normal forces occurred due to the loading. A horizontal displacement at the sliding bearing resulted only from a rotation of the cross-section around its centre of gravity, as simulated in the FE model (see Figure 8.9) or from thermal expansion.

```
1
 NODAL SOLUTION                                              ANSYS
                                                            R17.0
 STEP=1                                                    Academic
 SUB =1
 TIME=1                                          MAR 13 2017
 USUM     (AVG)                                    12:26:05
 RSYS=0
 DMX =.068007
 SMX =.068007
```

```
0           .015113        .030225        .045338        .060451
    .007556        .022669        .037782        .052894        .068007
```
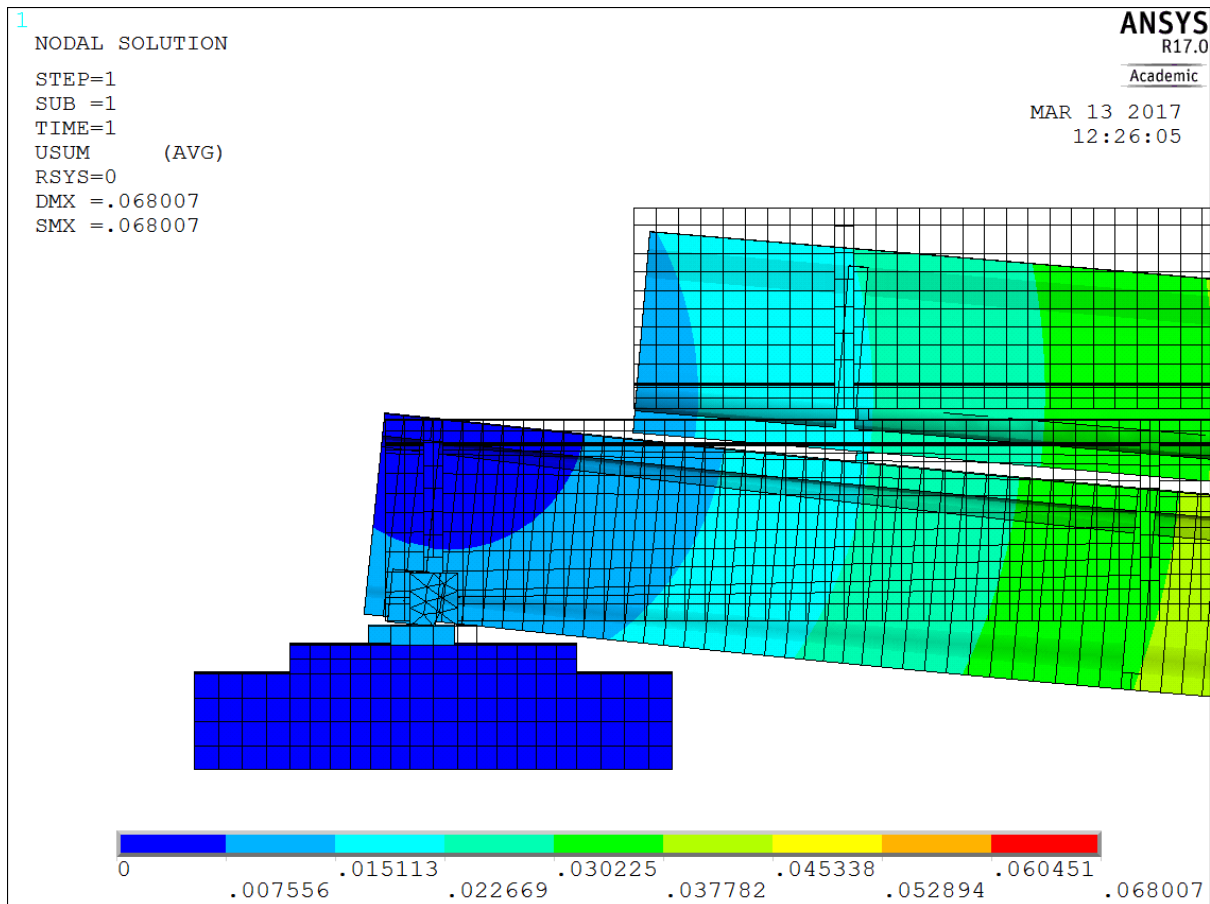
Figure 8.9: Postprocessor view with vector sum of deformation due to own weight with undeformed model

Normal forces due to thermal restricted expansion by friction in the sliding bearing were described in Chapter 5.2. The time required for a dynamic measurement of about 12-15 minutes was too short to change temperatures. Furthermore, the deformations caused by the vibrations were small compared to the deformations during a static load test. As a result, the sliding bearing behaved like a fixed bearing during dynamic measurements. This can be demonstrated by comparison of the modal analysis of the FE model to the measurements. Those fit better to the results of the modal analysis of an FE model with two blocked bearings.

To improve the model of the bearings, the cast concrete including the foundations and a part of the soil were also modelled as volumes. These were subsequently meshed, i.e. they were not rigid. In this way, the elasticity of the bearings and the soil could be incorporated into the simulation.

Now, the contact between these volume bodies had to be defined as well as the contact between the bearings and the beam. In order to simulate fixed connections, the APDL command VGLUE was executed before the meshing in ANSYS. As a result, on their

common surface, two bodies will be connected after the meshing by common nodes. Between the bearings and the main beam, this kind of connection was not possible or at least very time consuming to realise, since the already created mapped mesh of the test beam would need to be adapted again. Therefore, surface contact elements with the "always bonded" option were used here instead of the VGLUE command. This method was used for both bearings and at this point the model of the fixed bearing was finished, while for the sliding bearing additional movement possibilities had still to be modelled. These were simulated by two joints, which were created by using elements of type MPC184 revolute and planar joint, respectively. By this way of modelling, nonlinearities were avoided but only if the possibility of the MPC184 elements to alter the underlying constraint equations in the case of large deformations was switched off.

At the end the movements of 3 surfaces of the two cubes, representing the soil, were blocked in the direction perpendicular to the surfaces, thus fixing the soil.

In order to block the horizontal displacement of the sliding bearing for the modal analysis due to friction, the element type MPC184-planar was changed in MPC184-rigid beam by adapting the properties of the elements.

a) Sliding bearing   b) Fixed bearing
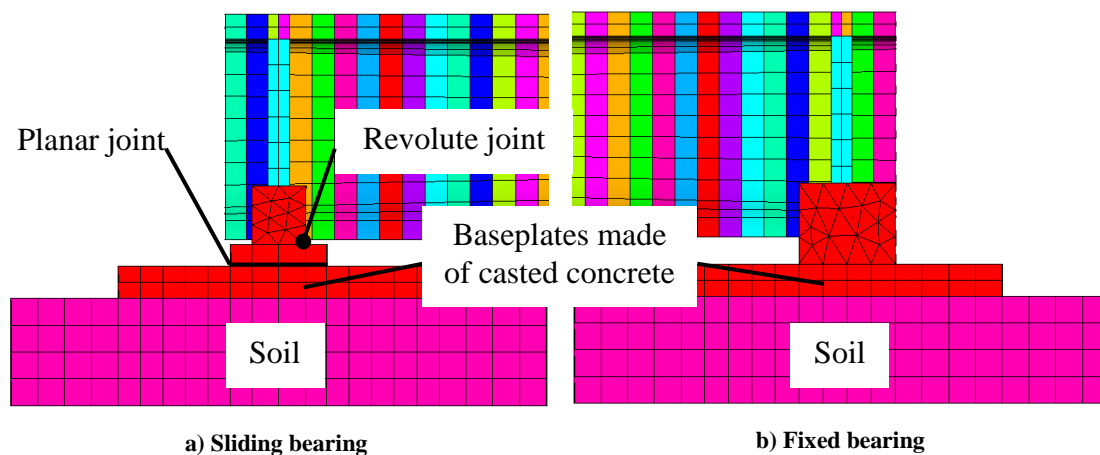
Figure 8.10: FE models of the bearings

Furthermore, a point mass was added to simulate the mass of the shaker. The additional loads $(2 \times 13t)$ for the static tests were supported by wooden beams, so in order to simulate the deflection due to these loads, their weight was added as pressure on the contact area between the wooden beams and the tested concrete beam. During the performed dynamic tests, they were always removed, so it was not necessary to take them into account for modal analysis.

The model was validated by comparing simulated results to measurements taken in the healthy state. The following Figures 8.11 to 8.16 show results from simulations using the finished model, as it was described above, in comparison to measured values. At first, in Figure 8.11 the deflection due to the additional loads is considered. Temperature compensated values of the displacements in loading #0-L2 were used. It can be seen that the measured and the simulated results match well.
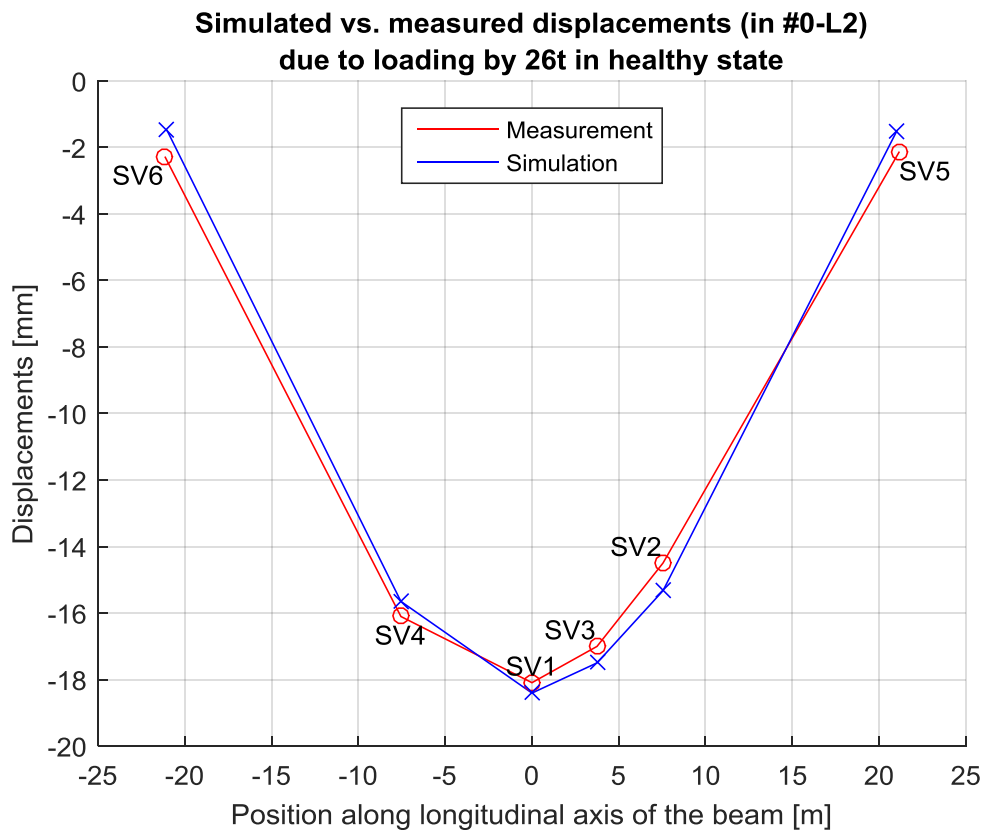
Figure 8.11: Comparison of the measured deflection in loading #0-L2 (healthy state) due to test weights to simulated vertical displacements at nodes closest to the sensor positions

In order to compare the results of the modal analysis, correlated mode shape pairs were formed by means of MAC after every simulation run as explained in Chapter 4.6. In the following the first 5 simulated modes are shown. They were correlated with the 5 measured modes as listed in Table 5.4.

The first simulated mode is a bending mode in the horizontal plane, i.e. x-y plane in Figure 8.12, which was not identified by the EMA, as only vertical DOFs were measured. The second simulated mode shown in Figure 8.13 is a vertical bending mode, which could be correlated either to measured mode B1a or B1b, since both mode shapes were rather similar. Here mode B1a was chosen and is shown as a diagram in Figure 8.13 for comparison.
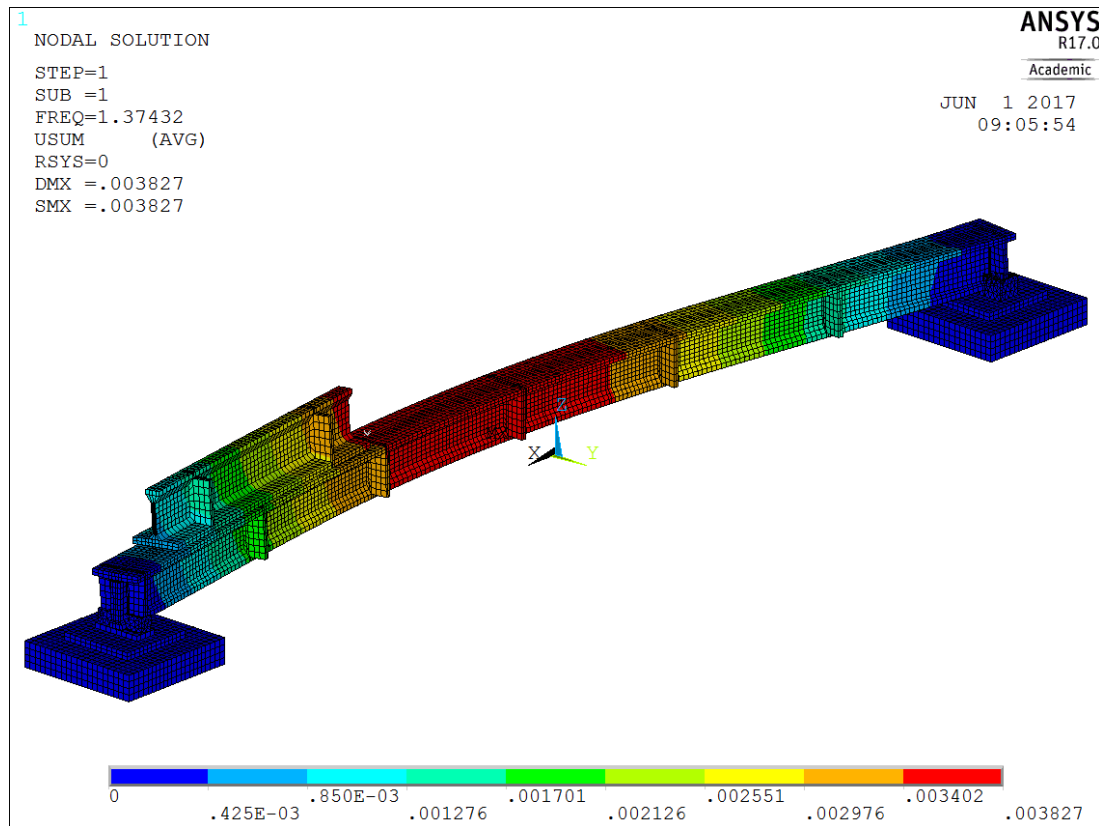
Figure 8.12: Mode 1 at 1.37 Hz – bending in y-direction
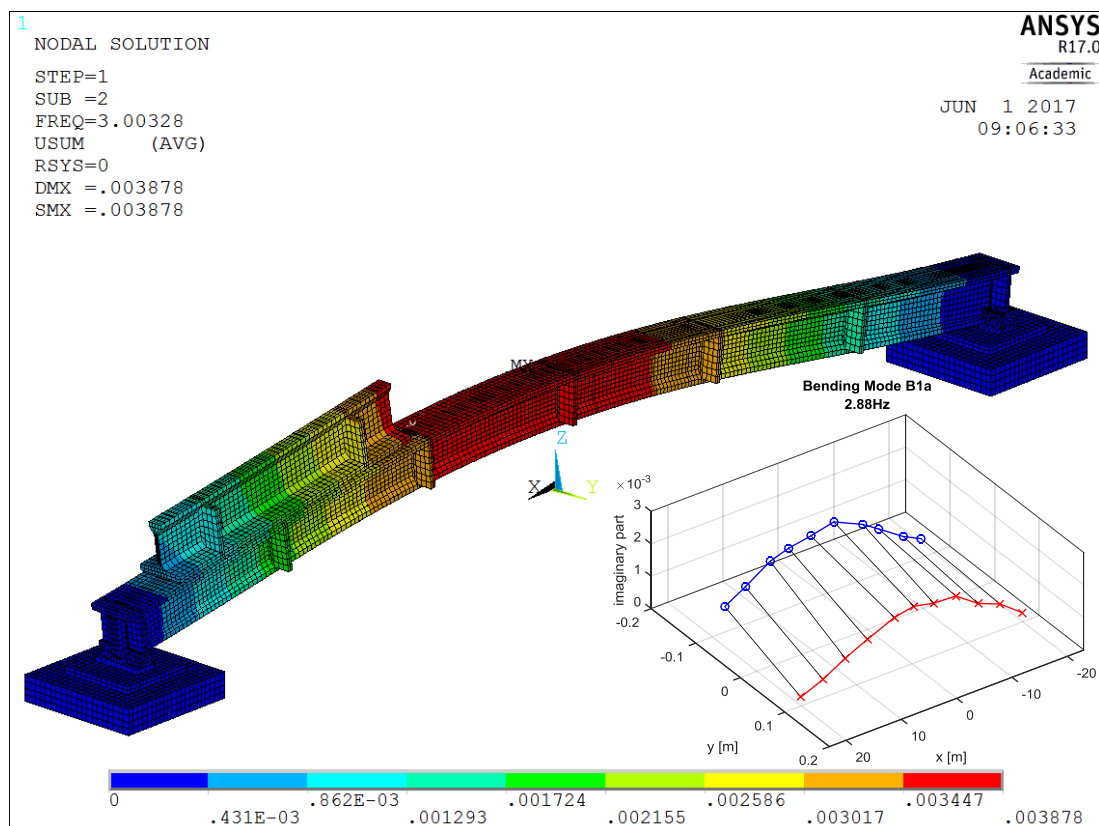
Figure 8.13: Simulated mode at 3.00 Hz – bending in z-direction; right: correlated measured mode B1a at 2.88 Hz (MAC=0.982)

The next two simulated modes were torsional ones, where mode 4 was correlated with simulated mode T1. The torsional modes were not well identified in the EMA, so the MAC values for correlated mode shape pairs with torsional modes were always rather small. This is also the reason, why measured mode T2 was omitted here.
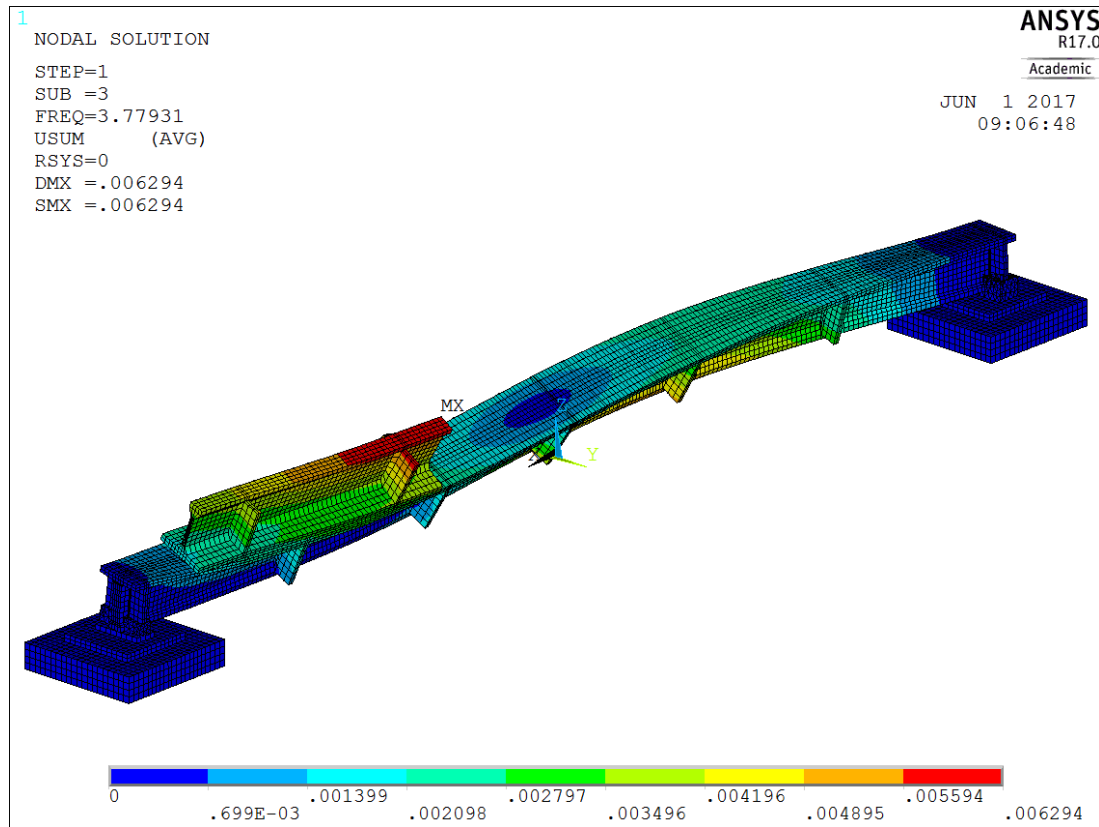
Figure 8.14: Mode 3 at 3.78 Hz - torsional
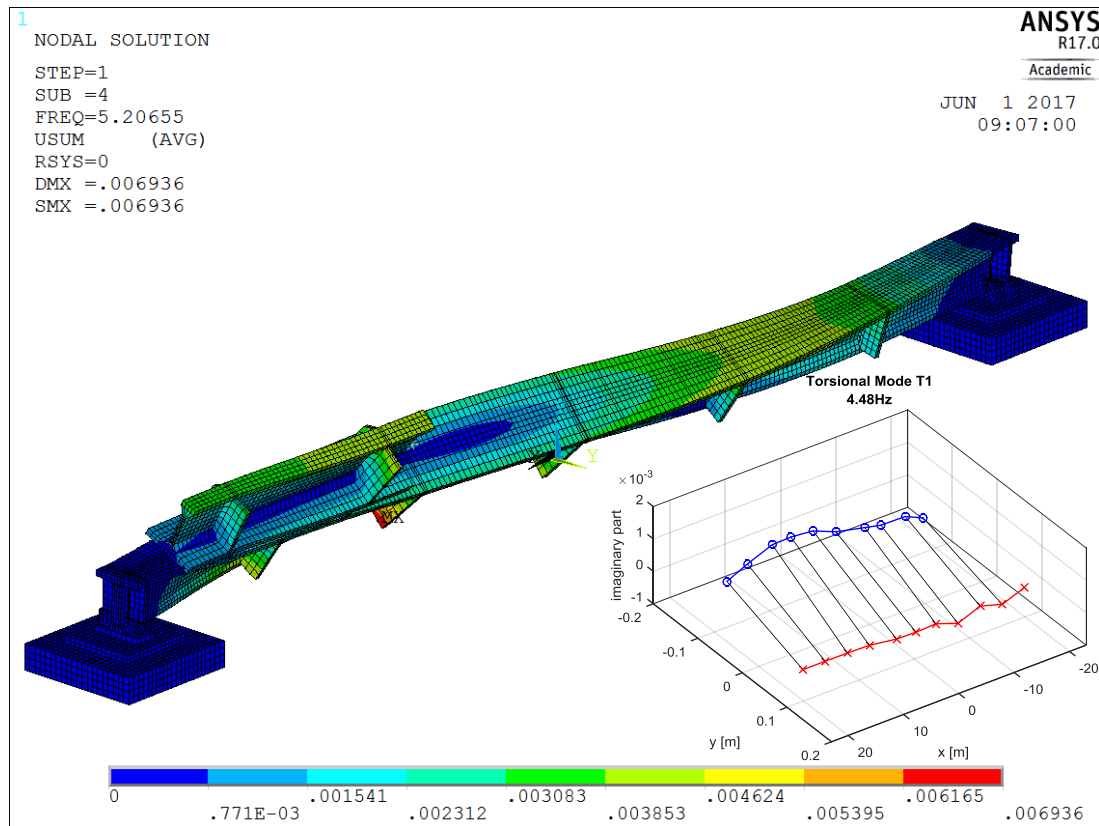
Figure 8.15: Simulated mode at 5.21 Hz - torsional; right: correlated measured mode T1 at 4.48 Hz (MAC=0.632)
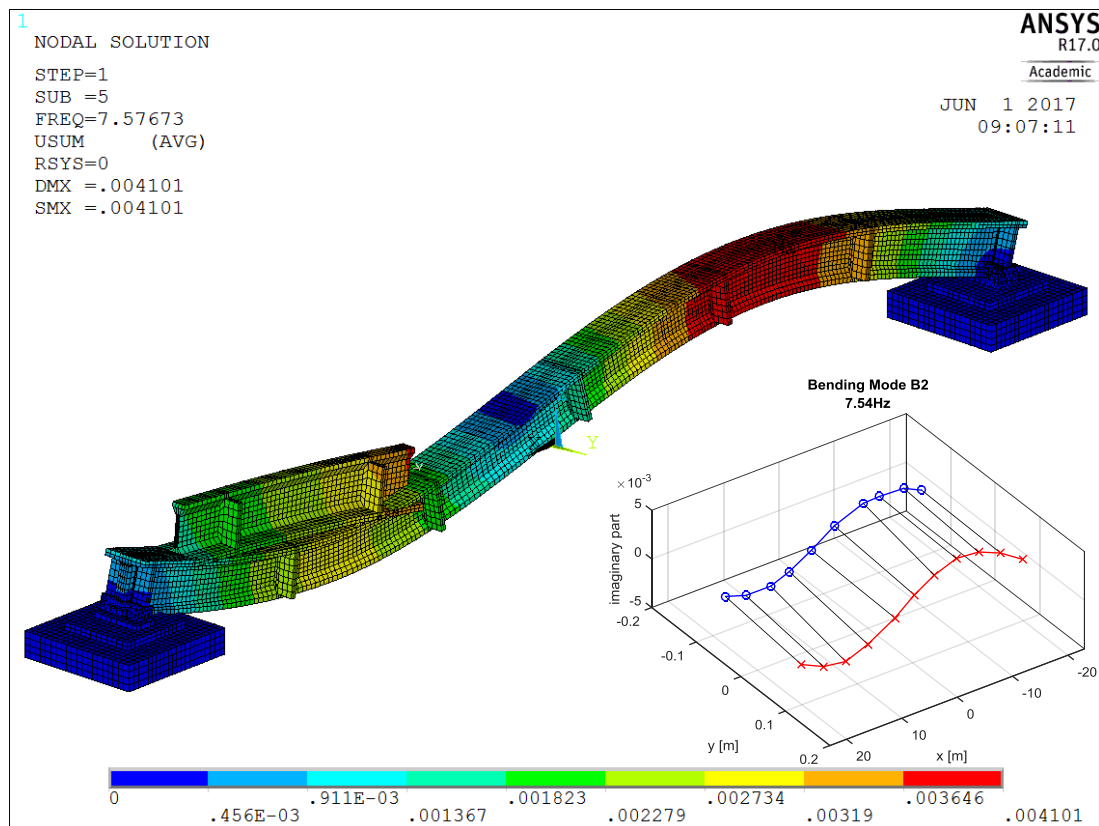
Figure 8.16: Simulated mode at 7.58 Hz – bending in z-direction; right: correlated measured mode B2 at 7.54 Hz (MAC=0.970)

At last measured bending mode B2 was correlated with the fifth simulated mode as shown above. As already stated in Chapter 4.6, these found correlated mode shape pairs might not be valid anymore when the model is changed in a model updating procedure. Therefore, this correlation must be performed after every simulation run. An automatic correlation based on MAC values was realised and worked quite stable with the 3 mode shape pairs, which were defined here.

After the validation of the reference model, it was now possible to modify the bending stiffness along the longitudinal axis of the beam for simulating the effect of damage. Therefore, Young's moduli were modified for the regions defined as slices of the beam.

In literature it is often proposed (e.g. Teughels et al. (2002) [36], Jaishi et al. (2006) [41]) not to use directly the physical properties, like for instance the Young's moduli, as model updating parameters. Instead of that, dimensionless parameters should be defined, which describe the relative change of the physical properties compared to their initial values. Hence, the following was used here:

$$a_i = \frac{E_{i0} - E_i}{E_{i0}}$$

$$E_i = E_{i0}(1 - a_i)$$

(8-4)

Where E_{i0} and E_i are the initial and the adapted Young's modulus for slice i, respectively and a_i is the dimensionless parameter. For the static analysis, i.e. for the simulation of the static deflection due to own weight (gravity) and due to loading with test weights of $26\ t$, the used initial Young's modulus E_{i0} was $30\ GPa$, while for the modal analysis it was set to $36\ GPa$. With these values the simulation results from the static as well as dynamic analysis matched well the measurements at the real beam in the healthy state. The difference can be explained by the fact, that the static deformations of the real test beam were higher than the ones caused by vibration during the dynamic tests. Therefore, cracks that were present at the beam opened wider due to the static deformations than due to the vibrations. Therefore, it is reasonable to assume that the stiffness of the beam was higher during the dynamic tests than during the static ones, which was simulated by the higher "dynamic" Young's modulus.

In the current problem, 227 parameters a would be necessary to modify the material properties of all slices. As already mentioned at the beginning of Chapter 8.2, the computing effort was too high for a model updating procedure.

Hence, the approach proposed by Teughels et. al. (2002) [36] was used here in a modified form. Teughels et al. described the procedure for an FE-model of a beam consisting of beam elements arranged along its axis. They proposed to group together a certain number of adjacent elements to form a so-called "damage element" and to define the reduction of the Young's modulus (i.e. the parameter a) along the beams axis by means of a "damage function". It is here possible to define several damage elements, each with its own damage function, but also to consider merely a specific part of the entire beam within a single damage element. Now the parameters a are no longer used directly, but they are calculated through the damage function. For the model updating parameters are used, which describe the damage function itself. In general, this procedure can reduce enormously the number of parameters.

The damage function provides a mathematical model reflecting the impact of an expected damage to the bending stiffness, like for instance of a crack. It thus provides additional information for the optimisation, which ensures that a physically meaningful result is achieved. Teughels et al. used Legendre polynomials to define the damage function.

Here, instead of a simple model consisting of beam elements, the volume model described before was used, which represents the reality more precisely. Furthermore, another damage function was introduced, namely a Gaussian bell curve with the function (8-5). As proposed by Teughels et al., the position on the beam's axis within the damage element was indicated by a normalised variable x_{norm}. The x_{norm}-axis starts with the value -1 at one end of the damage element and concludes with 1 at the other end. Thus, the value $x_{norm} = 0$ stands for the centre of the damage element. Three parameters p, μ and σ, were used to describe the damage function, which hence represent the model updating parameters.

$$a(x_{norm}, p, \mu, \sigma) = p \cdot e^{-0.5\left(\frac{x_{norm}-\mu}{\sigma}\right)^2} \tag{8-5}$$

a: Ratio between updated and initial Young's modulus

p: Maximal reduction, $p \in [0; 1]$

μ: Expected position of the damage inside the damage element

σ: Parameter that describes the widening of the Gaussian Curve

x_{norm}: Normalised position inside the damage element: $x_{norm} = \frac{2x-x_s-x_e}{x_e-x_s}$, $x \in [x_s; x_e]$

x: real axial position between $0\,m$ and $l = 46\,m$

x_s, x_e: start and end of the damage element measured along the beams axis

Figure 8.17 shows for example a damage of 80% peak (i.e. 20% of initial Young's modulus) at $\mu = 0.2 = x_{norm}$ with Gaussian bell form. For instance, if the limits x_s and x_e of the considered damage element are the beginning $(x_s = 0)$ and the end of a beam with length l $(x_e = l)$, then the maximum of the damage function would be located at position $x = \frac{1}{2}(x_{norm} \cdot (x_e - x_s) + x_s + x_e) = \frac{l}{2}(x_{norm} + 1) = \frac{l}{2}(0.2 + 1) = 0.6l$. Young's modulus of all slices between $x_{norm} \in [0; 0.4]$ would be reduced according to the form of the curve and its value at the mid of the slice.
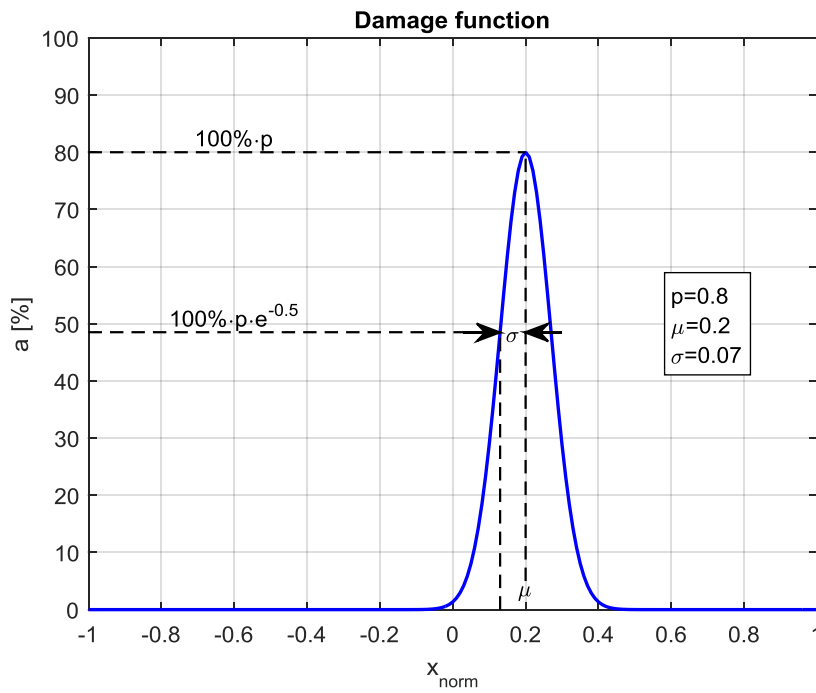
Figure 8.17: Graph of the damage function for the specified parameters p, μ and σ

So far, the slices were about 20 cm wide in axial direction. In best case, this will allow a quite coarse localisation of damage. In order to improve the definition of the damage localisation, the axial width of the slices must be reduced. Furthermore, since the width of a crack is only in the order of magnitude of millimetres or even less, it reduces the bending stiffness only in a small region of the beam. Directly at the location of a crack a large stiffness reduction occurs, because the supporting part of the cross-section is reduced by the crack. But already in a small distance from the crack, the cross-section is not affected, so it is logical to expect, that the stiffness loss decreases very fast with increasing distance from the crack. That means, the best way to accurately model the impact of a crack on the bending

stiffness would be to define the damage function as a narrow but high peak at the location of the crack.

But how far the width of the damage function, which is defined by the parameter σ, can be effectively reduced, depends on the axial width of the elements. In order to explain this, the two following figures shall be considered.
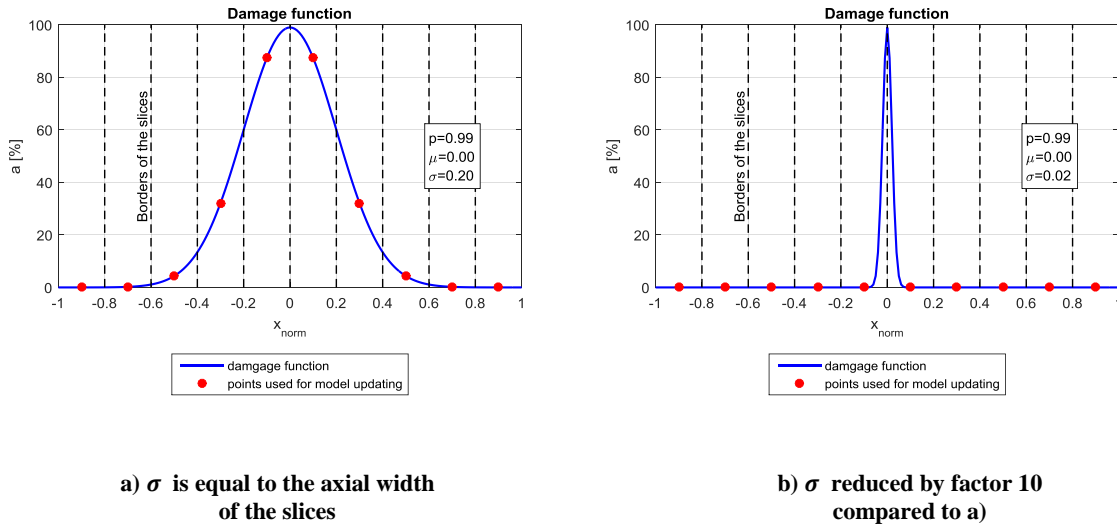

a) σ is equal to the axial width of the slices

b) σ reduced by factor 10 compared to a)

Figure 8.18: Used values of the damage function, if its maximum is located on the border between two slices

As stated above the reduction of the Young's modulus is defined by the parameter a, which is determined by calculating the value of the damage function at certain positions. In the model updating procedure, which was realised for this thesis, the Young's modulus was reduced uniformly for any of the previously defined slices of the beam. In order to ascertain the magnitude of the reduction, the normalised positions x_{norm} on the beams axis of the centre of gravity of each slice was substituted into the damage function. In Figure 8.18a the effectively used values of the damage function are marked by red dots while the axial width of the slices is marked by vertical dashed lines. It can be seen, that the maximum value of the damage function is not used, because it is located directly on the border between two slices. In this case, the maximum reduction of the Young's modulus will be only 87%, although the intended reduction, as defined by the parameter p, is 99%. The effect increases, if σ is further reduced, as can be seen in Figure 8.18b. Here, the stiffness of the beam would actually not be affected by the updating parameters. In order to avoid the described problem, it is proposed here that the parameter σ is not set lower as the axial width of the widest slice in a damage element.

However, if smaller σ shall be used, it is necessary to define the parameter μ in a way that it matches the centre of gravity of a slice, in order to reach the intended maximum stiffness

reduction without reducing the axial width of the slices. This situation is shown in Figure 8.19.
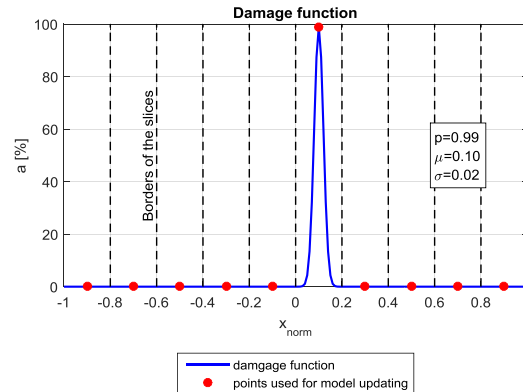

Figure 8.19: Used values of the damage function, if its maximum is located on the centre of gravity of a slice

Now at least the maximum value of the peak is used. But by additionally reducing the width of the slices, more points of the damage function would be used. Therefore, with a finer FE mesh, the influence of a crack can be modelled more realistic. The disadvantage of the reduction of the element size is of course that the computing effort becomes very high, especially if the axial width of the elements for a beam of length $46\ m$ is reduced to a few millimetres. Normally, one aim of damage assessment is to localise the damage, which means it is not previously known. Here the idea is, that a model like the one described so far with a coarse element size can be used to identify damaged areas with a coarse accuracy. Afterwards, if necessary, the mesh in the identified areas is refined to improve the damage localisation. For the tests in the port of Mertert, the advantage is that the damage location is known, because the damage was artificially introduced. Therefore, the proposed approach can be tested, by first evaluating results, which were obtained with a coarse mesh, and afterwards refining the mesh in the vicinity of the damage and repeating the evaluation.

Therefore, a second model was created with refined mesh in a region $1\ m$ left and right of the position, where the tendons were cut during the tests. In the middle of this region, were the largest vertical crack appeared in the tests, the axial width was reduced to $10\ mm$. The width was steadily increased with increasing distance from the crack location. To avoid warped elements with a large ratio between its height and width, the element size in vertical direction was reduced, too. Now a transition had still to be created between the refined and the coarse mesh. For this purpose a transition mesh was created, which consisted of elements of the

same type as the remaining concrete beam (BEAM186) but degenerated into tetrahedral or pyramid shape. The resulting mesh in the vicinity of the damage is shown below.
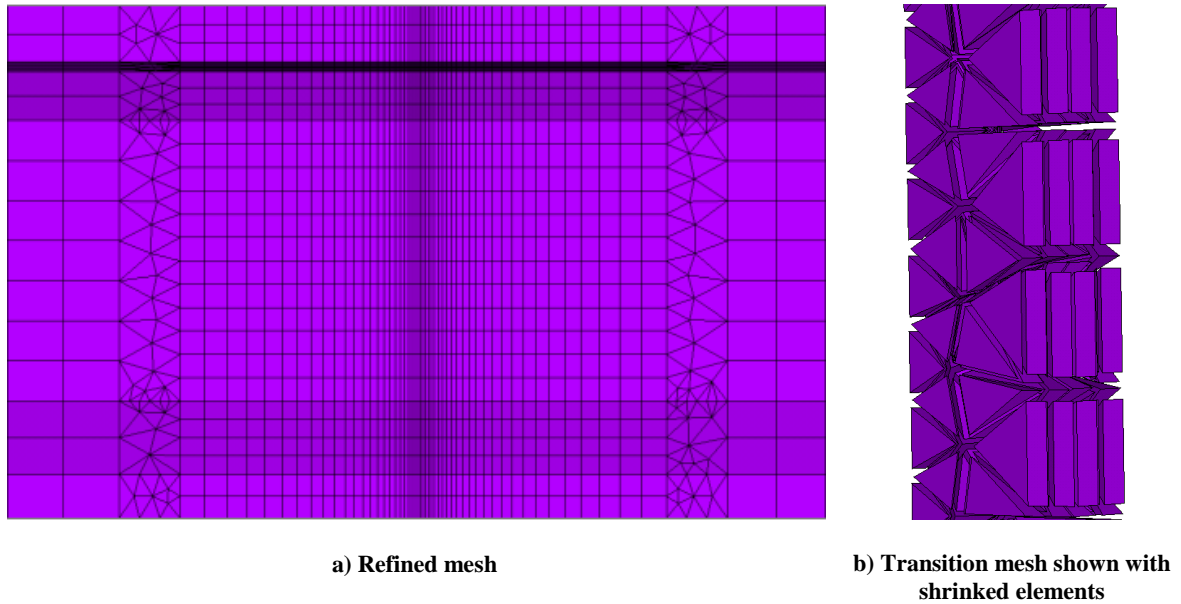

| a) Refined mesh | b) Transition mesh shown with shrinked elements |

Figure 8.20: Mesh refinement in the vicinity of the damage location

8.3 Definition of objective functions

Four objective functions are defined based on the considerations in Chapter 4.6. Different physical quantities, which were predicted by the FE-simulation and measured in reality, are considered in any of them. By evaluating these individual objective functions, the usability of any considered physical quantity for the purpose of damage detection by model updating is checked separately.

At first, the progressive downward movement of the beam due to gravity, i.e. the sagging by own weight, is considered. The vertical displacements measured by the displacement sensors SV6, SV4, SV1, SV3, SV2 and SV5 (cf. sensor positions in Figure 5.8) are evaluated. The data measured by these sensors were temperature-compensated as described in Chapter 6. Then from these temperature-compensated data, a value representative for each "unloading" (cf. Figure 5.18) and for each sensor was chosen as it was described in Chapter 7.1. These were the same values, which were already used for the plots in Figure 7.2. As for this figure, the values determined for the first unloading #0-UL1 were defined as baseline. The increase in deflection during the unloadings was analysed. The concrete values are listed in Table 8.3.

Table 8.3: Temperature compensated values of absolute displacements during the "unloadings" referred to as "sagging" (used values for model updating marked by green shading)

	Sensor position x [m]	#0-UL1 [mm]	#0-UL2 [mm]	#0-UL3 [mm]	#1-UL [mm]	#2-UL [mm]	#3-UL [mm]	#4-UL1 [mm]	#4-UL2 [mm]
fixed bearing	-23.00	0.00	0.00	0.00	0.00	0.00	0.00	0.00	0.00
SV6	-21.15	0.00	-0.35	-0.82	-0.34	-1.45	-1.83	-2.76	-4.11
SV4	-7.55	0.00	-1.33	-3.88	-0.75	-8.33	-11.63	-18.91	-26.58
SV1	0.00	0.00	-1.71	-4.31	-1.43	-9.75	-15.04	-24.81	-33.87
SV3	3.75	0.00	-1.64	-4.09	-1.79	-10.38	-17.66	-28.83	-38.63
SV2	7.55	0.00	-1.48	-3.59	-1.55	-8.41	-13.62	-22.33	-30.17
SV5	21.15	0.00	-0.35	-0.65	-0.46	-1.39	-2.26	-3.57	-5.02
sliding bearing	23.00	0.00	0.00	0.00	0.00	0.00	0.00	0.00	0.00
		Reference	Damage state #0		DS#1	DS#2	DS#3	DS#4	

During the FE-simulation, the nodes closest to the real sensor positions were selected and their displacements in vertical direction due to gravity were taken from the simulation results. First the healthy beam was simulated and the results were saved as a vector $\{z_{healthy}\}$. In the following simulations, the sagging of the model was defined as the difference from the calculated vertical displacements due to gravity to the values in the healthy state.

$$\{sim_{sagging}(\{p\})\} = \{z_{damaged}(\{p\})\} - \{z_{healthy}\} \tag{8-6}$$

Where $\{sim_{sagging}(\{p\})\}$ is the simulated sagging, which depends on the used updating parameter $\{p\}$, and $z_{damaged}(\{p\})$ is the simulated deflection due to gravity with parameter set $\{p\}$.

This procedure resulted in vectors containing the sagging of the beam at the 6 sensor locations. From real measurements a vector $\{exp_{sagging}\}$ was defined for any unloading, which actually were the values listed in Table 8.3. The measured vectors were compared to the simulated vectors $sim_{sagging}(\{p\})$ by means of an objective function. Thus, it is possible to determine from each simulation several objective values, one for each unloading. Furthermore, by selecting one unloading for each damage scenario DS#0-DS#4, an objective value from the function for each scenario was obtained.

In order to compare the vectors and to define the objective function depending on a set of updating parameters $\{p\}$, the Euclidian difference was calculated as defined in equation (4-45). By using a diagonal weighting matrix it would be possible to use different weighting factors for each component of the difference vector, e.g. to take into account different measurement accuracies. But here the weighting factors for each vector component are set the same in this study, so the weighting matrix $[\mathbf{W}]$ can be replaced by a single factor w.

$$obj_{sagging}(\{p\}) = w\|(\{exp_{sagging}\} - \{sim_{sagging}(\{p\})\})\|_2$$

$$= \frac{1}{N} \cdot \frac{1}{\Delta} \cdot \sqrt{\sum_{i=1}^{N} |\ _iexp_{sagging} - \ _isim_{sagging}\{p\}|^2} \tag{8-7}$$

The number of components of the compared vectors N and the measurement accuracy Δ are taken into account for the weighting. The Euclidian norm in equation (8-7) is multiplied by the reciprocals of N and Δ. Consequently, the objective function in equation (8-7) yields dimensionless values. In this problem, N is the number of sensors, i.e. equal to 6, and Δ is assumed as $0.1\ mm$ for the used displacement sensors. In the evaluation of the objective functions, the measured and simulated values were rounded to the number of decimal places, which corresponds to the accuracy Δ. The name of this function "$obj_{sagging}$" means "objective function based on sagging due to gravity".

The second considered physical quantity is the deflection of the beam due to the additional test load, which was used in the static tests. The approach is similar to the one for the deflection due to gravity. As for the unloadings, also for the loadings temperature–compensated displacements were determined as described in Chapter 7.1. Instead of calculating the difference of these displacements to a baseline, the differences to the displacements during the unloading just before a loading were determined and summarised in a vector $\{exp_{add}\}$.

$$\{exp_{add}\} = \{x_{loaded}\} - \{x_{unloaded}\} \tag{8-8}$$

Where $\{x_{loaded}\}$ and $\{x_{unloaded}\}$ are vectors containing the measured displacements when the beam was loaded and just before the loading, respectively (cf. Figure 5.18). This yields the values used in Figure 7.5 and listed in Table 8.4.

Table 8.4: Temperature compensated displacements due to loading with test weights (26t) (used values for model updating marked by green shading)

	x [m]		#0-L1 [mm]	#0-L2 [mm]	#1-L [mm]	#2-L [mm]	#3-L [mm]	#4-L1 [mm]	#4-L2 [mm]
fixed bearing	-23.00		0.00	0.00	0.00	0.00	0.00	0.00	0.00
SV6	-21.15		-2.63	-2.27	-2.16	-3.16	-3.09	-3.96	-2.53
SV4	-7.55		-17.72	-16.10	-15.58	-22.80	-22.98	-30.55	-19.41
SV1	0.00		-20.02	-18.09	-18.04	-25.74	-27.67	-37.51	-23.15
SV3	3.75		-18.75	-17.00	-17.35	-25.13	-30.49	-39.41	-23.48
SV2	7.55		-15.97	-14.50	-14.62	-20.93	-23.46	-32.27	-19.65
SV5	21.15		-2.35	-2.15	-2.10	-3.02	-3.46	-4.58	-2.86
sliding bearing	23.00		0.00	0.00	0.00	0.00	0.00	0.00	0.00
			Damage state #0	DS#1	DS#2	DS#3	DS#4		

In the simulation, the additional loads were not defined as solids with a mass, but their weight was defined as surface loading on the top flange of the test beam. The vertical displacements at the sensor locations due to these loads were taken from the simulation results as it was done for the displacements due to own weight. Again a result vector for any simulation $\{sim_{add}\}$ as well as a vector for each damage scenario including the measured values $\{exp_{add}\}$ (cf. Table 8.4), were defined.

The vectors were compared by an objective function similar to obj_{grav}, with the same values for N and Δ.

$$obj_{add}(\{p\}) = w\|(\{exp_{add}\} - \{sim_{add}(\{p\})\})\|_2$$

$$= \frac{1}{N} \cdot \frac{1}{\Delta} \cdot \sqrt{\sum_{i=1}^{N} |\ _i exp_{add} -\ _i sim_{add}\{p\}|^2} \qquad (8\text{-}9)$$

Furthermore, two objective functions based on the dynamic properties were defined. In the experimental modal analyses for the different damage scenarios, 5 modes were identified in the frequency range $2.5 - 15\ Hz$. One measurement was selected for every damage scenario and the eigenfrequencies of the identified modes are listed in Table 8.5.

Table 8.5: Eigenfrequencies identified in damage scenarios DS#0 - DS#4 (used modes for model updating marked by green shading)

Start time of measurement		31/01/14 11:28:18	04/02/14 11:00:26	06/02/14 11:10:09	11/02/14 10:56:52	17/02/14 12:03:24
Abbr.	**Description**	**f [Hz] DS#0**	**f [Hz] DS#1**	**f [Hz] DS#2**	**f [Hz] DS#3**	**f [Hz] DS#4**
B1a	Bending mode	2,88	2,88	2,85	2,84	2,78
B1b	Bending mode	3,03	3,04	3,01	2,99	2,99
T1	Torsional mode	4,48	4,49	4,46	4,46	4,45
T2	Torsional mode	7,29	7,32	7,27	7,26	7,24
B2	Bending mode	7,54	7,55	7,51	7,51	7,45

Before the evaluation of the objective functions for a simulation run, these 5 modes were automatically correlated to the simulated modes by means of the Modal Assurance Criterion (MAC according to equation (4-34)) as it is explained in Chapter 4.6, but finally only 3 of them could clearly be correlated. Above all, the identification of mode T2 was not very clear, so it did not match a simulated mode. Furthermore, the measured modes B1a and B1b are quite similar and recognised as highly coupled modes while the FE-simulation results in only one mode about $3\,Hz$ whose shape is similar to both B1a and B1b. In the following evaluations only measured mode B1a was considered.

In the first place, the eigenfrequencies of the correlated modes are compared by the following objective function obj_{ef}:

$$obj_{ef}(\{p\}) = w\|(\{exp_{ef}\} - \{sim_{ef}(\{p\})\})\|_2$$

$$= \frac{1}{N} \cdot \frac{1}{\Delta} \cdot \sqrt{\sum_{i=1}^{N} |\,_i exp_{ef} - \,_i sim_{ef}\{p\}|^2} \tag{8-10}$$

where vectors $\{exp_{ef}\}$ and $\{sim_{ef}\}$ contain the measured and simulated eigenfrequencies for the correlated mode pairs, respectively. Here $N = 3$ and $\Delta = 0.01\,Hz$ were used.

Finally, the unit modal mass (UMM) normalised mode shapes of the correlated mode pairs are compared by means of MAC according to equation (4-34).

$$obj_{MAC}(\{p\}) = \frac{1}{N} \sqrt{\sum_{i=1}^{N} |1 - MAC(\,_i\varphi_{meas}, \,_i\varphi_{sim}(\{p\}))|^2} \tag{8-11}$$

8.4 Results of model updating with coarse FE mesh

Several FE simulations using different parameter sets were performed, to carry out a parameter study. At first, the model with the coarse mesh was used. The resulting objective values are plotted and evaluated graphically. The intention was to examine if the model, the updating parameters and the used objective functions are appropriate for a detection and localisation of the artificially introduced damage.

Since the defined objective functions depend on the 3 model updating parameter p, μ and σ, the functional graphs are 4-dimensional, and hence cannot be plotted completely in a single 3-dimensional plot. Therefore, the functions are plotted as curves by always fixing 2 parameters.

The whole test beam can be considered as one damage element, so the normalised x-axis according to Figure 8.17 starts at the beginning of the beam at the location of the fixed bearing and ends at the sliding bearing. By this setting the location of the artificially introduced damage corresponds to $x_{norm} = 0.2$. Therefore, the parameter μ was fixed initially to this value and simulations were performed, where p and σ were varied (p: 0.1 to 0.99 and σ: 0.01 to 0.1). As elucidated in Chapter 8.2, it can happen that the intended maximum reduction of the stiffness, as defined by p, is not reached, if σ is chosen too small compared to the axial width of the slices. Therefore, the smallest used value for σ was here 0.01. This value corresponds approximately to the width of the slices if it is converted to the normalised x-axis of the damage element.

As an example the objective values are plotted, which were calculated by using the objective function based on the sagging of the test beam, i.e. $obj_{sagging}$.

Objective values for DS#4 with μ=0.20
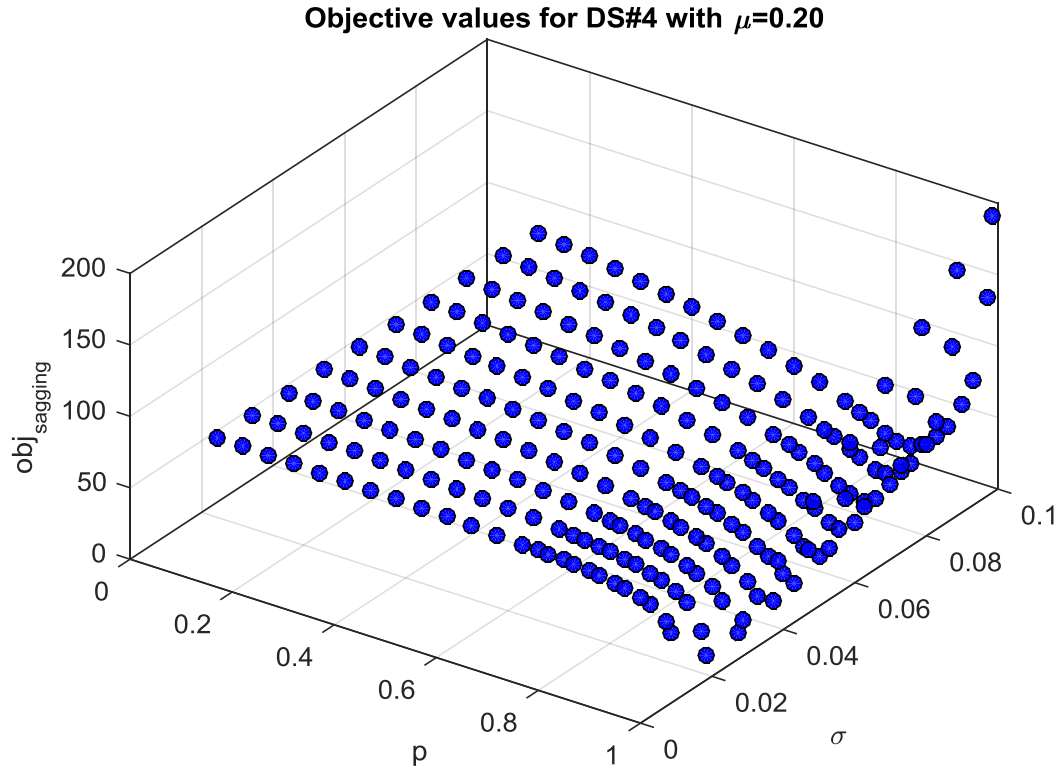
Figure 8.21: 3D scatter plot of objective function based on the sagging of the test beam for fixed μ

From the points plotted in the above diagram the parameter set with the lowest objective value was chosen, here $p = 0.9$, $\mu = 0.2$ and $\sigma = 0.07$. This was repeated for every damage scenario as well as all 4 damage functions. Table 8.6 lists the obtained optimal parameter sets.

Table 8.6: Parameter sets with minimal objective values for $\mu = 0.2$

DS#	**obj$_{\text{sagging}}$**			**obj$_{\text{add}}$**		
	p	μ	σ	p	μ	σ
1	0.25	0.20	0.04	0.10	0.20	0.01
2	0.50	0.20	0.10	0.88	0.20	0.09
3	0.73	0.20	0.08	0.98	0.20	0.06
4	0.90	0.20	0.07	0.95	0.20	0.04

DS#	**obj$_{\text{ef}}$**			**obj$_{\text{MAC}}$**		
	p	μ	σ	p	μ	σ
1	0.99	0.20	0.01	0.70	0.20	0.10
2	0.99	0.20	0.01	0.73	0.20	0.09
3	0.99	0.20	0.01	0.73	0.20	0.09
4	0.98	0.20	0.02	0.70	0.20	0.10

Plots of the objective functions according to these parameter sets are summarised in Figures 8.22 to 8.25. Each curve is determined by fixing 2 parameters while the third parameter varies. The curves reveal clearly that the positions of the minima of the objective functions on the abscissa are actually the parameters listed in Table 8.6.

a) μ and σ fixed

b) μ and p fixed
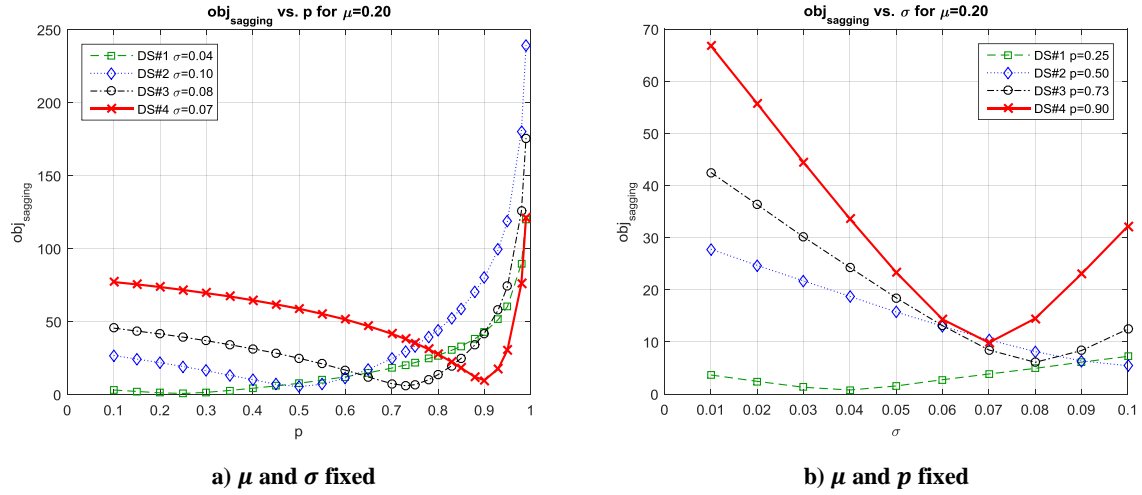
Figure 8.22: Objective function based on the sagging of the test beam

In Figure 8.22a shows that while using the damage function $obj_{sagging}$, optimal values for parameter p increase steadily with increasing damage, so it may properly indicate the severity of damage.

a) μ and σ fixed

b) μ and p fixed
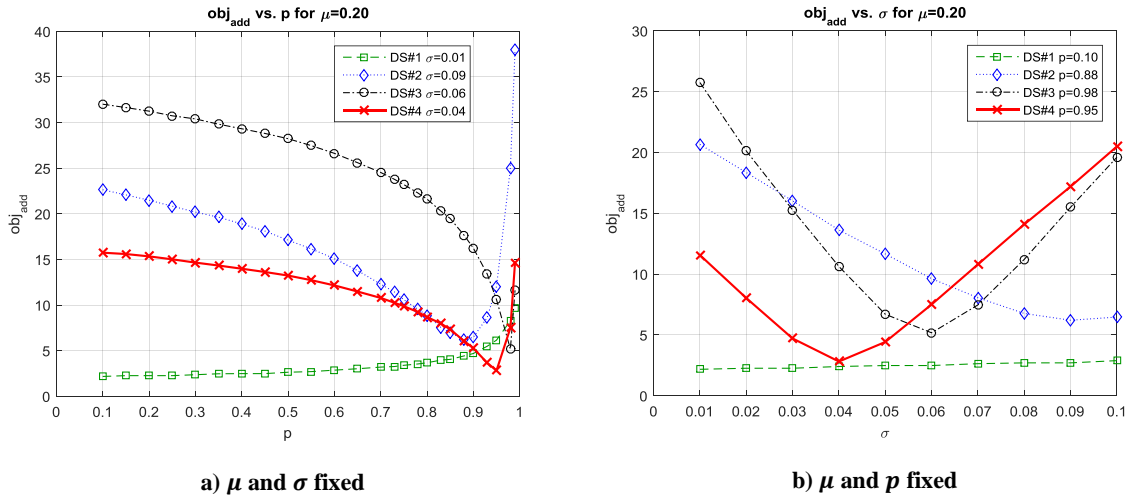
Figure 8.23: Objective function based on deflection due to additional test loading

a) μ and σ fixed

b) μ and p fixed
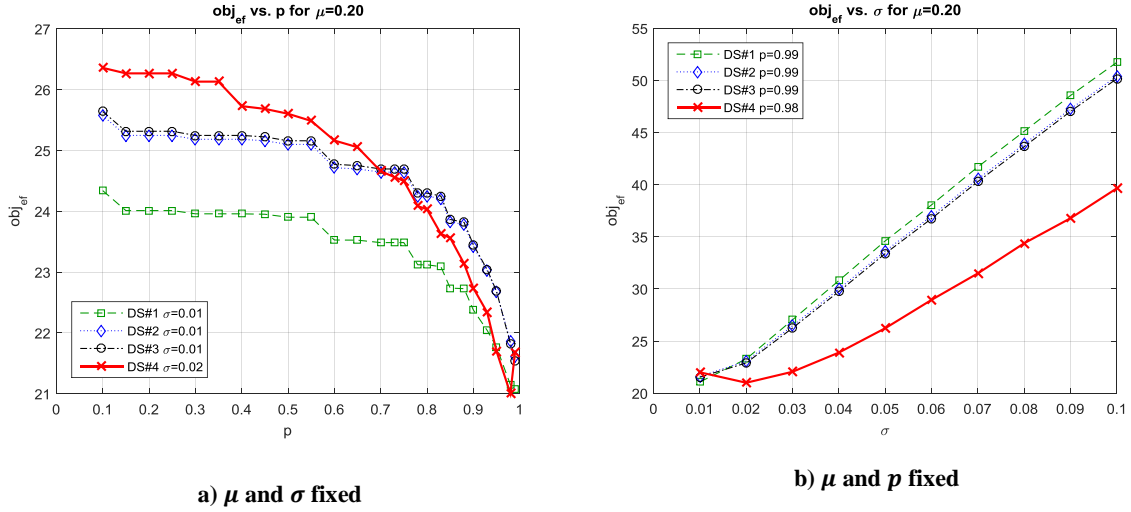
Figure 8.24: Objective function based on eigenfrequencies

a) μ and σ fixed

b) μ and p fixed
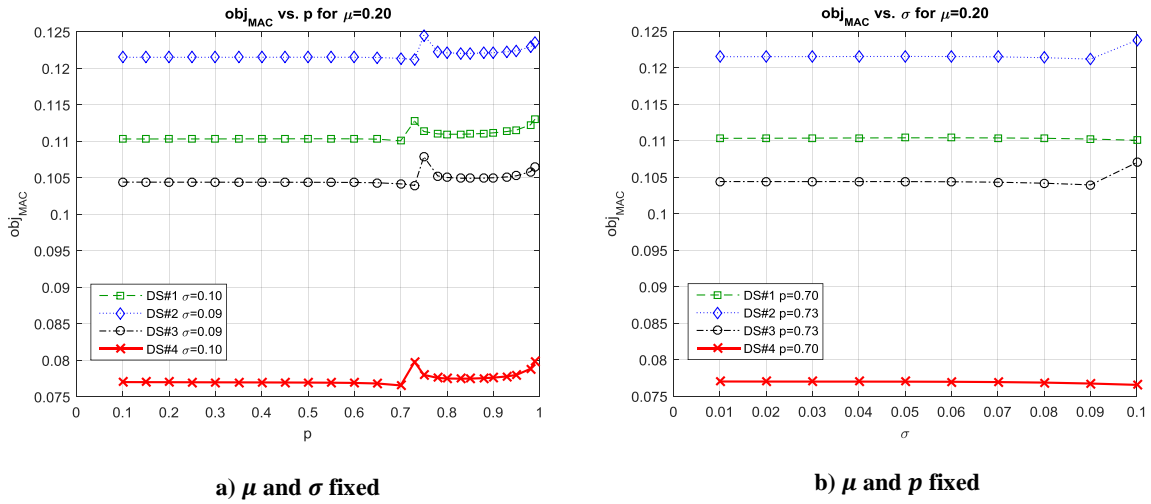
Figure 8.25: Objective function based on mode shape comparison by means of MAC

In order to plot the objective functions vs. parameter μ, i.e. the normalised x-position, μ was varied in the simulations. Figure 8.26 shows discrete values of $obj_{sagging}$, if for the different damage scenarios the parameters p and σ are fixed to the values from Table 8.6. The damage localisation becomes clearer with increasing damage, because the damage function increases faster from the minimum. However, it shows that the minima are not exactly at the real damage location $\mu = 0.2$, as assumed in Table 8.6 for the calculations. The observation is detailed by a zoom shown in In Figure 8.26b where the resulted minima are marked accompanied by X- and Y-coordinates, i.e. values for μ and $obj_{sagging}$ respectively.

a) Overall view

b) Zoom with
marked minima
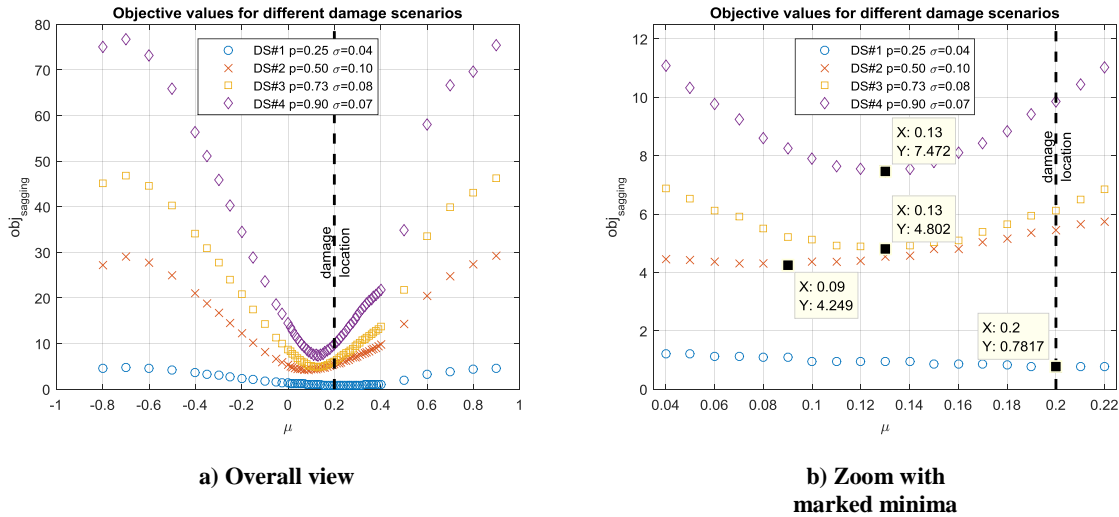
Figure 8.26: Objective values vs. μ using $obj_{sagging}$ for DS#1-DS#4

Figure 8.27 shows the objective values for $obj_{sagging}$ while fixing $\sigma = 0.07$ and varying p and μ for DS#4.
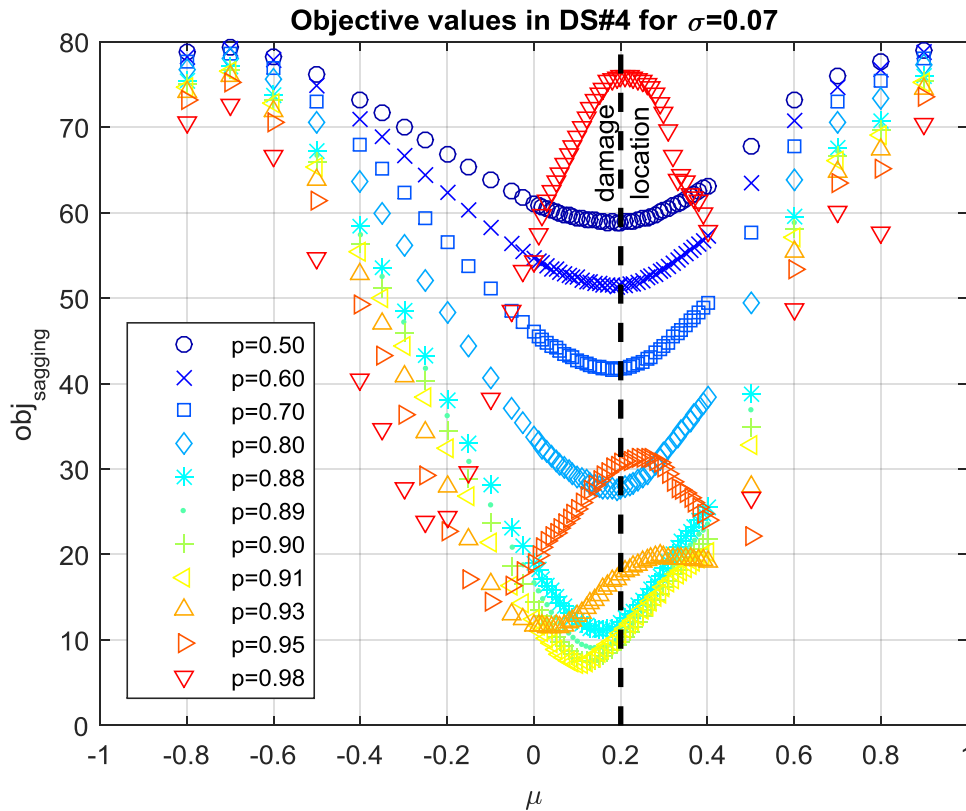
Figure 8.27: Values for $obj_{sagging}$ vs. μ in DS#4 with fixed $\sigma = 0.07$

For the most values of p, the minimal objective value can indeed be found at $\mu = 0.2$, the real damage location. But from $p = 0.88$ upwards, the localisation appears less accurate. For example, with $p = 0.91$, the smallest objective value can be found at $\mu = 0.11$. If p exceeds

this value, the behaviour of the objective function changes completely. In this case, around $\mu = 0.2$ a maximum appears instead of a minimum. This behaviour can be explained as follows. In DS#4 severe damage was already present, so the simulated displacements are too small with low values of p. If the parameter p increases, at first the deviation between simulation and measurement gets smaller. For an optimal p, they nearly match, but if p is moreover increased, the simulated displacements become higher than the measured ones. Therefore, simulation and reality veer away from each other.

Furthermore, for $p > 0.91$ two new local minima appear to the left and right of the damage location. This means the solution of the optimisation problem is not unique, because all minima represent a solution. If the objective function is not evaluated visually, as in this experiment, but an automatic optimisation algorithm is used, it can happen, depending on the algorithm, that not the minimum is found, which corresponds with the correct damage location. The global minimum is the smallest point of the whole objective function. It can be assumed, that this must be the "correct" minimum that indicates the damage, but in fact this is not guaranteed.

In Figure 8.28 the objective values are plotted for all four objective functions with the parameter p and σ fixed on the values from Table 8.6.

a) $obj_{sagging}$

b) obj_{add}

c) obj_{ef}

d) obj_{MAC}
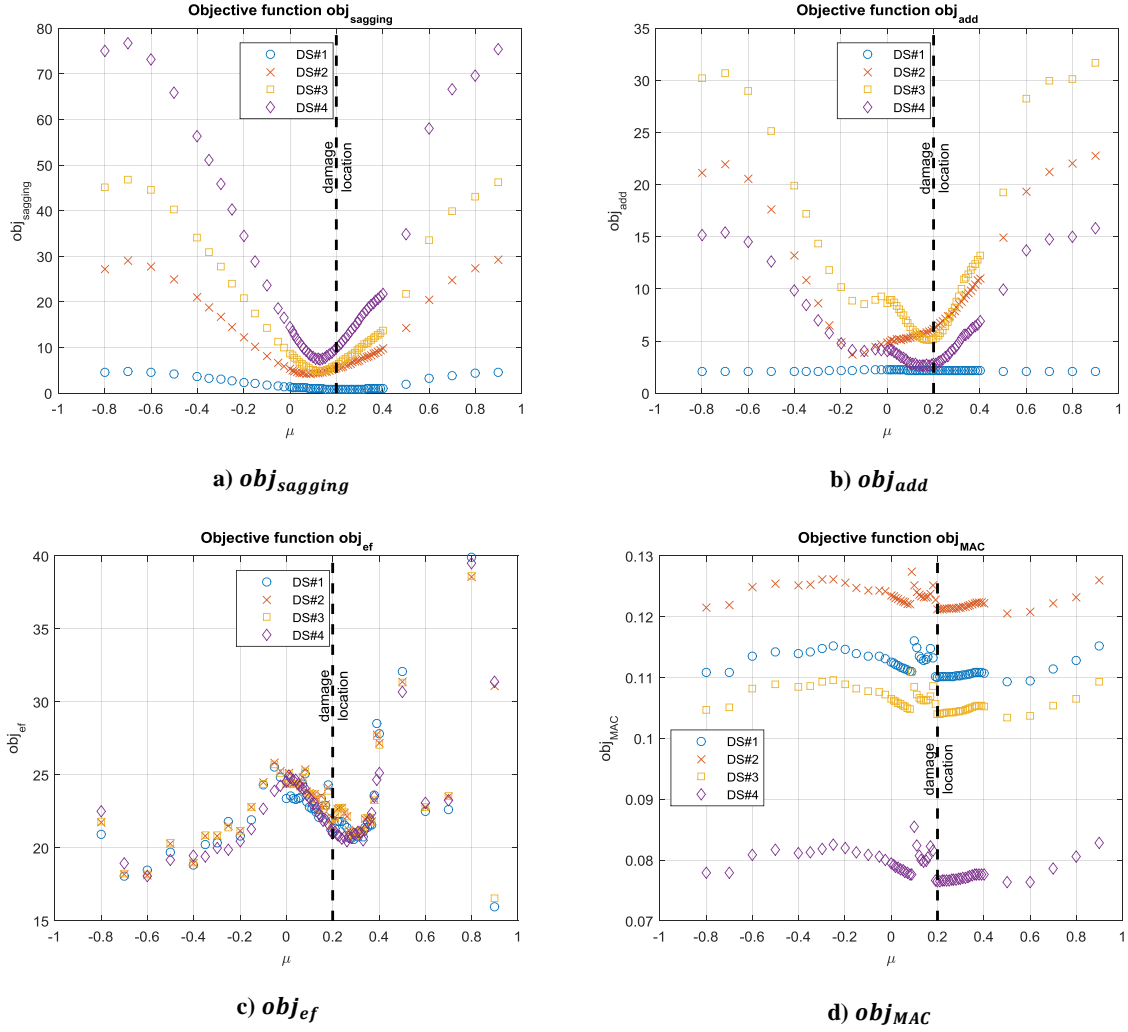
Figure 8.28: Objective functions vs. μ with optimal values from Table 8.6

Every function shows a minimum not far from the damage location, but additional minima may appear. In some cases they are even lower than the minimum near the damage location (e.g. for obj_{ef} in Figure 8.28c). The damage function based on the mode shapes obj_{MAC} (Figure 8.28d) shows a curious behaviour near the damage location, where the function seems to be unsteady as two steps appear. Caused by these steps, a local minimum appear left from the damage location but it is still higher as the value of the damage function directly at the damage location.

From the above plots the location of the minima, which are located nearest to the real damage position, were determined and Table 8.6 was updated as follows.

Table 8.7: Parameter sets with minimal objective values

DS#	**obj**$_\text{sagging}$			**obj**$_\text{add}$		
	p	μ	σ	p	μ	σ
1	0.25	0.20	0.04	0.10	0.50	0.01
2	0.50	0.09	0.10	0.88	-0.15	0.09
3	0.73	0.13	0.08	0.98	0.18	0.06
4	0.90	0.13	0.07	0.95	0.16	0.04
	obj$_\text{ef}$			**obj**$_\text{MAC}$		
DS#	p	μ	σ	p	μ	σ
1	0.99	0.29	0.01	0.70	0.50	0.10
2	0.99	0.29	0.01	0.73	0.50	0.09
3	0.99	0.29	0.01	0.73	0.50	0.09
4	0.98	0.26	0.02	0.70	0.50	0.10
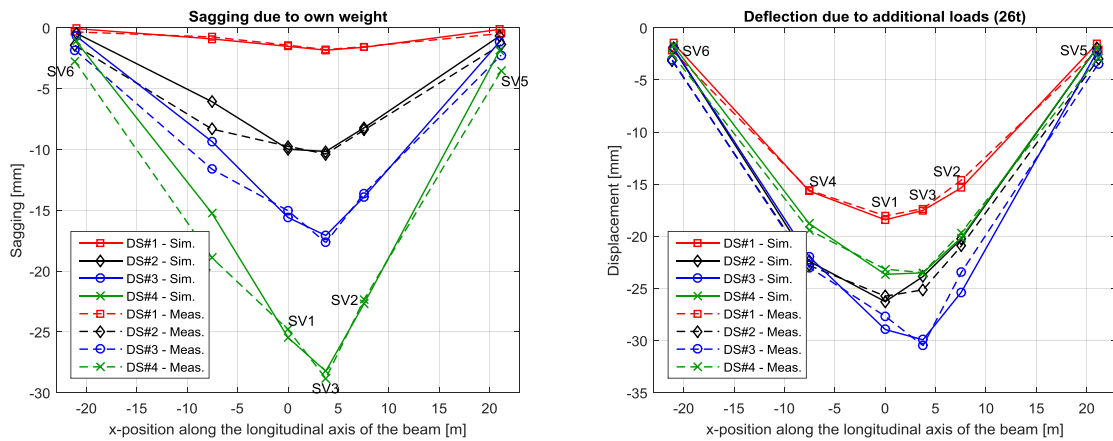
Figure 8.29: Comparison of measured to simulated deflections, if the found optimal parameter sets are used.

Table 8.8: Comparison of measured to simulated eigenfrequencies, if the found optimal parameter sets are used.

	DS#1		DS#2		DS#3		DS#4	
	meas.	sim.	meas.	sim.	meas.	sim.	meas.	sim.
B1a	2,88	2,76	2,85	2,76	2,84	2,76	2,78	2,67
T1	4,49	5,05	4,46	5,05	4,46	5,05	4,45	5,03
B2	7,55	7,32	7,51	7,32	7,51	7,32	7,45	7,28

For the found parameter sets, the reduction of the Young's modulus along the beam's axis compared to the initial value, is shown in the below figure for all damage scenarios.
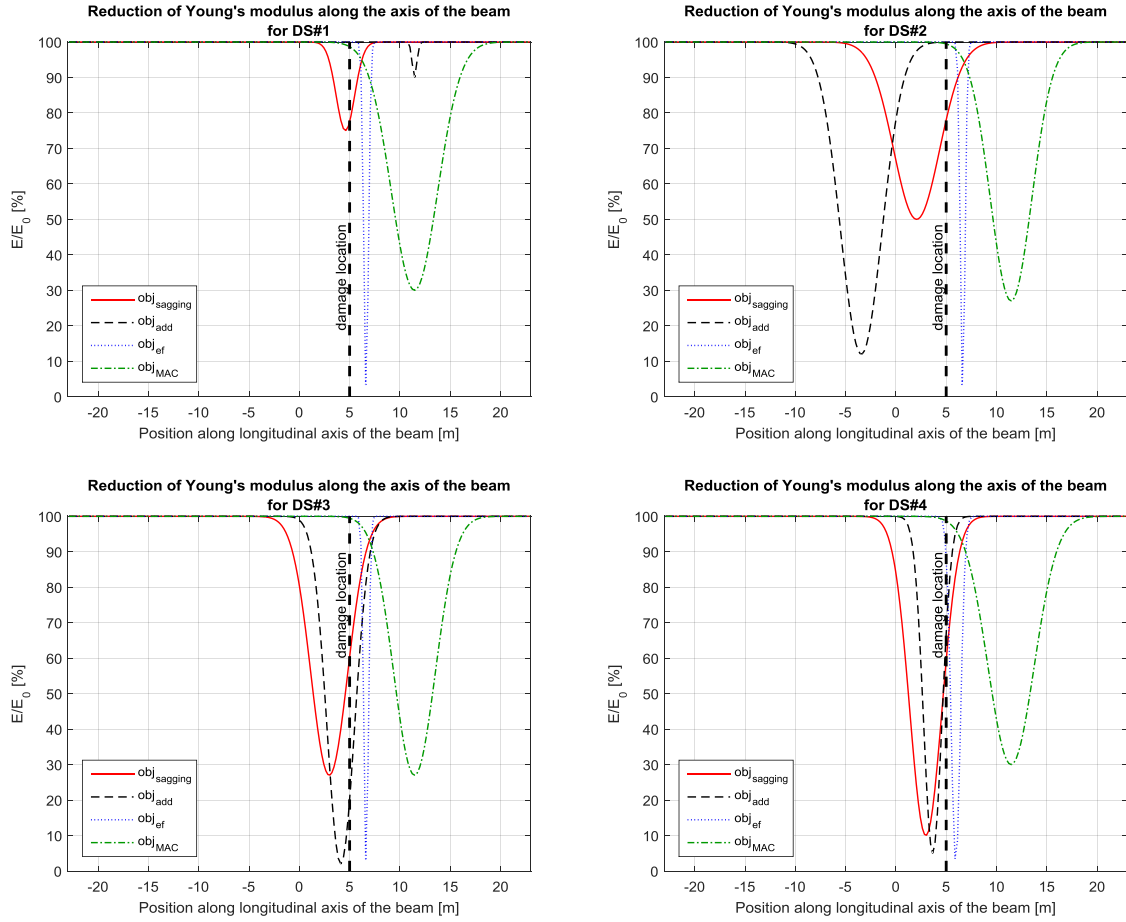
Figure 8.30: Reduction of Young's modulus along the axis of the beam in the FE-model based on the found optimal parameter sets

Finally, a plot is shown for $obj_{sagging}$, which shows the reduction of the Young's modulus over the axis of the beam according to the found optimal parameter sets for all damage scenarios.
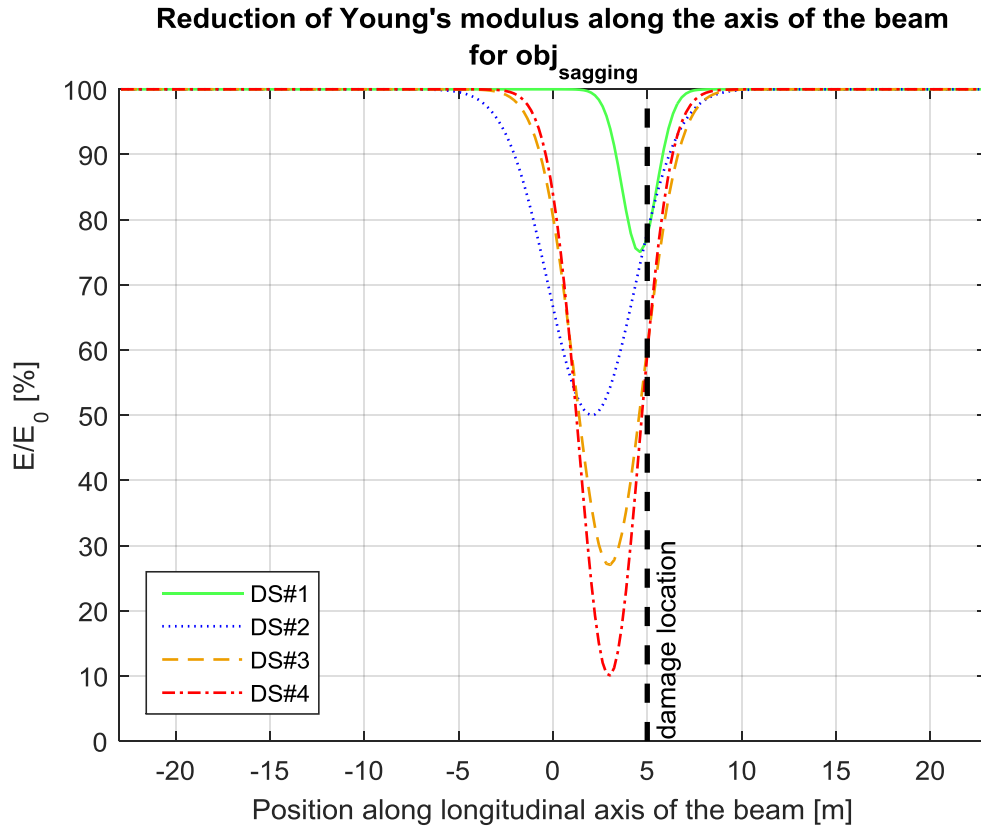
Figure 8.31: Reduction of Young's modulus along the axis of the beam in the FE-model based on the found optimal parameter sets for $obj_{sagging}$

As a conclusion it can be said, that the objective function, which based on the sagging of the beam, worked best in this evaluation. Figure 8.31 shows that, in spite of the coarse FE mesh, the location of the crack is well indicated by the peak of the damage function that depends on parameter μ. As a result, the maximum of the reduction of the Young's modulus in the model is located near the real damage location for all damage scenarios. Even the increasing severity of the damage from DS#1 to DS#4 can be seen by the magnitude of the reduction that is defined by parameter p. A less accurate parameter for the level of damage is parameter σ, i.e. the width of the damage function.

From the plots in Figure 8.30, it can be seen that also the other evaluated objective functions indicated the damage quite well. The objective function based on the comparison of the mode shapes by means of MAC (obj_{MAC}), shows less appropriate for damage detection. This was explained here by the fact that it was not possible to identify the mode shapes with sufficient accuracy in the experimental modal analysis, which was performed at the test beam.

8.5 Results of model updating with refined FE mesh

In Chapter 8.2 an FE-model was described with a finer mesh in the vicinity of the damage location. As elucidated there, the finer mesh allows modelling the impact of a crack on the stiffness more realistic. This can be done by defining the damage function as a narrow peak, i.e. by using small values for the updating parameter σ. By doing this, Young's modulus of the beam is affected only over a small region. Generally, this region of influence is smaller than in Chapter 8.4 for the coarse mesh. This also means that the impact on the simulated displacements are smaller, if the same values for p would further be used. Therefore, it was expected that higher values for p above 0.99 will here result as optimal parameter. The value $p = 1$ would mean a reduction by 100%, which would be the same as supressing the concerned elements before the simulation run, so it is the maximum. Although between 0.99 and 1 is not a far range, it has to be considered that $p = 0.999$ means a ten times higher reduction of the Young's moduli as it is achieved for $p = 0.99$. Therefore, by considering more decimal places for parameter p, the range of the stiffness reduction can be greatly expanded. The considered parameter range was here $p: 0.6$ to 0.9999 and $\sigma: 0.005$ to 0.3804.

While in Chapter 8.4 the complete beam was considered, here the region of interest is reduced to the part with the refined mesh, i.e. $1\,m$ left and right of the damage. For this purpose, the limits of the damage element were set to the beginning and the end of the refined mesh. When comparing the parameter values used in Chapter 8.4 to the ones used here, it has to be considered that since the damage element is now smaller, the values of σ cannot be directly compared, i.e. the same value for σ will now lead to a reduction of the Young's modulus in a smaller region than in the previous evaluation.

Since the damage is now located exactly in the middle of the damage element, the expected optimal value for μ is now zero. Furthermore, in Chapter 8.2, it was stated that depending on the parameter μ, it can happen that the intended reduction of the stiffness will not be reached, especially if small values for σ are used. In spite of the finer mesh this could happen in this evaluation, above all for the border areas of the damage element (μ near 1 or -1), because here the mesh becomes coarser. In order to guarantee here, that the maximum of the damage function is always used, the parameter μ is always set to match the centres of gravity of the slices.

At first, as for the coarse mesh, an example of the calculated objective values for the function $obj_{sagging}$ in damage scenario DS#4 is shown. In the first step the parameter μ was fixed to 0.0053, which is the nearest value to 0, beside -0.0053, that was evaluated.
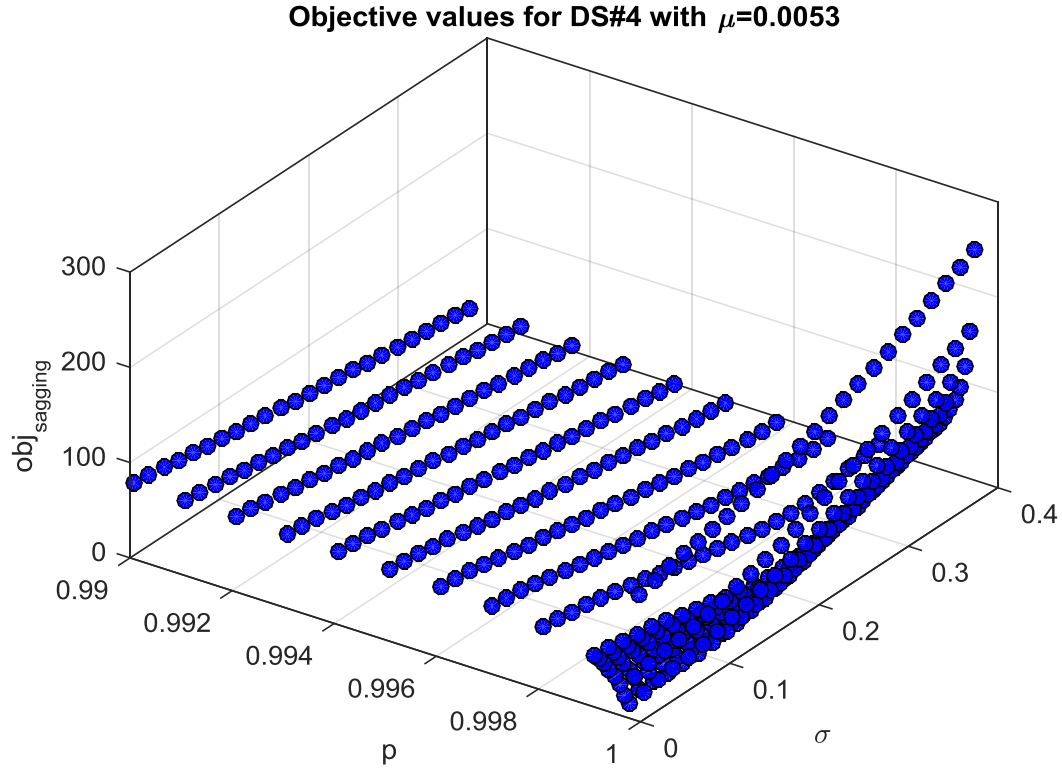

Figure 8.32: 3D scatter plot of objective function based on the sagging of the test beam for fixed μ

Here it can be seen that the minimum of the function can be found for values of p that are very near to 1, but also that the function rises again for even higher values. The parameter sets, which minimises the objective functions for a fixed $\mu = 0.0053$ were searched for all damaged scenarios. The results are listed in Table 8.9.

Table 8.9: Parameter sets with minimal objective values for $\mu = 0.0053$

DS#	**obj_sagging**			**obj_add**		
	p	μ	σ	p	μ	σ
1	0.9700	0.0053	0.0377	0.8000	0.0053	0.0050
2	0.9950	0.0053	0.1357	0.9991	0.0053	0.2500
3	0.9992	0.0053	0.0703	0.9996	0.0053	0.2500
4	0.9992	0.0053	0.1847	0.9994	0.0053	0.1030
	obj_ef			**obj_MAC**		
DS#	p	μ	σ	p	μ	σ
1	0.9990	0.0053	0.0213	0.6000	0.0053	0.0050
2	0.9991	0.0053	0.0540	0.6000	0.0053	0.0050
3	0.9991	0.0053	0.0540	0.9000	0.0053	0.0050
4	0.9992	0.0053	0.0540	0.6500	0.0053	0.3804

Again, the courses of the objective functions for the resulting optimal parameter sets are plotted in Figures 8.33 to 8.36. The minima of the objective functions for the different damage scenarios can be identified for the parameter sets listed in Table 8.9.

a) μ and σ fixed
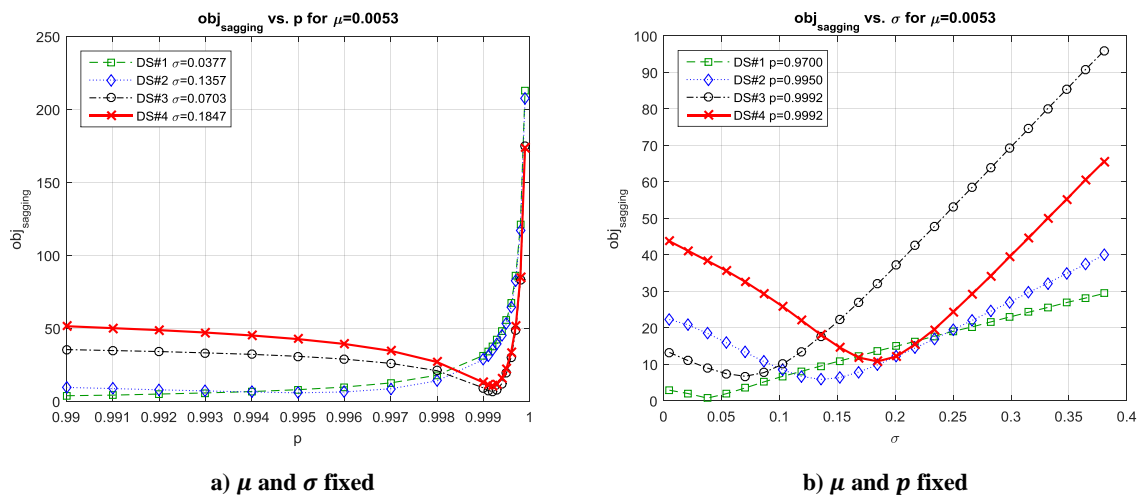
b) μ and p fixed

Figure 8.33: Objective function based on the sagging of the test beam

a) μ and σ fixed
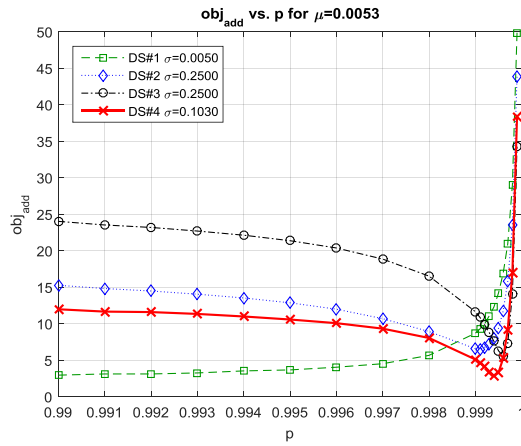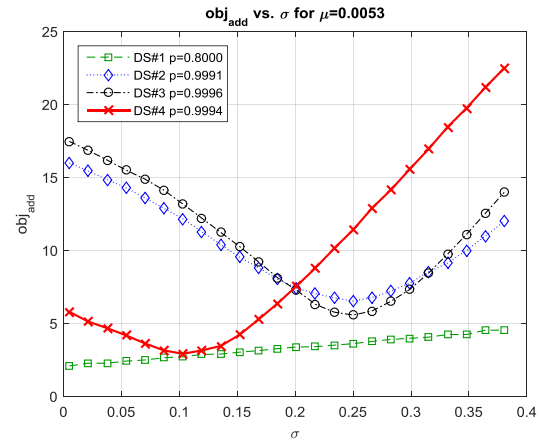
b) μ and p fixed

Figure 8.34: Objective function based on deflection due to additional loads

a) μ and σ fixed
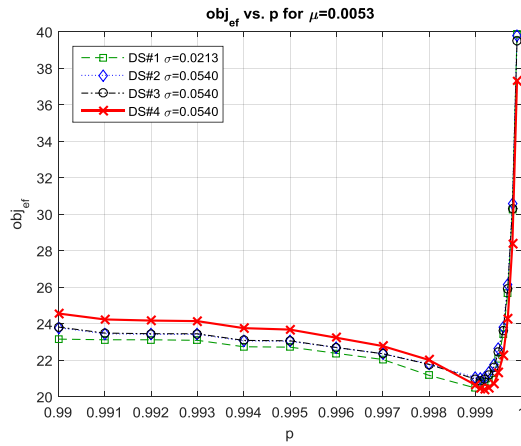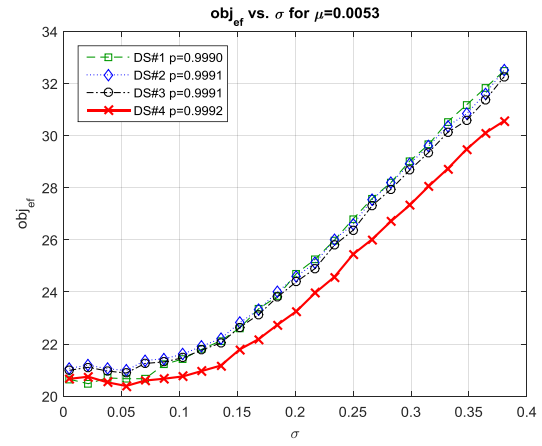
b) μ and p fixed

Figure 8.35: Objective function based on eigenfrequencies

a) obj_{MAC} **vs.** p **for fixed** μ **and** σ b) obj_{MAC} **vs.** σ **for fixed** μ **and** p
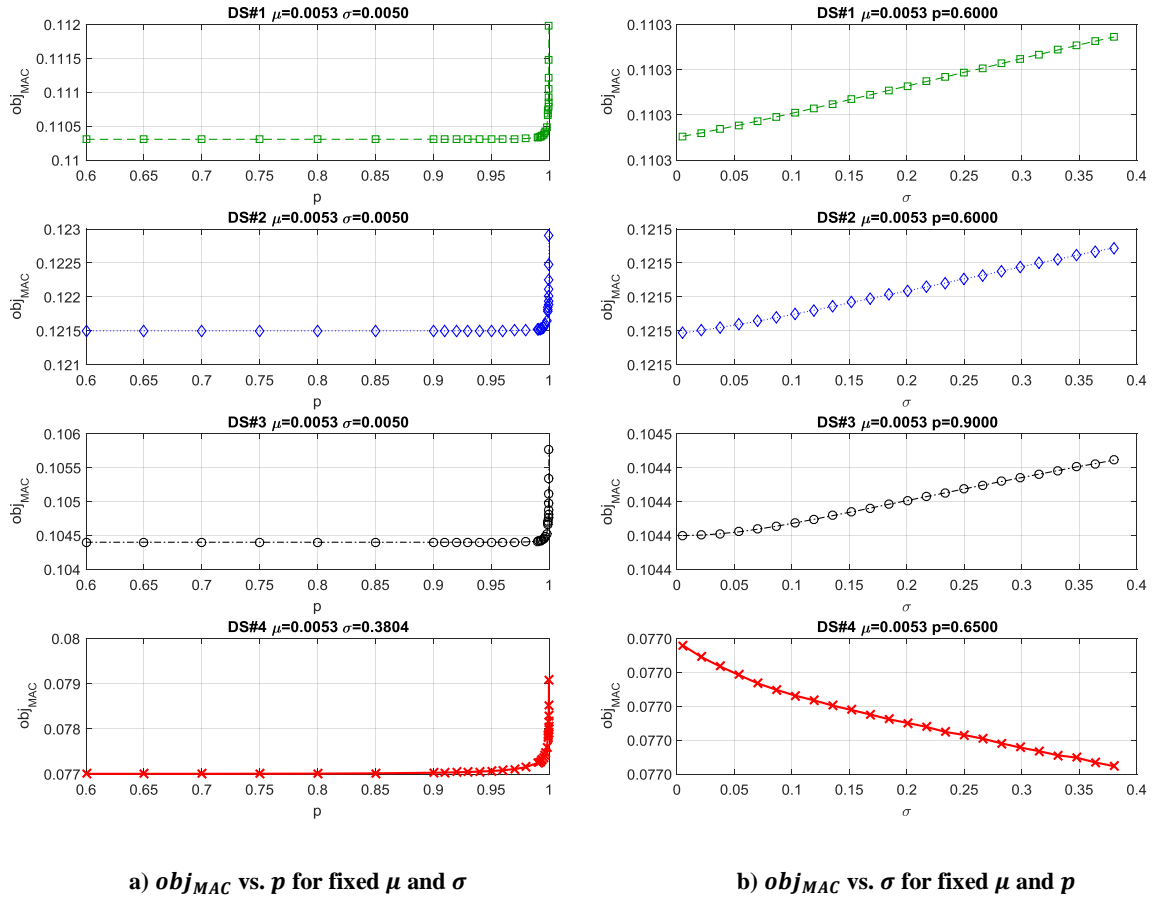
Figure 8.36: Objective function based on mode shape comparison by means of MAC

Now the objective functions vs. parameter μ, i.e. the normalised x-position are plotted, using for p and σ the values from Table 8.9. By doing this, it can be checked if the damage is properly localised.

a) $obj_{sagging}$

b) obj_{add}

c) obj_{ef}

d) obj_{MAC}
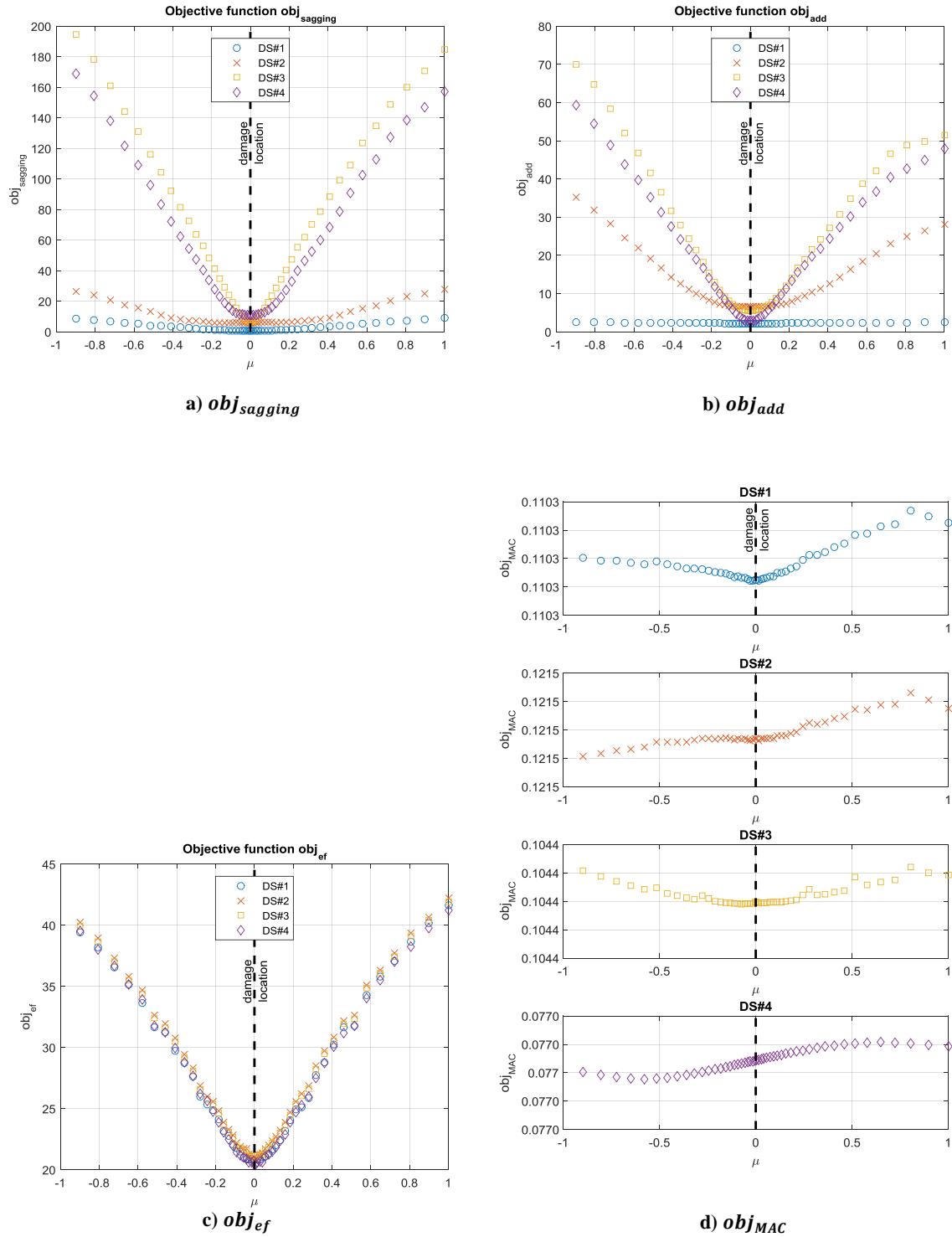
Figure 8.37: Objective functions vs. μ with optimal values from Table 8.9

The above plots show that the minima of the objective functions $obj_{sagging}$, obj_{add} and obj_{ef} appear very near to the damage location. Only for the objective function based on the mode shapes obj_{MAC}, this did not work so well. For $obj_{sagging}$ and obj_{add}, the damage localisation become clearer with increasing damage, as it was the case when using the coarse

mesh. Table 8.10 is again an update of Table 8.9 with the optimal values for μ that were found in Figure 8.37.

Table 8.10: Parameter sets with minimal objective values

DS#	$\mathbf{obj_{sagging}}$			$\mathbf{obj_{add}}$		
	p	μ	σ	p	μ	σ
1	0.9700	0.0053	0.0377	0.8000	0.0053	0.0050
2	0.9950	-0.1833	0.1357	0.9991	0.0053	0.2500
3	0.9992	0.0053	0.0703	0.9996	-0.0164	0.2500
4	0.9992	0.0053	0.1847	0.9994	0.0053	0.1030

DS#	$\mathbf{obj_{ef}}$			$\mathbf{obj_{MAC}}$		
	p	μ	σ	p	μ	σ
1	0.9990	0.0053	0.0213	0.6000	0.0164	0.0050
2	0.9991	0.0053	0.0540	0.6000	-0.8989	0.0050
3	0.9991	0.0053	0.0540	0.9000	-0.0733	0.0050
4	0.9992	0.0053	0.0540	0.6500	-0.5789	0.3804
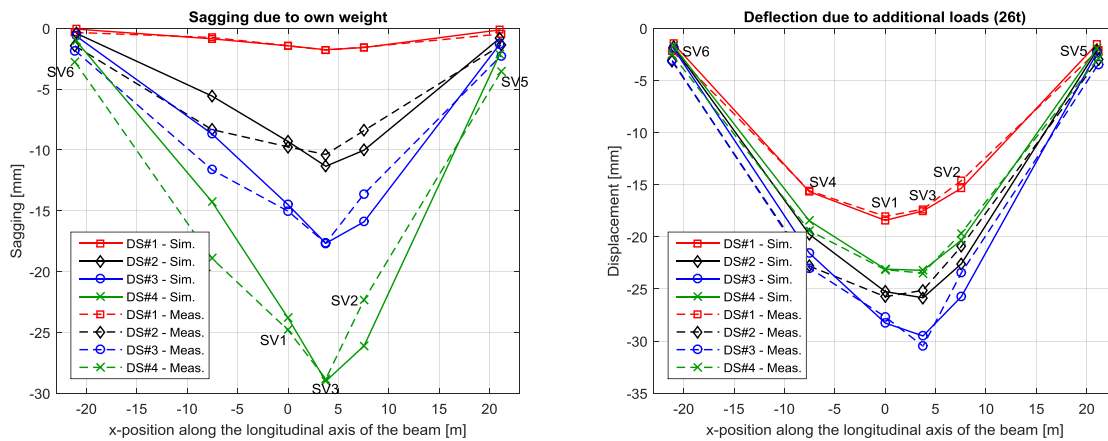
Figure 8.38: Comparison of measured to simulated deflections, if the found optimal parameter sets are used.

Table 8.11: Comparison of measured to simulated eigenfrequencies, if the found optimal parameter sets are used.

	DS#1		DS#2		DS#3		DS#4	
	meas.	sim.	meas.	sim.	meas.	sim.	meas.	sim.
B1a	2,88	2,71	2,85	2,66	2,84	2,66	2,78	2,63
T1	4,49	5,07	4,46	5,05	4,46	5,05	4,45	5,04
B2	7,55	7,44	7,51	7,40	7,51	7,40	7,45	7,39

Now the reduction of the Young's modulus along the length of the beam is plotted according to the optimal parameter sets from Table 8.10. When comparing the following plots to Figures 8.30 and 8.31, it must be considered that here the range of the abscissa does not cover the entire beam, but extends only from 4 to 6 m, i.e. the region with the refined FE mesh.
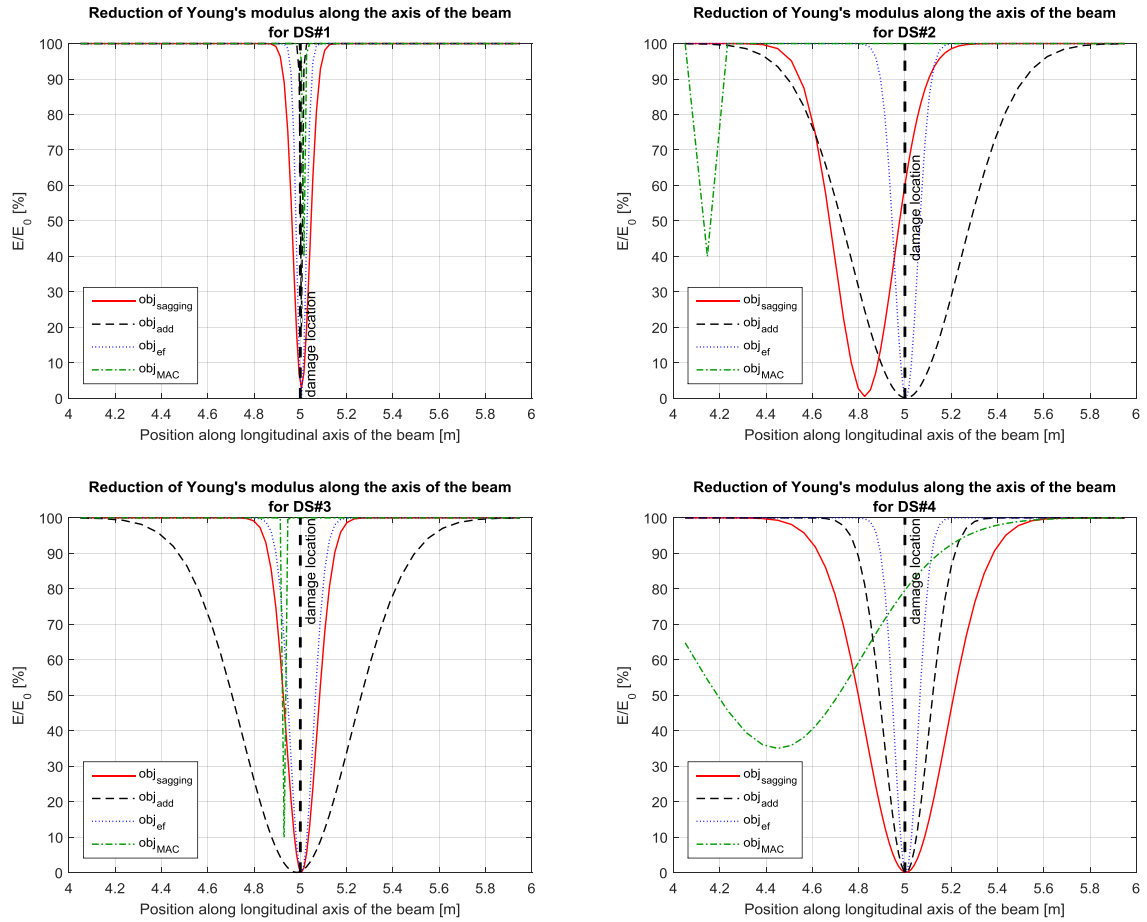
Figure 8.39: Reduction of Young's modulus along the axis of the beam in the FE-model based on the found optimal parameter sets

As in the previous evaluation for the coarse mesh, here a plot is shown for $obj_{sagging}$, which shows the reduction of the Young's modulus over the axis of the beam according to the found optimal parameter sets for all damage scenarios.
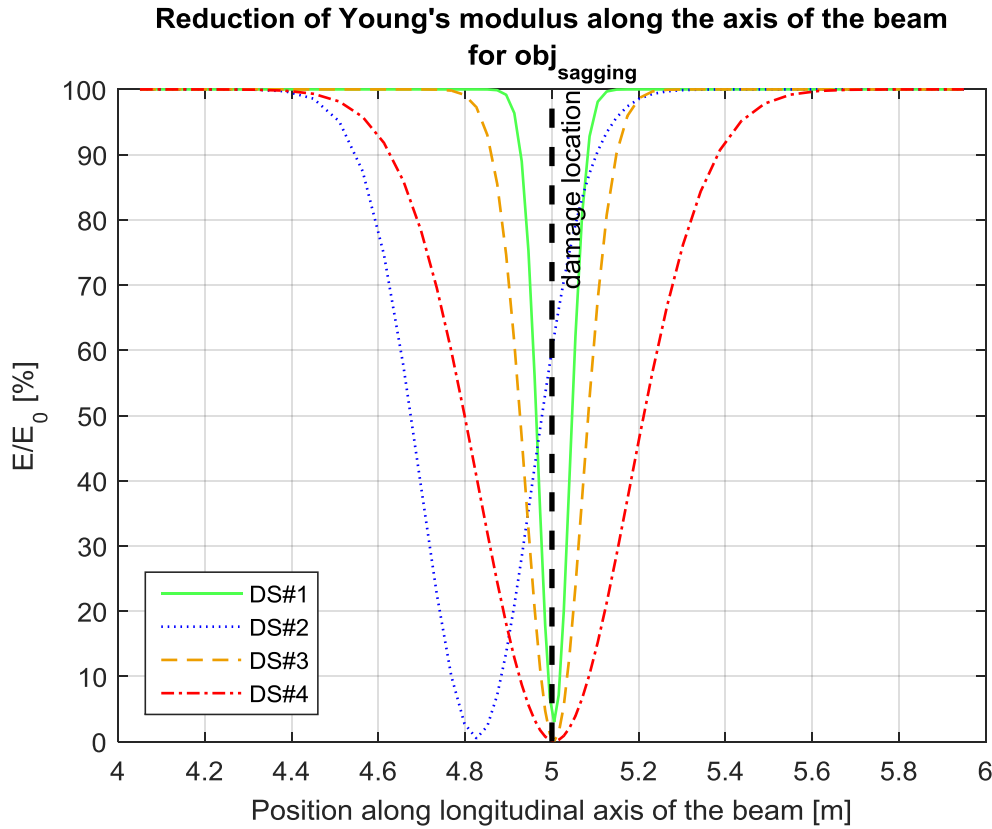
Figure 8.40: Reduction of Young's modulus along the axis of the beam in the FE-model based on the found optimal parameter sets for $obj_{sagging}$

The FE-mesh for the simulated test setup was refined for two reasons. The first one was to achieve a higher accuracy for the damage localisation. The second one was to be able to model the damage more realistic by defining the damage function as a narrow peak. For this reason, the parameter range for the search of minima of the objective function was changed compared to the evaluation with the coarse mesh. That means the width of the bell curve that was defined by the damage function was reduced by using smaller values for parameter σ. In order to compensate this, higher values for p must be used.

If in the model with the refined mesh the Young's modulus along the length of the beam is reduced according to the optimal parameter sets, which were found with the coarse mesh, quite similar simulation results and objective values can be expected. This is because the only difference between the models is the refined mesh. Therefore, using the same parameter range for both models makes no sense.

The result of the new evaluation with the refined mesh was that by using the previously defined objective functions based on the static properties sagging of the beam and bending due to a test load, the damage localisation worked very well. The same can be said, if the eigenfrequencies are considered. With these objective functions it is even possible to estimate

the severity of the damage by looking at the increase of parameter p with increasing damage. As it was the case for the coarse mesh, the objective function based on the comparison of the mode shapes by means of MAC was not appropriate. This is again due to the insufficient accuracy of the experimentally determined mode shapes.

8.6 Results of model updating with refined FE mesh using the L1-norm

In this chapter, the used norm for the calculation of the objective function will be changed from L2 to L1. Hence the four evaluated functions changes according to the following equations.

$$
\begin{aligned}
obj_{sagging}(\{p\}) &= w\left\|\left(\{exp_{sagging}\} - \{sim_{sagging}(\{p\})\}\right)\right\|_1 \\
&= \frac{1}{N} \cdot \frac{1}{\Delta} \cdot \sum_{i=1}^{N} \left| {_i}exp_{sagging} - {_i}sim_{sagging}\{p\}\right|
\end{aligned}
\tag{8-12}
$$

$$
\begin{aligned}
obj_{add}(\{p\}) &= w\left\|\left(\{exp_{add}\} - \{sim_{add}(\{p\})\}\right)\right\|_1 \\
&= \frac{1}{N} \cdot \frac{1}{\Delta} \cdot \sum_{i=1}^{N} \left| {_i}exp_{add} - {_i}sim_{add}\{p\}\right|
\end{aligned}
\tag{8-13}
$$

$$
\begin{aligned}
obj_{ef}(\{p\}) &= w\left\|\left(\{exp_{ef}\} - \{sim_{ef}(\{p\})\}\right)\right\|_1 \\
&= \frac{1}{N} \cdot \frac{1}{\Delta} \cdot \sum_{i=1}^{N} \left| {_i}exp_{ef} - {_i}sim_{ef}\{p\}\right|
\end{aligned}
\tag{8-14}
$$

$$
obj_{MAC}(\{p\}) = \frac{1}{N} \cdot \sum_{i=1}^{N} \left|1 - MAC\left({_i}\psi_{meas}, {_i}\psi_{sim}(\{p\})\right)\right|
\tag{8-15}
$$

Since the square root is missing in these definitions, the objective values obtained are in general higher as the ones obtained if the L2-norm is used. This effect can be seen when comparing the below Figure 8.41 to Figure 8.32, where the values of function $obj_{sagging}$ are plotted if L1- or L2-norm is used, respectively. Therefore, the range of values of the objective functions is larger with the L1-norm.

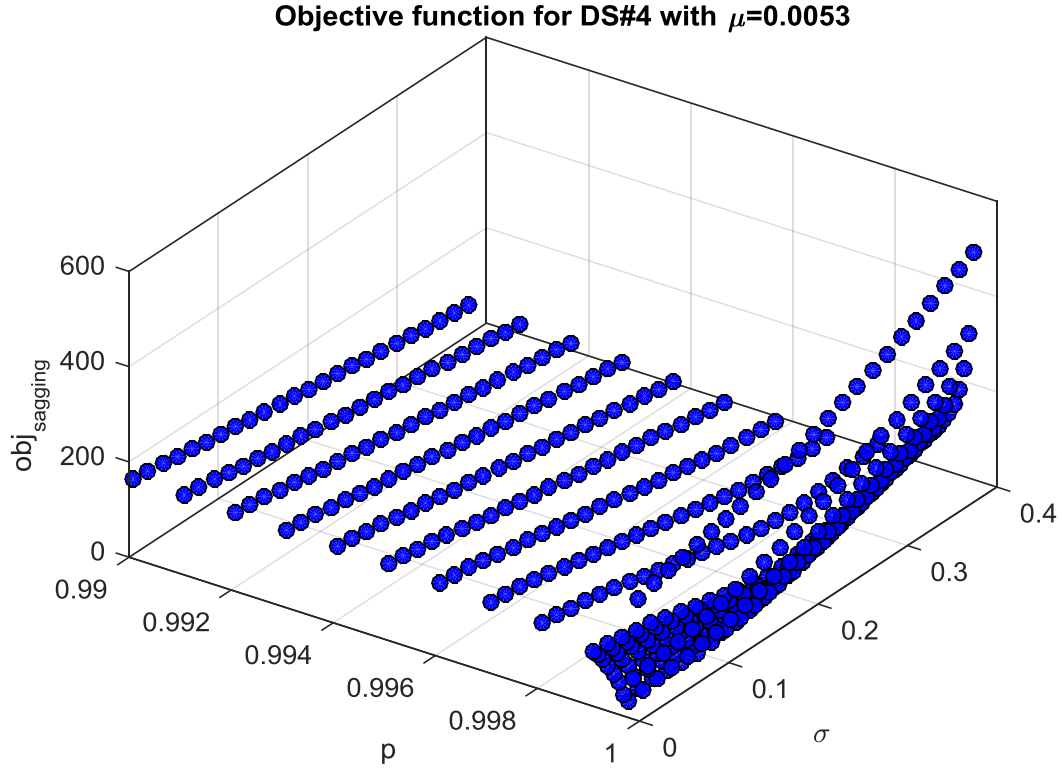Here, the same parameter range was considered as in the evaluation using the L2-norm.

Figure 8.41: 3D scatter plot of objective function based on the sagging of the test beam for fixed μ (L1-norm)

At first, it was expected that the minima of the objective functions with L1-norm are the same as the ones if L2-norm is used, but they slightly differ. The new values for fixed $\mu = 0.0053$ are listed in Table 8.12.

Table 8.12: Parameter sets with minimal objective values for $\mu = 0.0053$

	obj$_{\text{sagging}}$			**obj$_{\text{add}}$**		
DS#	p	μ	σ	p	μ	σ
1	0.9700	0.0053	0.0377	0.8000	0.0053	0.0050
2	0.9900	0.0053	0.1847	0.9990	0.0053	0.2337
3	0.9992	0.0053	0.0703	0.9993	0.0053	0.3478
4	0.9993	0.0053	0.1683	0.9960	0.0053	0.3315
	obj$_{\text{ef}}$			**obj$_{\text{MAC}}$**		
DS#	p	μ	σ	p	μ	σ
1	0.9970	0.0053	0.0213	0.6000	0.0053	0.0050
2	0.9980	0.0053	0.0050	0.7000	0.0053	0.0050
3	0.9980	0.0053	0.0213	0.6500	0.0053	0.0213
4	0.9980	0.0053	0.0703	0.7500	0.0053	0.3804

The plots of the objective functions vs. updating parameter p and μ based on these parameter sets can be found in Appendix A.3.

In the next step, like in the previous evaluations, simulations were performed, where the values of p and σ were fixed to the ones listed in Table 8.12 and μ was varied. By evaluating the results from these simulations the optimal value for μ that corresponds to the found parameter sets, was determined and Table 8.12 was updated as follows.

Table 8.13: Parameter sets with minimal objective values

DS#	$\mathbf{obj_{sagging}}$			$\mathbf{obj_{add}}$		
	p	μ	σ	p	μ	σ
1	0.9700	0.0053	0.0377	0.8000	0.0053	0.0050
2	0.9900	-0.4078	0.1847	0.9990	-0.0164	0.2337
3	0.9992	0.0053	0.0703	0.9993	0.0053	0.3478
4	0.9993	0.0053	0.1683	0.9960	-0.1833	0.3315
DS#	$\mathbf{obj_{ef}}$			$\mathbf{obj_{MAC}}$		
	p	μ	σ	p	μ	σ
1	0.9970	0.0053	0.0213	0.6000	0.0164	0.0050
2	0.9980	0.0053	0.0050	0.7000	-0.0053	0.0050
3	0.9980	0.0053	0.0213	0.6500	-0.8070	0.0213
4	0.9980	0.0053	0.0703	0.7500	-0.3608	0.3804
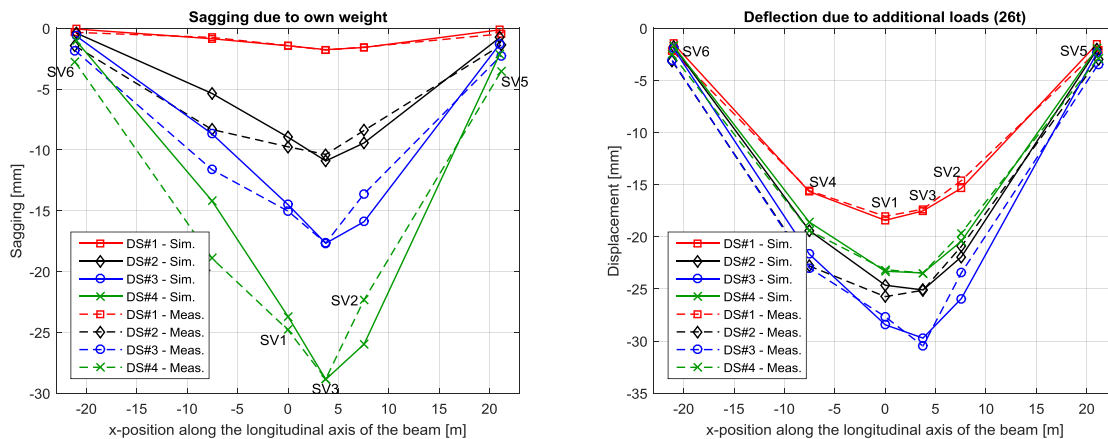
Figure 8.42: Comparison of measured to simulated deflections, if the found optimal parameter sets are used.

Table 8.14: Comparison of measured to simulated eigenfrequencies, if the found optimal parameter sets are used.

	DS#1		DS#2		DS#3		DS#4	
	meas.	sim.	meas.	sim.	meas.	sim.	meas.	sim.
B1a	2,88	2,88	2,85	2,85	2,84	2,84	2,78	2,77
T1	4,49	5,15	4,46	5,13	4,46	5,12	4,45	5,10
B2	7,55	7,51	7,51	7,50	7,51	7,48	7,45	7,45

Here not all plots are shown as in the previous chapters, but they can be found in Appendix A.3. Instead an interesting change that has been observed in the course of objective function

obj_{ef} will be discussed. Therefore, the following figure shows a comparison of obj_{ef} using L2 and L1-norm. For all simulations the model with the refined mesh was used.

<div align="center">

a) obj_{ef} with L2-norm   b) obj_{ef} with L1-norm
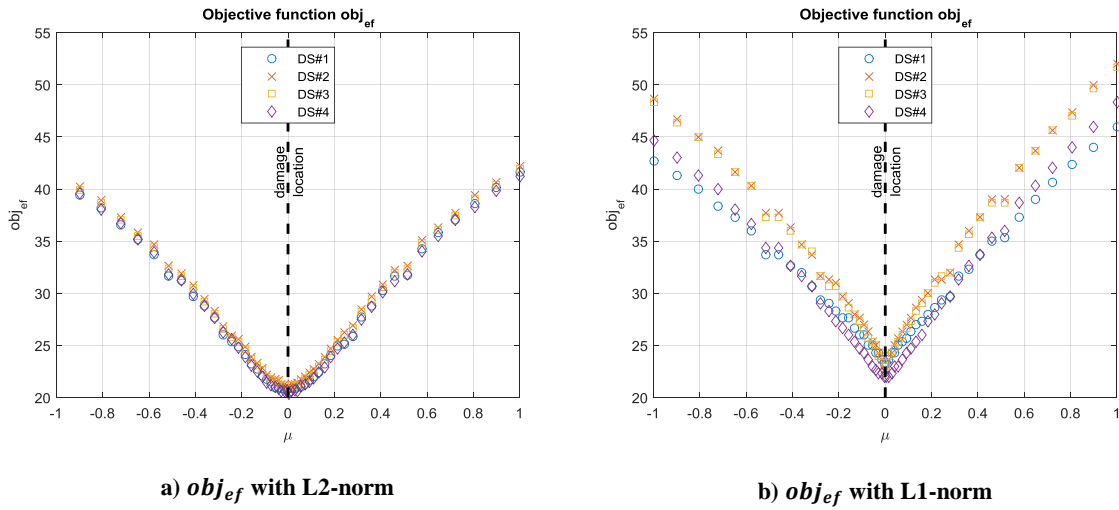
Figure 8.43: Objective functions based on eigenfrequencies vs. μ

</div>

When changing the norm from L2 to L1 the shape of the considered objective function in the vicinity of the damage changes from u-shaped to v-shaped. This has the effect that the position of the minimum is clearer with the L1-norm. Furthermore, since the slope of the objective function with L1-norm near the minimum is higher than with L2-norm, it can be assumed that an automatic optimisation algorithm will converge faster. But this was not tested here.

Finally, the reduction of the Young's modulus along the beam's axis is shown for $obj_{sagging}$ with L1-norm. Further plots for all objective functions can be found again in Appendix A3.
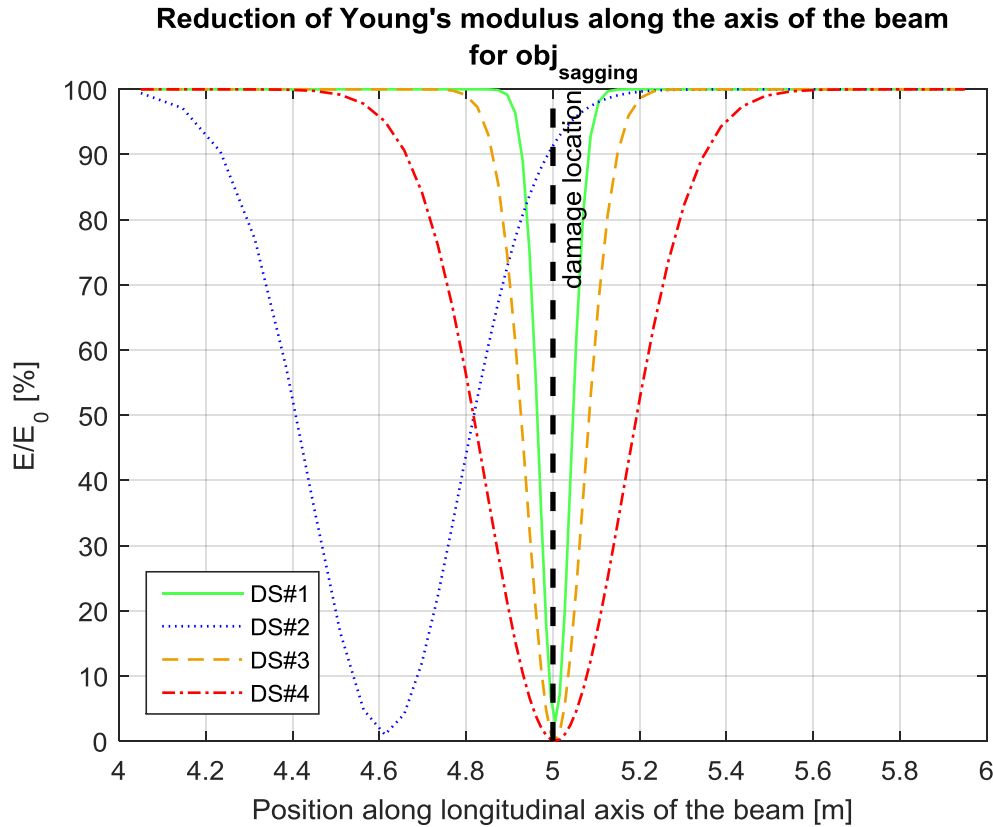
Figure 8.44: Reduction of Young's modulus along the axis of the beam in the FE-model based on the found optimal parameter sets for $obj_{sagging}$ with L1-norm

8.7 Conclusion

In this chapter three evaluations were performed using a model updating procedure for FE-models of the test setup described in Chapter 5. In this optimisation procedure four objective functions were evaluated. Two of them were based on static properties, which were the sagging of the beam and the deflections due to the test loads. Two additional objective functions were based on the dynamic properties eigenfrequencies and mode shapes. At first a model with a relative coarse FE mesh was used and the considered damage element was the whole beam. That means the location of the damage was searched over the complete length of the beam. It was shown by a parameter study, that the created parametrised FE-model, the chosen model updating parameters and the defined objective functions can be efficient to localise damage and to assess the severity of the damage to a certain extent. But because of the coarse FE-mesh the localisation was still quite inaccurate.

Afterwards, the mesh was refined in the vicinity of the found damage location. Furthermore, the damage was searched only in the region with the refined mesh, which means the length of the damage element was reduced. Additionally, the range of the model updating parameters

158

was changed in comparison to the previous evaluation. Now it was possible to locate the damage with high accuracy.

As a conclusion, it can be said that the objective function based on the sagging was the most effective one. It provided even better results as the objective function based on the deflections due to the test loads, which was most likely due to the fact that the sagging is caused by the whole own weight of the beam. Furthermore, the objective function based on the eigenfrequencies provided good results as well. But since variations in the measured eigenfrequencies with increasing damage were very small, the found optimal parameter sets using this objective function for the different damage scenarios were always nearly the same. Therefore, the possibility exists that these results are highly influenced by model uncertainties. The last objective function based on the mode shapes was less useful, which is most properly due to the insufficient accuracy of the identified mode shapes.

Finally, the evaluation with the refined FE-mesh was repeated but with the difference that in the definitions of the used objective functions the L1-norm was used instead of the L2 (Euclidian) norm. Since the L1-norm of a vector is in general higher as the L2-norm, the value range of the new objective functions increased. Therefore, they became more sensitive for changes in the model updating parameters. Furthermore, if the L1-norm is used instead of the L2-norm, the shape of the objective in the vicinity of the minima can change from u-shaped to v-shaped. This may lead to some advantages, if an automatic optimisation algorithm is used for the model updating, which were elucidated in Chapter 8.6.

9 SUMMARY AND DISCUSSION

This work focuses on the testing of various methods for detecting damage on bridges under realistic ambient conditions. The demolition of a prestressed concrete bridge provided the possibility of using one of its concrete beams for a test setup described in Chapter 5.1. The deflection of the beam as well as temperatures of the concrete at different positions and the ambient temperature were recorded permanently. Static loading tests were carried out by mounting two test weights (each $13\ t$) and removing them after at least 24 hours. In addition, an experimental modal analysis (EMA) was performed multiple times to determine the modal properties (eigenfrequencies, mode shapes, damping and modal masses) of the beam. For this purpose, a swept-sine excitation was applied using an electro-magnetic shaker. The resulting vibrations of the structure were detected by means of accelerometers. First, these static and dynamic tests were performed several times in the healthy state to define a reference state. Then in four predefined damage scenarios, artificial damage was stepwise introduced by cutting more and more of the tendons inside the concrete. This resulted in a local drop of prestress, which caused a loss of stiffness. Finally, visible vertical cracks occurred in the concrete, which reduced the supporting cross-section. In the subsequent evaluations of the measured data, it was tested whether these damages could be detected on the basis of the data. The performed tests were described in detail in Chapters 5.2 and 5.3, including an analysis of the influence of temperature fluctuations on the static displacements.

In Chapter 6, a method for compensating this temperature influence was proposed. It relies on the linear dependence of deflection on temperature. Then data measured by the displacement sensors were converted to a fixed reference temperature. As a result of the compensation, the fluctuations in the measured data caused by changes in temperature were reduced. Since these fluctuations are not related to damage, the temperature-compensated values were more suitable for damage detection than the raw data and were used in the following evaluations.

Several damage indicators were evaluated based on experimental measurements and presented in Chapter 7. At first, the static displacements were discussed. The permanently measured data were subdivided into different periods, in which the beam was loaded by the test weights (so-called "loadings") or when they were removed (so-called "unloadings"). For each period as well as for each sensor, a "representative" value for the displacement was derived from the temperature-compensated data. This allowed to plot the deflection of the

beam along its axis for every loading and unloading. Plots were created with the absolute values corresponding to a defined baseline as well as with the deflections due to the test loadings. Furthermore, a cubic spline interpolation was performed for values between the sensor positions. The first and the second derivations of these splines, which present the slopes and curvatures of the deflection lines, were also evaluated. The damage and its position are clearly detectable from these plots. The steady increase of the absolute displacements was denominated in this thesis as "sagging".

Subsequently, the dynamic parameters were also analysed. First, the measured eigenfrequencies were plotted vs. time. They clearly show a drop with increasing damage due to the loss of stiffness of the beam. It is necessary to recall that the settings of swept-sine excitation were always constant and the same algorithm was used for the modal analysis.

Secondly, mode shapes were compared, initially visually and afterwards by means of correlation methods. For the visual comparison, one measurement was selected for each damage scenario and the corresponding mode shapes were drawn. The damage detection from these plots was not successful due to the insufficient quality of the measured mode shapes. In addition, the damage was located near a node of the second bending mode B2 and therefore had little effect on this shape. The mode shapes were also compared by means of usual correlation methods (MAC, NMD, MSF and COMAC). For the first three methods, the mode shapes from 19 measurements were compared to the shapes derived from a measurement in the healthy state, so it was expected that the deviation would increase with increasing damage. It was possible to detect the damage. Afterwards, the same measurements that were used in the visual comparison were considered again. The mode shapes identified in the damaged states (DS#1-DS#4) were compared to the mode shapes in the healthy state by means of COMAC. Although the first visual comparison was not evident, it was now possible to approximately localise the damage in DS#3 and DS#4.

Finally, the modal parameters were summarised by using them for the calculation of a modal flexibility matrix. As explained in [74], this matrix can be used for damage detection, but the robustness of this method strongly depends on the bearing conditions and the damage location.

The most substantial contribution of the present work is in Chapter 8, relating to a model updating procedure. The first step was the creation of a complex FE model for the test setup. It was a 3D model, which consisted mainly of solid elements and the inner tendons modelled

with beam elements. A well designed mapped mesh was created for the meshing of the concrete beam. The aim is enabling the possibility to assemble several elements into a "slice" with determined position along the beam's axis, whose Young's modulus could be changed separately to simulate stiffness losses due to damage. Directly parameterising them would have led to a huge number of parameters for the model updating process. Therefore, the reduction of the Young's modulus along the beam axis was defined by a so-called damage function. This function included only 3 parameters, which now represented the model updating parameters. The simulation outputs were compared with the measurement results by means of 4 objective functions. The latter were defined based on different physical properties, sagging, deflection due to test loads, eigenfrequencies and mode shapes.

A parameter study was carried out, in which the simulation has been calculated many times with different parameter sets. The simulation results were then compared to measurements from every damage scenario. This means that values of all 4 objective functions for any damage scenario were derived from the results of each individual simulation. Now parameter sets had to be found which minimised the objective functions, i.e. which led to the best match between simulation and measurement. According to the damage function, these optimal parameter sets led to a certain reduction of the Young's modulus along the axis of the beam. As a final result, this reduction was shown graphically, where the damage location was indicated. The procedure was carried out with two models. At first a relative coarse mesh was used and the damage was searched over the whole length. After the damage location was approximately identified, the evaluation was repeated with a refined mesh in the vicinity of the damage, resulting in a changed parameter set. Now it was clearly possible to locate damage with high precision. The effectiveness of the method depends strongly on the considered physical quantities.

Finally, the second model with a refined mesh was evaluated again. This time, in the definition of objective functions, the L1 norm was used instead of the previously used L2 (Euclidian) norm. This increased the value range of the objective functions, i.e. equal changes in the measured characteristics lead to higher changes to the objective function values. This makes the objective function more sensitive to changes to the input data. In addition, the evaluation revealed that if the L1-norm is used, the objective functions can become v-shaped in the vicinity of the minima instead u-shaped as with the L2-norm. This leads to the fact that the minima can be localised more precisely. It can be assumed that the mentioned changes

due to the L1-norm is advantageous for an automatic optimisation algorithm. However, this has not been tested within this thesis.

10 MAIN CONCLUSIONS AND OUTLOOK

The static loading tests of the prestressed concrete beam in this thesis showed after loading with test weights increased deformation over time due to the formation of cracks. After the load was removed, deformations remained, i.e. the beam did not return to the initial position. In the present thesis the continuous downwards movement of the beam due to plastic effects is here referred to as "sagging". The plastic deformations were large in the first static tests directly after the beam was damaged, which led to large permanent deformations. However, the effects also occurred in the healthy state, but less. In a second static test in damage scenario DS#4, nearly no permanent deformations were observed, in opposite to the first test in the same scenario. This leads to the conclusion, that after changes at the structure, like for instance damage, it takes some time until a new steady state is reached. Therefore, it is recommended for future tests to always carry out at least 2 static loadings in each state and to evaluate only the results from the second loading.

The direct observation of the sagging together with model updating appeared to be very useful for damage detection. It is clear because stiffness losses are directly reflected in the sagging. It reveals that for damage assessment, measuring of sagging is even more efficient than measuring the deflection due to a test load, like it was also done in this thesis with a load of 26t. This can be explained by the fact that the sagging is caused by the own weight of the bridge, which is by far higher as its service load, i.e. the maximal test load.

But in order to monitor the sagging it is necessary to measure absolute deformations of the structure with respect to a fixed reference line. This is seldom realised, as it is difficult to define reference points, which remain fixed during the whole life of the bridge. It is believed that in the future, the sagging of bridges could be practically monitored by means of accurate GPS measurements or photogrammetry.

Furthermore, the measured static deformations revealed an unavoidable influence of temperature fluctuations. This temperature effect should be separated from the influence of damage. For this purpose a compensation method was proposed and it showed good results. Above all temperature gradients in the structure have a high influence on the deformations, as it was shown theoretically for a temperature difference between the upper and the lower region of a simple beam. In future tests the temperature gradients should be monitored more in detail to further examine the effect and to obtain a large data base for temperature

compensation. For instance, the temperature distribution along the cross-section of the beam at different positions along the axis should be of interest. Furthermore, a temperature compensation for the measured eigenfrequencies should be realised as well, though the asphalt layer was already removed on the test beam.

Of the measured modal parameters, eigenfrequencies appeared as a reliable damage indicator, although no localisation is possible from their direct observations. Damage detection also succeeded to a certain extent with mode shapes. But the mode shapes were not measured with sufficient accuracy. This was probably the reason, why the modal flexibility matrix was here not effective for damage detection. Above all, the torsional modes could not be well identified. This was the case, because only a few accelerometers were mounted near the edges of the top flange. In future tests these should be improved. Furthermore, the dynamic test should be carried out also during periods when the beam is loaded with test weights. This is because cracks will open due to the loading and so they can be detected easier. At real bridges dynamic tests while the bridge is loaded are costly and not appropriate to be realised with a monitoring system. But for the development of testing methods, a direct comparison between damage assessment results based on dynamic measurements in loaded and unloaded state maybe of interest.

Within the model updating, four objective functions were evaluated based on sagging, deflection due to test loads, eigenfrequencies and mode shapes, respectively. The objective functions, which were based on the static deformations ($obj_{sagging}$ and obj_{add}), appeared most effective for damage detection. But also the eigenfrequencies were useful. The mode shapes were not beneficial by the fact that they had not been identified well.

The objective functions were defined by using the L2-norm (Euclidian norm) as well as the L1-norm. Both evaluations were successful, but the evaluation using the L1-norm revealed some potential advantages, especially for an automatic optimisation algorithm. This argument should be tested in future evaluations. Additionally, it is proposed to test further norms, like other Lp-norms (cf. Appendix A1) or the Frobenius norm in case of comparison between matrices.

For the reason of efficiency and for practical application, the FE-model used in the present thesis is linear, in spite of the fact that nonlinearities are always present in bridges. Therefore, the model could be improved by considering these nonlinearities. For instance the Young's modulus could be defined according to a complete stress-strain diagram. As the inclusion of

nonlinearities in the model will cause a huge computing effort when performing simulations, the number of degrees of freedom should be reduced, e.g. by carrying out a static model condensation, like explained for instance in [73]. The possibilities of substructuring in ANSYS can be used for this purpose.

Furthermore, in the next step, objective functions based on different physical properties should be defined or a multi objective Pareto optimisation could be performed minimising several objective functions at the same time. Moreover, different optimisation algorithms can be tested, for instance the NLPQL algorithm developed by Schittkowsky [68].

In order to apply the results of research in the practical field of damage assessment of civil engineering structures, a highly automated expert system with different methods for damage assessment should be developed.

REFERENCES

[1]   Waltering M. Damage assessment of civil engineering structures and bridges using nonlinear dynamic characteristics. Dissertation Université du Luxembourg, 2009: Shaker Verlag Aachen.

[2]   Bungard V, Waldmann D, Maas S. Condition assessment of concrete structures and bridges using vibration monitoring in comparison to changes in their static properties. Dissertation Université du Luxembourg, 2010: Shaker Verlag Aachen.

[3]   Mahowald J. Evaluation of dynamic damage indicators on real-life civil engineering structures: Measurement uncertainty and environmental influences considered. Dissertation Université du Luxembourg, 2013: Shaker Verlag Aachen.

[4]   Rytter A. Vibrational based inspection of civil engineering structures. Dissertation Aalborg University, 1993.

[5]   Bauwerksprüfung nach DIN 1076: Bedeutung, Organisation, Kosten ; Dokumentation 2013. 06th ed. Berlin: Bundesministerium für Verkehr Bau und Stadtentwicklung; 2013.

[6]   Peeters B, Ventura CE. Comparative study of modal analysis techniques for bridge dynamic characteristics. Mechanical Systems and Signal Processing 2003;17(5):965–988.

[7]   Parloo E, Guillaume P, van Overmeire M. Damage assessment using mode shape sensitivities. Mechanical Systems and Signal Processing 2003;17(3):499–518.

[8]   Nguyen VH, Golinval J-C. Localization and quantification of damage in beam-like structures using sensitivies of principal component analysis results. Mechanical Systems and Signal Processing 2010;24(6):1831–1843.

[9]   Maas S, Schommer S, Nguyen VH, Waldmann D, Mahowald J, Zürbes A, Feltrin G. Some remarks on the influence of temperature-variations, non-linearities, repeatability and ageing on modal-analysis for structural health monitoring of real bridges. MATEC Web of Conferences 2015;24(EVACES'15, 6th International Conference on Experimental Vibration Analysis for Civil Engineering Structures).

[10] Nguyen VH, Schommer S, Zürbes A, Maas S. Damage detection for bridge structures based on dynamic and static measurements. QUALITY SPECIFICATIONS FOR ROADWAY BRIDGES, STANDARDIZATION AT A EUROPEAN LEVEL COST TU1406 2016.

References

[11] Nguyen VH, Schommer S, Zürbes A, Maas S. Structural health monitoring based on static measurements with temperature compensation. QUALITY SPECIFICATIONS FOR ROADWAY BRIDGES, STANDARDIZATION AT A EUROPEAN LEVEL COST TU1406 2016.

[12] Strauss A, Bergmeister K, Ivankovi AM, Matos JC. Applied and research based performance indicator database for highway bridges across Europe. In: Bakker J, Frangopol DM, van Breugel K, editors. Life-cycle of engineering systems: Emphasis on sustainable civil infrastructure. Leiden: CRC Press/Balkema; op. 2017.

[13] Pandey AK, Biswas M. Damage Detection in Structures Using Changes in Flexibility. Journal of Sound and Vibration 1994;169(1):3–17.

[14] Pandey AK, Biswas M. Experimental verification of flexibility difference method for locating damage in structures. Journal of Sound and Vibration 1995;184(2):311–328.

[15] Yan A-M, Golinval J-C. Structural damage localization by combining flexibility and stiffness methods. Engineering Structures 2005;27(12):1752–1761.

[16] Duan Z, Yan G, Ou J, Spencer BF. Damage localization in ambient vibration by constructing proportional flexibility matrix. Journal of Sound and Vibration 2005;284(1-2):455–466.

[17] Bernal D. Load Vectors for Damage Localization. Journal of Engineering Mechanics 2002;128(1):7–14.

[18] Duan Z, Yan G, Ou J, Spencer BF. Damage detection in ambient vibration using proportional flexibility matrix with incomplete measured DOFs. Struct. Control Health Monit. 2007;14(2):186–196.

[19] Shih HW, Thambiratnam DP, Chan THT. Vibration based structural damage detection in flexural members using multi-criteria approach. Journal of Sound and Vibration 2009;323(3):645–661.

[20] Nobahari M, Seyedpoor SM. An efficient method for structural damage localization based on the concepts of flexibility matrix and strain energy of a structure. Structural Engineering and Mechanics 2013;46(2):231–244.

[21] Montazer M, Seyedpoor SM. A New Flexibility Based Damage Index for Damage Detection of Truss Structures. Shock and Vibration 2014;2014(2):1–12.

[22] Reynders E, De Roeck G. A local flexibility method for vibration-based damage localization and quantification. Journal of Sound and Vibration 2010;329(12):2367–2383.

[23] Yan G, Duan Z, Ou J. Damage detection for beam structures using an angle-between-string-and-horizon flexibility matrix. Structural Engineering and Mechanics 2010;36(5):643–667.

[24] Weng S, Zhu H-P, Xia Y, Mao L. Damage detection using the eigenparameter decomposition of substructural flexibility matrix. Mechanical Systems and Signal Processing 2013;34(1-2):19–38.

[25] Chen J-T, Huang W-S, Lee J-W, Tu Y-C. A self-regularized approach for deriving the free–free flexibility and stiffness matrices. Computers & Structures 2014;145:12–22.

[26] Feng, Z., Katafygiotis, L.S. Bayesian model updating based on modal flexibility for structural health monitoring. In: Cunha Á, Caetano EdS, Ribeiro P, Müller G, editors. Eurodyn 2014: Proceedings of the 9th International Conference on Structural Dynamics, Porto, Portugal, 30 June - 2 July 2014. [Porto: Faculty of Engineering]; 2014.

[27] Sung SH, Jung HJ, Jung HY. Damage detection for beam-like structures using the normalized curvature of a uniform load surface. Journal of Sound and Vibration 2013;332(6):1501–1519.

[28] Sung SH, Koo KY, Jung HJ. Modal flexibility-based damage detection of cantilever beam-type structures using baseline modification. Journal of Sound and Vibration 2014;333(18):4123–4138.

[29] Masoumi M, Jamshidi E, Bamdad M. Application of generalized flexibility matrix in damage identification using Imperialist Competitive Algorithm. KSCE J Civ Eng 2015;19(4):994–1001.

[30] Li J, Wu B, Zeng QC, Lim CW. A generalized flexibility matrix based approach for structural damage detection. Journal of Sound and Vibration 2010;329(22):4583–4587.

[31] Perera R, Ruiz A, Manzano C. Performance assessment of multicriteria damage identification genetic algorithms. Computers & Structures 2009;87(1-2):120–127.

[32] Atashpaz-Gargari E, Lucas C. Imperialist competitive algorithm: An algorithm for optimization inspired by imperialistic competition. In: 2007 IEEE Congress on Evolutionary Computation, Singapore.

[33] Stutz LT, Tenenbaum RA, Corrêa RAP. The Differential Evolution method applied to continuum damage identification via flexibility matrix. Journal of Sound and Vibration 2015;345:86–102.

References

[34] Link M. UPDATING ANALYTICAL MODELS BY USING LOCAL AND GLOBAL PARAMETERS AND RELAXED OPTIMISATION REQUIREMENTS. Mechanical Systems and Signal Processing 1998;12(1):7–22.

[35] Link M. Updating of analytical models—review of numerical procedures and application aspects. In: Proc., Structural Dynamics Forum SD2000.

[36] Teughels A, Maeck J, De Roeck G. Damage assessment by FE model updating using damage functions. Computers & Structures 2002;80(25):1869–1879.

[37] Teughels A, De Roeck G. Structural damage identification of the highway bridge Z24 by FE model updating. Journal of Sound and Vibration 2004;278(3):589–610.

[38] Unger JF, Teughels A, De Roeck G. System Identification and Damage Detection of a Prestressed Concrete Beam. J. Struct. Eng. 2006;132(11):1691–1698.

[39] Titurus B, Friswell MI, Starek L. Damage detection using generic elements: Part I. Model updating. Computers & Structures 2003;81(24):2273–2286.

[40] Titurus B, Friswell MI, Starek L. Damage detection using generic elements: Part II. Damage detection. Computers & Structures 2003;81(24):2287–2299.

[41] Jaishi B, Ren W-X. Damage detection by finite element model updating using modal flexibility residual. Journal of Sound and Vibration 2006;290(1-2):369–387.

[42] Jaishi B, Kim H-J, Kim MK, Ren W-X, Lee S-H. Finite element model updating of concrete-filled steel tubular arch bridge under operational condition using modal flexibility. Mechanical Systems and Signal Processing 2007;21(6):2406–2426.

[43] Perera R, Ruiz A, Manzano C. An evolutionary multiobjective framework for structural damage localization and quantification. Engineering Structures 2007;29(10):2540–2550.

[44] Mordini A, Savov K, Wenzel H. The Finite Element Model Updating: A Powerful Tool for Structural Health Monitoring. Structural Engineering International 2007;17(4):352–358.

[45] Schlune H, Plos M, Gylltoft K. Improved bridge evaluation through finite element model updating using static and dynamic measurements. Engineering Structures 2009;31(7):1477–1485.

[46] Weng S, Xia Y, Zhou X-Q, Xu Y-L, Zhu H-P. Inverse substructure method for model updating of structures. Journal of Sound and Vibration 2012;331(25):5449–5468.

[47] Link M, M. Weiland. Extending a deterministic computational model updating technique to estimating the parameter variability caused by non-deterministic test data – a tool for Structural Health Monitoring. In: Sas P, D. Moens, H. Denayer, editors.

Proceedings of the International Conference on Noise and Vibration Engineering ISMA 2014. Leuven, Belgium; 2014, p. 2701–2713.

[48] Gutermann M. Ein Beitrag zur experimentell gestützten Tragsicherheitsbewertung von Massivbrücken. Dissertation Technische Universität Dresden; 2003.

[49] Nguyen VH, Mahowald J, Schommer S, Maas S, Zuerbes A. A Study of Temperature and Aging Effects on Eigenfrequencies of Concrete Bridges for Health Monitoring. ENG 2017;09(05):396–411.

[50] Peeters B, De Roeck G. One-year monitoring of the Z24-Bridge: environmental effects versus damage events. Earthquake engineering & structural dynamics 2001;30(2):149–171.

[51] van Overschee P, Moor B de. Subspace algorithms for the stochastic identification problem. Automatica 1993;29(3):649–660.

[52] Yan A-M, Kerschen G, Boe P de, Golinval J-C. Structural damage diagnosis under varying environmental conditions—Part I: A linear analysis. Mechanical Systems and Signal Processing 2005;19(4):847–864.

[53] Yan A-M, Kerschen G, Boe P de, Golinval J-C. Structural damage diagnosis under varying environmental conditions—part II: Local PCA for non-linear cases. Mechanical Systems and Signal Processing 2005;19(4):865–880.

[54] Nguyen VH, Mahowald J, Golinval J-C, Maas S. Damage detection in bridge structures including environmental effects. In: Cunha Á, Caetano EdS, Ribeiro P, Müller G, editors. Eurodyn 2014: Proceedings of the 9th International Conference on Structural Dynamics, Porto, Portugal, 30 June - 2 July 2014. [Porto: Faculty of Engineering]; 2014.

[55] Nguyen VH, Rutten C, Golinval J-C, Mahowald J, Maas S, Waldmann D. Damage detection on the Champangshiehl bridge using blind source separation. Life-Cycle and Sustainability of Civil Infrastructure Systems 2012.

[56] Mahowald J, Maas S, Scherbaum F, Waldmann D, Zürbes A. Dynamic damage identification using linear and nonlinear testing methods on a two-span prestressed concrete bridge. In: Strauss A, Frangopol D, Bergmeister K, editors. Life-Cycle and Sustainability of Civil Infrastructure Systems: Proceedings of the Third International Symposium on Life-Cycle Civil Engineering (IALCCE'12), Vienna, Austria, October 3-6, 2012. Hoboken: CRC Press; 2012, p. 157–164.

[57] Mahowald J, Maas S, Waldmann D, Zürbes A, Scherbaum F. Damage Identification and Localisation Using Changes in Modal Parameters for Civil Engineering Structures.

References

In: Sas P, editor. International Conference on Noise and Vibration Engineering 2012 (ISMA 2012): Including USD 2012 ; Leuven, Belgium, 17 - 19 September 2012. Red Hook, NY: Curran; 2013, p. 1103–1117.

[58] Maas S, Zürbes A, Waldmann D, Waltering M, Bungard V, De Roeck G. Damage assessment of concrete structures through dynamic testing methods: Part 2: Bridge tests. Engineering Structures 2012;34:483–494.

[59] Waltering M, Bungard V, Maas S, Zürbes A, Waldmann D, De Roeck G. Non-destructive Damage Assessment Using Non-linear Vibration. In: International Modal Analysis Conference, IMAC-XXVI.

[60] Zong Z, Lin X, Niu J. Finite element model validation of bridge based on structural health monitoring—Part I: Response surface-based finite element model updating. Journal of Traffic and Transportation Engineering (English Edition) 2015;2(4):258–278.

[61] Lin X, Zong Z, Niu J. Finite element model validation of bridge based on structural health monitoring—Part II: Uncertainty propagation and model validation. Journal of Traffic and Transportation Engineering (English Edition) 2015;2(4):279–289.

[62] Schommer S, Nguyen VH, Maas S, Zürbes A. Model updating for structural health monitoring using static and dynamic measurements. Procedia Engineering 2017;199:2146–2153.

[63] Heylen W, Lammens S, Sas P. Modal analysis theory and testing. 2nd ed. Belgium: Katholieke Universiteit Leuven, Faculty of Engineering, Dept. of Mechanical Engineering, Division of Production Engineering, Machine Design and Automation; 1998.

[64] Maia, Nuno Manuel Mendes, Montalvão e Silva, J. M. Theoretical and experimental modal analysis. Taunton, Somerset, England, New York: Research Studies Press; Wiley; 1997.

[65] Wang T, Zhang L, Tee KF. Extraction of real modes and physical matrices from modal testing. Earthq. Eng. Eng. Vib. 2011;10(2):219–227.

[66] Ewins DJ. Modal testing: Theory and practice. 2nd ed. Baldock, England: Research Studies Press; op. 2000.

[67] Nocedal J, Wright SJ. Numerical Optimization. New York, NY: Springer Science+Business Media, LLC; 2006.

[68] Schittkowski K. NLPQL: A FORTRAN subroutine solving constrained nonlinear programming problems. Annals of operations research 1986;5(2):485–500.

[69] Nguyen VH, Schommer S, Maas S, Zürbes A. Static load testing with temperature compensation for structural health monitoring of bridges. Engineering Structures 2016;127:700–718.

[70] Holzmann G, Meyer H, Schumpich G. Technische Mechanik Festigkeitslehre. 10th ed. Wiesbaden: Springer Vieweg; 2012.

[71] Häfele P, Issler L, Ruoß H. Festigkeitslehre - Grundlagen. 2nd ed. Berlin, Heidelberg: Springer-Verlag Berlin Heidelberg; 2003.

[72] Guillaume P, Verboven P, Vanlanduit S, van der Auweraer H, Peeters B. A poly-reference implementation of the least-squares complex frequency-domain estimator. In: Proceedings of IMAC.

[73] Gasch R, Knothe K, Liebich R. Strukturdynamik: Diskrete Systeme und Kontinua. 2nd ed. Berlin, Heidelberg: Springer Vieweg; 2012.

[74] Schommer S, Mahowald J, Nguyen VH, Waldmann D, Maas S, Zürbes A, Roeck GD. Health Monitoring Based on Dynamic Flexibility Matrix: Theoretical Models versus In-Situ Tests. Engineering 2017;09(02):37–67.

References

APPENDIX

A.1 Definition of vector and matrix norms

A norm is a function that assigns a positive value to a vector or matrix, in order to define its magnitude. Different possibilities exist for this purpose. Here the ones used in the present thesis are described.

p-norm

The p-norm, also called Lp-norm, of a vector $\{x\} = \{x_1\ x_2\ ...\ x_i\ ...\ x_n\}$ with $x_i \in \mathbb{C}$ is defined as:

$$\|\{x\}\|_p := \left(\sum_{i=1}^{n} |x_i|^p \right)^{\frac{1}{p}} \tag{A-1}$$

Where p is a positive integer, i.e. $p \in [0, 1, 2, ..., \infty]$.

For $p = 2$ one obtains the Euclidean or L2-norm, which is most commonly used to define the magnitude or length of a vector.

$$\|\{x\}\|_2 := \sqrt{\sum_{i=1}^{n} |x_i|^2} \tag{A-2}$$

Here for real vectors, i.e. $x_i \in \mathbb{R}$ the absolute value bars in equation (A-2) can be omitted.

For $p = 1$ equation (A-1) gives the L1-norm, which is in fact the sum of the absolute values of the components x_i.

$$\|\{x\}\|_1 := \sum_{i=1}^{n} |x_i| \tag{A-3}$$

For a complete definition of the p-norms, two special cases $p = 0$ and $p = \infty$, must be considered. The L0-norm is commonly defined as the total number of non-zero elements of a vector, while the L∞-norm is the magnitude of the maximum component of vector $\{x\}$.

Frobenius norm

For matrices the so-called Frobenius norm can be calculated, which is defined for a matrix of dimension $N \times M$ as:

$$\|[\mathbf{A}]\|_F = \sum_{i=1}^{N} \sum_{j=1}^{M} |a_{ij}|^2 \qquad \text{(A-4)}$$

Thus, it is the sum of the squared components of the matrix.

A.2 FEM results for the healthy state of the test setup in the port of Mertert
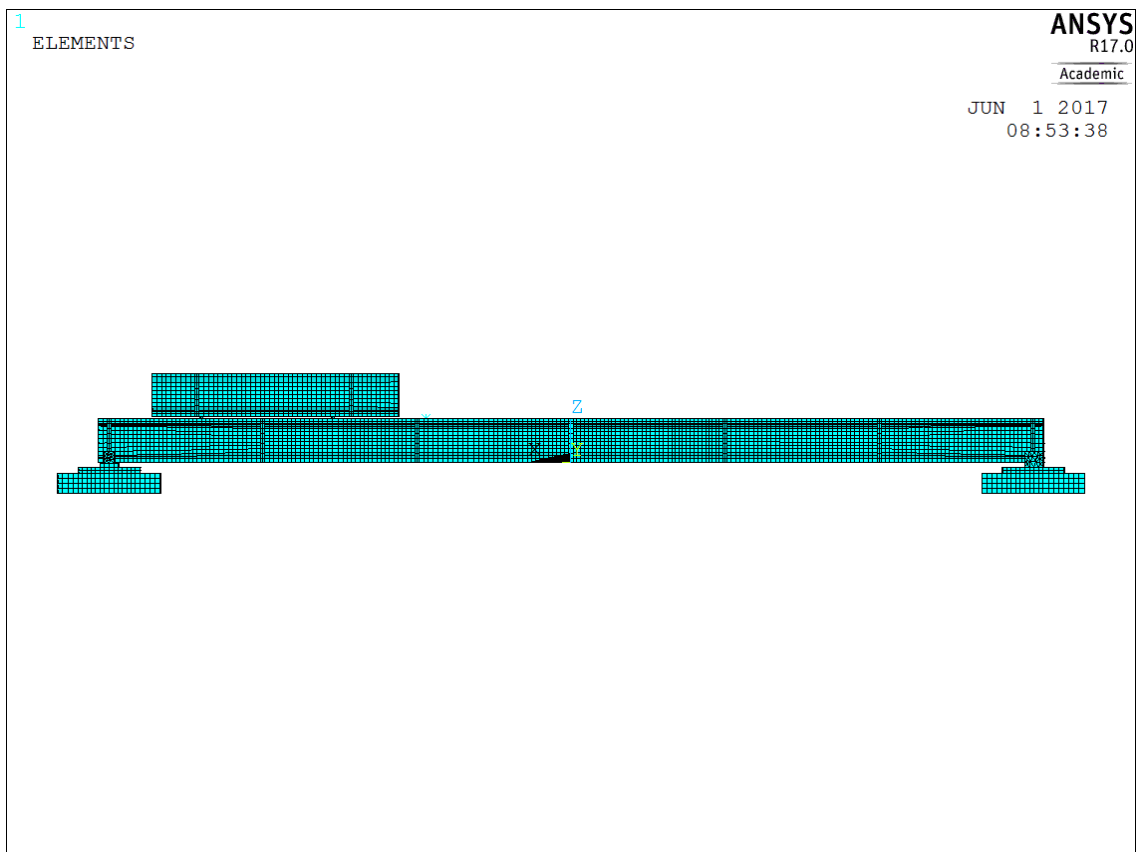
Figure A.1: FE-model
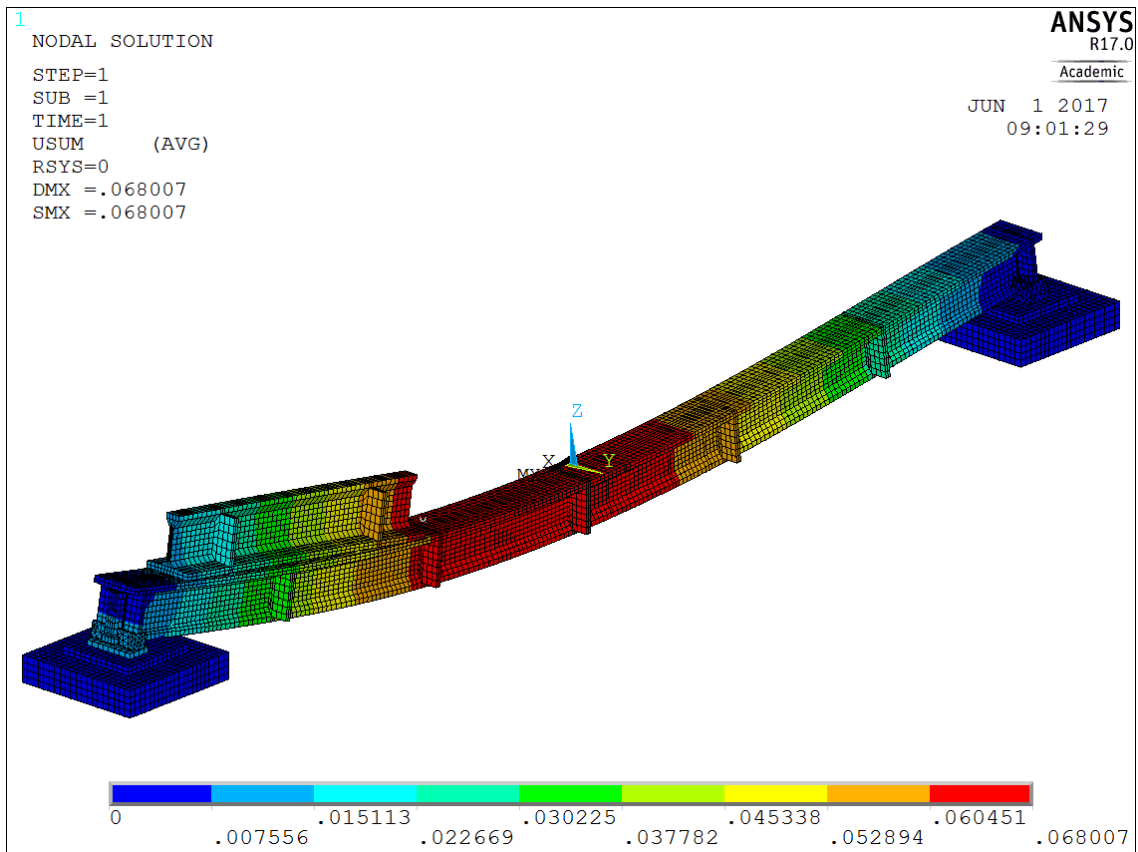
Figure A.2: Deflection due to gravity
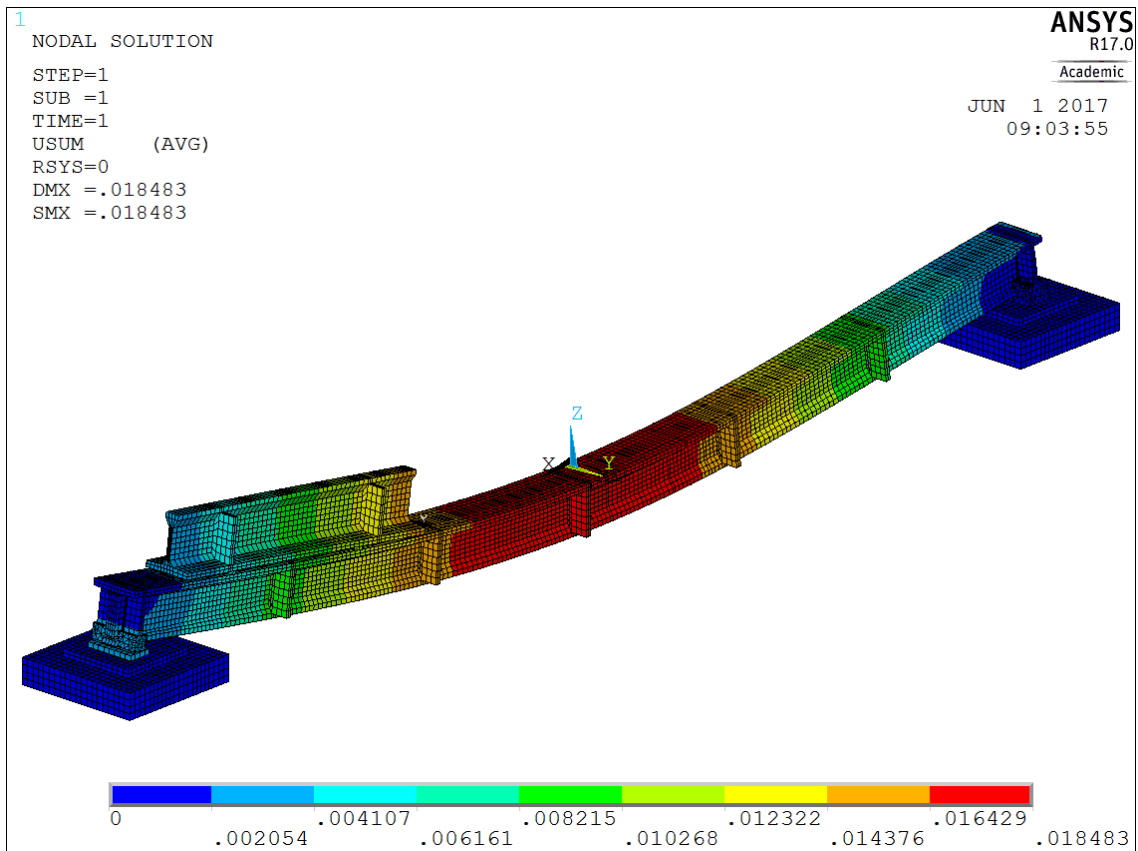
Figure A.3: Deflection due to loading with 2 weights of each 13t
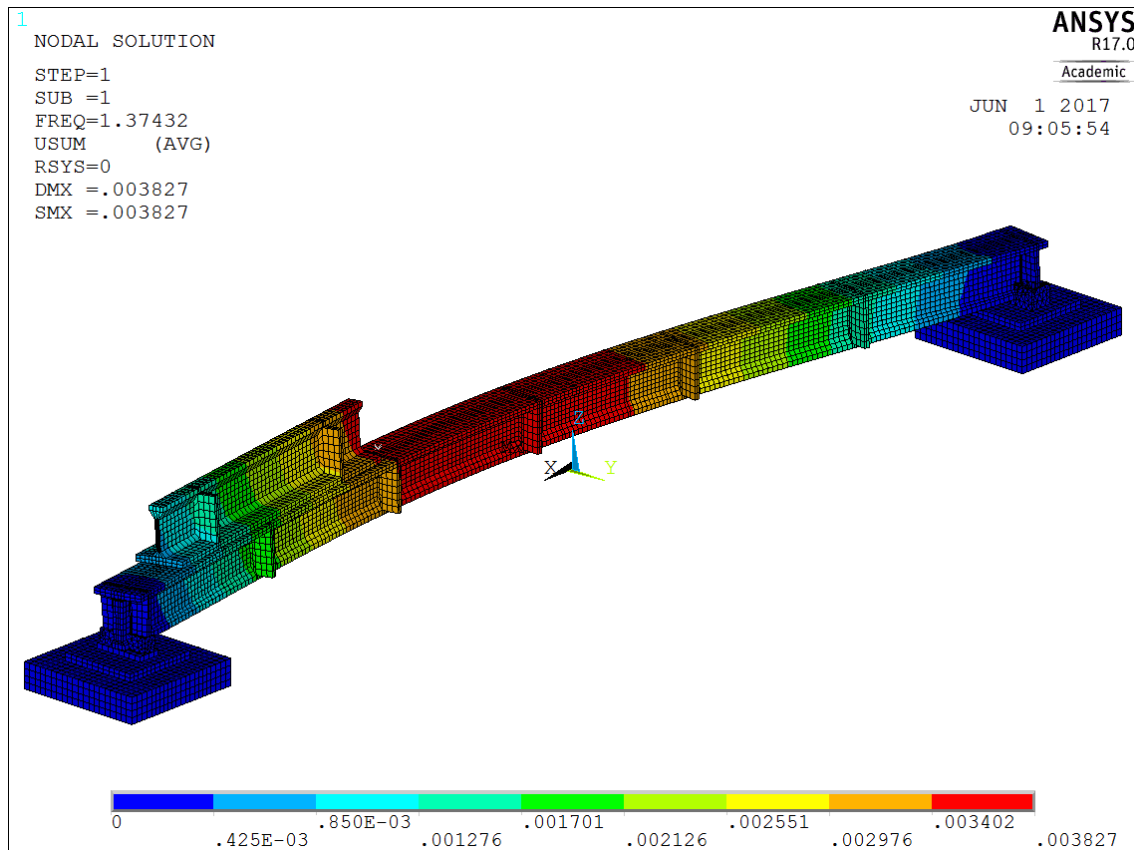
Figure A.4: Mode 1 at 1.37 Hz – bending in y-direction
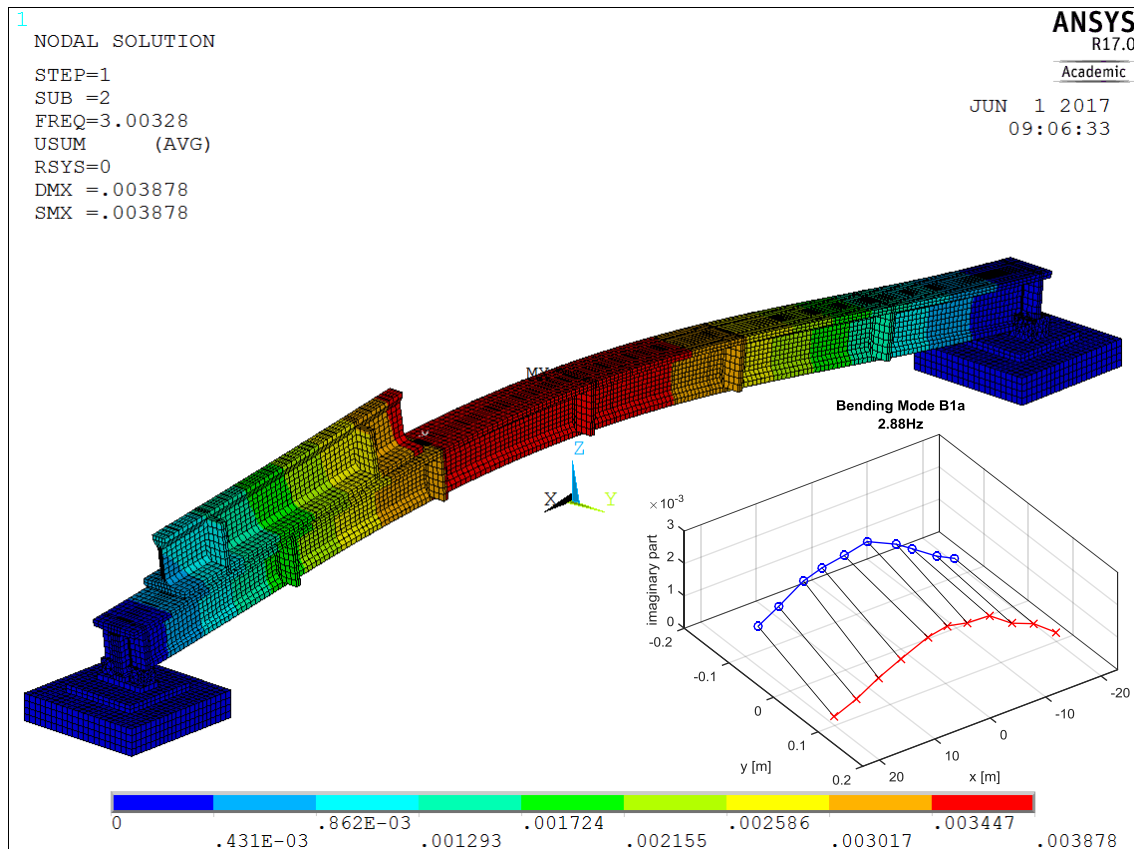
Figure A.5: Mode 2 at 3.00 Hz – bending in z-direction; right: correlated measured mode
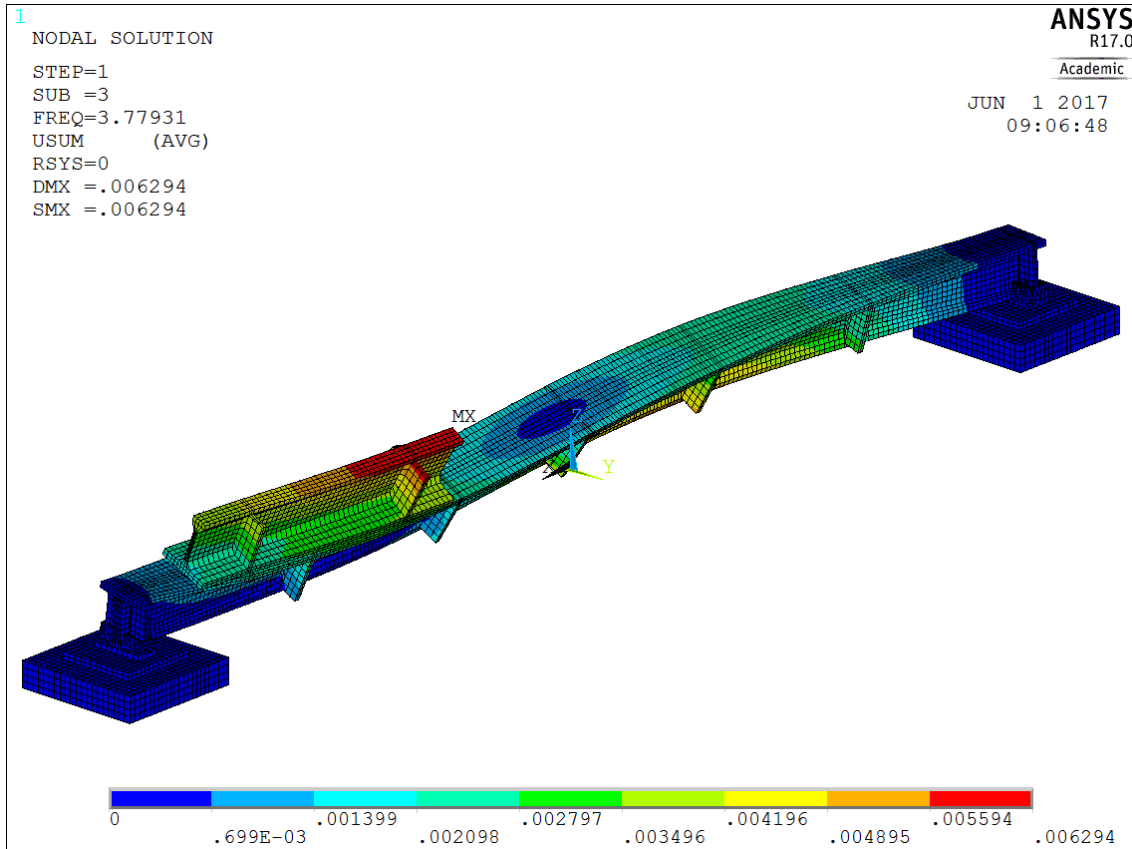
Figure A.6: Mode 3 at 3.78 Hz - torsional
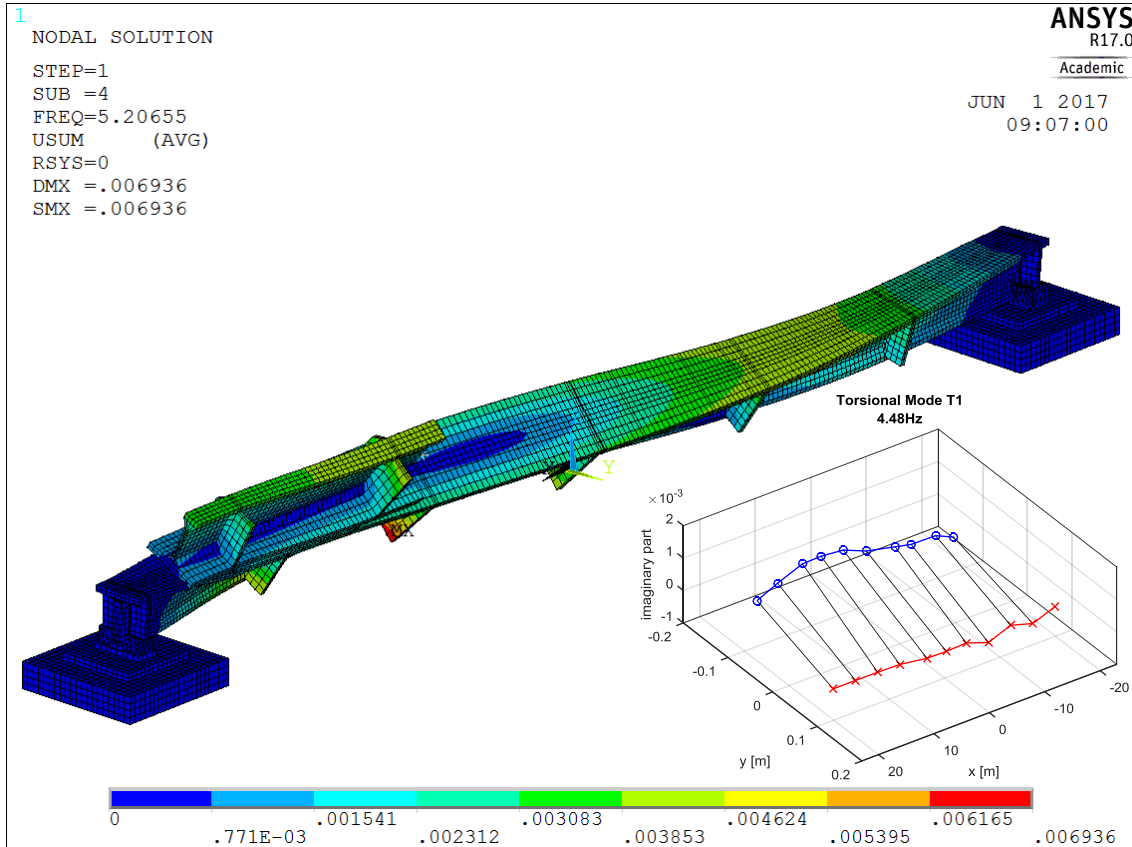
Figure A.7: Mode 4 at 5.21 Hz - torsional; right: correlated measured mode
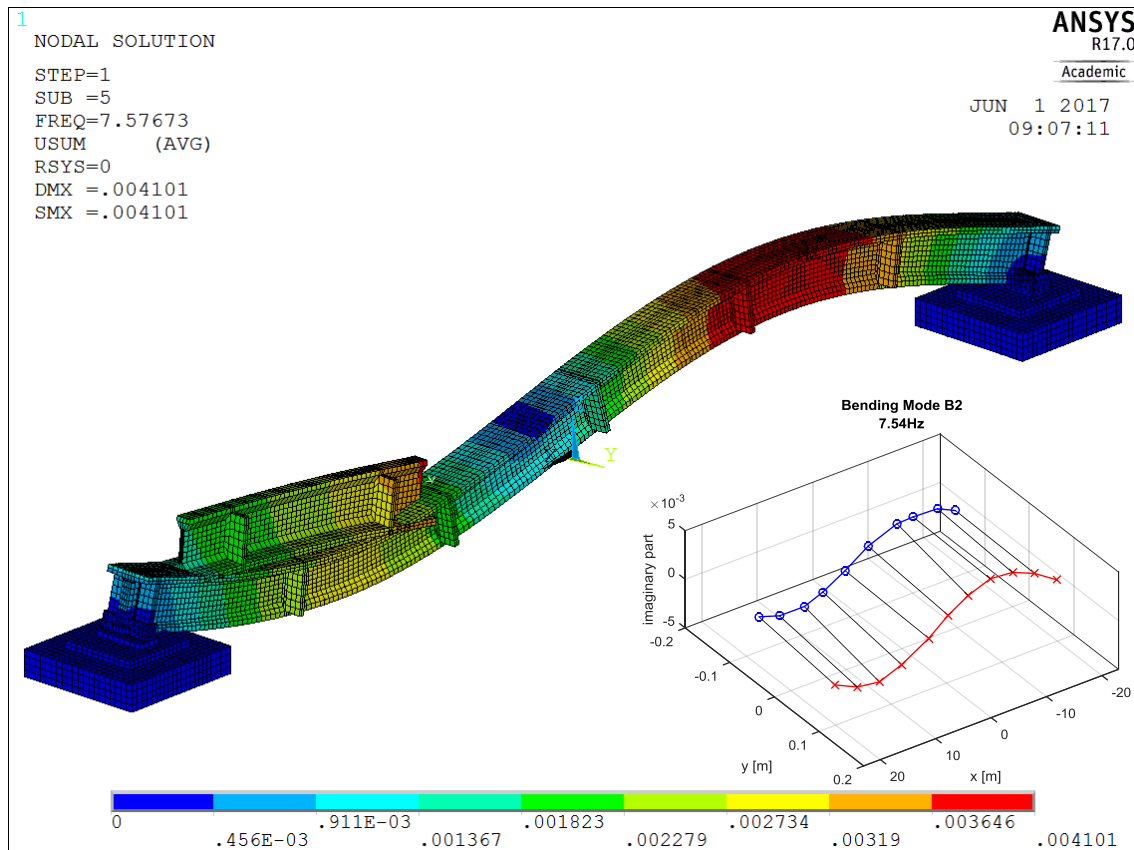
Figure A.8: Mode 5 at 7.58 Hz – bending in z-direction; right: correlated measured mode
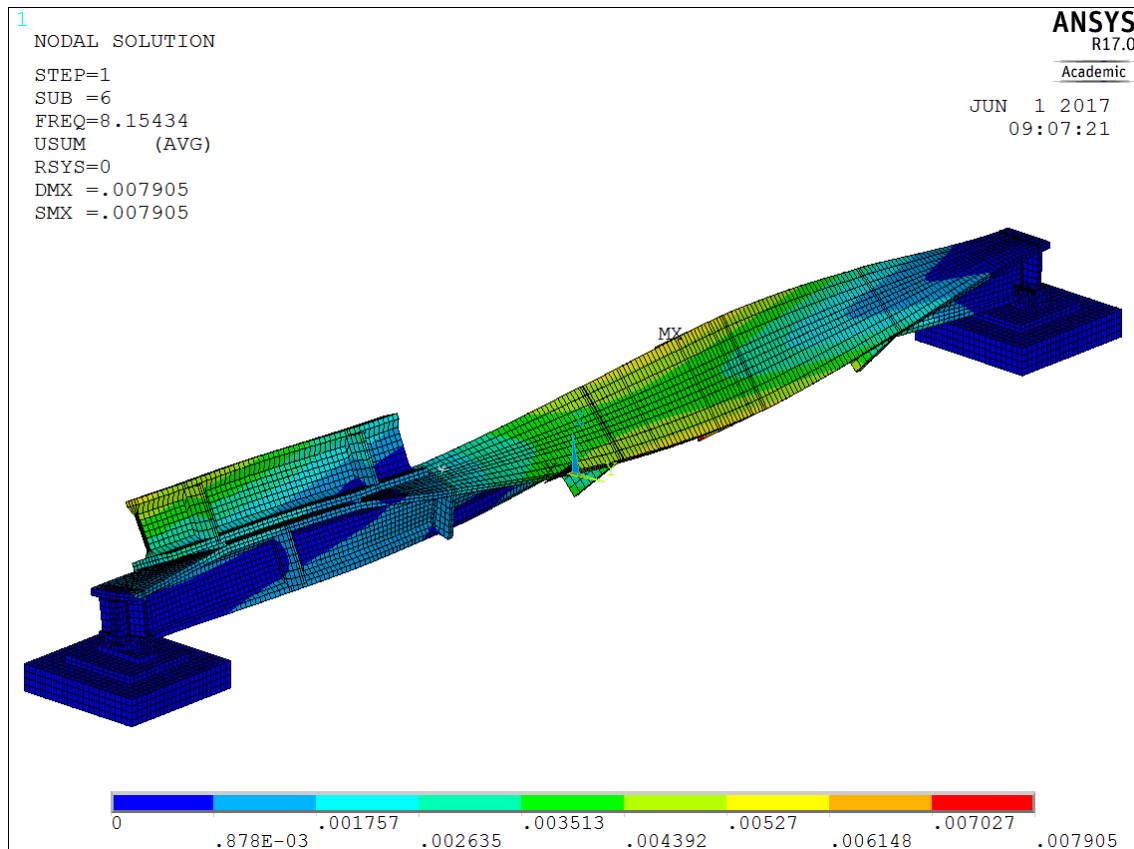
Figure A.9: Mode 6 at 8.15 Hz - torsional
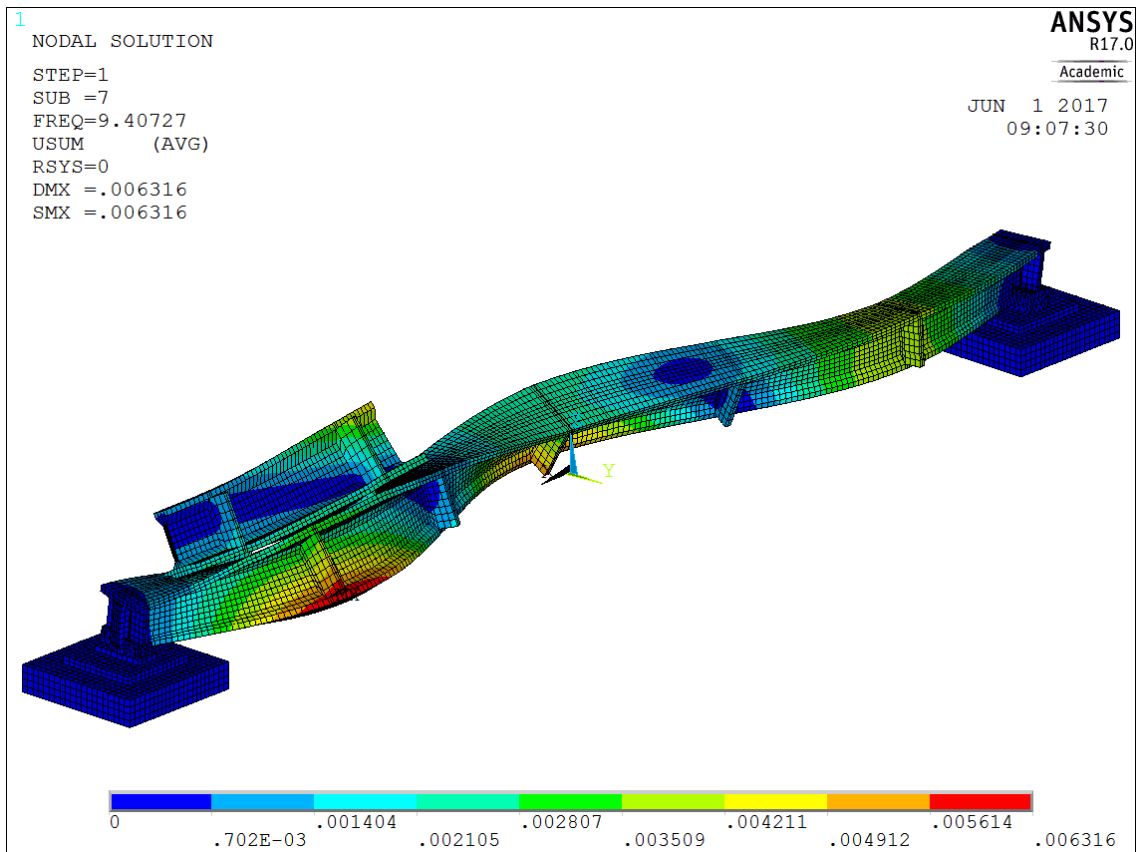
Figure A.10: Mode 7 at 9.41 Hz - torsional
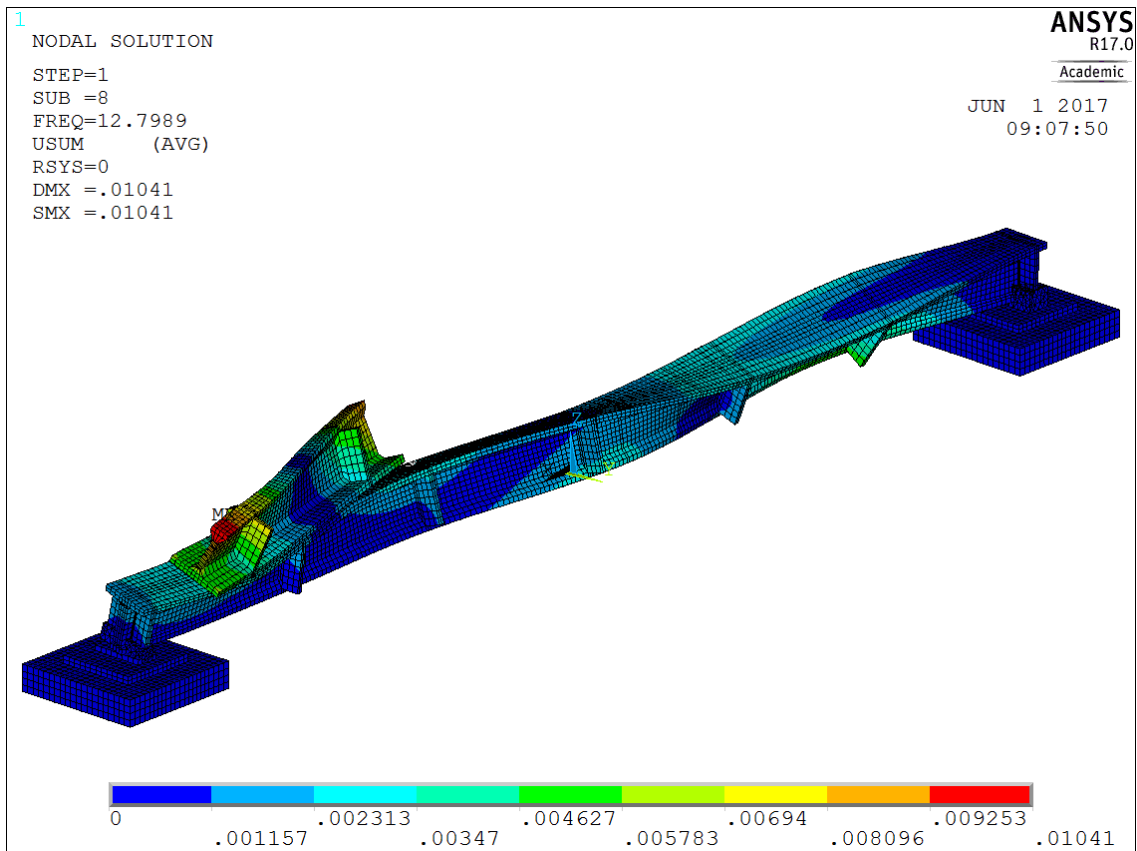
Figure A.11: Mode 8 at 12.80 Hz - torsional

A.3 Additional results for the evaluation in Chapter 8.6

Plots of the objective functions, if the parameter sets from Table 8.12 are used:

a) μ and σ fixed   b) μ and p fixed
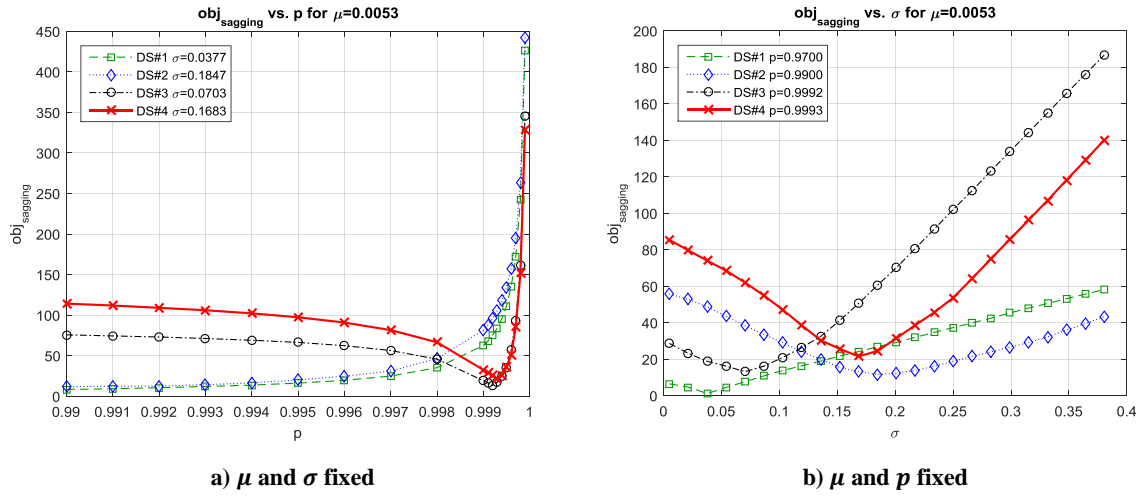
Figure A.12: Objective function based on the sagging of the test beam (L1-norm)

a) μ and σ fixed   b) μ and p fixed
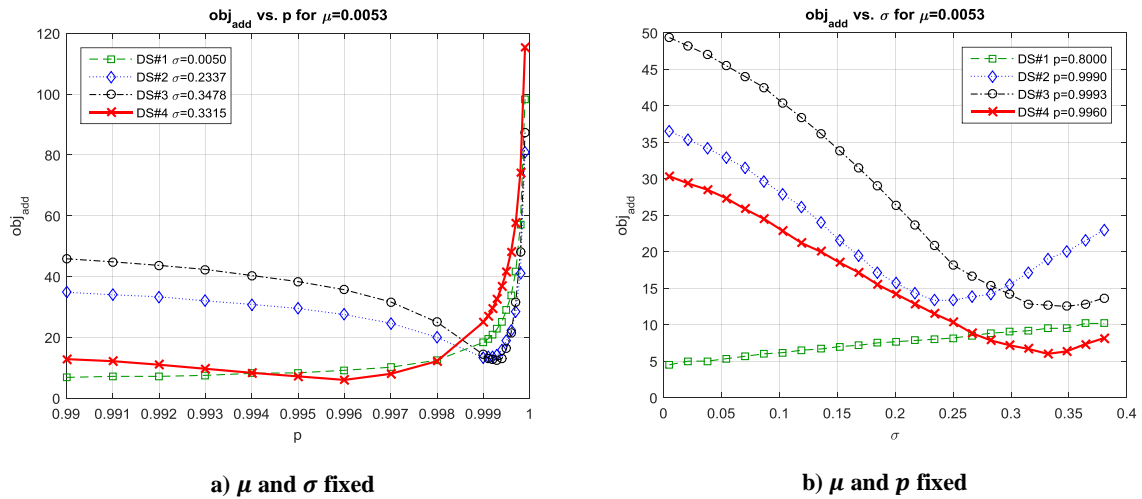
Figure A.13: Objective function based on deflection due to additional loads (L1-norm)

a) μ and σ fixed
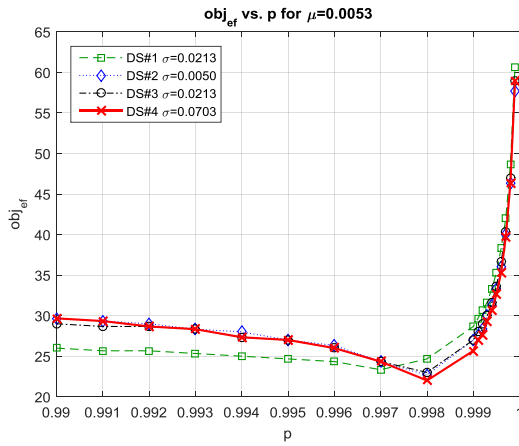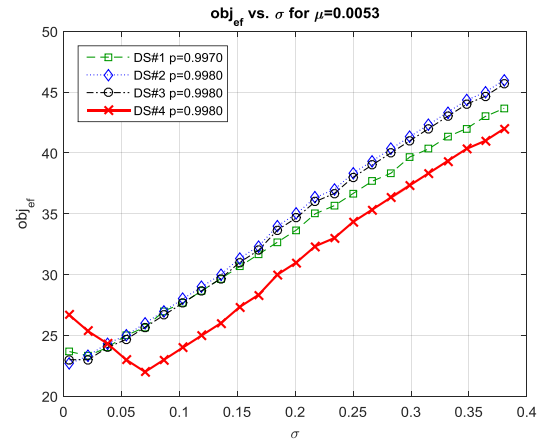
b) μ and p fixed

Figure A.14: Objective function based on eigenfrequencies (L1-norm)
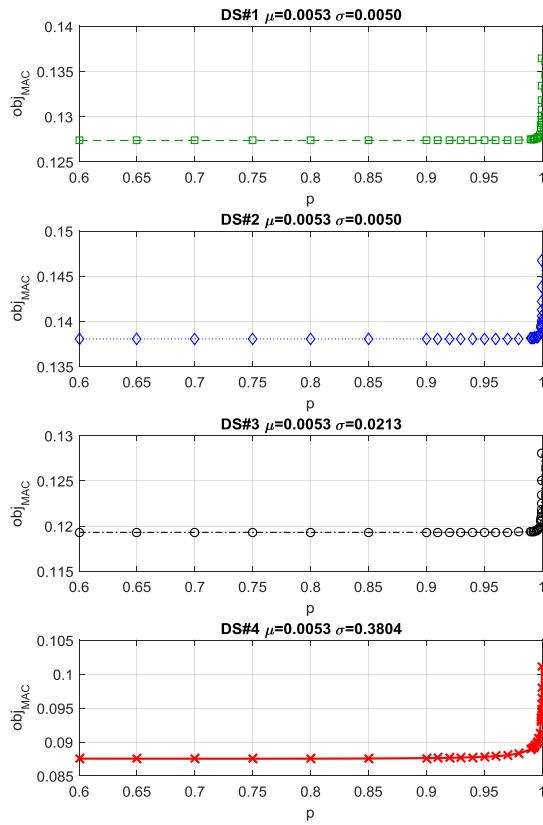
a) obj_{MAC} vs. p for fixed μ and σ
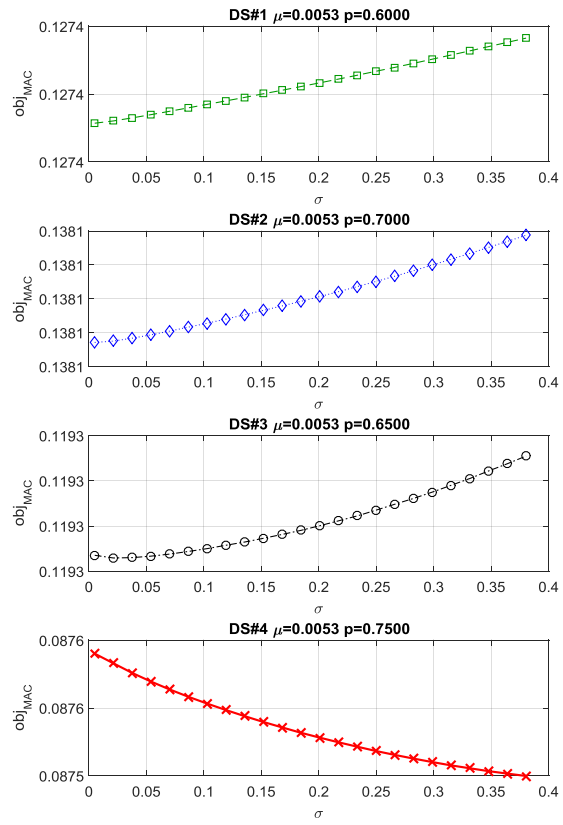
b) obj_{MAC} vs. σ for fixed μ and p

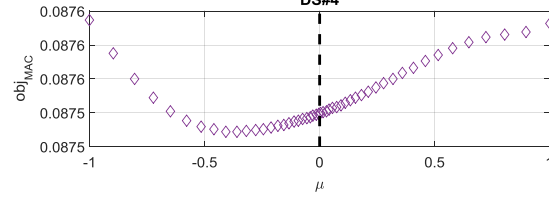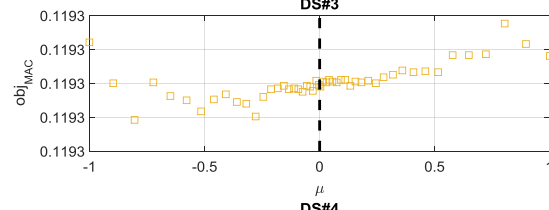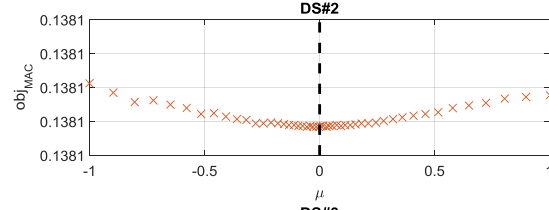**Figure A.15: Objective function based on mode shape comparison by means of MAC (L1-norm)**
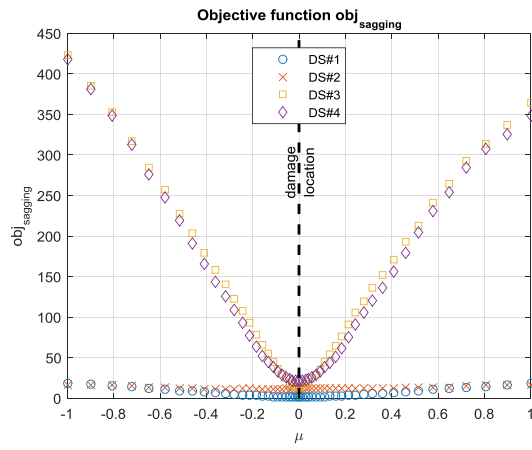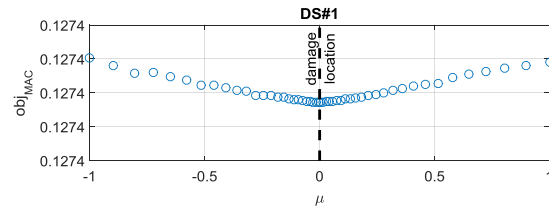
a) $obj_{sagging}$
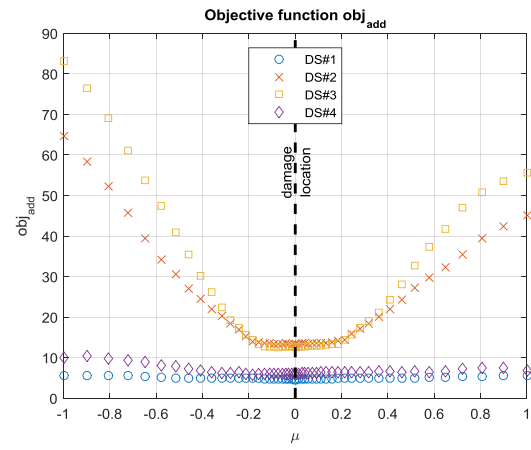
b) obj_{add}
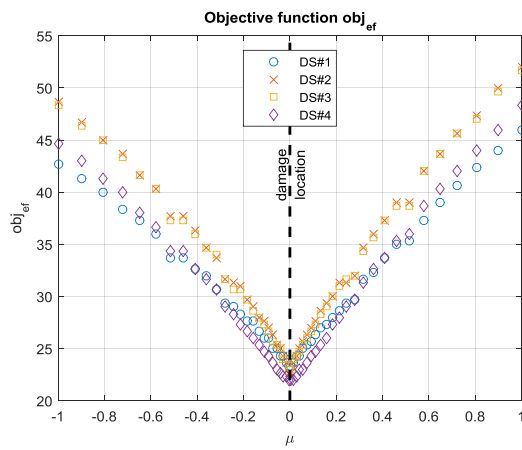
c) obj_{ef}

d) obj_{MAC}

Figure A.16: Objective functions vs. μ with optimal values from Table 8.12

Reduction of Young's modulus, if objective functions with L1-norm are used:
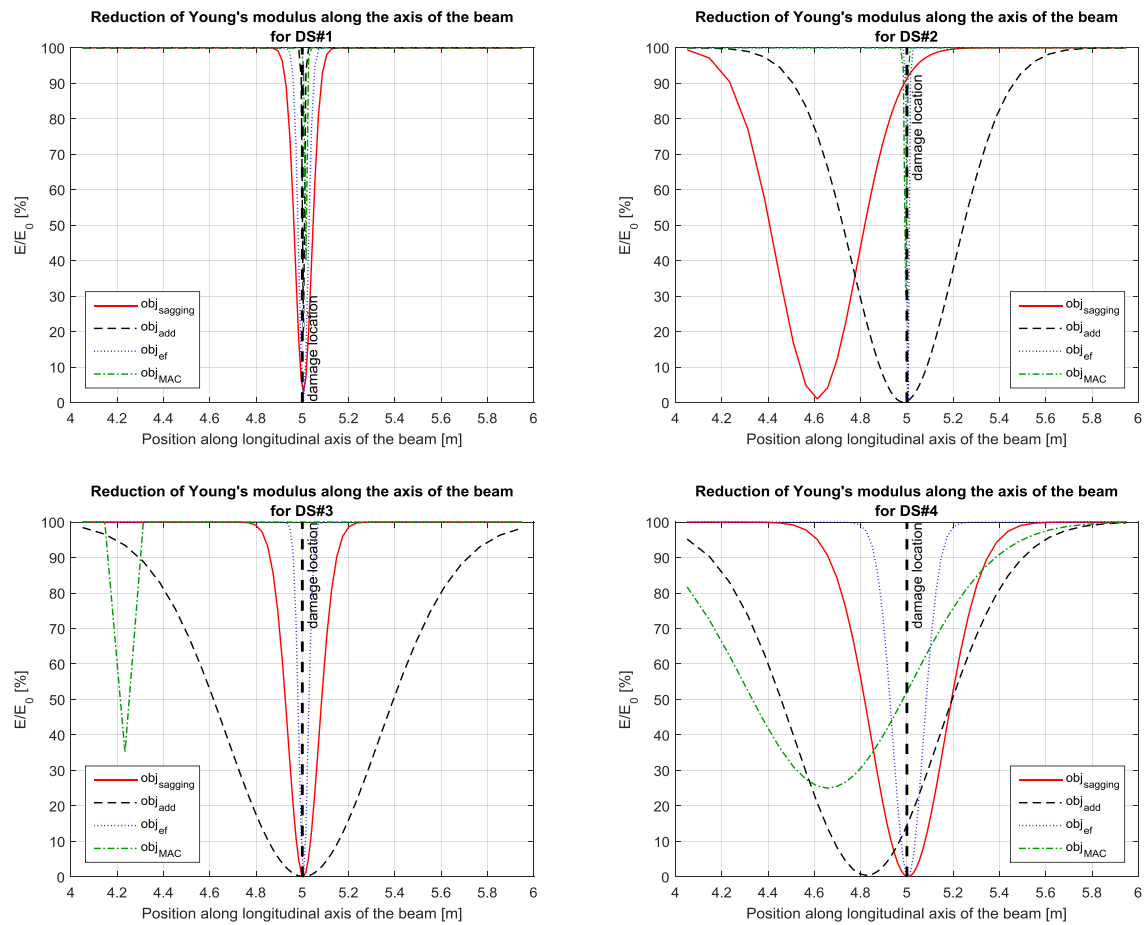

Figure A.17: Reduction of Young's modulus along the axis of the beam in the FE-model based on the found optimal parameter sets if objective functions with L1-norm are used